Soft materials fabrication and simulation for drug delivery and tissue engineering

Yunong Yuan

A thesis submitted to fulfil of the requirements for the degree of

Doctor of Philosophy

Sydney Pharmacy School

Faculty of Medicine and Health

The University of Sydney

2024

Statement of Originality

I certify that the intellectual content of this thesis is the product of my own work and that all the assistance received in preparing this thesis and sources have been acknowledged. No portion of the work referred to in the thesis has been submitted in support of an application for another degree or qualification of this or any other university or other institutes of learning.

Yunong Yuan, BEng, MPhil

Acknowledgement

I would like to sincerely thank my supervisors, Dr Lifeng Kang and Dr Philip Kwok, for the continued support, help and the excellent collaboration throughout my PhD study. I do appreciate everything they have done to help me, and I am grateful for everything they have taught me. Meanwhile, I would also like to thank the whole support team from Sydney Pharmacy School, Charles Perkin Centre, Sydney Microscopy & Microanalysis centre, and Faculty of Engineering, in University of Sydney, for the training and equipment support.

This thesis was supported by the award of a Research Training Program scholarship and John A Lamberton Research Scholarships to the PhD Candidate.

Table of Contents

Statement of Originality ii
Acknowledgement iii
List of Publications vi
Copyright Information viii
Abstract ix
List of Abbreviations xi
Thesis Authorship Statement xiv
Chapter 1 Introduction 1
1.1 Background 1
1.2 Thesis structure 2
Chapter 2 Literature review on additive manufacturing: biomaterials, photocrosslinkable mechanism and simulation. 5
2.1 Classification of additive manufacturing 5
2.2 The mechanism of free radical chain growth polymerisation 9
2.3 Photocrosslinkable biomaterials used in digital light processing 11
2.3.1 Natural materials modified photocrosslinkable materials 12
2.3.2 Synthetic biomaterials modified photocrosslinkable materials 14
2.3.3 Degree of substitution 16
2.4 Photoinitiators used in digital light processing. 17
2.5 Potential of toxicity during DLP Printing 21
2.6 Simulation application in AM based biomedical engineering 23
2.6.1 Theory used in the 3D bioprinting simulation 24
2.6.2 The application of simulation methods in the 3D bioprinting area 30
2.6.3 Discussion 47
Reference 53
Chapter 3 Controlled Release of Vancomycin From PEGylated Fibrinogen Polyethylene Glycol Diacrylate Hydrogel 65
3.1 Introduction 66
3.2 Materials and Methods 69
3.3 Results 76
3.4 Discussion 86
3.5 Conclusion 90
References 91
Supplementary Information 94
Chapter 4 Manufacture Hydrogel Microwells Using Optical 3D Printers for Human Spheroids Culture in Vitro 98

Abstract....99
4.1 Introduction....100
4.2 Methods....101
4.3 Results....110
4.4 Discussion....120
4.5 Conclusion....125
Reference....125
Chapter 5 Oxygen Penetration Through Full-Thickness Skin by Oxygen-Releasing Sutures for Skin Graft Transplantation....133
Abstract....134
5.1 Introduction....134
5.2 Methods....135
5.3 Results....137
5.4 Discussion....144
5.5 Conclusion....125
Reference....125
Chapter 6 Prediction of Drug Permeation Through Microneedled Skin by Machine Learning....151
Abstract....152
6.1 Introduction....152
6.2 Methods....153
6.3 Results....156
6.4 Discussion....161
6.5 Conclusion....164
Reference....125
Chapter 7 Conclusion and Future works....169
7.1 Conclusion....169
7.2 Future studies....171
Appendix 1. The Published Version of Chapter 3....174

List of Publications

Published articles in peer-reviewed journal:

1. W Zai, **Y Yuan** (co-first author), L Kang, J Xu, Y Hu, L Kang, J Wu, Oxygen Penetration Through Full-Thickness Skin by Oxygen-Releasing Sutures for Skin Graft Transplantation, Engineering 29, 83-94. https://doi.org/10.1016/j.eng.2023.05.006.

2. **Y Yuan**, Y Han, CW Yap, JS Kochhar, H Li, X Xiang, L Kang, Prediction of drug permeation through microneedled skin by machine learning, Bioengineering & Translational Medicine 8 (6), e10512. https://doi.org/10.1002/btm2.10512.

3. D.V. Nguyen, **Y. Yuan** (co-first author), M. Kukumberg, L. Wang, S.H. Lim, A.M. Hassanbhai, M. Chong, T. Kofidis, E.C.K. Tan, D. Seliktar, L. Kang, A.J. Rufaihah, Controlled release of vancomycin from PEGylated fibrinogen polyethylene glycol diacrylate hydrogel, Biomaterials Advances 161, 213896. https://doi.org/10.1016/j.bioadv.2024.213896.

4. AF Anwar-Fadzil, **Y Yuan**, L Wang, JS Kochhar, NN Kachouie, L Kang, Recent progress in three-dimensionally-printed dosage forms from a pharmacist perspective, Journal of Pharmacy and Pharmacology 74 (10), 1367-1390. https://doi.org/10.1093/jpp/rgab168.

5. K Yang, L Wang, S Vijayavenkataraman, **Y Yuan**, E Tan, L Kang, Recent applications of three-dimensional bioprinting in drug discovery and development, Advanced Drug Delivery Reviews 214, 115456. https://doi.org/10.1016/j.addr.2024.115456

Manuscripts under review and in preparation:

1. **Y Yuan**, L Kang. Manufacture Hydrogel Microwells Using Optical 3D Printers for Human Spheroids Culture in Vitro.

2. **Y Yuan,** AF Anwar-Fadzil, TJ Jeon, Y Hu, J Wu, NN Kachouie, L Kang, Numerical Simulation Aided Optimization of Bioprinting.

3. **Y Yuan**, M Nasri, A Manayi, J Zhang, C Wu, TJ Jeon, L Kang, Sericin coats of silk fibres, a degumming waste or future material? (Materials Today Bio, under review)

Presentation in scientific conferences:

Y Yuan, Y Han, CW Yap, JS Kochhar, H Li, X Xiang, L Kang, Prediction of drug permeation through microneedled skin by machine learning, Asian Society for Precision Engineering and Nanotechnology, Singapore, 15th-18th, November 2022.

Awards related to this research：

1. Australasian Society for Dermatology Research (ASDR) Publication Awards
2. Drug Discovery Initiative ECR Awards 2023 (Honours/ HDR Student Category)
3. Top 10 in 2024 Healthcare Innovation Initiative, Sprint2Create (S2C)
4. Top 4 in 2024 Big IDEA

Copyright Information

Controlled release of vancomycin from PEGylated fibrinogen polyethylene glycol diacrylate hydrogel © 2024 by D.V. Nguyen, Y. Yuan, M. Kukumberg, L. Wang, S.H. Lim, A.M. Hassanbhai, M. Chong, T. Kofidis, E.C.K. Tan, D. Seliktar, L. Kang, A.J. Rufaihah is licensed under CC BY 4.0

Oxygen Penetration Through Full-Thickness Skin by Oxygen-Releasing Sutures for Skin Graft Transplantation © 2024 by W Zai, Y Yuan (co-first author), L Kang, J Xu, Y Hu, L Kang, J Wu is licensed under CC BY-NC-ND 4.0

Prediction of drug permeation through microneedled skin by machine learning © 2024 by Y Yuan, Y Han, CW Yap, JS Kochhar, H Li, X Xiang, L Kang is licensed under CC BY 4.0

Abstract

Human civilization has always advanced alongside the development of materials, from the Stone Age to the Silicon Age. Materials are categorized into soft and hard based on stiffness. Hard materials have driven economic progress, but there is growing interest in soft materials for their unique properties like elasticity, flexibility, and biocompatibility. These characteristics make soft materials crucial in fields such as drug delivery, tissue engineering, and medical implants. The advent of advanced manufacturing techniques, like additive manufacturing, is further expanding their applications. Despite their potential, designing soft materials remains a challenging task. For decades, modelling and simulation have helped address these challenges, providing insights and accelerating material design and applications.

This thesis introduces three simulation approaches, namely, **mathematical modelling**, **domain discretization**, and **machine learning**, to develop models that support the use of soft materials in drug delivery and tissue engineering.

Mathematical modelling enables the rapid and direct extraction of desired results from input variables. For example, PEGylated fibrinogen–PEGDA hydrogel impregnated with an antimicrobial agent vancomycin, can be used to tailor the release vancomycin in a controlled manner, helping to prevent surgical site infections. Compared with stiff hydrogels, soft hydrogels can facilitate quicker drug diffusion. The mathematical models have been developed, based on Fick's law of diffusion. The models can simulate drug release from the hydrogels of varying rheological properties, to predict vancomycin release, allowing for the personalized treatment using the PEGylated fibrinogen–PEGDA hydrogels.

Domain discretization allows for the capture of the dynamic evolution of a process from start to finish, enabling the tracking and recording of all points within the system. For example, a 3D-printed hydrogel microwell system was developed and optimized using domain discretization to improve nutrition delivery to cellular spheroids, boosting drug screening efficiency. In another example, domain discretization has been applied to oxygen gas release from surgical sutures. The oxygen release profile from the suture was simulated to examine real-time oxygen penetration, enhancing the success of full-thickness skin graft transplants for surgical procedures.

The **machine learning** approach offers a data-driven simulation method, providing enhanced prediction accuracy. For example, decision tree-based methods have been applied to predict drug permeation through skin facilitated by microneedles. With this approach, we can minimize the need for performing in vitro skin permeation studies, which requires scarce human skin grafts, costly drug candidates and lengthy wet-lab experiments. Among the machine learning methods used, extreme gradient boosting (XGBoost) proved to be the most accurate, demonstrating the potential of data-driven simulations for applications in drug delivery and tissue engineering.

In summary, simulation methods are valuable tools for advancing the understanding of soft material applications in drug delivery and tissue engineering. These applications include controlled drug release, tissue culture platforms, skin grafting, and identifying key factors for optimizing drug delivery systems. Leveraging simulation can guide material design, enhance device structures, expedite the development of new therapies, and enable personalized drug administration, ultimately leading to improved clinical outcomes.

List of Abbreviations

3D: three-dimensional

4-HNE: 4-hydroxynonenal

AM: Additive manufacturing

ANOVA: Analysis of variance

ASTM: American Society for Testing and Materials

BD: Bone density

BJT: Binder jetting

BSA: Bovine serum albumin

Calcein-AM: Calcium acetoxymethyl ester

CAD: Computer aided design

CFD: Computational fluid dynamics

CT: Computed tomography

DED: Directed energy deposition

DLP: Digital light processing

DM: Degree of methacrylation

DMEM: Dulbecco's Modified Eagle Medium

DS: Degree of substitution

DSWI: Deep sternal wound infection

FBS: Fetal bovine serum

FDA: Food and Drug Administration

FEM: Finite element methods

FTSGs: Full-thickness skin grafts

GelMA: Gelatine methacrylate

HA: Hyaluronic acid

HAMA: Hyaluronic acid methacrylate

HPLC: High performance liquid chromatography

HU: Hounsfield units

I2959: 2-hydroxy-4-(2-hydroxyethoxy)-2-methylpropiophenone

PBF: Powder bed fusion

PBS: Phosphate-buffered saline

PDMS: Polydimethylsiloxane

PEG: Polyethylene glycol

PEGDA: Polyethylene glycol diacrylate

PEGDMA: Polyethylene glycol dimethacrylate

PF-PEGDA: PEGylated fibrinogen–polyethylene glycol diacrylate

PGS: Poly(glycerol-co-sebacate)

PI: Propidium iodide

PLGA: Poly(lactic-co-glycolic acid)

PVA: Poly (vinyl alcohol)

LAP: Lithium phenyl-2,4,6-trimethylbenzoylphosphinate

MEM: Minimum Essential Medium

MMP: Matrix metalloproteinase

MNs: Microneedles

MEX: Material extrusion

MJT: Material jetting

MLR: Multiple linear regression

MRI: Magnetic resonance imaging

MRSA: Methicillin-resistant Staphylococcus aureus

MW: Molecular weight

NACLAR: National Advisory Committee for Laboratory Animal Research

RF: Random forest

RGD: Arginine-glycine-aspartic acid

ROI: Region of interest

ROS: Reactive oxygen species

SEM: Scanning electron microscopy

SHL: Sheet lamination

SF: Silk fibroin

SilMA: Silk fibroin methacrylate

RMSE: Root mean square error

SPS: Sodium persulfate

SS: Silk sericin

SSI: Surgical site infection

STL: Stereolithography

TGO: Topical gaseous oxygen

UV: Ultraviolet

VAM: Volumetric additive manufacturing

VA-086: 2,2-azobis [2-methyl-n-(2-hydroxyethyl) propionamide]

VPP: Vat photopolymerization

XGBoost: Extreme gradient boosting

Thesis Authorship Statement

Chapter 2 will be submitted for journal publication as:

> **Y Yuan,** AF Anwar-Fadzil, J Wu, L Kang, Numerical Simulation Aided Optimization of Bioprinting.

This study was conceived and designed by all authors. Y.Y. Conceptualization, Writing – original draft, Methodology, Software, Formal analysis, Investigation, Data curation, Project administration. A.F. Writing – review & editing. J.W. Writing – review & editing. L.K. Conceptualization, Methodology, Software, Formal analysis, Investigation, Data curation, Writing – original draft, Writing – review & editing, Supervision, Project administration. The final manuscript will be approved by all authors.

Chapter 3 has been published as:

> D.V. Nguyen, **Y. Yuan** (co-first author), M. Kukumberg, L. Wang, S.H. Lim, A.M. Hassanbhai, M. Chong, T. Kofidis, E.C.K. Tan, D. Seliktar, L. Kang, A.J. Rufaihah, Controlled release of vancomycin from PEGylated fibrinogen polyethylene glycol diacrylate hydrogel, Biomaterials Advances 161, 213896. https://doi.org/10.1016/j.bioadv.2024.213896.

This study was conceived and designed by all authors. D.N.: Writing – original draft, Methodology, Investigation, Formal analysis, Data curation. Y.Y.: Writing – review & editing, Visualization, Validation, Software, Methodology, Investigation, Formal analysis, Data curation. M. K.: Data curation, Investigation, Validation, Visualization, Writing – original draft. L.W.: Writing – review & editing, Visualization, Validation, Formal analysis, Data curation, Conceptualization. S.H.L.: Writing – original draft, Methodology, Investigation, Formal analysis. A.M.H.: Writing – review & editing, Methodology, Investigation. M.C.: Writing – review & editing, Investigation, Formal analysis, Conceptualization. T.K.: Validation, Supervision, Resources, Funding acquisition. E. C.K. T.: Writing – review & editing, Validation. D. S.: Validation, Methodology, Investigation. L.K.: Writing – review & editing, Validation, Supervision, Resources, Methodology, Investigation, Formal analysis, Conceptualization. A.J.R.: Writing – review & editing, Supervision, Resources, Project administration, Methodology, Investigation, Funding acquisition, Conceptualization. The final manuscript was approved by all authors.

Chapter 4 will be submitted for journal publication as:

> **Y Yuan**, L. Kang. Manufacture Hydrogel Microwells Using Optical 3D Printers for Human Spheroids Culture in Vitro.

This study was conceived and designed by all authors. Y.Y.: Writing – original draft, Methodology, Investigation, Formal analysis, Data curation. Writing – review & editing, Visualization, Validation, Software. L.K.: Writing – review & editing, Validation, Supervision, Resources, Methodology, Investigation, Formal analysis, Conceptualization. The final manuscript will be approved by all authors.

Chapter 5 has been published as:

> W Zai, **Y Yuan** (co-first author), L Kang, J Xu, Y Hu, L Kang, J Wu, Oxygen Penetration Through Full-Thickness Skin by Oxygen-Releasing Sutures for Skin Graft Transplantation, Engineering 29, 83-94. https://doi.org/10.1016/j.eng.2023.05.006

This study was conceived and designed by all authors. W.Z.: Writing – original draft, Methodology, Investigation, Formal analysis, Data curation. Y.Y.: Writing – original draft, Methodology, Investigation, Formal analysis, Data curation. Writing – review & editing, Visualization, Validation, Software. L. K.: Writing – original draft, Methodology, Investigation, Formal analysis. J. X.: Writing – review & editing, Investigation, Formal analysis. Y. H.: Writing – review & editing, Validation, Supervision, Resources. L.K.: Writing – review & editing, Validation, Supervision, Resources, Methodology, Investigation, Formal analysis, Conceptualization. J. W.: Writing – review & editing, Validation, Supervision, Resources, Methodology, Investigation, Formal analysis, Conceptualization. The final manuscript will be approved by all authors.

Chapter 6 has been published as:

> **Y Yuan**, Y Han, CW Yap, JS Kochhar, H Li, X Xiang, L Kang, Prediction of drug permeation through microneedled skin by machine learning, Bioengineering & Translational Medicine 8 (6), e10512. https://doi.org/10.1002/btm2.10512.

This study was conceived and designed by all authors. Y.Y.: Formal analysis, investigation, methodology, software, validation, visualization, writing – original draft, writing – review and editing. Y.H.: Conceptualization, data curation, investigation, methodology, writing – review and editing. C. W. Y.: Investigation, methodology, supervision, writing – review and editing. J. S. K.: Data curation, investigation, methodology, writing – review and editing. H. L.: Data curation, investigation, methodology, writing – review and editing. X.X.: Conceptualization, funding acquisition, investigation, methodology, resources, writing – review and editing. L. K.: Conceptualization, data curation, formal analysis, funding acquisition, investigation, methodology, project administration, resources, supervision, visualization, writing – review and editing. The final manuscript was approved by all authors.

In addition to the statements above, in cases where I am not the corresponding author of a published item, permission to include the published material has been granted by the corresponding author.

Yunong Yuan

As supervisor for the candidature upon which this thesis is based, I can confirm that the authorship attribution statements above are correct.

Dr. Lifeng Kang

Chapter 1 Introduction

1.1 Background

The development of materials matters human civilization since the Stone Age. With the development of society, humanity has transitioned from the Stone age to the Silicon age. All the revolution of the ages are always accompanied by the development and application of new materials. Materials can generally be categorized as soft and hard materials based on the stiffness. The functional hard materials have significantly contributed to the development of world economic. While the contribution of hard materials continues, there is a growing interest in soft materials, due to their elasticity, flexibility, biocompatibility, and tunability. Not surprisingly, the soft materials have been studied intensively and applied in various fields owing to their unique properties. Applications include drug delivery, tissue engineering, organ or disease models, medical implants, wound dressings, and contact lenses. More recently, advanced manufacturing like additive manufacturing devotes the soft materials exploring in broader areas, such as hydrogel sensors, actuators, soft robots, electronic devices, batteries, optical devices, acoustic devices, living devices, underwater adhesives, and bioadhesive devices. The physiological and mechanical properties of soft materials are crucial for above mentioned applications. However, designing soft materials with the necessary physiological and mechanical properties still remains challenge, time consuming, and costly.

For the past few decades, modelling or simulation of material behaviour has been employed to address these challenges. This mathematical based method involves the solving equations, identifying critical parameters and developing simulation algorithms to predict physiological and mechanical properties of materials. These simulations provide insights and understanding of materials at wide scales, from electrons, atoms, and molecules to their assembles, structure, characteristics, and functionalities. Besides, simulation methods also enable the utilization in composite materials, which further broaden the potential applications in materials design and manufacturing. The ability of solving these complexed issues has attracted widespread attention and interest, making simulation methods a potentially valuable tool for accelerating materials design and applications.

To this end, we would like to utilise different simulation methods to accelerate the design and application of soft materials, especially in biomedical and drug delivery system. The specific objectives of this thesis are fourfold:

1. To use traditional mathematical methods to guide the design of drug-loaded hydrogels for controlled and combined drug release.
2. To employ Finite Element Methods (FEM) to assist and optimize gas therapy in the biomedical field.
3. To develop a tuneable cell culturing platform using advanced manufacturing methods and to employ advanced simulation methods to guide platform design.
4. To use state-of-the-art machine learning methods to predict non-linear drug release profiles, find the key features influencing the releasing profile and accelerate microneedle applications.

1.2 Thesis structure

This thesis covers 3 simulation methods including mathematical model, domain discretisation, and machine learning to investigate the soft materials-based tissue engineering and drug delivery system. All the proposed models in this thesis are generalised and highly flexible. They can be adjusted by modifying the properties of the drug or hydrogel to meet the requirements of different choices or studies. The thesis consists of seven chapters which can be exhibited in **Figure 1**. Chapter 2 reviewed various additive manufacturing (AM) methods, biomaterials, and simulation techniques. These simulation methods were developed to improve the understanding and control of key properties in hydrogel-based drug delivery and tissue engineering systems. Chapter 3 introduces the application of the first method: mathematical modelling in a controlled hydrogel-based drug delivery system. Non-linear drug releasing always happens in hydrogel drug carrier system. Controlling the drug releasing profile from different hydrogel-based drug delivery systems can allow for maximizing drug efficacy and safety, and therefore achieving a desired therapeutic response. The choice of PF-PEGDA hydrogels as the drug delivery vehicle for bone repair provides a direct case where controlled drug release and material behaviour are critical, thus exemplifying the methods introduced earlier. Two configurations were developed to study the effect of the hydrogel on drug release, namely, vancomycin laden hydrogel and vancomycin solution on top of blank hydrogel, which exhibited burst and lag release profiles. A mathematical model was developed to simulate the drug releasing profile from these two configurations and

investigate the effect of different parameters on customizing this system for personalised medicine (Chapter 3).

Domain discretisation is a method that mesh the whole system to individual independent element, which can calculate the time dependent evolution of the system. Using this advanced method, various areas including small molecule, gases, stress, fluid dynamics, and thermodynamics can be figured out and visualized the distribution of the targeted variables in the system. We use domain discretisation method for simulating spheroids culturing in the 3D printed hydrogel microwell system (Chapter 4). Meanwhile, we build a model to investigate the gas therapy from the advanced oxygen suture for full thickness transplantation (Chapter 5). Positioning Chapter 5 immediately after Chapter 4 was intended to showcase the application of domain discretization and Fick's law across different biological scenarios, transitioning from liquid-based drug diffusion systems in Chapter 4 to gas-phase diffusion in Chapter 5. These chapters collectively highlight the flexibility and effectiveness of this mathematical modelling approach in tackling diverse challenges within tissue engineering and drug delivery.

Microneedle is a painless, topological drug administration method to deliver drug through skin. To determine the amount of drug delivered through skin, in vitro drug permeation testing is commonly used, but the testing is costly and time consuming. Machine learning is one of the most state-of-the-art simulation methods, which can address classification and regression challenges. Here, we propose both domain discretization and machine learning methods to predict the non-linear drug releasing profile from microneedle with several key parameters, which can explore customized design for microneedle, inform optimal dose and applied time of microneedle, and accelerate its marketing applications in the future (Chapter 6). Overall conclusions and future studies are provided in Chapter 7.

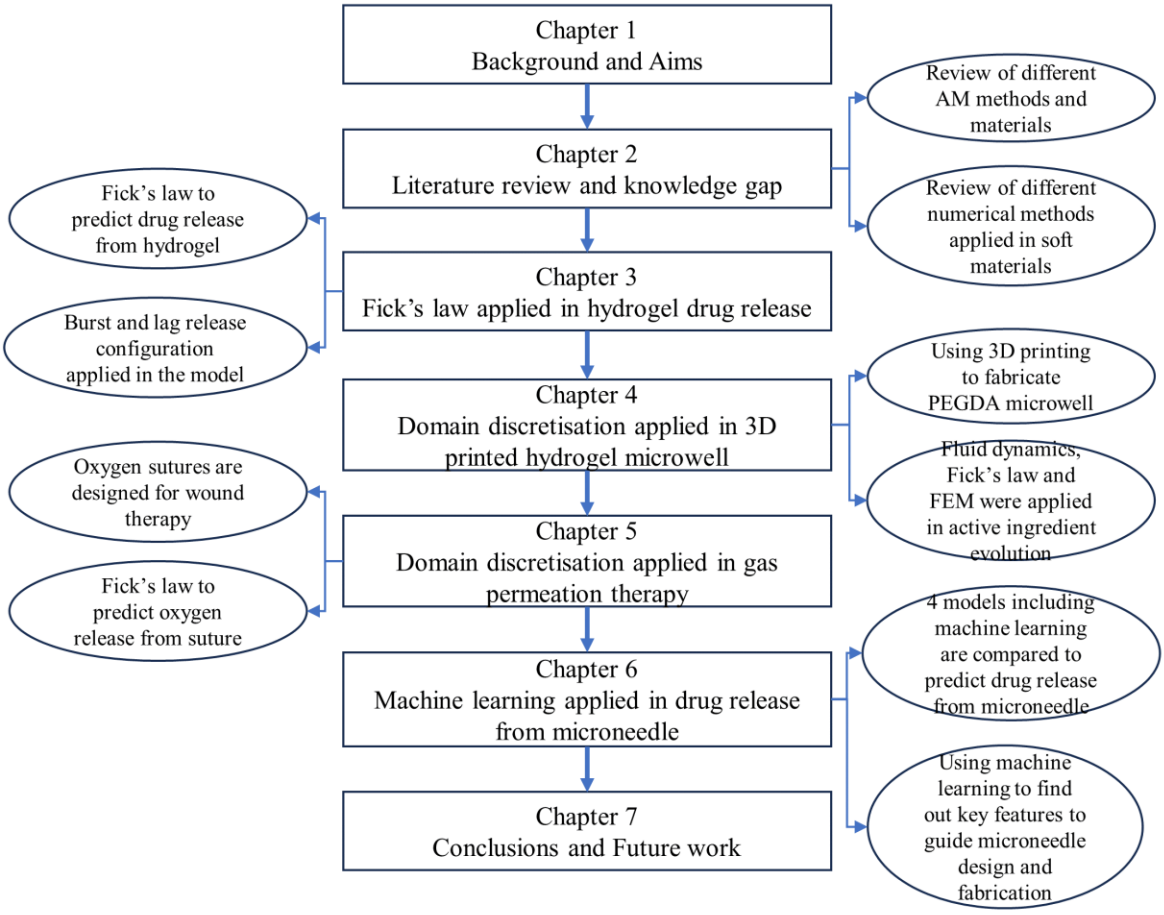


Figure 1 Diagram of thesis structure.

Chapter 2 Literature review on additive manufacturing: biomaterials, photocrosslinkable mechanism and simulation.

2.1 Classification of additive manufacturing

Additive Manufacturing (AM), unlike traditional subtractive and formative manufacturing, is based on a geometry morphology to create physical objects via successive accumulation of materials. Generally, the manufacturing process begins with a digital data file of the physical product, which could be obtained from clinical images, such as magnetic resonance imaging (MRI) scans or computed tomography (CT) scans or created with computer aided design (CAD) software. Once the design of products is finished, the digital data file will be converted into a Stereolithography (STL) file. This STL file can be uploaded to a slicer software, which calculates the print path and create G-code to control the 3D printer. Prior to printing, several key parameters are required to be set or optimised, such as the printing orientation, layer thickness, energy source intensity, support structure, printing time, and environmental circumstances. Subsequently, suitable materials and machines will be applied to print the aimed products with the tailored settings via a layer-by-layer process. The printing time might vary from minutes to days, depending on the volume and setting. This new manufacturing technology has been successfully applied to various areas, such as engineering, energy, medicine, education, architecture, and entertainment [1-4]. According to the International Organization for Standardization (ISO)/ American Society for Testing and Materials (ASTM) 52900, the AM process could be classified into seven categories: (1) binder jetting (BJT); (2) directed energy deposition (DED); (3) material extrusion (MEX); (4) material jetting (MJT); (5) powder bed fusion (PBF); (6) sheet lamination (SHL) and (7) vat photopolymerization (VPP). Table 1 summarizes the basic principles, materials, advantages, disadvantages, and printing resolution of these seven systems [3, 5].

In the biomedical area, 3D printed biological samples should promise proper biostability and well biocompatibility. The major 3D printing methods used in the biomedical area include 3D inkjet technology, materials extrusion, laser-assisted bioprinting, two-photon polymerization-based bioprinting, digital light processing, and volumetric additive manufacturing. Listed below are the information about these 3D printing methods, principles, and their operational mechanisms. Additionally, **Figure 2** provides a schematic representation of these methods [6]:

Table 1 Basic principles, materials, advantages, disadvantages, and printing resolution of seven ISO/ASTM categories of AM [3, 5]

ISO/ASTM category	Basic principle	Example technology	Advantages	Disadvantages	Materials	Minimum printing feature size	Ref
BJT	Liquid bonding agent is selectively deposited to join powder materials	• 3D inkjet technology	▪ Free of support/substrate ▪ Design freedom ▪ Large build volume ▪ High print speed ▪ Relatively low cost	▪ Fragile parts with limited mechanical properties ▪ May require post processing	• Polymers • Ceramics • Composites • Metals • Hybrid	~1 mm	[7]
DED	Focused thermal energy is used to fuse materials by melting as they are being deposited	• Laser deposition • Electron beam • Plasma arc melting	▪ High degree control of grain structure ▪ High quality parts ▪ Excellent for repair applications	▪ Surface quality and speed need balanced ▪ Limited to metals/metal based hybrids	• Metals • Hybrid	~300 μm	[8]
MEX	Material is selectively dispensed through a nozzle or orifice	• Fused deposition modelling/ Fused filament fabrication • Fused layer modelling	▪ Widespread use ▪ Inexpensive ▪ Scalable ▪ Can build fully functional parts	▪ Vertical anisotropy ▪ Step-structured surface ▪ Not amenable to fine details	• Polymers • Composites	~200 μm	[9]
MJT	Droplets of feedstock material are selectively deposited	• 3D inkjet technology • Direct ink writing	▪ High accuracy of droplet deposition ▪ Low waste ▪ Multiple materials parts ▪ Multicolour	▪ Support material is often required ▪ Mainly photopolymers and thermoset resin can be used ▪ Viscosity of materials need considered	• Polymers • Ceramics • Composites • Metals • Hybrid	~100 μm	[10]
PBF	Thermal energy selectively fuses regions of a powder bed	• Electron beam melting • Direct metal laser sintering • Selective laser sintering/melting	▪ Relatively inexpensive ▪ Small footprint ▪ High accuracy ▪ Powder bed acts as an integrated support structure ▪ Large range of material options	▪ Relatively slow ▪ Lack of structural integrity ▪ Size limitations ▪ High power required ▪ Finish depends on precursor powder size	• Polymers • Ceramics • Composites • Metals • Hybrid	~500 μm	[11]
SHL	Sheets of material are bonded to form a part	• Laminated object manufacturing • Ultrasound consolidation/Ultrasound additive manufacturing	▪ High speed ▪ Low cost ▪ Ease of material handling	▪ Strength and integrity of parts depend on adhesive used ▪ Finishes may require post processing ▪ Limited material use	• Polymers • Ceramics • Metals Hybrid	~400 μm	[12]
VPP	Liquid photopolymer in a vat is selectively cured by light-activated polymerization	• Stereolithography • Digital light processing • Volumetric additive manufacturing	▪ Large parts ▪ Low oxygen inhibition ▪ Excellent accuracy ▪ Excellent surface finish and details	▪ Limited to photopolymers only ▪ Low shelf life, poor mechanical properties of photopolymers ▪ Expensive precursors/Slow build process	• Polymers • Ceramics	~1 μm	[13]

a) 3D inkjet technology.

3D inkjet technology creates 3D products by depositing volume-controlled droplets of bioinks from a nozzle. The creation of droplet is controlled by thermal, piezoelectric, or electrostatic mechanisms and placed onto the printing platform, which generate localized air bubbles or pressure to eject the droplets onto the printing platform (**Figure 2a**) [14, 15]. Then, the specific wavelength light is applied to activate the photoinitiators and solidify the bioinks. The nozzle moves up in step, depositing layers of material in the vertical direction. This technology offers simplicity, low cost, and high resolution with good cell viability. However, the cell density and the viscosity of bioinks needed to be considered, as high cell density can increase shear force, reducing cell viability, and higher viscosity can clog the nozzle. Balancing target resolution, material viscosity, nozzle size, and printing speed is crucial for effective 3D inkjet printing [16].

b) Materials extrusion.

The materials extrusion printing method is continuing materials deposition from a nozzle (**Figure 2b**) [16, 17]. This continuous material produces a smoother surface than 3D inkjet technology and is similar in mechanism. The bioink is pumped and deposited continuously through a nozzle line by line to the platform, creating patterns layer by layer in the vertical direction. The driving force to extrude the materials could be pneumatic-based and mechanical-based, which has a better capability for high viscosity inks. The printing resolution is limited by the nozzle diameter, driving force, printing speed, materials viscosity, and gelation kinetics. Material extrusion is the most widely used bioprinting technique for tissue engineering due to its ease of operation and versatility [17-19].

c) Laser assisted bioprinting.

Lasser assisted bioprinting is made up of a pulsed laser source, a receiving substrate, and a ribbon consisting of a bioink layer and a metal laser-absorbing layer usually made of gold or titanium (**Figure 2c**) [20, 21]. The laser pulse will induce a vapour bubble on the donor layer, ejecting droplets of bioink onto the receiving substrate. This method overcomes the limitations of the bioink viscosity and cell density seen in the 3D inkjet technology.

d) Two-photon polymerisation.

Two-photon polymerisation uses an ultrafast laser beam to scan and polymerise the sliced pattern layer by layer (**Figure 2d**) [22, 23]. Two photons will be simultaneously absorbed by the bioinks, polymerizing the target exposure area. The resolution mainly depends on the light source, and diffraction affects the quality of the final printed pattern. This high-

resolution method is suitable for the application in fine patterning of biomaterials and single cell studies, despite slower bioprinting speed and limitation in scalability.

e) Digital light processing.

Digital light processing (DLP) is b a rapid fabrication process based on projection stereolithography, faster than two-photon polymerisation. DLP printer is composed of a digital micromirror device chip, a motorized stage or bioprinting probe, a set of optical paths, and a computer to synchronise the movement of the stage or the probe to corresponding patterns (**Figure 2e**) [24]. The digital micromirror device chip consists of millions of micromirrors that can display user-defined patterns with micrometre-scale features. Bioinks polymerise where the light is projected from the digital micromirror device chip. DLP can achieve resolutions of a few micrometres, making it meets the majority of requirements from regenerative medicine, high-throughput drug testing, and tissue and disease modelling [25-28].

f) Volumetric additive manufacturing.

Volumetric additive manufacturing (VAM) is relatively new compared to the above-mentioned technologies. This technique was first reported by Shusteff et al in 2017 using the superposition of two or more light beams to solidify the resin [29]. Later, Kelly et al upgraded the system to tomographic VAM, which has become the most popular VAM method [30]. It uses light energy delivered to a rotating resin vat as a set of 2D images (**Figure 2f**). The system is made up of a DLP projector, a rotating stage with uncured bioink, and a tank with index matching fluid. In the printing process, Radon transform was used to convert 3D model into several 2D images. These 2D images could represent the 3D model from different perspectives. An inverse Radon transform calculates the 3D distribution of light intensity from projectors, completing the printing process. The VAM address the support structure issue in creation of overhanging and spanning geometries and eliminates poor surface quality and directional mechanical property differences seen in traditional 3D printing methods. Besides, it can print external parts onto the pre-existing structure with minimum mechanical stress on the printed part [31]. Although this fast printing method offers promising alternatives to conventional 3D printing, it is still in its infancy. Limited commercial availability and material understanding present challenges for research in this topic.

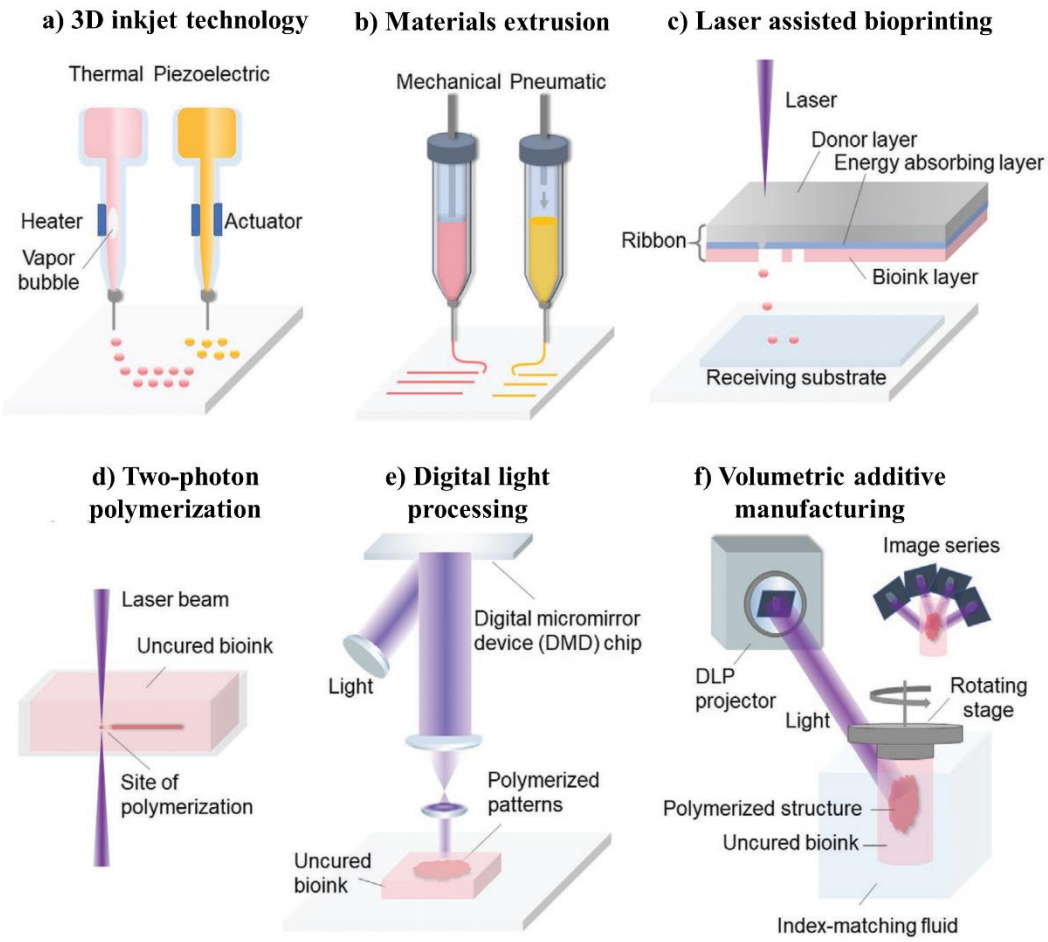


Figure 2 Schematic illustrations of major 3D printing methods used in the biomedical area. a) 3D inkjet technology, b) Materials extrusion, c) Laser-assisted bioprinting, d) Two-photon polymerization, e) Digital Light Processing, and f) Volumetric additive manufacturing [6].

2.2 The mechanism of free radical chain growth polymerisation

The majority of photocrosslinking materials systems are based on free radical chain growth polymerisation theory to form hydrogels. In specific, the photoinitiators will decompose into free radicals under the specific wavelength of light exposure (e.g., I2959 at 365nm, LAP at 365 and 405 nm). Then, these free radical initiates the polymerization process by linking monomers to form polymer chains.

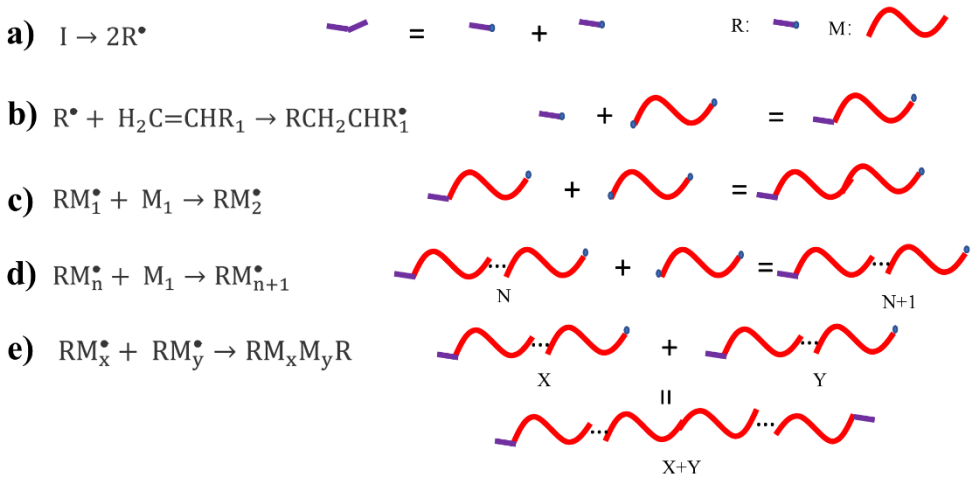


Figure 3 Schematic of the chain-growth polymerisation mechanism. a) Photoinitiator molecular decomposes to two free radicals. b) Free radicals initiate polymer chain growth. c) and d) the radicalised monomer link to nearby monomers. e) the termination reaction of polymer chain growth. (R: free radicals, M: monomer)

Chain growth polymerisation process can be divided into 3 stages: 1) initiation, 2) chain growth, and 3) termination (**Figure 3**). In the initial stage, the photoinitiator decomposes into two free radicals under specific wavelengths of light (**Figure 3a**). Then, the free radicals react with and rearrange monomers, which typically have the carbon-carbon double bonds structures (**Figure 3b**). The radicalised monomer links to nearby monomers to form a chain like structure (**Figure 3c and d**). To terminate the chain growth polymerisation process, the radicalised monomers need to meet with: 1) another radicalised monomer (**Figure 3e**), 2) free radicals, 3) a monomer or polymer chain for free radical transfer, or 4) impurities and inhibitors (e.g., oxygen). Meanwhile, the termination can also occur via hydrogen abstraction, which forms two separate terminated polymer chains. The mode of termination, whether by monomer combination or hydrogen abstraction, depends on the molecular type and reaction temperature [32-34].

The kinetics of a photoinitiator can be described by the following equation [33]:

$$R_i = \frac{2\phi\varepsilon I_0 f C_i}{N_A h\nu} \qquad (1)$$

Where, R_i is the initiation rate, ϕ is quantum yield, ε is extinction coefficient, I_0 is the light exposure intensity, f is the photoinitiator efficiency, C_i is the concentration of the photoinitiator, N_A is the Avogadro's number, h is the Planck's constant, and ν is the

frequency of initiating light. Based on the steady-state assumption, the relationship between the initiation rate and the polymerization rate (v_p) can be determined by:

$$v_p = k_p[M]\left(\frac{R_i}{2k_t}\right)^{1/2} \quad (2)$$

Where, k_t is the termination rate coefficient, and M is the monomer concentration. For a low efficiency initiator f becomes a function of $[M]$. Substituting Eq. (1 to the Eq. (2), the rate of photopolymerisation can be determined by the following equation [33, 34]:

$$v_p = k_p\left(\frac{\phi\varepsilon I_0 C_i}{N_A h\nu k_t}\right)^{1/2}[M]^{3/2} \quad (3)$$

From the Eq. (3), the photopolymerisation rate is proportional to the square of the light exposure intensity and the concentration of the photoinitiator. Meanwhile, the rate is dependent on the concentration of photocrosslinkable monomer to the power of 1.5. It indicates that increasing the concentration of photocrosslinkable monomer, light exposure intensity, concentration of the photoinitiator, and selecting appropriate materials can enhance the efficiency of the photocrosslinking process.

2.3 Photocrosslinkable biomaterials used in digital light processing.

Using biomaterials to mimic the *in vivo* environment for cell culture *in vitro* requires good biocompatibility and tissue-specific properties, including appropriate biophysical, biochemical properties, and degradation kinetics. Biomaterials based hydrogel can provide the spatiotemporal environment for cell adhesion, proliferation, migration and conducting cell behaviours. The biomaterials used in DLP printing could be divided into two categories: 1) natural materials and 2) synthetic materials. Natural materials are favoured for their inherent biocompatibility and bioactivity. These materials provide excellent biochemical and biophysical features that biomimic in vivo environments. Additionally, they can also be remodelled and degraded through natural mechanism. On the other hand, synthetic materials have determined chemical structure and tailorable properties. However, synthetic materials require modification or the addition of other chemicals to achieve biocompatibility and bioactivity. To utilise either natural or synthetic materials in DLP, it is essential to modify the biomaterials to be photocrosslinkable, which enables rapid and selective solidification (**Figure 4**). Photoreactive moieties include methacrylate, acrylate, or thiol−ene groups are common groups or molecules, which are synthesized into the target natural or synthetic materials to enable photocrosslinking [35-37]. For effective DLP printing, the printability and

biomimicry of the materials are critical. The viscosity, thermosensitivity, photosensitivity, rheological properties, crosslinking mechanisms, kinetics, and postprinting mechanical properties of materials are key parameters leading the DLP printing accurately and precisely. Furthermore, to enhance the biomimicry, small molecular such as growth factors and cytokines can be added for specific biological applications. Combining several biomaterials to leverage the unique features of each component is another strategy to mimic specific biological environments effectively.

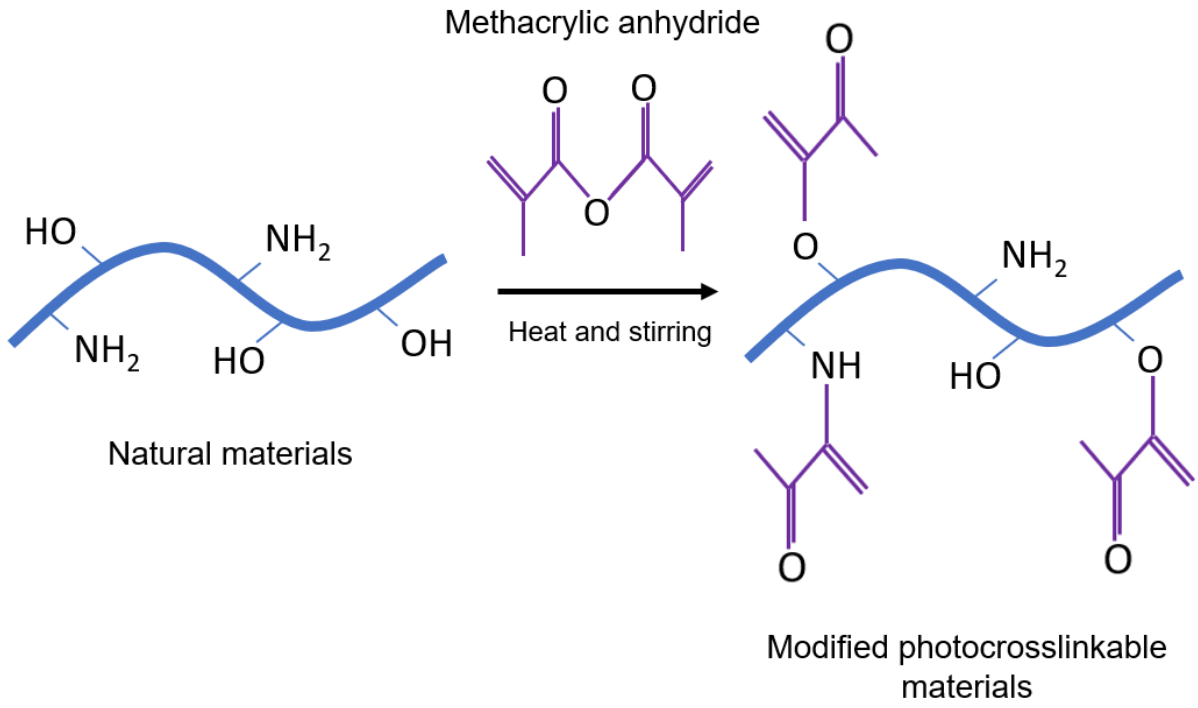


Figure 4 The natural materials containing -OH and -NH_2 group can be modified into photocrosslinkable materials.

2.3.1 Natural materials modified photocrosslinkable materials

2.3.1.1 Gelatine

Gelatine methacrylate (GelMA) is modified from gelatine, a partially hydrolysed product of collagen [38]. Gelatine with its derivatives have excellent inherent bioactivities, rheological properties, and thermally responsive characteristics, including integrin binding arginine-glycine-aspartic acid (RGD) sequences and matrix metalloproteinase (MMP) digestion sites. These features make gelatine widely used in 3D tissue modelling. To synthesise GelMA, gelatine replaces its lysine and hydroxyl groups with methacrylamide and methacrylate side groups, making it photocrosslinkable in the presence of photoinitiators under specific

wavelengths of light [38, 39]. Methacrylic anhydride is the most commonly used reagent to introduce methacrylate groups into gelatine under alkaline conditions. Notably, the modification process does not replace all amino acids in gelatine, which preserves most functional amino acids, including RGD, thus maintaining good cell adhesive properties [38]. The synthesised GelMA has been applied in a wide range of biomedical applications including bone regeneration [40, 41], organ tissue regeneration [42-44], blood vessel [45], disease model, and drug screening [46, 47].

2.3.1.2 Hyaluronic acid

Hyaluronic acid methacrylate (HAMA) is modified from Hyaluronic acid (HA) [48]. HA, a nonsulfated glycosaminoglycan, exists in many tissues and plays a significant role in biological processes including development, wound healing, and the function and structure of adult tissues. Its ability to degrade via oxidative species and hyaluronidases makes it attractive for modification and processing into hydrogel for biomedical applications [49]. HA can be esterified to photocrosslinkable HAMA through methacrylic anhydride or glycidyl methacrylate [50, 51]. HA can also be modified with norbornenes, cysteines, dithiobis (propanoic dihydrazide), maleimide groups, and tyramine groups to provide photocrosslinking capabilities [52]. The molecular weight of HA influences its biological behaviours, so it must be carefully considered in specific biomedical applications [53].

2.3.1.3 Silk fibroin

Silk fibroin methacrylate (SilMA) is derived from silk fibroin (SF), which is extracted from silk cocoons. SF is a fibrous protein composed of delicate twin threads linked by disulphide bonds and enveloped by three successive sticky layers of sericin. SF has extensively reviewed for its biomedical applications, including tissue engineering, regenerative medicine, drug delivery and medical devices [54-58]. To synthesise SilMA, SF reacts with glycidyl methacrylate in lithium bromide at 60 °C [59, 60]. Compared to GelMA, SilMA could be applied at room temperature in the liquid phase for printing and offers superior stability and mechanical properties. Moreover, Xie et al exhibited SF itself could be photocrosslinked between the tyrosine group in combination with the photoinitiator tris-bipyridylruthenium (II) hexahydrate (Ru)/sodium persulfate (SPS) under visible light volumetric additive manufacturing [61].

2.3.1.4 Silk sericin

Another protein material derived from silk is silk sericin (SS), which accounts for approximately 20-30% of the silk mass. It was previously considered a waste by-product in silk fibroin extraction. However, its extensive biological and pharmacological characteristics including antibacterial performance, antioxidant effects, good biocompatibility, low immunogenicity, controlled biodegradability, and induction of cell proliferation have attracted a strong interest among scientists to employ sericin for various applications [57, 62, 63]. The general degumming process segregates silk cocoons to extract SS involving the following steps: First, cutting the cocoons into pieces. Next, boiling them in hot water, continuously stirring to separate SS and insoluble SF. Then, centrifuging the SS solution to remove impurities. Lastly, dialyzing the solution against deionized water and lyophilizing to obtain SS powder. Other methods to extract SS include alkaline extraction, boiling in aqueous urea solution, acid extraction, and genetically engineered self-degumming cocoons [64, 65]. SS can also be recovered from wastewater from textile processing [66]. To make SS photocrosslinkable, it is functionalised with methacrylic anhydride, allowing for double bonds in methacrylic groups to conjugate with neighbour SerMA monomers [67, 68]. As mentioned above, pure SS can also be photocrosslinked between the tyrosine group in combination with the photoinitiator via volumetric additive manufacturing [61].

Other natural materials can be modified to become photocrosslinkable bioinks and bioresins including dextran, collagen, decellularized ECM, alginate, κ-carrageenan, and chitosan [69-74]. All of these materials use similar mechanisms to modify their function groups to be suitable for photocrosslinking.

2.3.2 Synthetic biomaterials modified photocrosslinkable materials

2.3.2.1 Polyethylene glycol

Polyethylene glycol (PEG) based hydrogels have been approved for use in various biomedical applications by the Food and Drug Administration (FDA) due to their high biocompatibility and low immunogenicity [75]. The mechanical and physical properties can be easily tailored to the design by controlling the molecular weight and concentration of PEG monomers [76]. Additionally, PEG based hydrogels are nonadhesive to cells and proteins, which provide a blank slate for the addition of desired biologically or chemically functionalities [25]. This property has enabled their use in various geometries to guide

cellular alignment and patterning [25, 77-79]. To synthesise photocrosslinkable PEG based materials, PEG and triethylamine are dissolved in dichloromethane, and acryloyl chloride or methacryloyl chloride is added to create PEG diacrylate (PEGDA) or PEG dimethacrylate (PEGDMA) [80]. These photocrosslinkable materials facilitate the fabrication of 3D structures, such as microwells and negative Poisson's ratio structures, to study cellular behaviour under different stimuli [78, 79, 81]. PEGDA and its mixed bioinks are also widely used in drug delivery, tissue engineering, and regenerative medicine, including spinal cord and nerve regeneration [82, 83].

2.3.2.2 Poly (glycerol-co-sebacate)

Poly(glycerol-co-sebacate) (PGS) was first synthesised in 2002. PGS is a strong, biodegradable, and biocompatible elastomer capable of withstanding dynamic tissue environments [84]. PGS is synthesised from natural products glycerol and sebacic acid via polycondensation reaction, both of which are FDA-approved for medical devices [85, 86]. However, the reaction for PGS synthesising requires extended times and harsh conditions, including vacuum and high temperatures, which can hinder its production and applications. To make PGS photocrosslinkable, PGS can be modified with acrylate or methacrylate groups to make the modified monomer easily crosslinkable at room temperature within a short period [85, 87-89]. The mechanical properties of photocrosslinkable PGS can be tuned by adjusting factors via molecular weight, degree of substitution, light exposure time, intensity, and concentrations [85]. This flexibility makes PGS suitable for various biomedical applications, including cell encapsulation, surgical adhesives, and 3D printing [90-94].

2.3.2.3 Poly (vinyl alcohol)

Poly (vinyl alcohol) (PVA) is a synthesised hydrophilic material rich in hydroxyl groups, which can be modified with methacrylic groups make it photocrosslinkable. Similar like the modification of most natural materials, the PVA is methacrylated via esterification reaction or modified with tyramine groups through carboxylation with succinic anhydride and subsequent coupling via carbodiimide chemistry [95, 96]. However, synthesis materials often lack suitable sites for cells adhesion. Functionalize the side groups of synthesis materials with adhesive sequence or heparin binding sites can enhance the interaction between cells and materials [97, 98]. Besides, the combination of both natural and

synthesised materials can leverage the advantages of both categories to form the hybrid bioinks [99].

2.3.3 Degree of substitution

The degree of substitution (DS) for methacrylation significantly influences the porosity rate and mechanical strength of hydrogels [38, 100]. The degree of methacrylation (DM) in feedstocks can be quantified calculating the ratio of substituted amino groups to free amino groups in gelatine. The free amino in gelatine be determined using Habeeb methods or ^{1}H NMR assay [101, 102]. The substituted amino groups are analysed via the ^{1}H NMR assay. The ^{1}H NMR spectra for methacrylated materials will display characteristic peaks between 5.0 and 6.5 ppm, reflecting the presence of double bonds introduced by the methacrylation process as shown in Figure 5. Specifically, the peaks for methacrylate and methacrylamide appear between 5.5 – 5.9 ppm, methacrylate peaks between 5.9 – 6.3 ppm, and methacrylic acid peaks at 1.88, 5.35, and 5.66 ppm [100, 102]. A known material can be used as an internal reference to quantify the DM value of the methacrylated materials. The DM value can be expressed using the following equation in Eq. (4):

$$\mathrm{DM}(mmol/g)=\frac{\int \text{methacryloyl}}{\int \text{internal reference}}\times\frac{\mathrm{xH}}{1\mathrm{H}}\times\frac{n\ mmol(\text{internal reference})}{m\ g(\text{MA modified materials})} \qquad (4)$$

Then, the DS could be calculated as the ratio of DM to the total amount of free amino in feedstocks, as shown in Eq. (5):

$$\mathrm{DS}=\frac{\mathrm{DM}}{\text{Free amino}}\times 100\% \qquad (5)$$

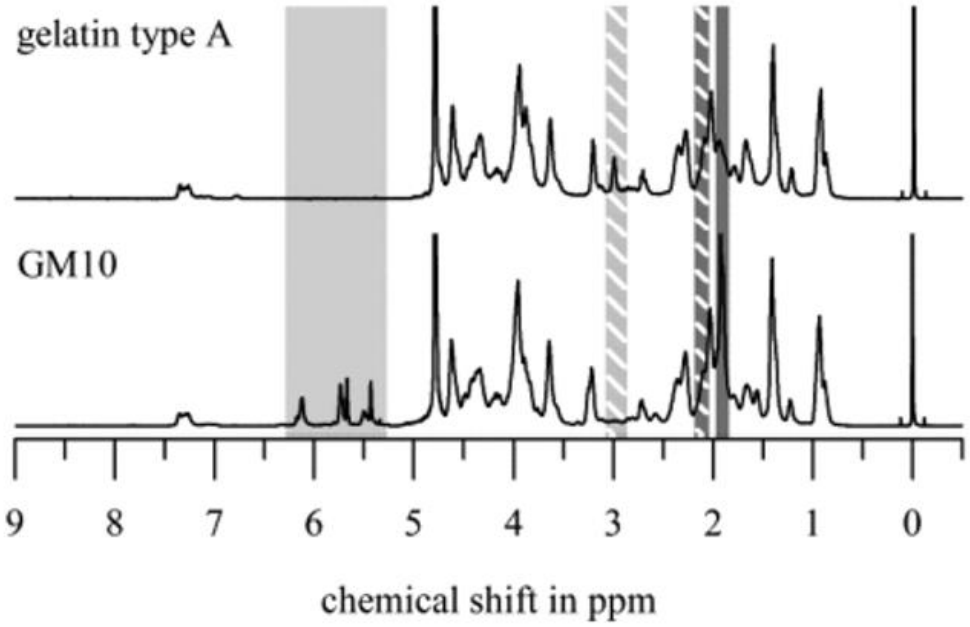


Figure 5 1H NMR spectra in D2O of gelatine and gelatine derivatives[100]

By integrating the peaks corresponding to the substituted amino groups and comparing them to the peaks of the internal reference, the DM value provides a precise measure of the degree of methacrylation. This quantification is crucial for tailoring the mechanical properties and porosity of hydrogels for specific biomedical applications.

2.4 Photoinitiators used in digital light processing.

The photoinitiators are crucial molecules in the photopolymerization process as they generate free radicals under UV or visible light. The free radicals open the double bonds on photocrosslinkable monomer (e.g., methacrylates, acrylates, acrylamides) and initialize the crosslinking process for materials. After printing, the final printed constructs are thoroughly washed multiple times using deionized water or complete culture medium to remove unreacted bioink, photoinitiators, and photoinhibitors. Photoinitiators could be classified into two main types according to the mechanism for forming free radicals: cleavable photoinitiators (Type I) and bimolecular photoinitiating systems (Type II) [103]. The type I photoinitiators (e.g. I 2959 and LAP) decompose into two free radicals after absorbing light at specific wavelengths (**Figure 6**). The type II photoinitiators (e.g. benzophenone) require coinitiators (e.g. tertiary amine) to create free radicals through a more complex process involving electron and proton transfers (**Figure 7**). The coinitiators transfer an electron to initialise the photoinitiators excited.

Followed by a slower proton transfer, two radicals are formed, where only amine-based radicals could initialise photopolymerization [104, 105].

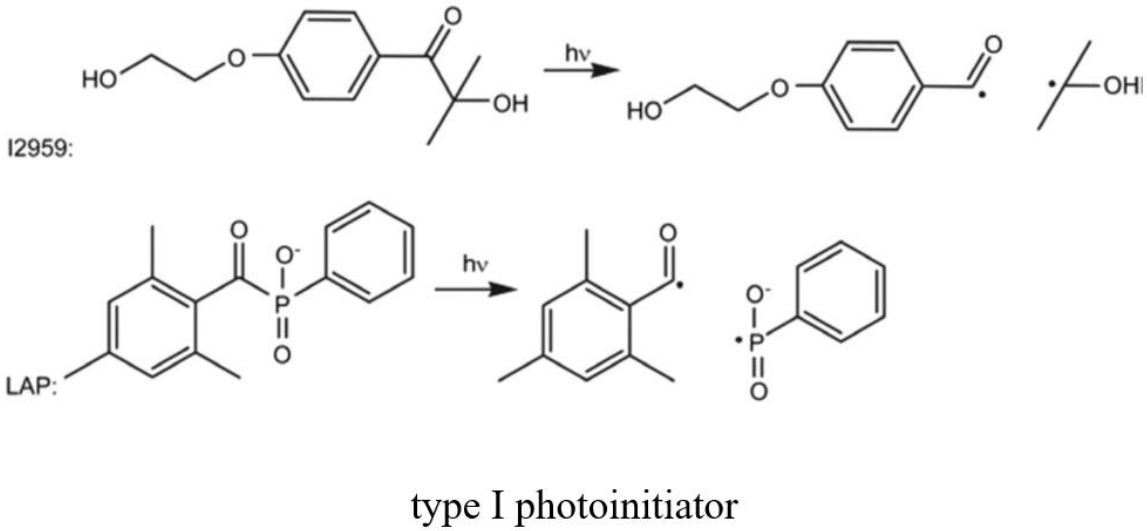


Figure 6 the mechanism of the type I photoinitiator [106]

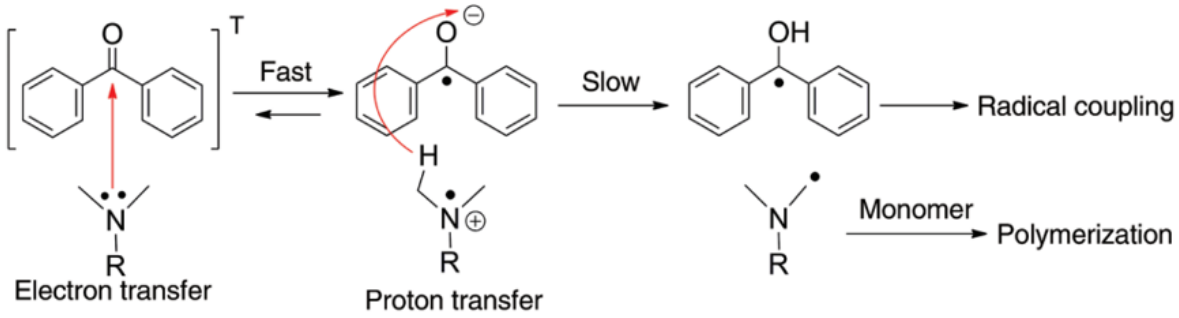


Figure 7 the mechanism of the type II photoinitiator [105]

One of the most used photoinitiators in bioprinting is 2-hydroxy-4-(2-hydroxyethoxy)-2-methylpropiophenone (I2959). Although I2959 has p-hydroxyethoxy group, its solubility is limited to less than 1% (w/v) [107]. Previous research has shown that the I2959 has been shown to support high cell viability in various cell types, including keratinocytes, human hepatocellular carcinoma cells, human umbilical vein endothelial cells, and human mesenchymal stromal cells when used with GelMA and PEGDA [102, 108-110]. Its effective wavelength range is 200–370 nm, typically applied at 365 nm to avoid the cytotoxicity and

oxidative effects of shorter wavelengths. However, its efficiency at 365 nm is relatively low, necessitating extended UV exposure times.

2,2-azobis [2-methyl-n-(2-hydroxyethyl) propionamide] (VA-086) has higher water solubility and lower cytotoxicity compared to I2959 [111, 112]. It has an absorption peak at 375nm, which potentially reduces the toxicity and DNA damage during the DLP printing. For both VA-086 and I2959, increasing the light intensity will decrease the porosity ratio, swelling ratio and enhance mechanical properties of printed hydrogel due to forming the tighter and more crosslinked structure. However, its use can lead to increased hydrogel porosity due to nitrogen gas production during photocrosslinking [111, 113].

Lithium phenyl-2,4,6-trimethylbenzoylphos-phinate (LAP) was synthesized by Majima et al [114]. LAP has higher gelation efficiency and water solubility, which reaches up to 8.5% (w/v), compared with I2959. Its absorption peak spans 365 to 420 nm, making it suitable for photopolymerization with visible light, thus reducing oxidative stress and cytotoxicity [115]. Higher wavelength absorption improves light penetration, accelerating the DLP printing process. LAP has been successfully used in various biomedical applications with different cell types within hydrogel matrices, maintaining high cell viability [32, 115, 116].

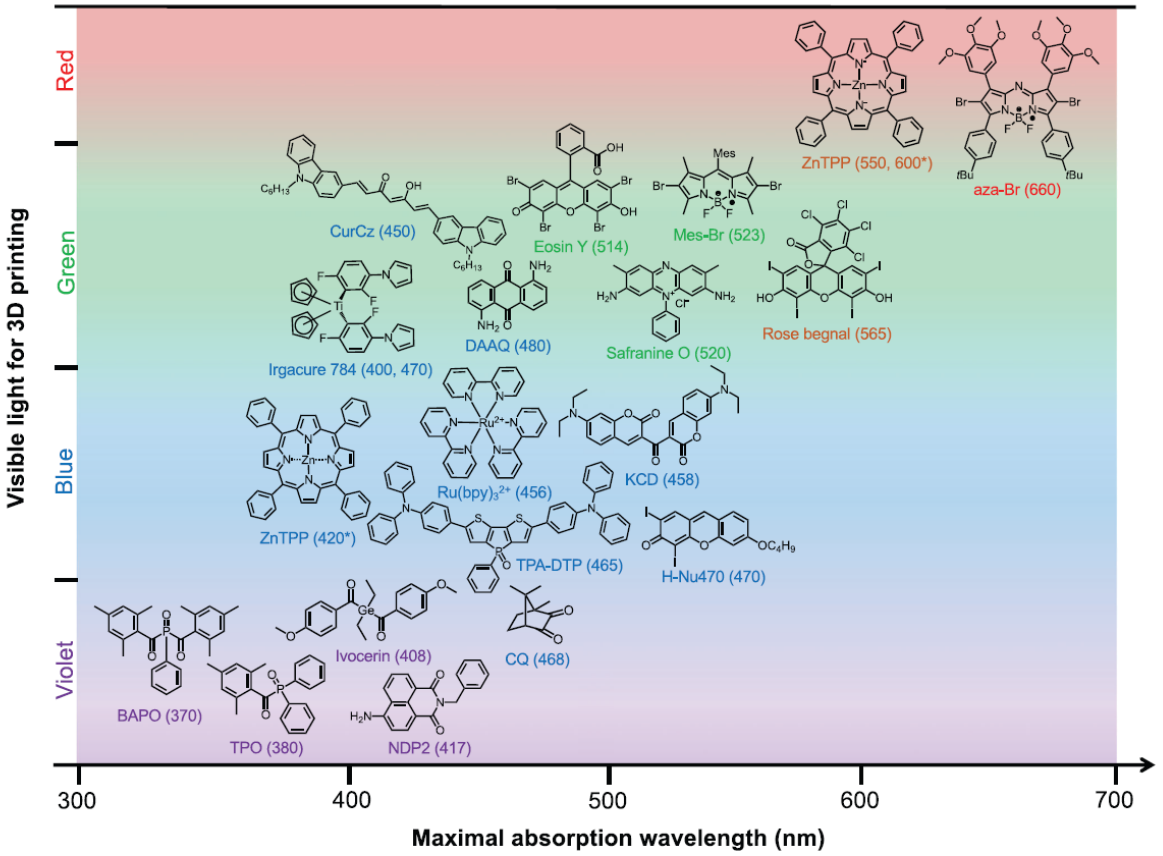


Figure 8 Visible light photoinitiators for photopolymerization 3D printing using violet to red light irradiation [117]

In addition to UV light activated photoinitiators, recent advancements include photoinitiating systems activated by low-energy irradiation, making them suitable for visible light applications, as illustrated in **Figure 8** [117]. For example, camphorquinone (2,3-bornanedione) and Eosin Y (fluorescent dye) are commonly used as the type II photoinitiators, with absorption peaks around 467 nm and 514 nm, respectively [118, 119]. They both used in biomaterials capsulated with cells and maintain high cell viability [118, 120]. However, the excitation and emission spectra of Eosin Y overlap with many fluorescent groups used in cell imaging, potentially limiting its biomedical applications.

To overcome the oxygen inhibition and improve print fidelity, Lim et al. developed a novel visible light initiating system via combining ruthenium (Ru) and sodium persulfate (SPS) to activate the photocrosslinking process [121]. Ruthenium belongs to the transition metal category and has reduced toxicity compared with platinum. Its octahedral structure makes it own bioconjugation functionality like the haem group in haemoglobin (Fe), which has less chance to damage DNA. Ruthenium complexes have strong absorption ability at 452nm and

can be modified via ligands to tune their physico-chemical properties [122, 123]. Under visible light exposure, the photo excited Ru^{2+} oxidizes into Ru^{3+} via transferring electrons to SPS. After obtaining electrons, SPS departs into sulphate anions and sulphate radicals. These radicals are then facilitating bioink aggregation via linking double bonds in monomers. The Ru/SPS system exhibits a relatively high molar extinction coefficient of 14600 L mol^{-1} cm^{-1} at 450 nm, suggesting it requires lower light intensity or concentration for effective crosslinking compared to other photoinitiators. The biocompatibility of this ruthenium based photoinitiator has been tested *in vitro* up to 2mM, which exhibited significantly improved cell viability compared to the commonly used photoinitiator I2959 [124].

Future exploration and development of new photoinitiators for visible light range applications should focus on designing chemical structures with large π-conjugated systems or incorporating electron-donating and electron-accepting substituents to facilitate charge transfer between molecules. This approach mirrors the principles used in organic dye molecule design but requires additional considerations for rapid photo-triggered cleavage or redox reactions.

2.5 Potential of toxicity during DLP Printing

Despite its advantages in high print resolution, fidelity, and speed, DLP printing using photocrosslinking processes can potentially introduce toxicity to cells through several mechanisms. First, UV light (wavelength: 200 – 400 nm) commonly used for photocrosslinking in polymerisation and it can induce DNA damage and cell apoptosis [106]. UV light is categorized into UVA (315 – 400 nm), UVB (280 – 315 nm) and UVC (200 - 280 nm) based on wavelength. UVA, being longer in wavelength, is relatively safer for cell-laden bioinks as it induces weaker cellular DNA damage [125]. Conversely, the irradiation of UVB is potent enough to cause DNA lesions [126]. If the DNA lesions occur, three outcomes would appear as shown in **Figure 9**: self-repair, apoptosis due to double-strand breaks, or incorrect repair leading to abnormal cell programming or potential tumorigenesis [127, 128]. Moreover, UV light can induce cytotoxicity indirectly by sensitizing cellular chromophores to generate reactive oxygen species (ROS), which can cause damage to proteins, lipids, and DNA, including double-strand breaks [129, 130].

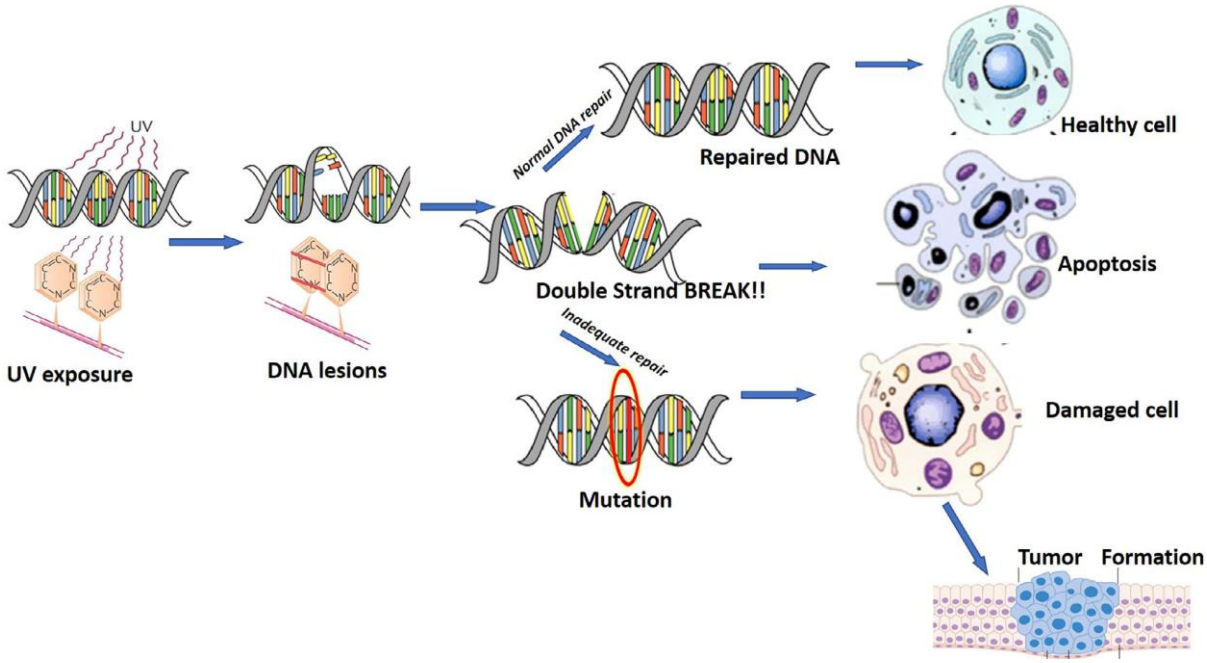


Figure 9 Three outcomes of DNA lesions lead by UV light exposure [106]

Secondly, the photoinitiator itself might be harmful to the cells, depending on its chemical structure, functional groups, and concentration. Photoinitiators with nonpolar function group can penetrate through the cellular membrane. The more hydrophobic the photoinitiator, the higher toxic it will be (**Figure 10**) [131]. Reducing the concentration of applied photoinitiator can mitigate the cytotoxicity [115, 132], but it costs a longer light exposure time or higher intensity to achieve equivalent hydrogel strength [133].

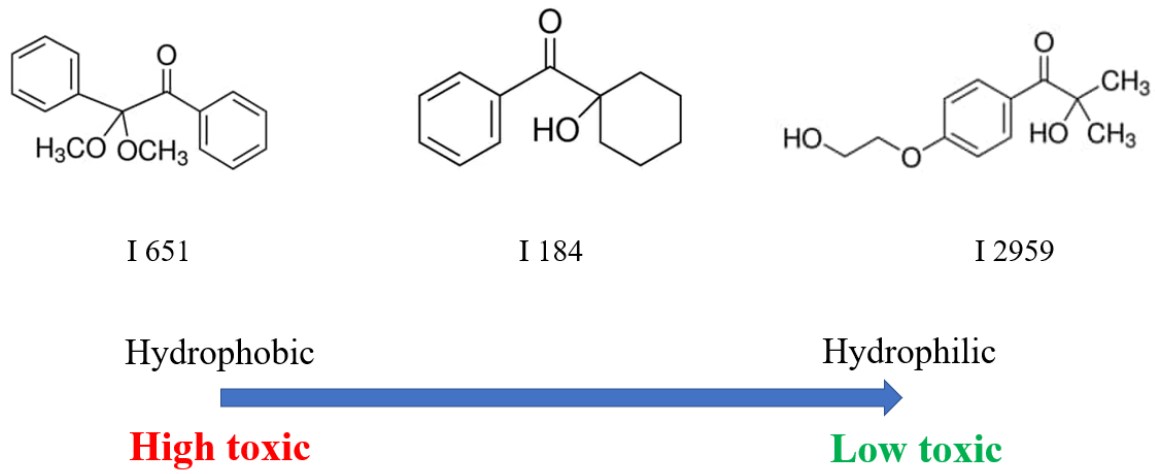


Figure 10 the effect of photoinitiator hydrophilicity on cytotoxicity [131]

Finally, after exposure to UV light, the photoinitiators generate free radicals. The generated free radicals not only initialise the photopolymerization, but also threaten the cell viability, metabolism, and DNA integrity. These free radicals can react with double bonds in membranes, proteins, and DNA, leading to oxidative product formation such as ROS. ROS can degrade lipids and produce toxic aldehyde end products like 4-hydroxynonenal (4-HNE) [134].

2.6 Simulation application in AM based biomedical engineering

Simulation employs mathematical equation to model real world process or system over time, which are widely applied across various engineering field, including aerospace, automotive, energy, tooling, and biomedical areas. Simulations provide insights into system dynamics, predict outcomes, test hypotheses, and optimise performance, particularly when direct experimentation is impractical, costly, or impossible. By developing suitable model, it is possible to predict creep behaviour, mechanical strength, fluid dynamics and optimise structures of targeted products [135-138]. Within the scope of bioprinting, in-silico modelling of 3D printing processes has attracted significant attention in biomedical AM [139, 140]. Conducting numerous repetitions with varying parameters in AM fabrication can be both time-consuming and expensive. Simulations can assist in optimization of AM materials, fabrications techniques, and processes for various biomedical applications, such as materials design, custom implants, drug delivery system, and tissue engineering. These optimizations accelerate the development of new bioinks, construct in vitro models, enable personalised treatments, increase therapeutics efficacy, and enhance patient outcomes. Previous researchers have intensively explored machine learning for prediction and optimisation of AM [140-147]. However, machine learning always requires extensive datasets to increase the accuracy of predication. Conversely, conventional theory based models effectively visualise the underlying problems and explain the relationship between input parameters and the results.

we explore the applications and optimization of simulations in biomedical area, focusing on AM methods including 3D inkjet technology, materials extrusion, and digital light processing (DLP) printing. Each AM method is analysed across pre-processing, in-process, and post-printing stages as shown in **Figure 11**.

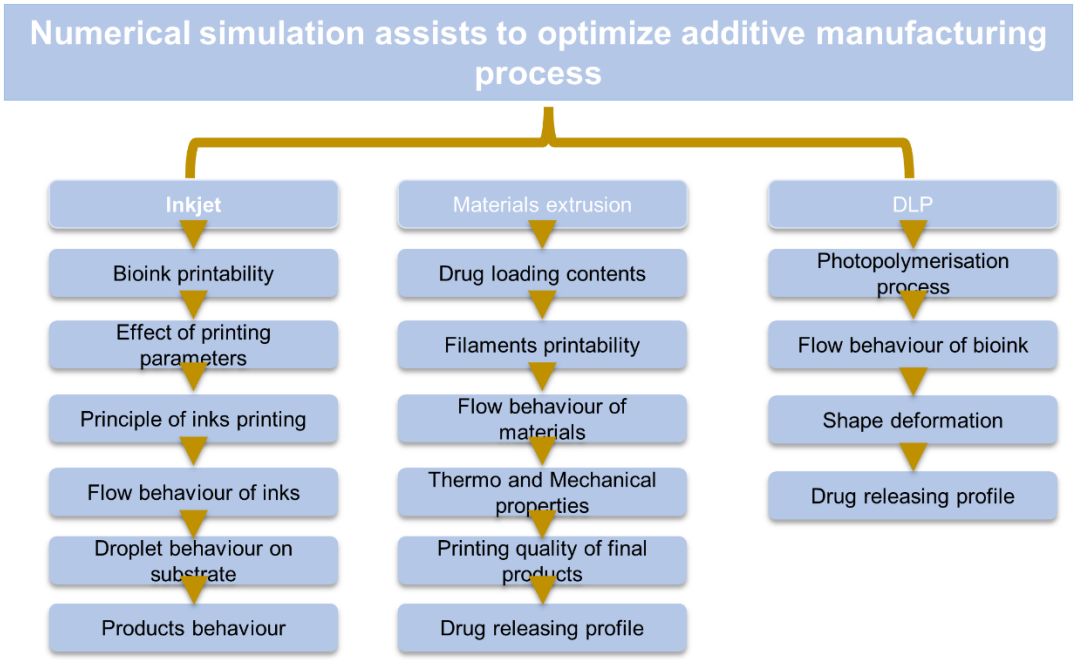


Figure 11 The flow chart outlining contents of the review, covering 3D inkjet printing, ME, and DLP printing processes.

2.6.1 Theory used in the 3D bioprinting simulation

2.6.1.1 Dimensionless numbers

Dimensionless numbers are helpful in predicting the consistency of droplet formation and extrusion from the nozzle in inkjet printing. In the context of bioink printing, Reynolds (Re), Weber (We), and Ohnesorge (Oh) numbers are used to characterise the behaviour of the bioink during the printing process. These numbers are defined as below:

$$\mathrm{Re} = \frac{\rho R V}{\eta} \qquad (1)$$

$$\mathrm{We} = \frac{\rho R V^2}{\sigma} \qquad (2)$$

$$\mathrm{Oh} = \frac{\sqrt{\mathrm{We}}}{\mathrm{Re}} = \frac{\eta}{\sqrt{\sigma \rho R}} \qquad (3)$$

where, ρ is the liquid density, R is characteristic length, V is the liquid velocity, η is the liquid dynamic viscosity, and σ is the surface tension of the bioink. The Reynolds number represents the ratio of inertial forces to viscous forces in the fluid. It is used to assess the flow regime, helping to determine whether the flow is laminar or turbulent, which influences the stability of droplet formation. The Weber number is the ratio of inertial forces to surface tension forces. It helps in predicting the tendency of the droplet to break up during extrusion,

with higher We numbers indicating a greater likelihood of droplet disintegration. The Ohnesorge number combines the effects of viscosity, surface tension, and inertial forces, providing a dimensionless measure of the relative importance of viscous forces in droplet formation and stability. A low Oh number typically indicates that the fluid can form droplets easily, while a high Oh number suggests that viscous forces may dominate, potentially inhibiting droplet formation.

2.6.1.2 Temperature evolution

3D printing processes often involve phase changes, with heat being a primary factor driving these transformations. When a material is heated above melting temperature, it undergoes a phase change from solid to liquid. Conversely, when the temperature decreases below the melting point, the material transitions from a liquid to a solid phase. In 3D bioprinting, accurately modelling the time-dependent temperature profile is crucial for predicting these phase changes. This modelling is typically based on Fourier's second law of heat conduction, as shown in Eq. (4) [148].

$$\rho C_p \left(\frac{\partial T}{\partial t} \right) = \nabla (k \nabla T) + h \nabla T + Q \qquad (4)$$

In this heat equation, ρ is the density, C_p is the heat capacity, T is the temperature, t is the time, k is the thermal conductivity coefficient, h is the convection coefficient, Q is the internal heat source. Fourier's second law provides a mathematical framework for understanding how heat diffuses through a material over time, which is essential for controlling the phase transitions that occur during the bioprinting process.

2.6.1.3 Fluid dynamics during printing

Considering the flow of the bioink or melted filament in the nozzle, it is generally regarded as incompressible and exhibiting non-Newtonian fluid behaviour. This flow behaviour can be effectively modelled using the Navier-Stokes (N-S) equation with modifications to the fluid viscosity coefficient to account for the non-Newtonian characteristics [149, 150]. The N-S equation describe the conservation of momentum and conservation of mass for fluids. The form of the N-S equation is shown below:

$$\nabla \mathbf{u} = 0 \qquad (5)$$

$$\rho \frac{D\mathbf{u}}{Dt} = \rho \mathbf{F}_{\mathrm{v}} - \nabla p + \mu \nabla^2 \mathbf{u} \qquad (6)$$

Where, ρ is the flow density, $\frac{D}{Dt}$ is the material derivative, defined as $\frac{\partial}{\partial t} + \mathbf{u} \cdot \nabla$, $\mathbf{u}$ is the velocity of the fluid, $\mathbf{F}_{\mathrm{v}}$ is the external forces, p is the pressure, μ is fluid viscosity coefficient. For non-Newtonian fluid, μ depends on the rate of fluid deformation at specific temperature. The first equation ensures the conservation of mass for an incompressible fluid, requiring that the divergence of the velocity field is zero. The second equation represents the conservation of momentum, capturing the balance between inertial forces, pressure gradients, viscous forces, and any external forces. These equations are essential for accurately modelling the flow of bioinks and melted filaments during the 3D bioprinting process, where understanding the fluid dynamics is crucial for optimizing printing performance and material behaviour.

2.6.1.4 Fick's second law

Fick's second law describes the time-dependent passive diffusion of small molecules from regions of high concentration to low concentration. This law can be derived from Fick's first law, which describes the diffusion flux, and the principle of mass conservation, assuming no chemical reactions are involved.:

$$\frac{\partial \varphi}{\partial t} = D \Delta \varphi \qquad (7)$$

Where, φ is the concentration that depends on location and time, t is time, D is the diffusion coefficient. The Fick's second law has similar mathematical form as heat equation, where switch the thermal conductivity k with diffusion coefficient D. Fick's second law describes how the concentration of a substance changes with time due to diffusion, providing a critical framework for modelling diffusion-driven processes in various applications, including 3D bioprinting. In bioprinting, understanding this diffusion behaviour is essential for predicting the distribution of nutrients, drugs, or other molecules within printed tissues and ensuring uniformity and efficacy in the final constructs.

2.6.1.5 Mechanics and strength of materials

The printed structures or products should meet the requirement of the mechanical properties to withstand various loading conditions. In continuum mechanics, materials subjected to external forces undergo deformation, which can be quantitatively described by stress, strain, and shear stress:

$$\sigma = \frac{F}{A} \tag{8}$$

$$\tau = \frac{F}{A} \tag{9}$$

$$\varepsilon = \frac{\triangle L}{L} \tag{10}$$

Where, σ is the stress, τ is the shear stress, ε is the strain, F is the applied force, A is the applied cross section area, $\triangle L$ is the deformation, L is the original length. These quantities are fundamental in assessing how a material deforms and behaves under various forces, ensuring that printed structures achieve the necessary mechanical integrity and performance for their intended applications. When a solid material is applied a small load and exhibits elastic deformation, the relationship between stress and strain is typically linear and can be expressed as:

$$\sigma = E\varepsilon \tag{11}$$

$$\tau = G\gamma \tag{12}$$

Where, E is Young's modulus, which exhibits the ability to resist the deformation of applied force. G is shear modulus, and γ is shear strain, which is defined by the change of the angle. In this linear elastic regime, the material will return to its original shape once the load is removed, provided the applied stress does not exceed the material's elastic limit. The relationship between E and G is given by:

$$G = \frac{E}{2(1+\upsilon)} \tag{13}$$

υ is Poisson's ratio.

2.6.1.6 Finite element methods

Finite element method (FEM) is a widely used mathematical simulation method in engineering area, particularly for solving complex structural or time-dependent problems that

do not conform to simple geometries and cannot be addressed through closed-form solutions. FEM is highly regarded in the engineering community due to its versatility and effectiveness in handling a wide range of circumstances and problems. With advancements in high-performance computing, FEM has become an integral component of modern computer-aided design (CAD) and computer-aided manufacturing (CAM).

Before applying FEM to solve a specific problem, it is essential to define the variables, underlying theory, solution domain, and boundary conditions. The application of FEM typically involves three key steps:

1) Domain discretisation. The structure or continuous body of interest is divided into several subdomains or elements. These elements are interconnected at shared edges and nodes, forming a mesh that represents the entire problem domain.
2) Apply the factors. Essential parameters, including material properties, boundary conditions, and environmental factors, are applied to the meshed structure. These inputs are critical for accurately modelling the physical behaviour of the system under study.
3) Solve the model. The model is solved by applying the equilibrium equations to the discretized domain. This analysis allows for the calculation of the desired quantities, such as stress, strain, temperature distribution, or displacement, providing insights into the behaviour of the system under the specified conditions.

2.6.1.7 Lattice Boltzmann method

Modelling fluid flow using the Navier-Stokes (N-S) equations in structures with porous surfaces, complex boundaries, or under multiphase conditions poses significant challenges. These scenarios often involve intricate geometries and interactions that are difficult to capture using traditional methods. The Lattice Boltzmann Method (LBM) provides an alternative approach for simulating fluid dynamics in such complex situations [151-153]. LBM simulates fluid behaviour on a discrete lattice, where fluid particles move and interact in a manner that bridges the gap between macroscopic continuum mechanics and microscopic molecular dynamics. Similar to the FEM, the geometry of the domain must be discretized into elements or lattices. Each node in the lattice represents a specific point in space where fluid particles

can reside. In LBM, fluid particles move from one node to another along predefined lattice links, simulating the fluid's advection. When particles meet at a node, they undergo a redistribution of velocities according to a collision rule, which is designed to conserve mass and momentum. This collision step effectively mimics the advection and collision processes of particles, allowing LBM to capture complex fluid behaviours in porous media, irregular boundaries, and multiphase flows with high accuracy. The general formula of the Lattice Boltzmann equation is shown in Eq. (14).

$$f_i(\mathbf{x}+\triangle t\vec{\mathbf{c}}_i, t+\triangle t) = f_i(\mathbf{x},t)+\mathbf{\Omega_i} \quad (14)$$

where f_i is the concentration of particles that travels with velocity $\vec{\mathbf{c}}_\mathbf{i}$ at the $\mathbf{x}$ poistion at time $\mathbf{t}$, $\triangle t$ is the time step, $\mathbf{\Omega_i}$ is the collision operator. The Lattice Boltzmann Method's ability to handle complex boundaries and porous structures, along with its inherent parallelism, makes it a powerful tool for simulating fluid dynamics in scenarios where traditional methods like the N-S equations might struggle.

2.6.1.8 The Beer–Lambert law

The Beer Lambert law describes the absorption of light by a chemical species in a solution as a function of its concentration. This law is crucial in various fields such as chemistry, physics, and biology for analysing solutions and determining the concentrations of substances. The expression of Beer-Lambert Law is:

$$\log_{10}(I_0 / I) = A = \varepsilon l c \qquad (18)$$

Where, I_0 is the intensity of the incident light, I is the intensity of the transmitted light, A is the absorbance, ε is the molar attenuation coefficient or absorptivity of the attenuating species, l is the optical path length, and c is the concentration of the attenuating species. Based on the Beer-Lambert's Law, the light energy used for photopolymerise an infinitesimal layer can be expressed by considering the absorption of light as it passes through the photopolymerizable material. The intensity of light decreases exponentially as it penetrates the material, and the energy absorbed by a thin layer of thickness dh at depth h can be expressed as:

$$dI = -\varepsilon \cdot c \cdot I(h) \cdot dh \qquad (19)$$

dI is the differential decrease in light intensity as it passes through an infinitesimal layer of thickness, and $I(h)$ is the light intensity at depth h within the material. Integrating this expression over the entire thickness of the material would give the total energy absorbed, but for an infinitesimal layer, this differential form captures the energy required to initiate photopolymerization at that specific depth. The total energy absorbed in a layer of thickness dh can be used to model the rate of photopolymerization and to optimize the exposure parameters in processes like 3D bioprinting that rely on precise light-based curing techniques.

2.6.1.9 Monte Carlo method

Monte Carlo methods, which rely on repeated random sampling to obtain numerical results, are particularly useful for solving problems with significant uncertainty in their inputs. For example, Monte Carlo simulations can be applied to calculate the formation and distribution of crystal cores in printed plastic crystal materials, where the stochastic nature of nucleation and growth processes introduces uncertainty. Similarly, in bioprinting, Monte Carlo methods can model the distribution of printed cells within a hydrogel matrix, accounting for the randomness in cell placement and movement during the printing process. Additionally, in Digital Light Processing (DLP) printing, Monte Carlo simulations can help assess the influence of cell membranes on light distribution, which is critical for accurately predicting the curing patterns in the photopolymerization process. By implementing these methods through computer programming, approximate solutions to these complex problems can be achieved. Monte Carlo simulations enable the exploration of a wide range of potential outcomes, providing insights into the behaviour of systems under uncertainty and aiding in the optimization and refinement of 3D bioprinting processes.

2.6.2 The application of simulation methods in the 3D bioprinting area

The operational process of bioink-based 3D printing devices can generally be divided into three major steps, namely, preparation, in-process, and post-processing. In the preparation phase, a detailed analysis of the bioink's properties is conducted to assess its suitability for the printing process. This involves modelling the rheological behaviour of the bioink, which is crucial for maintaining uniformity in fluid dynamics and preserving cell morphology. The in-process phase focuses on modelling the formation, morphology, and movement of droplets/bioinks, which are key factors that influence the precision, resolution, and overall

quality of the printed microstructures. Simulation of various printing parameters during this stage plays a pivotal role in optimizing the process by enhancing print speed, minimizing errors, and reducing operational costs. In the post-processing phase, the properties of cell- or drug-laden bioinks can alter post-extrusion, especially when exposed to crosslinking agents or changes in external conditions. Modelling the relevant physicochemical parameters at this stage is essential for optimizing drug release profiles, ensuring cell viability, and enhancing the mechanical properties of the final printed constructs.

2.6.2.1 3D inkjet technology

The printing process begins with the design and preparation of the bioink. Unlike traditional biomaterials, bioink may contain cells and operates under varying temperature, pressure, and flow speed conditions. By acquiring the nozzle and bioink parameters and calculating them in Eqs. (1) - (3), a diagram can be drawn as shown in **Figure 12** [154, 155]. Four dashed lines divide the diagram into five distinct areas. The centre grey area represents the standard and desirable printable bioink region. The surrounded area represents: 1) low velocity: droplets cannot overcome the surface energy; 2) splashing on substrate: droplets scatter on the substrate; 3) too viscous: droplets breakup cannot occur and 4) satellite droplets: a series of discrete droplets would form. However, the boundary lines for determining these areas are conditional. The degree of bioink viscosity controls the size of centre grey area [154].

Another study assessed the relationship between the printability of the formulation with its dynamic viscosity, surface tension, ink density, and nozzle diameter under various pressure and temperatures via a proposed high throughput system [156]. When bioink meets with various nanoparticles, it is significant to consider the influence of the nanoparticles on the viscoelasticity, which later affects the printability of bioinks. Particle volume fraction, particle size, and its distribution were included in the model to make prediction [157]. Utilizing the applied model, can greatly accelerate the development of new bioink

formulations, with or without additives, and result in cost reductions.

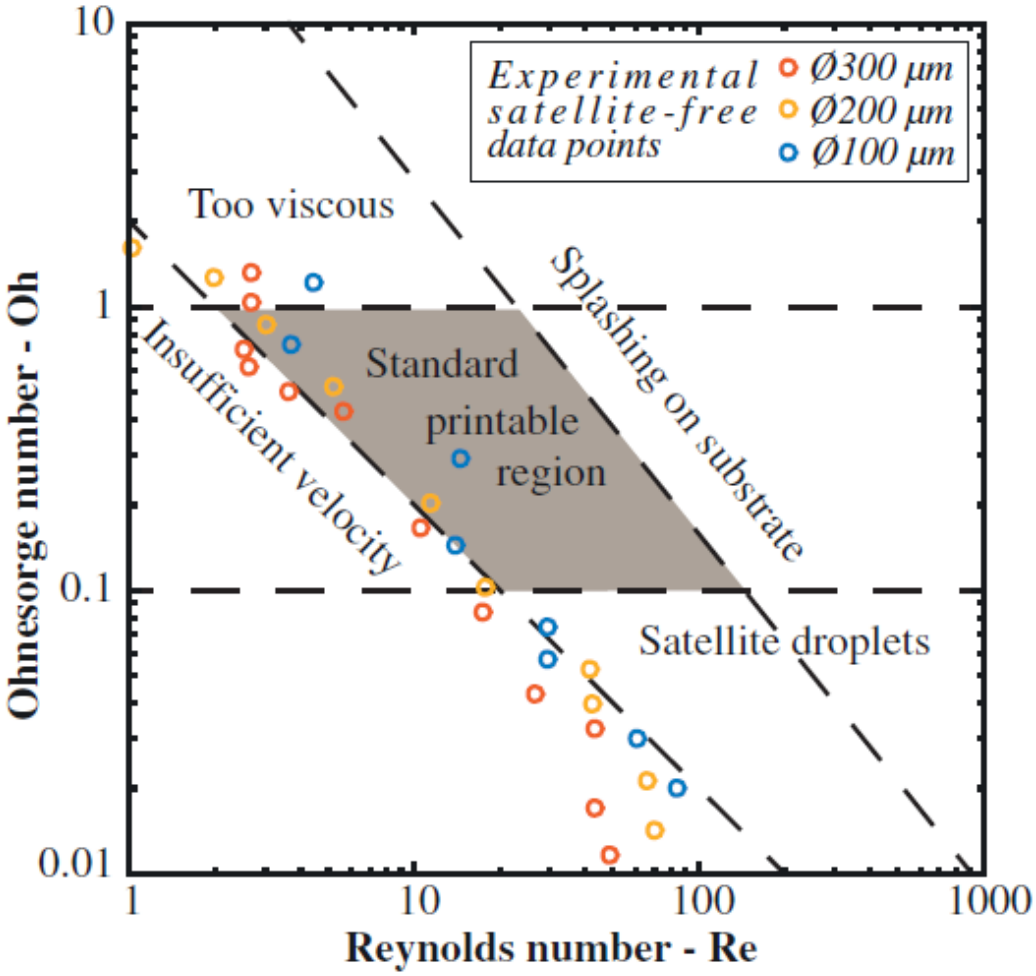


Figure 12. Illustration of the inkjet-printability diagram which can be divided into 5 distinct areas. The grey area in the middle indicates the bioink with the suitable printing characteristics [154, 155].

After examining the printability of bioink, and loading the bioink into the printer, the 3D inkjet printing is ready to work. During the printing process, the droplet morphology is important as it formed the printed structures and determined printing resolution, surface quality, and structural integrity of the final products. The key parameters in the printing process including pressure, viscosity of bioink, temperature, and nozzle morphology, can determine the printability, cell viability and shape fidelity.

The viscosity of bioink and inlet pressure are key factors affecting the printing speed [158]. Increasing the viscosity of the bioinks slows down the droplet formation, whereas increasing surface tension accelerates it [159]. High viscosity bioink requires high inlet pressure to

maintain a consistent extrusion rate, which in turn increases shear stress through the printing path due to the increased fluid speed. The high shear stress can influence the distribution of particles within the bioink. Increasing the inlet temperature enhances extrusion velocity, reduces shear stress, and decreases outlet pressure [160, 161].

A nomogram has been developed to illustrate the relationship between 1) outlet diameter, 2) pressure difference between inlet and outlet, 3) mass flow rate and 4) maximum shear stress based on the Herschel–Bulkley model (**Figure 13**) [162]. This model can be adjusted to create new nomograms for different bioinks.

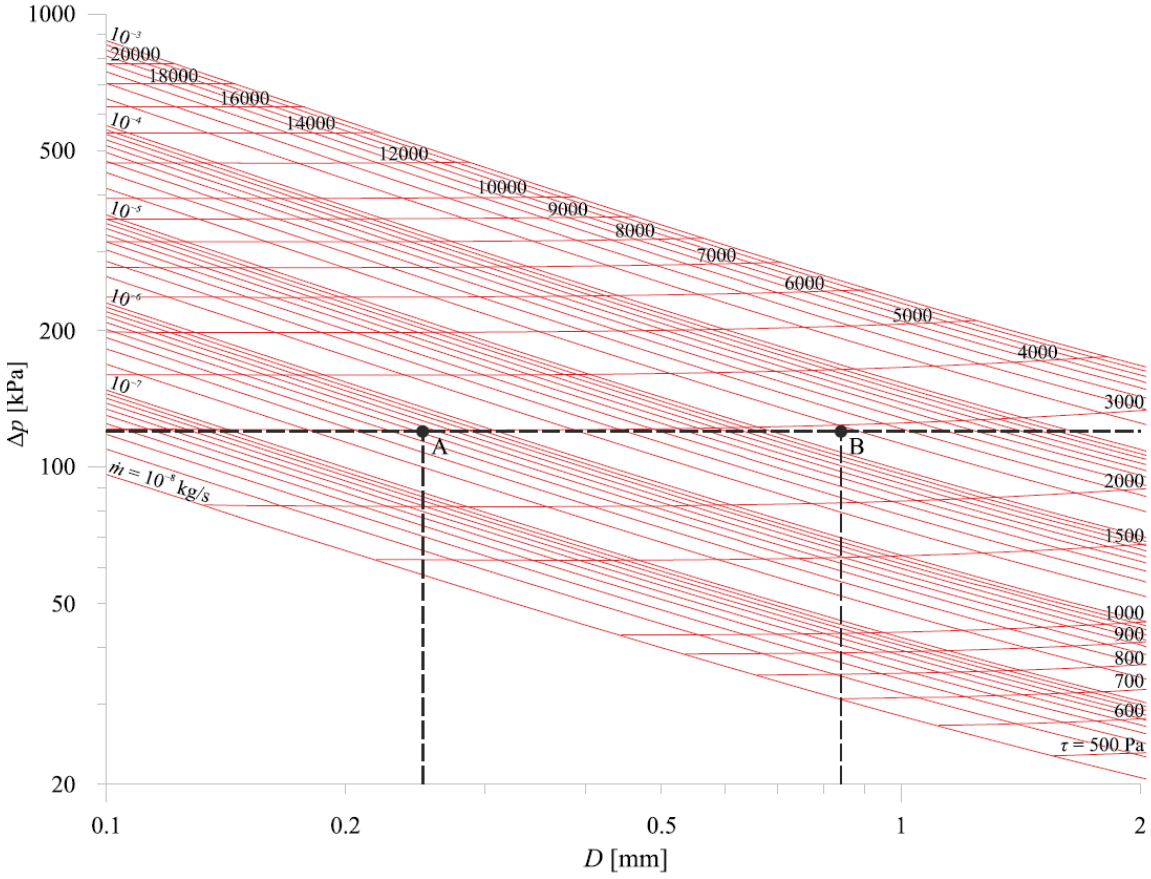


Figure 13 Nomogram for the mass flow rate and the maximum shear stress at the outlet of the printing needle as functions of the outlet diameter and pressure.

Typical droplet formation in inkjet printing involves three steps: 1) negative pressure forms a meniscus surface; 2) positive pressure creates a jet window; 3) negative pressure breaks the droplet and forms a new meniscus surface for next droplet. This dynamic phenomenon can be expressed by the N-S equation and exhibited through simulations **Figure 14** (a) [163]. Due to the velocity difference between the centre to the edge of the fluid, shear force thins the stream

until it reaches a critical value, where the surface tension pinches it into droplets. In laser-induced inkjet printing, the high-energy laser hit the liquid layer, creating a bubble that forces the bioink downward until the bubble bursts. The remaining momentum causes the bioink to continue moving downward, forming a droplet when the momentum exceeds the restrictive forces of viscosity and surface tension (**Figure 14** b). Simulating this process can assist in optimising the energy input, droplet formation, and bioink layer thickness to control droplet size accurately [164]. To minimise the thermal effect of the laser on the ink, a dual chamber system with propellant liquid and bioink separated by a plastic membrane was designed (**Figure 14 c**) [165]. When the propellant liquid is exposed to the laser, a phase change from liquid to gas occurs, creating a pressure variation that extrudes bioink through the nozzle. The study also examined how nozzle diameter, membrane thickness, and laser energy affect the printing process, finding that a smaller nozzle diameter requires less laser energy, thus minimizing thermal impact. Conversely, a thicker membrane increases laser power usage due to higher damping capacity.

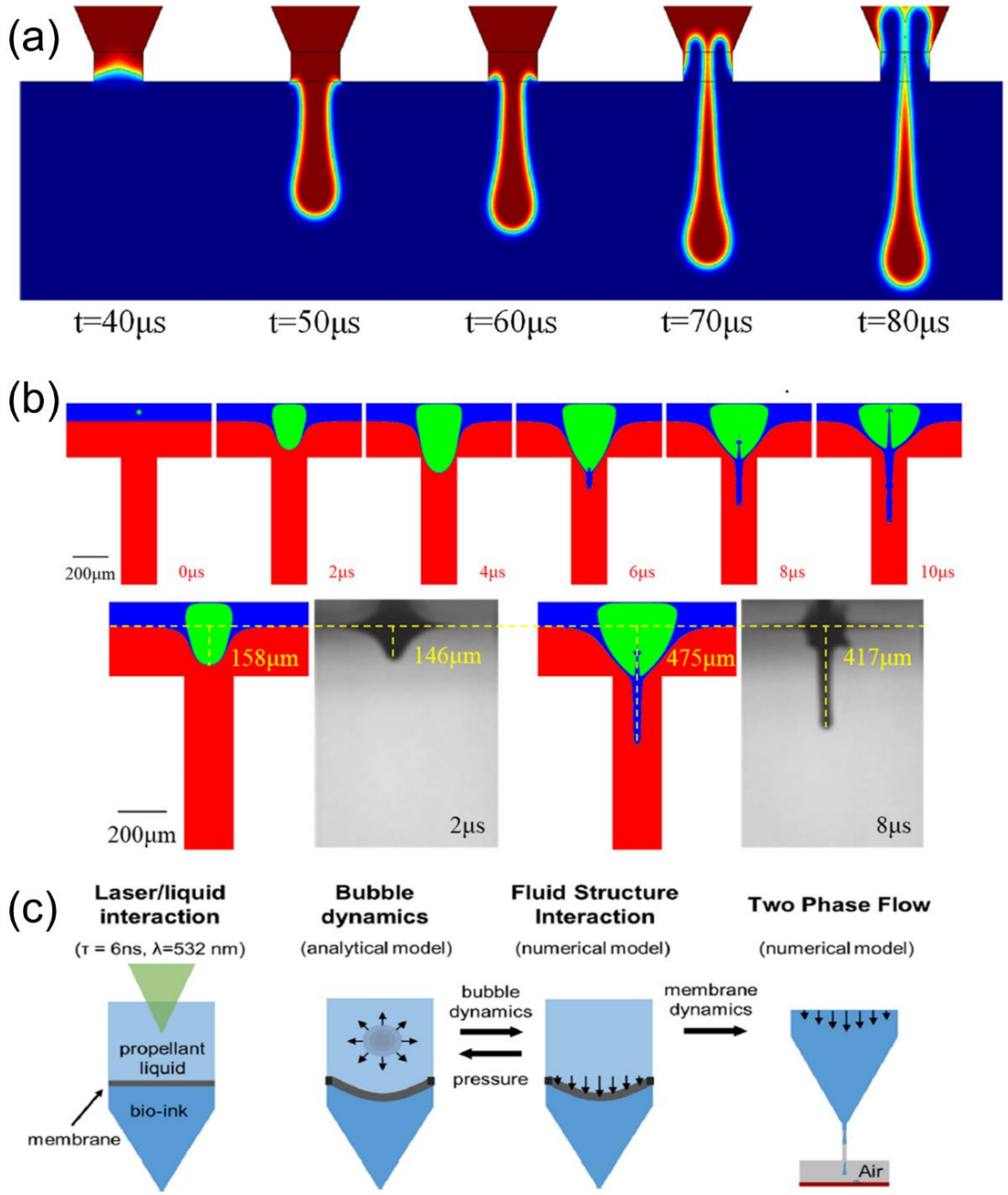


Figure 14 a) Droplet formation process by hybrid drive [163]; **b)** Simulation of jet flow and compare it with experiments [164]; **c)** the schematic of the laser-based microdroplets printing process[165].

After extrusion, the droplet forms a spherical shape before landing on the platform, where it spreads out upon collision. Due to the combined effects of inertial force, surface tension, and viscosity, the droplet retracts to form a hemisphere. Each droplet individually reaches the substrate surface, collectively forming a linear structure. A mathematical simulation proposed to analyse the landing process showed that a larger surface contact angle leads to a broader

spreading radius, faster transformation, and thicker film formation. Conversely, higher droplet velocity causes wider spreading and potential separation into scattered shapes [166].

Direct printing onto objects with complex surfaces is common in the medical field. Arango and colleagues proposed a mathematical model to compensate for the distance from the nozzle to the non-flat substrate based on energy balance [167]. Triangular prisms and truncated cylinders were used to verify experimental and simulation results. Using high-density bioink and larger volume droplets helps prevent deviations from the intended target, though it reduces printing resolution and may cause rheological issues. This underscores the importance of optimizing printing parameters, especially for curved surfaces.

However, using the N-S equation to model fluid flow in structures with porous surfaces or complex boundaries, and under multiphase conditions, presents several challenges. The Lattice Boltzmann method offers an alternative for simulating fluid dynamics in these scenarios [152, 153]. This method simulates fluid behaviour using a lattice that includes streaming and collision. Monteferrante and colleagues used the Lattice Boltzmann method to simulate the ink printing process, constructing a model with two phases representing the ink and air evolution to predict internal forces acting on cells or nanoparticles within the flow channel [168]. The common simulation methods in 3D inkjet technology are summarized in **Table 2**.

Table 2. Summary of inkjet printing simulation.

Type	Aims	Methods	Ref
Inkjet	Predict printability of droplet	Re, We and Oh numbers	[154]
Inkjet	Predict printability of droplet	A high-throughput approach	[156]
Direct ink writing	Design multi material inks to match rheological and mechanical properties	Calculate particle interaction potential	[157]
Inkjet	Predict droplet formation	CFD and Fluent	[159]
Inkjet	Temperature on shear stress, pressure, velocity	COMSOL Multiphysics 5.4a	[160]
Inkjet	Model the flow behaviour and rate of bioink	Herschel–Bulkley model	[161]
Inkjet	Optimize a high temperature microheater	COMSOL 5.1. A	[148]
Inkjet	Optimize printing parameters	Ansys Workbench18.2	[162]

Inkjet	Predict the flow state in the channel	Linear time-varying system equivalent circuit model	[149]
Inkjet	Pressure field control and optimization	N-S equation	[150]
Inkjet	Predict droplet formation	N-S equation	[163]
Inkjet	Predict droplet formation	N-S equation	[164]
Inkjet	Predict ink extrusion process	Analytical/numerical modelling	[165]
Inkjet	Predict the printing process	Numerical calculation	[166]
Inkjet	Predict drop distance of the ink in non-planar substrate	Numerical calculation	[167]
Direct ink writing	Predict non-Newtonian inks printing process	Lattice Boltzmann model	[168]
Direct ink writing	Predict equivalent stress of printed valve	Finite element methods	[169]

2.6.2.2 Material extrusion

ME is another printing technique, which continuously deposits materials to create objects. The materials used in ME can include bioink or thermoplastic filaments. The morphology of the printed materials is important as it affects the printing resolution, surface quality, and structural integrity of the final product. Various printing parameters such as pressure, nozzle size, melting temperature, extrusion speed, and distance from nozzle to platform play significant roles in determining the quality of the final products. A comprehensive understanding of about the ME process is essential for optimising strength, speed, and fidelity of the printed product. **Table 3** provides a summary of simulation-based prediction methods pertinent to this process.

The bioink used in the ME is same as that used in inkjet printing. The primary difference between ME and inkjet printing is that the ME continuously deposits materials rather than creating droplet. Therefore, the preparation of bioink-based materials for ME can follow similar protocols to those used in inkjet printing. Another material used in the ME is the thermoplastic filament, which is manufactured to specific diameter specifications. The filaments used for ME is usually mixed with appropriate drug concentrations and exhibit adequate mechanical properties to ensure they can be loaded into the printer without issue. Filaments should possess the desired mechanical properties. Otherwise, they may suffer from various issues such as 1) breakage by feeding gears if the materials are too fragile, 2) undeliverability if the material is too soft, or 3) surface breakdown due to low toughness. Modelling printability and passive drug diffusion into the filaments is crucial for developing new filaments materials. These filaments are heated above their melting point before being

extruded from the nozzle, and as the filament transitions from a solid to a liquid phase, its rheological properties significantly impact the printing accuracy and sensitivity.

There are two main methods for drug loading in ME: hot-melt mixture and passive diffusion in tablet printing. The hot-melt mixture method requires careful consideration of the melting temperatures of both the filaments and the drugs, as excessively high temperatures can degrade or inactivate the drugs. The major limitation of the passive diffusion method is the maximum drug loading percentage that can be incorporated into the filaments. Previously reports indicate that drug-loaded percentage is less than 2% w/w via using passive diffusion method [170, 171]. The printability of new filament can be predicted by acquiring the bending test [172, 173]. A decision tree as shown in **Figure 15** illustrates the relationship between the printability of filaments and the maximum displacement and force in a bending test, enabling the prediction of filament printability based on these parameters. To validate the prediction accuracy of this model, new filaments can be produced and tested for their maximum displacement and applied force, allowing for the prediction of their printability and comparison with actual experimental results. According to the author, the model's current predictive accuracy is 84.85%. To further improve its accuracy, additional parameters should be incorporated into the model [172].

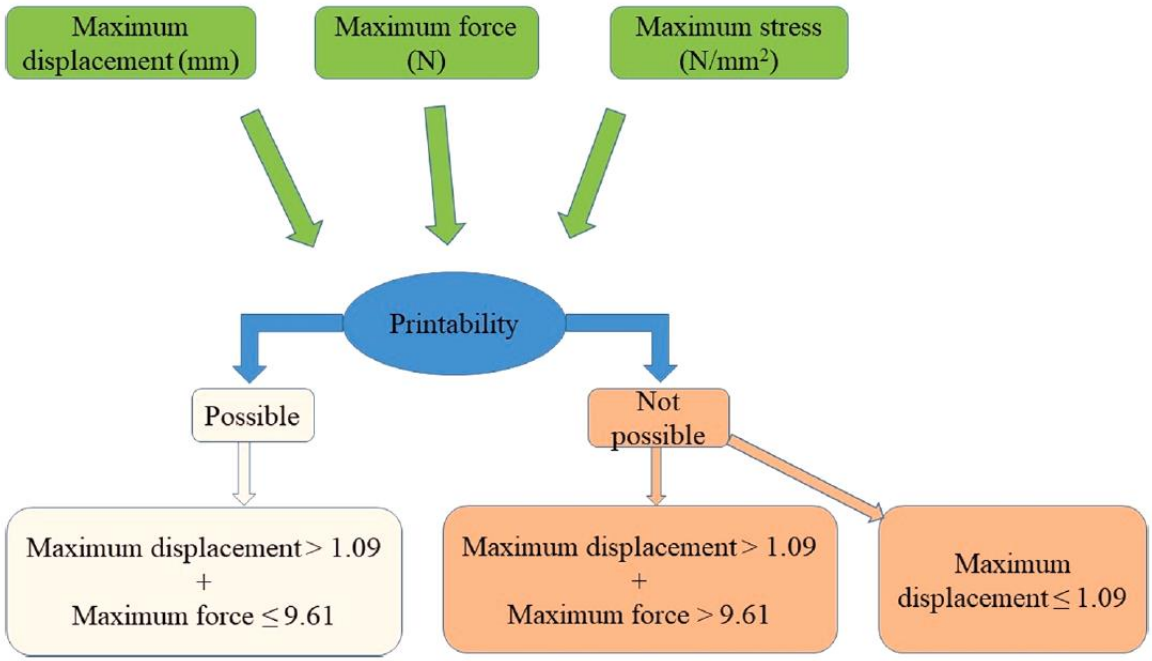


Figure 15 A decision tree shows the relationship between filament printability with maximum displacement and force in the 3-point bending test [172].

After the materials have been designed to meet specific requirements and loaded into the printer, the next step is to analyse the effect of printing parameters on their physical and chemical performance post-extrusion. By simulating the dynamic deposition process, it is possible to understand the fluid dynamics of the filaments from nozzle to platform, optimize the shear force due to the viscosity, and balance the cell viability or the quality of printed products with the printing parameters. The shape of the printing nozzle can significantly affect shear stress. For instance, a tapered conical nozzle generates lower shear stress compared to a conical nozzle (**Figure 16**a). Meanwhile, decreasing pressure and increasing nozzle diameter can significantly reduce shear force [174, 175]. Göhl et al. assessed the printed shape in relation to printing parameters, predicting the effects of nozzle height, line width, and printing speed on the shape and viscoelastic stress distribution of extruded materials [176]. The evolution of printed line shape can be predicted using the N-S equation for its evolution. The extrusion velocity is the major parameter affecting on morphology changes, while surface tension and shear viscosity have minimal influence (**Figure 16**b) [177]. Achieving high printing resolution at corners or turns during the printing process is challenging due to factors like capillarity, nozzle retracing, and printer vibration [178]. A mathematical model was built to investigate the influence of 3 printing parameters, namely, printing direction, corner accuracy and fluid support on ink extrusion [178-180]. The proposed model can predict the particle distribution and width difference between corner and centre, including these 3 factors, allowing for the controlled distribution of particle-loaded materials in ME.

For the fabrication of hollow structures, such as vascular regeneration, a coaxial material extrusion method is particularly suitable (**Figure 16**c). The shear stress within outflow channel significantly influences the distribution and survival rate of cells. FEM model can analyse flow behaviour and extrusion process, optimizing the input pressure. To balance the mechanical property of fabricated vascular with printing materials, they optimize the formulation and printing parameters to meet the requirements [181-184].

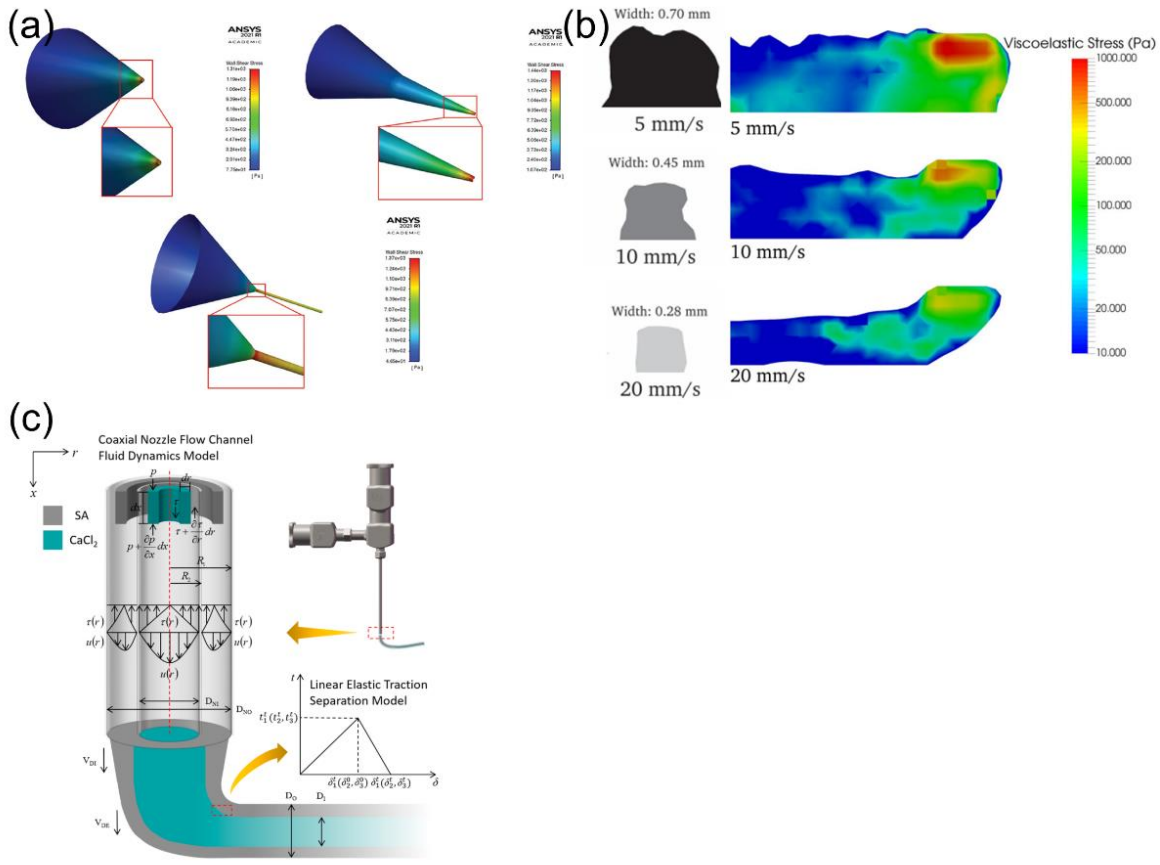


Figure 16 a) Contour of wall shear stress for tapered conical, conical, and cylindrical nozzle [174] ; **b)** Comparison of the cross section area and distribution of viscoelastic stresses in lines printed with different printing speed [177]; **c)** Schematic diagram of the theoretical model for each stage of the coaxial jet process [181].

Thermal dynamic presents another challenge in 3D printing fabrication, inducing morphology changes, and limiting the prediction accuracy. The proposed models used numerical finite-difference approaches to predict temperature changes (**Figure 17**) [185-187]. These models accounted for phase changes through latent heat resources and included critical parameters such as thermal convection coefficient, thermal conductivity, nozzle diameter, and printing speed. By modelling and optimizing these parameters, spatial heat administration can be controlled and homogenized, preventing thermal and crystallization damage to feedstocks during the development of new multi-printing drugs. Additionally, adjusting these critical factors can accelerate printing speed while maintaining product functionality, thereby enhancing the production process.

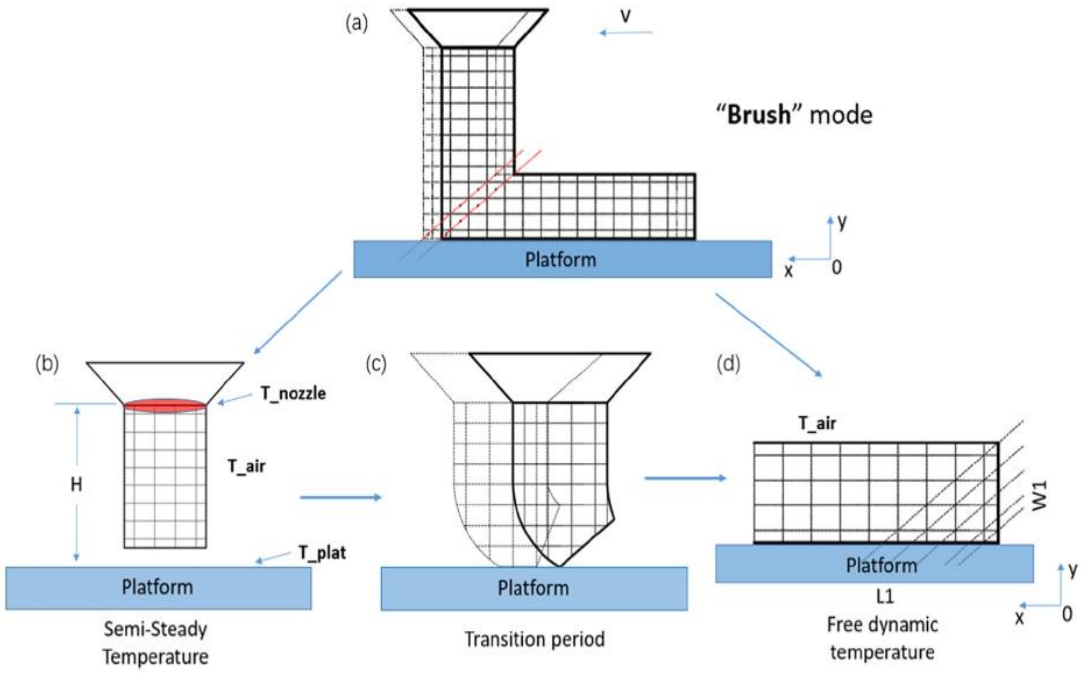


Figure 17 Meshed filaments of three periods in time sequence starting from semi-steady temperature to transition period and finally, free-dynamic temperature during ME printing process [186].

To further improve the precision and quality of the printing process, it is recommended to combine simulation with digital twin in-process monitoring, enabling real-time adjustments of the targeted products. The digital twin monitoring system can detect the edges of printed parts and compare them with the original CAD model to assess differences, as shown in **Figure 18** [188]. The blue line represents the ideal printed edge of the deposited filaments, while the green line indicates the actual edge of the extruded material. By using the information gathered from the digital twin monitoring system, users can ensure that the deposited filaments remain within the acceptable threshold distance.

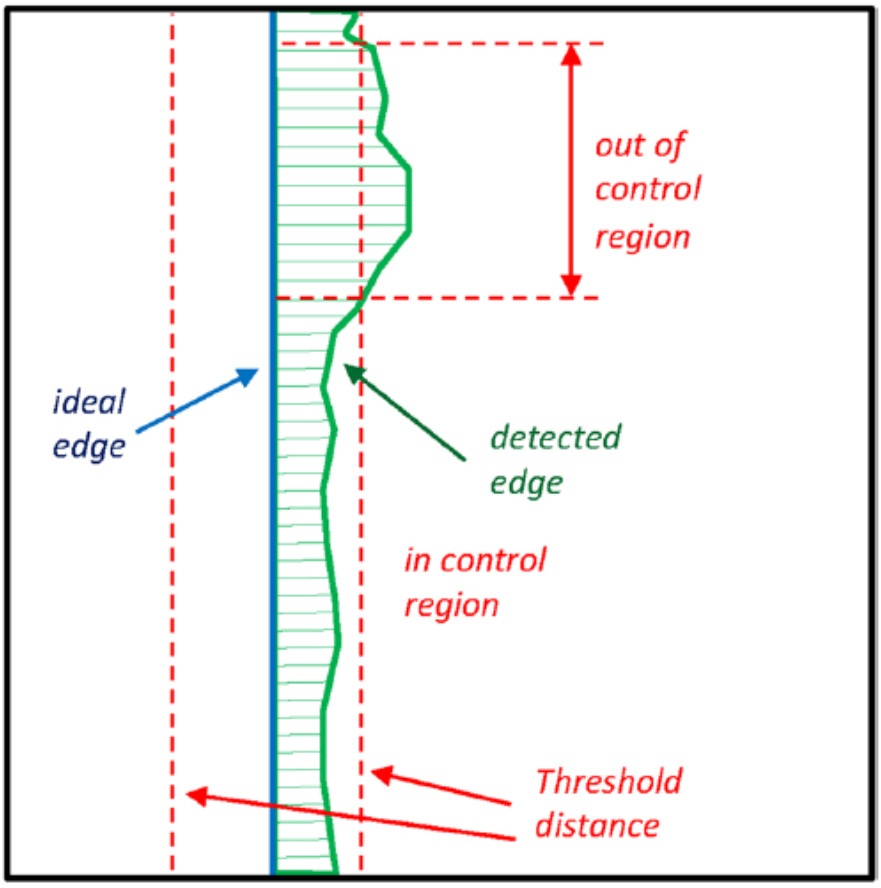


Figure 18 An example of the digital twin monitoring system detected the printed edge and analysis process [188].

The various prediction in device design, materials properties and characteristics, and printing processing parameters have been systematically reviewed above. The following sections will focus on the simulation of the ME printed products and drug-release kinetics.

For printed products, mathematical simulation and FEM are frequently utilized to simulate mechanical properties [169, 189, 190]. In ME printing, fill density is critical in determining the mechanical property, porosity, and structure degradation of printed products. Fill density particularly vital in biomedical applications, as porosity is a key parameter that affects the additive diffusion rate, subsequently influencing the growth and proliferation of cells seeded within the construct [191]. Void density between printed filaments is crucial for the quality of final printed products. Controlling the temperature could improve sintering processing and reduce the void density [192]. Thereby improving the mechanical properties of the final

product. Meanwhile, the mechanical property of the transverse direction is always weaker than the axial direction of printed products. Optimal selection of printing direction and parameters ensures that the final products meet the required mechanical properties [193]. Besides structural optimization, composite interlocking scaffolds with different formulation can also facilitate load transfer and enhance interfacial integration. Soft materials, due to their larger deformation, are always unsuitable as solo materials for fabricating interlocking scaffolds. When the difference in Young's modulus between materials is less than an order of magnitude, the combination of soft and hard materials can result in the lowest von Mises stresses while maximizing load transfer abilities [194].

Microneedles are more convenient and less painful for drug administration compared to the conventional needle injections. The drug diffusion process from microneedle to skin can be illustrated in **Figure 19** [195]. Through the simulation, the drug releasing profile and degradation can be in silico replicated and controlled drug administration can be designed via changing the materials, shape and drug loaded amount of microneedle or capsules [195, 196].

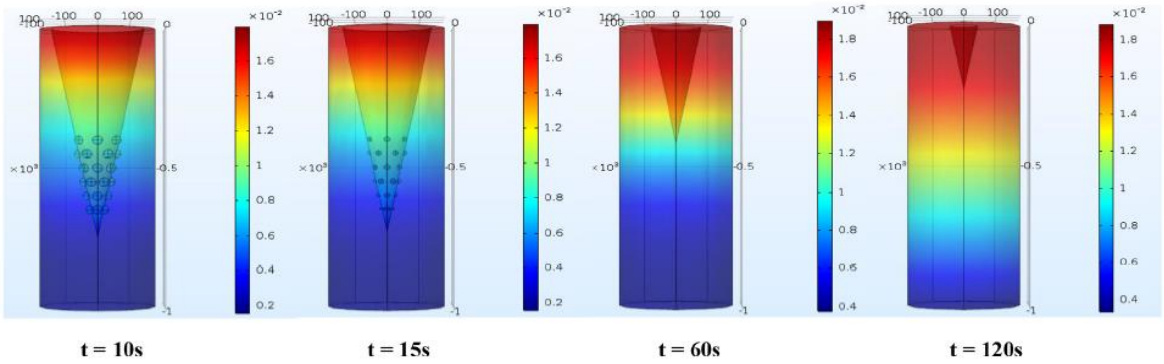


Figure 19 Illustrates the microneedle dissolution process with time [195].

In addition to mathematical and FEM simulation, machine learning methods have been widely applied to the ME printed products. It can link printing parameters with the error detection [197, 198], printing efficiency [199], quality [200], or functionality [201]. Different machine learning methods have unique advantages and can lead to varying degrees of efficiency and accuracy [202, 203]. For example, the hexagon classification results of 5 machine learning methods used to predict filament mechanical characteristics are shown in **Figure 20**. Random forest and Support vector machine achieve an overall high accuracy, while deep learning, neural network, and k nearest neighbour exhibit relatively limited

predictability score [203]. Therefore, careful consideration should be given when selecting and applying machine learning methods based on type, amount, and conditions of data available.

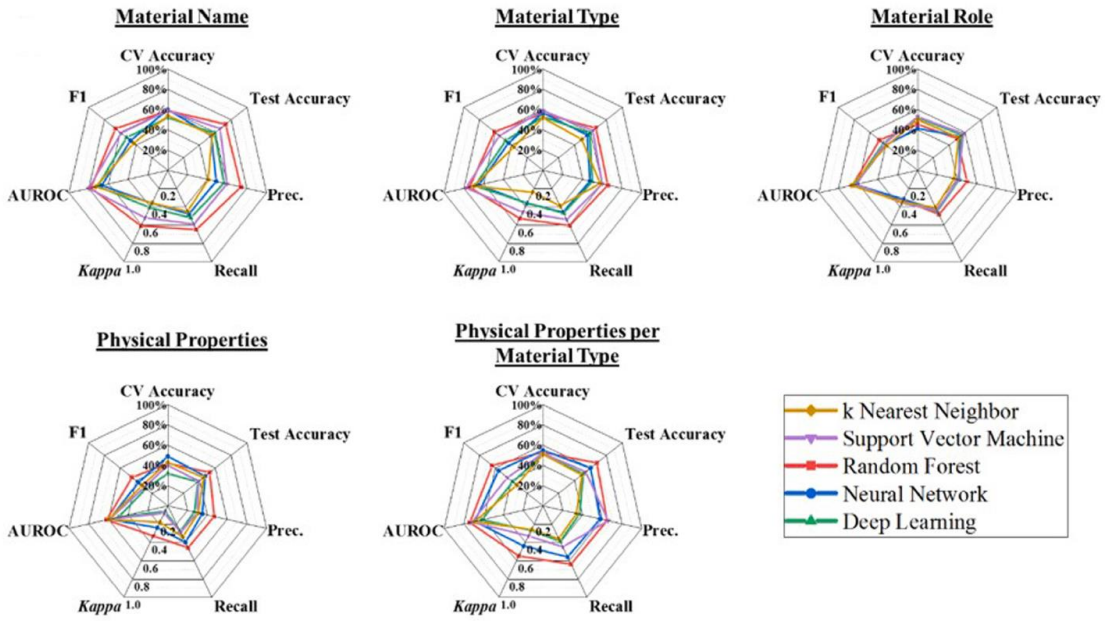


Figure 20 Hexagon of predicted results of the filaments mechanical characteristics such as material name, type, role, physical properties and physical properties per material type using 5 different simulation methodology [203].

Table 3 Summary of ME-based simulation.

Aims	Methods	Ref:
Predict printability of filaments	3-point bending test and decision tree	[172]
Predict printability of filaments	3-point bending test	[173]
Nozzle optimization	Finite element method	[174, 175]
Predict printed filaments morphology	Finite element method	[177]
Control the behaviour of deposited lines at corners for moderate viscosity inks	Numerical calculation	[178]
Control the direction-dependent microstructures	Analytical model	[179]
Bioink flow behaviour in coaxial material extrusion method	Theoretical model	[181, 182, 184]
Predict filament deformation in coaxial material extrusion method	Finite element analysis	[183]
Predict temperature evolution	Domain discretization	[185]
Predict temperature evolution and crystallization	Domain discretization	[186]
Predict part distortion in materials extrusion of semi-crystalline polymers	COMSOL	[187]
Predict mechanical property of passive-diffused filaments	Finite element methods	[189]
Predict the fill density of final products	Numerical calculation	[191]
Predict mechanical properties of printed products	Numerical calculation	[192]
Predict mechanical behaviour of material printing direction	classical laminate theory	[193]

Draw monogram to predict mass variation coefficient of printed products, printing time, and the drug release performance	Design of experiments	[204]
Predict Drug releasing profile	Numerical calculation	[196]

2.6.2.3 Digital light processing

There are relatively fewer simulations studies on DLP printing than inkjet and ME printing. In DLP printing, simulations primarily aim to predict the photo-crosslinking process, and the quality of printed products based on relevant processing parameters. These parameters include bioink properties, light intensity, light exposure time, print layer thickness, geometry, and physicochemical and mechanical properties.

In DLP printing, the light exposure plays a critical role in determining the photopolymerization process. The photocuring process was normally divided into 3 steps, i.e., 1) pre-curing, 2) completion of curing, and 3) preparation for the next curing cycle. The energy absorption happened in the first two stages following Beer's law [205]. By determining values such as solid absorbance, liquid absorbance, and gelation time, the curing time of each layer can be predicted using Jacobs' curve. This curve illustrates the relationship between absorbed UV light time and the thickness of solidified photocurable material (**Figure 21**a) [206].

Functional gradient structure can be achieved via DLP method with changing the grayscale light patterns. A radiative transfer coupled chemical reaction – diffusion model was proposed to simulate how different grayscale light patterns affect the quality of printed layers. Light exposure triggers photoinitiators to break down into free radicals, which then initiate localized polymerization. As a result, printed shapes, especially at pattern boundaries, exhibit significant variations with varying grayscale light intensities [207]. Light scattering can also appear when particles or high density cells loaded in bioink [208]. In cell-loaded bioink, light scattering primarily arises from two sources: the refractive index mismatch between the cytoplasm and the surrounding biomaterial, and subcellular components such as the nucleus and organelles. To mitigate the former effect, which can be reduced effectively by incorporating iodixanol, a biocompatible supplement (**Figure 21**b). A Monte Carlo-based model was utilized to simulate the propagation of light, demonstrating a 10-fold reduction in light scattering [209]. When the viscosity of bioink is high, removing partially solidified

bioinks from the walls of printed products becomes challenging. These residual bioinks can cause overcuring during subsequent curing processes, thereby reducing the final resolution of printed products. Moreover, high viscosity bioinks can lead to significant adhesive forces, potentially resulting in product failure. An acoustic approach was proposed to enhance the bioink flow and prevent overcuring. Numerical simulations can predict the velocity distribution of bioink in the system under varying frequencies of acoustic agitation. Optimizing the frequency through simulation aims to maximize ink flow rates and enhance replenishment of the build area [210].

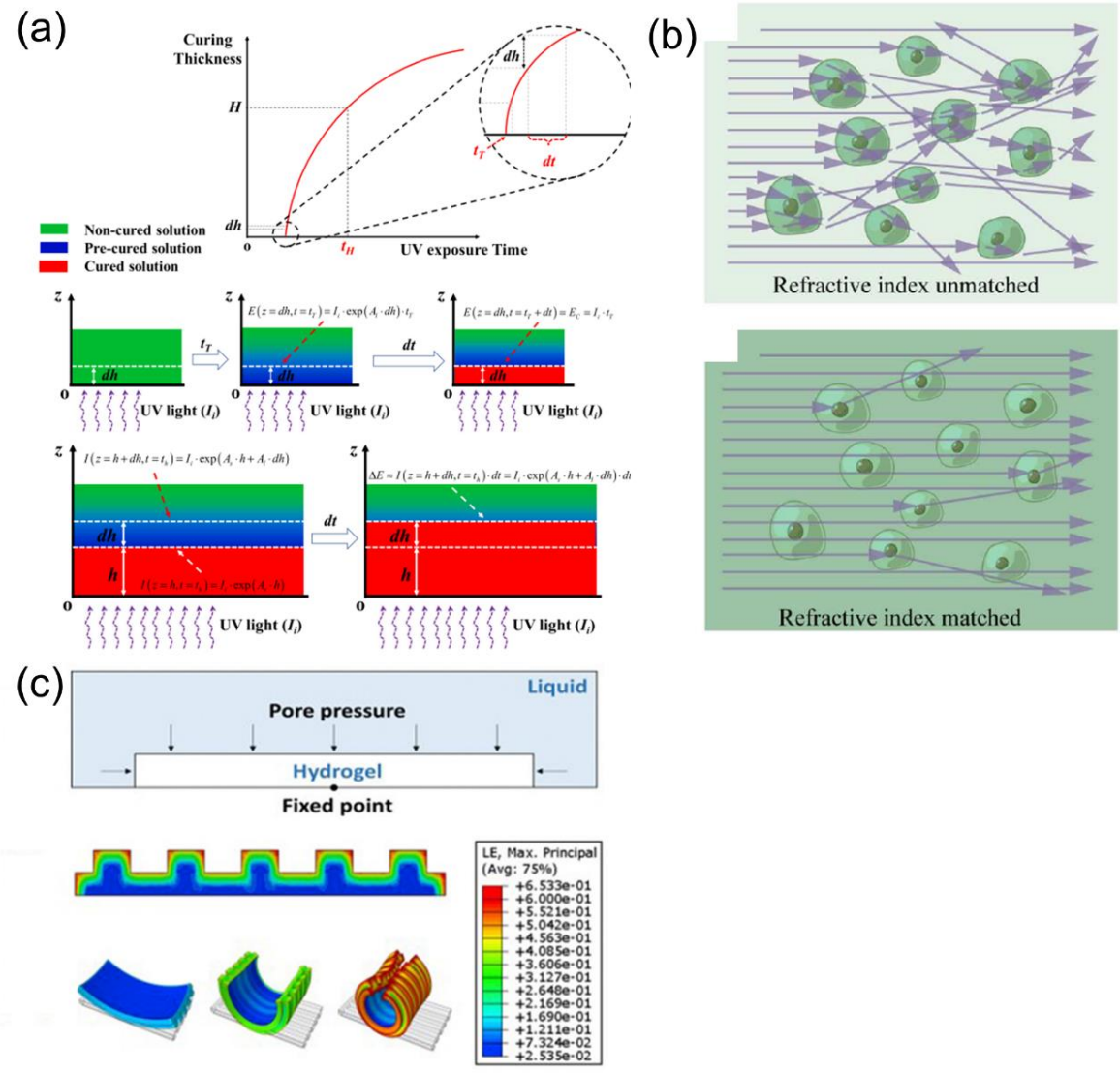


Figure 21 a) Schematic diagram of a Jacobs working curve, the beginning of curing with an infinitesimal thickness dh, and curing with an infinitesimal thickness dh of a completely cured solid with a thickness of h [206] ; **b)** A schematic showing light propagation in a refractive index–unmatched and matched bioink [209]; **c)** Moisture swelling model used for the FEA simulations. Distribution of hydrostatic pressure and Shape

morphing. The volume expansion started from the surface, and the deformation progressed due to the relative differences in the hydrogel interior in terms of the volume expansion rate [211].

DLP printed products exhibit anisotropic properties along the z-axis due to the layer-by-layer printing process. When printed hydrogels are immersed in water, their designed structure leads to differential swelling and expansion rates, resulting in internal forces that cause directional deformation of the printed structure. This deformation process can be analysed using FEM models, which assist in optimizing pattern designs to achieve the desired shape deformation (**Figure 21**c) [211, 212]. In another study, varying tablet thickness and drug loading can adjust drug releasing profile. This affected drug realising profile can be simulated by artificial neural network [213].

2.6.3 Discussion

The field of numerical simulation is still in its infancy, presenting numerous challenges that require more comprehensive and efficient modelling efforts. Numerical analysis and simulation codes can provide the theoretical foundation essential for a deeper understanding of the physical and chemical aspects of 3D printing. This approach has significantly improved state-of-the-art prediction and optimisation of the 3D printing processes and final product.

2.6.3.1 Theory used in the 3D bioprinting simulation

The simulation of 3D bioprinting processes is deeply rooted in various theoretical frameworks that guide the optimisation and control of bioprinting parameters. These theories encompass aspects of fluid dynamics, material science, cell biology, and computational modelling, all of which are significant to predict and enhance the performance of bioinks and printed structures.

One of the foundational theories employed in 3D bioprinting simulation is fluid dynamics, particularly as it aims to simulate the rheological behaviour of bioinks. The N-S equations, which describe the motion of viscous fluid substances, are frequently used to model the flow characteristics of bioinks during the printing process. The modified N-S equations are also

utilized to predict the non-Newtonian flow behaviour of bioinks, which is crucial for ensuring consistent extrusion and maintaining the integrity of the printed structures. In the more complexed boundary conditions, Lattice Boltzmann method provides an appliable tool to discretizes the fluid domain into a lattice grid and solve the fluid particles move and collide.

In addition to fluid dynamics, continuum mechanics plays a significant role in the simulation of 3D bioprinting. Theories in this domain help model the mechanical properties of both the bioink before printing and the constructs post-printing. Constitutive models describe how materials respond to different loading conditions, which is critical for predicting the mechanical stability of bioprinted tissues and scaffolds. This is particularly relevant in the post-processing phase, where the material properties may change due to factors such as crosslinking or environmental stimuli. FEM allows for the detailed analysis of stress, strain, and deformation within the printed constructs under various conditions. This is essential for optimizing the mechanical performance and ensuring the structural integrity of the final product. For example, fabrication of a regenerative skin tissue needs to meet the elastic properties before turning it into a clinical tool. Furthermore, FEM can also be employed to predict the behaviour of bioinks during deposition, helping to optimize droplet formation and resolution. However, when applying the FEM in solving problems, it is not necessary to always create a high-density mesh with a maximum possible number of nodes and elements, even if the higher number of elements and nodes gives a higher accuracy. It is smart to balance a desired level of accuracy and the mesh density using the available hardware resources.

The core theories underlying light-based simulation in 3D bioprinting are based on optics and photophysics, particularly the principles of light propagation, absorption, scattering, and photopolymerization kinetics. These principles are used to model how light interacts with the bioinks during the printing process. The Beer-Lambert law is commonly used to describe how light attenuates as it passes through a medium, such as a bioink. This law is fundamental in modelling the absorption of light by the photoinitiators in the bioink, which triggers the photopolymerization process. The law helps predict the intensity of light at different depths within the bioink, which directly impacts the curing depth and resolution of the printed structures. Photopolymerization kinetics is another critical theoretical aspect. This theory

involves modelling the chemical reactions that occur when the photoinitiators in the bioink absorb light and generate free radicals that initiate polymerization. The rate of polymerization, the conversion of monomers to polymers, and the resulting mechanical properties of the cured material are all governed by these kinetics.

Moreover, the complexity of 3D bioprinting often requires not only a single theory, but a multi-physics approach, where different physical phenomena (e.g., fluid dynamics, heat transfer, mechanical deformation) are modelled simultaneously to capture the interactions between them. Multi-scale modelling further enhances this by bridging the gap between the macro-scale (overall structure) and micro-scale (cellular level) processes, allowing for a more comprehensive simulation that accounts for both the material and biological aspects of bioprinting.

2.6.3.2 Inkjet printing

In inkjet printing, the dimensionless numbers such as Reynolds, Weber, and Ohnesorge are widely used to predict ink printability. The rheological behaviour of the bioink, both within the channel and during extrusion from the nozzle, is significantly influenced by the printing parameters. The N-S equations and their modifications are critical for modelling motion behaviour and droplet formation processes, aiding in the understanding of physical properties during printing. Developing constitutive equations that link stress, deformation rate, and fluid boundaries can significantly reduce the need for extensive experimental trials. The physical and biochemical environment notably impacts cell or drug-laden bioink printing, with factors such as shear stress, temperature, and bioink type impacting drug degradation, stability, cell viability, and proliferation. Although the N-S equations are invaluable for designing and optimizing these bioinks, their application becomes limited when addressing complex structures with intricate boundary conditions or multiphase flows. The LBM offers potential solutions for these challenges, especially when combined with parallel computing to enhance simulation efficiency.

Once droplets reach the platform, the properties of the ink and support materials also affect printing accuracy. High-fidelity printing requires consideration of factors such as capillarity,

spreading, and ringing phenomena. The performance of printed products, including drug release and mechanical properties, can be predicted using conventional theories like Fick's law, dynamic numerical calculation algorithms, or machine learning algorithms, which link printing parameters to the desired outcomes. However, simulation research on bioactive products, such as printed cell-laden hydrogels and organoids, remains limited, highlighting the need for more comprehensive models that integrate these objectives.

2.6.3.3 Materials extrusion

Extensive simulation research on ME has covered various aspects, from material preparation and printing parameters to rheological behaviour, phase change, product quality, and functional properties. The printability of filaments is primarily determined by their mechanical properties, with general predictions relying on displacement and applied maximum forces. Both printing parameters and material properties are essential factors in ME simulation, influencing phenomena such as temperature evolution, rheological behaviour, and state changes. Traditional theories and methods, including the N-S equation, Fourier's Law, and Hoffman theory, have been applied in these models. Real-time monitoring systems can detect defect or over-extrusion, with the collected data used for future product optimization. The development of more complex systems that integrate monitoring with real-time optimization of material feeding is anticipated.

Currently, most models consider mono-material filaments. However, the use of fibre-reinforced composite materials is increasing. The distribution of nano or microparticles in the filaments post-printing is critical for the enhancing or functionalising mechanical properties of the printed products. Modelling composite filaments can accurately reflect the actual microstructure and particle distribution of printed lines and filaments. Additionally, the development of a dynamic adhesion model that links thermal dynamics with the morphology of printed lines is expected. Optimizing printing parameters can help control heat distribution, sintering degree, and the mechanical properties of the printed products.

2.6.3.4 Digital light processing

There is relatively limited simulation research focused on understanding and optimizing DLP printing. Various aspects of the DLP printing process should be explored, including material properties, temperature effects, UV light intensity, curing time, printing accuracy, and overall product quality. A deeper understanding of these factors would significantly enhance the speed, efficient, and potential applications of DLP technology, enabling the development of novel properties and uses. It is worthy to mention that the conditions under which theoretical models are applied. When cell density in bioink is high, the deviation of Beer-Lambert Law might occur due to aggregation or changes in refractive index. Moreover, volumetric bioprinting, a relatively new technique that builds 3D structures in a single step rather than layer by layer as in DLP, could benefit from applying theories related to bioink flow, light propagation, absorption, scattering, and photopolymerization kinetics to accelerate optimization and reduce costs.

2.6.3.5 Machine learning

Apart from mechanism analysis, machine learning is a valuable tool for predicting product outcomes in various fields, including speech recognition, visual object recognition, object detection, drug discovery, and genomics [214]. Typical machine learning methods include linear regression, logistic regression (LR), k-nearest neighbour (KNN), support vector machine (SVM), kernel learning (KL), random forest (RF), and gradient boosting trees (GBT). More advanced techniques include artificial neural networks (ANN), convolutional neural networks (CNN), U-Net, graph neural networks (GNN), generative adversarial networks (GAN), long short-term memory (LSTM), autoencoders, transformers, transfer learning, active learning, graph-based semi-supervised learning, as well as approaches that combine deep learning with traditional machine learning or utilize physical model-based data augmentation [215]. Machine learning serves as a powerful tool for linking printing settings and material properties with the characteristics of final products, regardless of the printing method used, including: drug loading contents [216], printability [172], printing error detection [197, 198], printing efficiency [217], quality [200, 218], or drug releasing [201, 219, 220]. Appropriately chosen machine learning algorithms can accurately predict the geometry, surface quality, and post-printing performance of printed parts [202, 203]. However, several challenges remain, including the need for large amounts of experimental data for model training and the risk of overfitting, which could reduce the effectiveness of the

algorithms. The concept of small dataset machine learning has been proposed to address these challenges, although its reliability depends on the time allocated for arbitration [215, 221]. Data imbalance in small dataset machine learning can introduce noise or result in overly uniform data, affecting model performance. To address these challenges, it is crucial to develop and optimize machine learning algorithms tailored for small datasets, particularly when designing new bioinks or filaments. This ensures more accurate predictions and reliable outcomes in biofabrication processes [215]. Combining traditional theories with machine learning could minimize the required input data, accelerate model development, and enhance both the speed and accuracy of predictions [222, 223].

Reference

[1] S. Cooke, K. Ahmadi, S. Willerth, R. Herring, Metal additive manufacturing: Technology, metallurgy and modelling, Journal of Manufacturing Processes 57 (2020) 978-1003.
[2] Y. Lakhdar, C. Tuck, J. Binner, A. Terry, R. Goodridge, Additive manufacturing of advanced ceramic materials, Progress in Materials Science 116 (2021).
[3] G. Liu, X. Zhang, X. Chen, Y. He, L. Cheng, M. Huo, J. Yin, F. Hao, S. Chen, P. Wang, S. Yi, L. Wan, Z. Mao, Z. Chen, X. Wang, Z. Cao, J. Lu, Additive manufacturing of structural materials, Materials Science and Engineering: R: Reports 145 (2021).
[4] C. Sun, Y. Wang, M.D. McMurtrey, N.D. Jerred, F. Liou, J. Li, Additive manufacturing for energy: A review, Applied Energy 282 (2021).
[5] M. Bhuvanesh Kumar, P. Sathiya, Methods and materials for additive manufacturing: A critical review on advancements and challenges, Thin-Walled Structures 159 (2021).
[6] M. Tang, J.N. Rich, S. Chen, Biomaterials and 3D Bioprinting Strategies to Model Glioblastoma and the Blood-Brain Barrier, Adv Mater 33(5) (2021) e2004776.
[7] M. Ziaee, N.B. Crane, Binder jetting: A review of process, materials, and methods, Additive Manufacturing 28 (2019) 781-801.
[8] D. Svetlizky, M. Das, B. Zheng, A.L. Vyatskikh, S. Bose, A. Bandyopadhyay, J.M. Schoenung, E.J. Lavernia, N. Eliaz, Directed energy deposition (DED) additive manufacturing: Physical characteristics, defects, challenges and applications, Materials Today 49 (2021) 271-295.
[9] L. Chaunier, S. Guessasma, S. Belhabib, G. Della Valle, D. Lourdin, E. Leroy, Material extrusion of plant biopolymers: Opportunities & challenges for 3D printing, Additive Manufacturing 21 (2018) 220-233.
[10] A. Elkaseer, K.J. Chen, J.C. Janhsen, O. Refle, V. Hagenmeyer, S.G. Scholz, Material jetting for advanced applications: A state-of-the-art review, gaps and future directions, Additive Manufacturing 60 (2022).
[11] R. Singh, A. Gupta, O. Tripathi, S. Srivastava, B. Singh, A. Awasthi, S.K. Rajput, P. Sonia, P. Singhal, K.K. Saxena, Powder bed fusion process in additive manufacturing: An overview, Materials Today: Proceedings 26 (2020) 3058-3070.
[12] B. Dermeik, N. Travitzky, Laminated Object Manufacturing of Ceramic‐Based Materials, Advanced Engineering Materials 22(9) (2020).
[13] F. Zhang, L. Zhu, Z. Li, S. Wang, J. Shi, W. Tang, N. Li, J. Yang, The recent development of vat photopolymerization: A review, Additive Manufacturing 48 (2021).
[14] T. Xu, J. Jin, C. Gregory, J.J. Hickman, T. Boland, Inkjet printing of viable mammalian cells, Biomaterials 26(1) (2005) 93-9.
[15] H. Gudapati, M. Dey, I. Ozbolat, A comprehensive review on droplet-based bioprinting: Past, present and future, Biomaterials 102 (2016) 20-42.
[16] S.V. Murphy, A. Atala, 3D bioprinting of tissues and organs, Nature biotechnology 32(8) (2014) 773-85.
[17] K. Holzl, S. Lin, L. Tytgat, S. Van Vlierberghe, L. Gu, A. Ovsianikov, Bioink properties before, during and after 3D bioprinting, Biofabrication 8(3) (2016) 032002.
[18] V. Mironov, R.P. Visconti, V. Kasyanov, G. Forgacs, C.J. Drake, R.R. Markwald, Organ printing: tissue spheroids as building blocks, Biomaterials 30(12) (2009) 2164-74.
[19] J. Malda, J. Visser, F.P. Melchels, T. Jungst, W.E. Hennink, W.J. Dhert, J. Groll, D.W. Hutmacher, 25th anniversary article: Engineering hydrogels for biofabrication, Adv Mater 25(36) (2013) 5011-28.
[20] J.A. Barron, B.R. Ringeisen, H. Kim, B.J. Spargo, D.B. Chrisey, Application of laser printing to mammalian cells, Thin Solid Films 453-454 (2004) 383-387.
[21] B. Guillotin, A. Souquet, S. Catros, M. Duocastella, B. Pippenger, S. Bellance, R. Bareille, M. Remy, L. Bordenave, J. Amedee, F. Guillemot, Laser assisted bioprinting of engineered tissue with high cell density and microscale organization, Biomaterials 31(28) (2010) 7250-6.
[22] W. Zhang, S. Chen, Femtosecond laser nanofabrication of hydrogel biomaterial, MRS Bulletin 36(12) (2011) 1028-1033.

[23] K.C. Hribar, P. Soman, J. Warner, P. Chung, S. Chen, Light-assisted direct-write of 3D functional biomaterials, Lab Chip 14(2) (2014) 268-75.
[24] W. Zhu, X. Qu, J. Zhu, X. Ma, S. Patel, J. Liu, P. Wang, C.S. Lai, M. Gou, Y. Xu, K. Zhang, S. Chen, Direct 3D bioprinting of prevascularized tissue constructs with complex microarchitecture, Biomaterials 124 (2017) 106-115.
[25] X. Qu, W. Zhu, S. Huang, J.Y. Li, S. Chien, K. Zhang, S. Chen, Relative impact of uniaxial alignment vs. form-induced stress on differentiation of human adipose derived stem cells, Biomaterials 34(38) (2013) 9812-8.
[26] X. Ma, X. Qu, W. Zhu, Y.S. Li, S. Yuan, H. Zhang, J. Liu, P. Wang, C.S. Lai, F. Zanella, G.S. Feng, F. Sheikh, S. Chien, S. Chen, Deterministically patterned biomimetic human iPSC-derived hepatic model via rapid 3D bioprinting, Proc Natl Acad Sci U S A 113(8) (2016) 2206-11.
[27] X. Ma, C. Yu, P. Wang, W. Xu, X. Wan, C.S.E. Lai, J. Liu, A. Koroleva-Maharajh, S. Chen, Rapid 3D bioprinting of decellularized extracellular matrix with regionally varied mechanical properties and biomimetic microarchitecture, Biomaterials 185 (2018) 310-321.
[28] X. Ma, S. Dewan, J. Liu, M. Tang, K.L. Miller, C. Yu, N. Lawrence, A.D. McCulloch, S. Chen, 3D printed micro-scale force gauge arrays to improve human cardiac tissue maturation and enable high throughput drug testing, Acta Biomater 95 (2019) 319-327.
[29] Maxim Shusteff, Allison E. M. Browar, Brett E. Kelly, Johannes Henriksson, Todd H. Weisgraber, Robert M. Panas, Nicholas X. Fang, C.M. Spadaccini, One-step volumetric additive manufacturing of complex polymer structures, Sci Adv 3 (2017) eaao5496.
[30] B.E. Kelly, I. Bhattacharya, H. Heidari, M. Shusteff, C.M. Spadaccini, H.K. Taylor, Volumetric additive manufacturing via tomographic reconstruction, Science 363 (2019) 1075-1079.
[31] D.J. Whyte, E.H. Doeven, A. Sutti, A.Z. Kouzani, S.D. Adams, Volumetric additive manufacturing: A new frontier in layer-less 3D printing, Additive Manufacturing 84 (2024).
[32] C. Yu, J. Schimelman, P. Wang, K.L. Miller, X. Ma, S. You, J. Guan, B. Sun, W. Zhu, S. Chen, Photopolymerizable Biomaterials and Light-Based 3D Printing Strategies for Biomedical Applications, Chemical reviews 120(19) (2020) 10695-10743.
[33] G. Odian, Radical Chain Polymerization, Principles of Polymerization2004, pp. 198-349.
[34] J.M.G. Cowie, V. Arrighi, Free-Radical Addition Polymerization, Polymers: Chemistry and Physics of Modern Materials2007, pp. 57-97.
[35] K.T. Nguyen, J.L. West, Photopolymerizable hydrogels for tissue engineering applications, Biomaterials 23 (2002) 4307-4314.
[36] Busaina Dhariwala, Elaine Hunt, T. Boland, Rapid Prototyping of Tissue-Engineering Constructs, Using Photopolymerizable Hydrogels and Stereolithography, Tissue Eng 10(9/10) (2004).
[37] J.L. Ifkovits, J.A. Burdick, Photopolymerizable and degradable biomaterials for tissue engineering applications, Tissue Eng 13(10) (2007) 2369-85.
[38] B.B. An I. Van Den Bulcke, Nadine De Rooze, Etienne H. Schacht,*, Maria Cornelissen,‡ and Hugo Berghmans, Structural and Rheological Properties of Methacrylamide Modified Gelatin Hydrogels, Biomacromolecules 1(1) (2000) 31-38.
[39] J.W. Nichol, S.T. Koshy, H. Bae, C.M. Hwang, S. Yamanlar, A. Khademhosseini, Cell-laden microengineered gelatin methacrylate hydrogels, Biomaterials 31(21) (2010) 5536-44.
[40] G. Jiang, S. Li, K. Yu, B. He, J. Hong, T. Xu, J. Meng, C. Ye, Y. Chen, Z. Shi, G. Feng, W. Chen, S. Yan, Y. He, R. Yan, A 3D-printed PRP-GelMA hydrogel promotes osteochondral regeneration through M2 macrophage polarization in a rabbit model, Acta Biomater 128 (2021) 150-162.
[41] Y. Zhu, X. Yu, H. Liu, J. Li, M. Gholipourmalekabadi, K. Lin, C. Yuan, P. Wang, Strategies of functionalized GelMA-based bioinks for bone regeneration: Recent advances and future perspectives, Bioactive Materials 38 (2024) 346-373.
[42] S.R. Shin, C. Zihlmann, M. Akbari, P. Assawes, L. Cheung, K. Zhang, V. Manoharan, Y.S. Zhang, M. Yuksekkaya, K.T. Wan, M. Nikkhah, M.R. Dokmeci, X.S. Tang, A. Khademhosseini, Reduced Graphene Oxide-GelMA Hybrid Hydrogels as Scaffolds for Cardiac Tissue Engineering, Small 12(27) (2016) 3677-89.

[43] B. Kong, Y. Chen, R. Liu, X. Liu, C. Liu, Z. Shao, L. Xiong, X. Liu, W. Sun, S. Mi, Fiber reinforced GelMA hydrogel to induce the regeneration of corneal stroma, Nat Commun 11(1) (2020) 1435.
[44] E. Choi, D. Kim, D. Kang, G.H. Yang, B. Jung, M. Yeo, M.J. Park, S. An, K. Lee, J.S. Kim, J.C. Kim, W. Jeong, H.H. Yoo, H. Jeon, 3D-printed gelatin methacrylate (GelMA)/silanated silica scaffold assisted by two-stage cooling system for hard tissue regeneration, Regen Biomater 8(2) (2021) rbab001.
[45] K.A. DiVito, M.A. Daniele, S.A. Roberts, F.S. Ligler, A.A. Adams, Microfabricated blood vessels undergo neoangiogenesis, Biomaterials 138 (2017) 142-152.
[46] M. Cuvellier, F. Ezan, H. Oliveira, S. Rose, J.C. Fricain, S. Langouet, V. Legagneux, G. Baffet, 3D culture of HepaRG cells in GelMa and its application to bioprinting of a multicellular hepatic model, Biomaterials 269 (2021) 120611.
[47] A.G. Kurian, R.K. Singh, K.D. Patel, J.H. Lee, H.W. Kim, Multifunctional GelMA platforms with nanomaterials for advanced tissue therapeutics, Bioact Mater 8 (2022) 267-295.
[48] S.K. Seidlits, Z.Z. Khaing, R.R. Petersen, J.D. Nickels, J.E. Vanscoy, J.B. Shear, C.E. Schmidt, The effects of hyaluronic acid hydrogels with tunable mechanical properties on neural progenitor cell differentiation, Biomaterials 31(14) (2010) 3930-40.
[49] C.B. Highley, G.D. Prestwich, J.A. Burdick, Recent advances in hyaluronic acid hydrogels for biomedical applications, Curr Opin Biotechnol 40 (2016) 35-40.
[50] C.D. O'Connell, S. Duchi, C. Onofrillo, L.M. Caballero-Aguilar, A. Trengove, S.E. Doyle, W.J. Zywicki, E. Pirogova, C. Di Bella, Within or Without You? A Perspective Comparing In Situ and Ex Situ Tissue Engineering Strategies for Articular Cartilage Repair, Adv Healthc Mater 11(24) (2022) e2201305.
[51] X. Zuo, S. Wang, Y. Zhou, C. Wu, A. Huang, T. Wang, Y. Yang, Fluorescent hydrogel actuators with simultaneous morphing- and color/brightness-changes enabled by light-activated 3D printing, Chemical Engineering Journal 447 (2022).
[52] K.S. Lim, J.H. Galarraga, X. Cui, G.C.J. Lindberg, J.A. Burdick, T.B.F. Woodfield, Fundamentals and Applications of Photo-Cross-Linking in Bioprinting, Chemical reviews 120(19) (2020) 10662-10694.
[53] P. Snetkov, K. Zakharova, S. Morozkina, R. Olekhnovich, M. Uspenskaya, Hyaluronic Acid: The Influence of Molecular Weight on Structural, Physical, Physico-Chemical, and Degradable Properties of Biopolymer, Polymers (Basel) 12(8) (2020).
[54] F.D. Gregory H. Altman, Caroline Jakuba, Tara Calabro, Rebecca L. Horan, Jingsong Chen, Helen Lu, John Richmond, David L. Kaplan, Silk-based biomaterials, biomaterials 24 (2003) 401-416.
[55] F.G. Omenetto, D.L. Kaplan, New opportunities for an ancient material, Science 329(5991) (2010) 528-31.
[56] J.K. Sahoo, O. Hasturk, T. Falcucci, D.L. Kaplan, Silk chemistry and biomedical material designs, Nature Reviews Chemistry (2023).
[57] Y. Song, H. Wang, F. Yue, Q. Lv, B. Cai, N. Dong, Z. Wang, L. Wang, Silk-Based Biomaterials for Cardiac Tissue Engineering, Adv Healthc Mater (2020) e2000735.
[58] M. Gholipourmalekabadi, S. Sapru, A. Samadikuchaksaraei, R.L. Reis, D.L. Kaplan, S.C. Kundu, Silk fibroin for skin injury repair: Where do things stand?, Advanced drug delivery reviews 153 (2020) 28-53.
[59] S.H. Kim, Y.K. Yeon, J.M. Lee, J.R. Chao, Y.J. Lee, Y.B. Seo, M.T. Sultan, O.J. Lee, J.S. Lee, S.I. Yoon, I.S. Hong, G. Khang, S.J. Lee, J.J. Yoo, C.H. Park, Precisely printable and biocompatible silk fibroin bioink for digital light processing 3D printing, Nat Commun 9(1) (2018) 1620.
[60] S.H. Kim, H. Hong, O. Ajiteru, M.T. Sultan, Y.J. Lee, J.S. Lee, O.J. Lee, H. Lee, H.S. Park, K.Y. Choi, J.S. Lee, H.W. Ju, I.S. Hong, C.H. Park, 3D bioprinted silk fibroin hydrogels for tissue engineering, Nat Protoc 16(12) (2021) 5484-5532.
[61] M. Xie, L. Lian, X. Mu, Z. Luo, C.E. Garciamendez-Mijares, Z. Zhang, A. Lopez, J. Manriquez, X. Kuang, J. Wu, J.K. Sahoo, F.Z. Gonzalez, G. Li, G. Tang, S. Maharjan, J. Guo, D.L. Kaplan, Y.S. Zhang, Volumetric additive manufacturing of pristine silk-based (bio)inks, Nat Commun 14(1) (2023) 210.
[62] J. Liu, L. Shi, Y. Deng, M. Zou, B. Cai, Y. Song, Z. Wang, L. Wang, Silk sericin-based materials for biomedical applications, Biomaterials 287 (2022) 121638.

[63] A.F. R. Fatahian, E. Fatahian, H. Fatahian, A Critical Review on Application of Silk Sericin and its Mechnical Properties in Various Industries, Transactions of the TSME 9(2) (2021).
[64] Z.-L. Zhao, Y.-Q. Zhang, Greener degumming production of layered sericin peptides from a silkworm cocoon and their physicochemical characteristics and bioactivities in vitro, Journal of Cleaner Production 261 (2020) 121080.
[65] Z.-L. Zhao, W.-W. Li, F. Wang, Y.-Q. Zhang, Using of hydrated lime water as a novel degumming agent of silk and sericin recycling from wastewater, Journal of Cleaner Production 172 (2018) 2090-2096.
[66] G. Orlandi, S. Faragò, S. Menato, M. Sorlini, F. Butti, M. Mocchi, I. Donelli, L. Catenacci, M.L. Sorrenti, S. Croce, L. Segale, M.L. Torre, S. Perteghella, Eco-sustainable silk sericin from by-product of textile industry can be employed for cosmetic, dermatology and drug delivery, Journal of Chemical Technology & Biotechnology 95(9) (2020) 2549-2560.
[67] C. Qi, J. Liu, Y. Jin, L. Xu, G. Wang, Z. Wang, L. Wang, Photo-crosslinkable, injectable sericin hydrogel as 3D biomimetic extracellular matrix for minimally invasive repairing cartilage, Biomaterials 163 (2018) 89-104.
[68] C. Qi, L. Xu, Y. Deng, G. Wang, Z. Wang, L. Wang, Sericin hydrogels promote skin wound healing with effective regeneration of hair follicles and sebaceous glands after complete loss of epidermis and dermis, Biomater Sci 6(11) (2018) 2859-2870.
[69] L. Pescosolido, W. Schuurman, J. Malda, P. Matricardi, F. Alhaique, T. Coviello, P.R. van Weeren, W.J. Dhert, W.E. Hennink, T. Vermonden, Hyaluronic acid and dextran-based semi-IPN hydrogels as biomaterials for bioprinting, Biomacromolecules 12(5) (2011) 1831-8.
[70] A.D. Rouillard, C.M. Berglund, J.Y. Lee, W.J. Polacheck, Y. Tsui, L.J. Bonassar, B.J. Kirby, Methods for photocrosslinking alginate hydrogel scaffolds with high cell viability, Tissue Eng Part C Methods 17(2) (2011) 173-9.
[71] K.E. Drzewiecki, A.S. Parmar, I.D. Gaudet, J.R. Branch, D.H. Pike, V. Nanda, D.I. Shreiber, Methacrylation induces rapid, temperature-dependent, reversible self-assembly of type-I collagen, Langmuir 30(37) (2014) 11204-11.
[72] J. Jang, T.G. Kim, B.S. Kim, S.W. Kim, S.M. Kwon, D.W. Cho, Tailoring mechanical properties of decellularized extracellular matrix bioink by vitamin B2-induced photo-crosslinking, Acta Biomater 33 (2016) 88-95.
[73] A. Thakur, M.K. Jaiswal, C.W. Peak, J.K. Carrow, J. Gentry, A. Dolatshahi-Pirouz, A.K. Gaharwar, Injectable shear-thinning nanoengineered hydrogels for stem cell delivery, Nanoscale 8(24) (2016) 12362-72.
[74] T. Cebe, N. Ahuja, F. Monte, K. Awad, K. Vyavhare, P. Aswath, J. Huang, M. Brotto, V. Varanasi, Novel 3D-printed methacrylated chitosan-laponite nanosilicate composite scaffolds enhance cell growth and biomineral formation in MC3T3 pre-osteoblasts, J Mater Res 35(1) (2020) 58-75.
[75] S.N.S. Alconcel, A.S. Baas, H.D. Maynard, FDA-approved poly(ethylene glycol)–protein conjugate drugs, Polymer Chemistry 2(7) (2011).
[76] C. Cha, P. Soman, W. Zhu, M. Nikkhah, G. Camci-Unal, S. Chen, A. Khademhosseini, Structural Reinforcement of Cell-Laden Hydrogels with Microfabricated Three Dimensional Scaffolds, Biomater Sci 2(5) (2014) 703-709.
[77] A.P. Zhang, X. Qu, P. Soman, K.C. Hribar, J.W. Lee, S. Chen, S. He, Rapid fabrication of complex 3D extracellular microenvironments by dynamic optical projection stereolithography, Adv Mater 24(31) (2012) 4266-70.
[78] K.C. Hribar, D. Finlay, X. Ma, X. Qu, M.G. Ondeck, P.H. Chung, F. Zanella, A.J. Engler, F. Sheikh, K. Vuori, S.C. Chen, Nonlinear 3D projection printing of concave hydrogel microstructures for long-term multicellular spheroid and embryoid body culture, Lab Chip 15(11) (2015) 2412-8.
[79] J. Warner, P. Soman, W. Zhu, M. Tom, S. Chen, Design and 3D Printing of Hydrogel Scaffolds with Fractal Geometries, ACS Biomater Sci Eng 2(10) (2016) 1763-1770.

[80] H.R. Ashjari, A. Ahmadi, M.S.S. Dorraji, Synthesis and employment of PEGDA for fabrication of superhydrophilic PVDF/PEGDA electrospun nanofibrous membranes by in-situ visible photopolymerization, Korean Journal of Chemical Engineering 35(1) (2017) 289-297.
[81] W. Zhang, P. Soman, K. Meggs, X. Qu, S. Chen, Tuning the Poisson's Ratio of Biomaterials for Investigating Cellular Response, Adv Funct Mater 23(25) (2013).
[82] W. Zhu, K.R. Tringale, S.A. Woller, S. You, S. Johnson, H. Shen, J. Schimelman, M. Whitney, J. Steinauer, W. Xu, T.L. Yaksh, Q.T. Nguyen, S. Chen, Rapid continuous 3D printing of customizable peripheral nerve guidance conduits, Mater Today (Kidlington) 21(9) (2018) 951-959.
[83] J. Koffler, W. Zhu, X. Qu, O. Platoshyn, J.N. Dulin, J. Brock, L. Graham, P. Lu, J. Sakamoto, M. Marsala, S. Chen, M.H. Tuszynski, Biomimetic 3D-printed scaffolds for spinal cord injury repair, Nat Med 25(2) (2019) 263-269.
[84] Y. Wang, G.A. Ameer, B.J. Sheppard, R. Langer, A tough biodegradable elastomer, Nature biotechnology 20 (2002) 602-606.
[85] C.L.E. Nijst, J.P. Bruggeman, J.M. Karp, L. Ferreira, A. Zumbuehl, C.J. Bettinger, R. Langer, Synthesis and Characterization of Photocurable Elastomers from Poly(glycerol-co-sebacate), Biomacromolecules 8(10) (2007) 3067-3073.
[86] R. Rai, M. Tallawi, A. Grigore, A.R. Boccaccini, Synthesis, properties and biomedical applications of poly(glycerol sebacate) (PGS): A review, Progress in Polymer Science 37(8) (2012) 1051-1078.
[87] J.Y. Chen, J.V. Hwang, W.S. Ao-Ieong, Y.C. Lin, Y.K. Hsieh, Y.L. Cheng, J. Wang, Study of Physical and Degradation Properties of 3D-Printed Biodegradable, Photocurable Copolymers, PGSA-co-PEGDA and PGSA-co-PCLDA, Polymers (Basel) 10(11) (2018).
[88] S. Pashneh-Tala, R. Owen, H. Bahmaee, S. Rekštytė, M. Malinauskas, F. Claeyssens, Synthesis, Characterization and 3D Micro-Structuring via 2-Photon Polymerization of Poly(glycerol sebacate)-Methacrylate–An Elastomeric Degradable Polymer, Frontiers in Physics 6 (2018).
[89] D. Singh, A.J. Harding, E. Albadawi, F.M. Boissonade, J.W. Haycock, F. Claeyssens, Additive manufactured biodegradable poly(glycerol sebacate methacrylate) nerve guidance conduits, Acta Biomater 78 (2018) 48-63.
[90] Q.Z. Chen, A. Bismarck, U. Hansen, S. Junaid, M.Q. Tran, S.E. Harding, N.N. Ali, A.R. Boccaccini, Characterisation of a soft elastomer poly(glycerol sebacate) designed to match the mechanical properties of myocardial tissue, Biomaterials 29(1) (2008) 47-57.
[91] A. Mahdavi, L. Ferreira, C. Sundback, J.W. Nichol, E.P. Chan, D.J.D. Carter, C.J. Bettinger, S. Patanavanich, L. Chignozha, E. Ben-Joseph, A. Galakatos, H. Pryor, I. Pomerantseva, P.T. Masiakos, W. Faquin, A. Zumbuehl, S. Hong, J. Borenstein, J. Vacanti, R. Langer, a.J.M. Karp, A biodegradable and biocompatible gecko-inspired tissue adhesive, PNAS 103(7) (2008) 2307-2312.
[92] Y. Li, W.D. Cook, C. Moorhoff, W.C. Huang, Q.Z. Chen, Synthesis, characterization and properties of biocompatible poly(glycerol sebacate) pre‐polymer and gel, Polymer International 62(4) (2012) 534-547.
[93] N. Lang, M.J. Pereira, Y. Lee, I. Friehs, N.V. Vasilyev, E.N. Feins, K. Ablasser, E.D. O'Cearbhaill, C. Xu, A. Fabozzo, R. Padera, S. Wasserman, F. Freudenthal, L.S. Ferreira, R. Langer, J.M. Karp, P.J.d. Nido, A Blood-Resistant Surgical Glue for Minimally Invasive Repair of Vessels and Heart Defects, Sci Transl Med 6(218) (2014).
[94] Y.C. Yeh, C.B. Highley, L. Ouyang, J.A. Burdick, 3D printing of photocurable poly(glycerol sebacate) elastomers, Biofabrication 8(4) (2016) 045004.
[95] K.S. Lim, R. Levato, P.F. Costa, M.D. Castilho, C.R. Alcala-Orozco, K.M.A. van Dorenmalen, F.P.W. Melchels, D. Gawlitta, G.J. Hooper, J. Malda, T.B.F. Woodfield, Bio-resin for high resolution lithography-based biofabrication of complex cell-laden constructs, Biofabrication 10(3) (2018) 034101.
[96] K.S. Lim, M.H. Alves, L.A. Poole-Warren, P.J. Martens, Covalent incorporation of non-chemically modified gelatin into degradable PVA-tyramine hydrogels, Biomaterials 34(29) (2013) 7097-105.
[97] D.L. Hern, J.A. Hubbell, Incorporation of adhesion peptides into nonadhesive hydrogels useful for tissue resurfacing, Journal of Biomedical Materials Research 39(2) (1998) 266-276.

[98] M.P. Lutolf, J.L. Lauer-Fields, H.G. Schmoekel, A.T. Metters, F.E. Weber, G.B. Fields, J.A. Hubbell, Synthetic matrix metalloproteinase-sensitive hydrogels for the conduction of tissue regeneration: Engineering cell-invasion characteristics, PNAS 100(9) (2003) 5413-5418.
[99] X. Ma, J. Liu, W. Zhu, M. Tang, N. Lawrence, C. Yu, M. Gou, S. Chen, 3D bioprinting of functional tissue models for personalized drug screening and in vitro disease modeling, Advanced drug delivery reviews 132 (2018) 235-251.
[100] C. Claassen, M.H. Claassen, V. Truffault, L. Sewald, G.E.M. Tovar, K. Borchers, A. Southan, Quantification of Substitution of Gelatin Methacryloyl: Best Practice and Current Pitfalls, Biomacromolecules 19(1) (2018) 42-52.
[101] A.F.S.A. HABEEB, Determination of Free Amino Groups in Proteins by Trinitrobenzenesulfonic Acid, Analytocal Biochemistry 14 (1966) 328-336.
[102] M. Zhu, Y. Wang, G. Ferracci, J. Zheng, N.J. Cho, B.H. Lee, Gelatin methacryloyl and its hydrogels with an exceptional degree of controllability and batch-to-batch consistency, Sci Rep 9(1) (2019) 6863.
[103] A. Sun, X. He, X. Ji, D. Hu, M. Pan, L. Zhang, Z. Qian, Current research progress of photopolymerized hydrogels in tissue engineering, Chinese Chemical Letters 32(7) (2021) 2117-2126.
[104] G. Ullrich, P. Burtscher, U. Salz, N. Moszner, R. Liska, Phenylglycine derivatives as coinitiators for the radical photopolymerization of acidic aqueous formulations, Journal of Polymer Science Part A: Polymer Chemistry 44(1) (2006) 115-125.
[105] X.-H. Qin, A. Ovsianikov, J. Stampfl, R. Liska, Additive manufacturing of photosensitive hydrogels for tissue engineering applications, BioNanoMaterials 15(3-4) (2014).
[106] C. Lee, C.D. O'Connell, C. Onofrillo, P.F.M. Choong, C. Di Bella, S. Duchi, Human articular cartilage repair: Sources and detection of cytotoxicity and genotoxicity in photo-crosslinkable hydrogel bioscaffolds, Stem Cells Transl Med 9(3) (2020) 302-315.
[107] S.J. Bryant, C.R. Nuttelman, K.S. Anseth, Cytocompatibility of UV and visible light photoinitiating systems on cultured NIH/3T3 fibroblasts in vitro, J Biomater Sci Polym Ed 11(5) (2000) 439-57.
[108] J.J.Y. Tan, D.V. Nguyen, J.E. Common, C. Wu, P.C.L. Ho, L. Kang, Investigating PEGDA and GelMA Microgel Models for Sustained 3D Heterotypic Dermal Papilla and Keratinocyte Co-Cultures, Int J Mol Sci 22(4) (2021).
[109] T.U. Nguyen, K.E. Watkins, V. Kishore, Photochemically crosslinked cell-laden methacrylated collagen hydrogels with high cell viability and functionality, J Biomed Mater Res A 107(7) (2019) 1541-1550.
[110] D. Rana, A. Kandar, N. Salehi-Nik, I. Inci, B. Koopman, J. Rouwkema, Spatiotemporally controlled, aptamers-mediated growth factor release locally manipulates microvasculature formation within engineered tissues, Bioact Mater 12 (2022) 71-84.
[111] P. Occhetta, R. Visone, L. Russo, L. Cipolla, M. Moretti, M. Rasponi, VA-086 methacrylate gelatine photopolymerizable hydrogels: A parametric study for highly biocompatible 3D cell embedding, J Biomed Mater Res A 103(6) (2015) 2109-17.
[112] T. Billiet, E. Gevaert, T. De Schryver, M. Cornelissen, P. Dubruel, The 3D printing of gelatin methacrylamide cell-laden tissue-engineered constructs with high cell viability, Biomaterials 35(1) (2014) 49-62.
[113] P. Occhetta, N. Sadr, F. Piraino, A. Redaelli, M. Moretti, M. Rasponi, Fabrication of 3D cell-laden hydrogel microstructures through photo-mold patterning, Biofabrication 5(3) (2013) 035002.
[114] T. Majima, W. Schnabel, W. Weber, Phenyl‐2,4,6‐trimethylbenzoylphosphinates as water‐soluble photoinitiators. Generation and reactivity of O□Ṗ(C6H5)(O−) radical anions, Die Makromolekulare Chemie 192(10) (2003) 2307-2315.
[115] B.D. Fairbanks, M.P. Schwartz, C.N. Bowman, K.S. Anseth, Photoinitiated polymerization of PEG-diacrylate with lithium phenyl-2,4,6-trimethylbenzoylphosphinate: polymerization rate and cytocompatibility, Biomaterials 30(35) (2009) 6702-7.

[116] W. Ye, H. Li, K. Yu, C. Xie, P. Wang, Y. Zheng, P. Zhang, J. Xiu, Y. Yang, F. Zhang, Y. He, Q. Gao, 3D printing of gelatin methacrylate-based nerve guidance conduits with multiple channels, Materials & Design 192 (2020) 108757.
[117] Y. Bao, Recent Trends in Advanced Photoinitiators for Vat Photopolymerization 3D Printing, Macromol Rapid Commun (2022) e2200202.
[118] Z. Wang, R. Abdulla, B. Parker, R. Samanipour, S. Ghosh, K. Kim, A simple and high-resolution stereolithography-based 3D bioprinting system using visible light crosslinkable bioinks, Biofabrication 7(4) (2015) 045009.
[119] E.A. Kamoun, A. Winkel, M. Eisenburger, H. Menzel, Carboxylated camphorquinone as visible-light photoinitiator for biomedical application: Synthesis, characterization, and application, Arabian Journal of Chemistry 9(5) (2016) 745-754.
[120] J.A. Werkmeister, R. Adhikari, J.F. White, T.A. Tebb, T.P. Le, H.C. Taing, R. Mayadunne, P.A. Gunatillake, S.J. Danon, J.A. Ramshaw, Biodegradable and injectable cure-on-demand polyurethane scaffolds for regeneration of articular cartilage, Acta Biomater 6(9) (2010) 3471-81.
[121] K.S. Lim, B.S. Schon, N.V. Mekhileri, G.C.J. Brown, C.M. Chia, S. Prabakar, G.J. Hooper, T.B.F. Woodfield, New Visible-Light Photoinitiating System for Improved Print Fidelity in Gelatin-Based Bioinks, ACS Biomater Sci Eng 2(10) (2016) 1752-1762.
[122] V. Brabec, O. Novakova, DNA binding mode of ruthenium complexes and relationship to tumor cell toxicity, Drug Resist Updat 9(3) (2006) 111-22.
[123] M. Martínez-Alonso, G. Gasser, Ruthenium polypyridyl complex-containing bioconjugates, Coordination Chemistry Reviews 434 (2021).
[124] K.S. Lim, B.J. Klotz, G.C.J. Lindberg, F.P.W. Melchels, G.J. Hooper, J. Malda, D. Gawlitta, T.B.F. Woodfield, Visible Light Cross-Linking of Gelatin Hydrogels Offers an Enhanced Cell Microenvironment with Improved Light Penetration Depth, Macromol Biosci 19(6) (2019) e1900098.
[125] D.Y. Wong, T. Ranganath, A.M. Kasko, Low-Dose, Long-Wave UV Light Does Not Affect Gene Expression of Human Mesenchymal Stem Cells, PLoS One 10(9) (2015) e0139307.
[126] J. Cadet, E. Sage, T. Douki, Ultraviolet radiation-mediated damage to cellular DNA, Mutat Res 571(1-2) (2005) 3-17.
[127] H.L. Lo, S. Nakajima, L. Ma, B. Walter, A. Yasui, D.W. Ethell, L.B. Owen, Differential biologic effects of CPD and 6-4PP UV-induced DNA damage on the induction of apoptosis and cell-cycle arrest, BMC Cancer 5 (2005) 135.
[128] J. Cadet, T. Douki, Formation of UV-induced DNA damage contributing to skin cancer development, Photochem Photobiol Sci 17(12) (2018) 1816-1841.
[129] R. Brem, M. Guven, P. Karran, Oxidatively-generated damage to DNA and proteins mediated by photosensitized UVA, Free Radic Biol Med 107 (2017) 101-109.
[130] M.M.V.a.A.G. Knudson, Endogenous DNA double-strand breaks: Production, fidelity of repair, and induction of cancer, PNAS 100(22) (2003) 12871-12876.
[131] C.G. Williams, A.N. Malik, T.K. Kim, P.N. Manson, J.H. Elisseeff, Variable cytocompatibility of six cell lines with photoinitiators used for polymerizing hydrogels and cell encapsulation, Biomaterials 26(11) (2005) 1211-8.
[132] H. Xu, J. Casillas, S. Krishnamoorthy, C. Xu, Effects of Irgacure 2959 and lithium phenyl-2,4,6-trimethylbenzoylphosphinate on cell viability, physical properties, and microstructure in 3D bioprinting of vascular-like constructs, Biomed Mater 15(5) (2020) 055021.
[133] C.D. O'Connell, B. Zhang, C. Onofrillo, S. Duchi, R. Blanchard, A. Quigley, J. Bourke, S. Gambhir, R. Kapsa, C. Di Bella, P. Choong, G.G. Wallace, Tailoring the mechanical properties of gelatin methacryloyl hydrogels through manipulation of the photocrosslinking conditions, Soft Matter 14(11) (2018) 2142-2151.
[134] H. Zhong, H. Yin, Role of lipid peroxidation derived 4-hydroxynonenal (4-HNE) in cancer: focusing on mitochondria, Redox Biol 4 (2015) 193-9.

[135] L. Sun, P. Dong, Y. Zeng, J. Chen, Fabrication of hollow lattice alumina ceramic with good mechanical properties by Digital Light Processing 3D printing technology, Ceramics International 47(18) (2021) 26519-26527.
[136] C. Paredes, F.J. Martínez-Vázquez, A. Pajares, P. Miranda, Co-continuous calcium phosphate/polycaprolactone composite bone scaffolds fabricated by digital light processing and polymer melt suction, Ceramics International 47(12) (2021) 17726-17735.
[137] R. Hu, X. Zhang, Y. Chen, C. Zhang, Characterization and prediction of the nonlinear creep behavior of 3D-printed polyurethane acrylate, Additive Manufacturing 50 (2022).
[138] J.A. J, J. Schneider, A. Schiffer, F. Hafeez, S. Kumar, Dynamic crushing of tailored honeycombs realized via additive manufacturing, International Journal of Mechanical Sciences 219 (2022).
[139] H. Zhu, H. Yang, Y. Ma, T.J. Lu, F. Xu, G.M. Genin, M. Lin, Spatiotemporally Controlled Photoresponsive Hydrogels: Design and Predictive Modeling from Processing through Application, Adv Funct Mater 30(32) (2020) 2000639.
[140] Z. Zhu, D.W.H. Ng, H.S. Park, M.C. McAlpine, 3D-printed multifunctional materials enabled by artificial-intelligence-assisted fabrication technologies, Nature Reviews Materials 6(1) (2020) 27-47.
[141] G.D. Goh, S.L. Sing, W.Y. Yeong, A review on machine learning in 3D printing: applications, potential, and challenges, Artificial Intelligence Review 54(1) (2020) 63-94.
[142] Z. Jin, Z. Zhang, K. Demir, G.X. Gu, Machine Learning for Advanced Additive Manufacturing, Matter 3(5) (2020) 1541-1556.
[143] M. Elbadawi, L.E. McCoubrey, F.K.H. Gavins, J.J. Ong, A. Goyanes, S. Gaisford, A.W. Basit, Harnessing artificial intelligence for the next generation of 3D printed medicines, Advanced drug delivery reviews 175 (2021) 113805.
[144] J. Guan, S. You, Y. Xiang, J. Schimelman, J. Alido, X. Ma, M. Tang, S. Chen, Compensating the cell-induced light scattering effect in light-based bioprinting using deep learning, Biofabrication 14(1) (2021).
[145] J. Qin, F. Hu, Y. Liu, P. Witherell, C.C.L. Wang, D.W. Rosen, T.W. Simpson, Y. Lu, Q. Tang, Research and application of machine learning for additive manufacturing, Additive Manufacturing 52 (2022).
[146] A.F. Bonatti, G. Vozzi, C. De Maria, Enhancing quality control in bioprinting through machine learning, Biofabrication 16(2) (2024).
[147] W.L. Ng, G.L. Goh, G.D. Goh, J.S.J. Ten, W.Y. Yeong, Progress and Opportunities for Machine Learning in Materials and Processes of Additive Manufacturing, Adv Mater (2024) e2310006.
[148] A. VanHorn, W. Zhou, Design and optimization of a high temperature microheater for inkjet deposition, The International Journal of Advanced Manufacturing Technology 86(9-12) (2016) 3101-3111.
[149] J. Wang, J. Huang, J. Peng, Hydrodynamic response model of a piezoelectric inkjet print-head, Sensors and Actuators A: Physical 285 (2019) 50-58.
[150] H. Zhu, R. Li, S. Li, K. Guo, C. Ji, F. Gao, Y. Zheng, R. Zhu, H. Wang, L. Zhang, L. Liu, X. Zheng, Multi-physical field control piezoelectric inkjet bioprinting for 3D tissue-like structure manufacturing, International Journal of Bioprinting 10 (2024) 2120.
[151] E. Hamidi, P.B. Ganesan, R.K. Sharma, K.W. Yong, Computational study of heat transfer enhancement using porous foams with phase change materials: A comparative review, Renewable and Sustainable Energy Reviews 176 (2023) 113196.
[152] S.A. Hosseini, P. Boivin, D. Thévenin, I. Karlin, Lattice Boltzmann methods for combustion applications, Progress in Energy and Combustion Science 102 (2024) 101140.
[153] S.J. Lim, K.-J. Lee, H. Nam, S.H. Kim, E.-j. Kim, S. Lee, J. Chung, Progress and future directions bridging microplastics transport from pore to continuum scale: A comprehensive review for experimental and modeling approaches, TrAC Trends in Analytical Chemistry 179 (2024) 117851.
[154] P. Delrot, M.A. Modestino, F. Gallaire, D. Psaltis, C. Moser, Inkjet Printing of Viscous Monodisperse Microdroplets by Laser-Induced Flow Focusing, Physical Review Applied 6(2) (2016) 024003.

[155] B. Derby, Inkjet Printing of Functional and Structural Materials: Fluid Property Requirements, Feature Stability, and Resolution, Annual Review of Materials Research 40(1) (2010) 395-414.
[156] Z. Zhou, L. Ruiz Cantu, X. Chen, M.R. Alexander, C.J. Roberts, R. Hague, C. Tuck, D. Irvine, R. Wildman, High-throughput characterization of fluid properties to predict droplet ejection for three-dimensional inkjet printing formulations, Additive Manufacturing 29 (2019) 100792.
[157] N.A. Dudukovic, L.L. Wong, D.T. Nguyen, J.F. Destino, T.D. Yee, F.J. Ryerson, T. Suratwala, E.B. Duoss, R. Dylla-Spears, Predicting Nanoparticle Suspension Viscoelasticity for Multimaterial 3D Printing of Silica–Titania Glass, ACS Applied Nano Materials 1(8) (2018) 4038-4044.
[158] Y. Yang, X. Wang, X. Lin, L. Xie, R. Ivone, J. Shen, G. Yang, A tunable extruded 3D printing platform using thermo-sensitive pastes, International journal of pharmaceutics 583 (2020) 119360.
[159] J. Chang, M. Chi, T. Shen, Z. Liang, A comprehensive study on the droplet formation processes and its influencing factors of a tubular piezoelectric print head, Journal of Adhesion Science and Technology 34 (2019) 1128-1143.
[160] J.C. Gómez-Blanco, E. Mancha-Sánchez, A.C. Marcos, M. Matamoros, A. Díaz-Parralejo, J.B. Pagador, Bioink Temperature Influence on Shear Stress, Pressure and Velocity Using Computational Simulation, Processes 8(7) (2020) 865.
[161] M. Sarker, X.B. Chen, Modeling the Flow Behavior and Flow Rate of Medium Viscosity Alginate for Scaffold Fabrication With a Three-Dimensional Bioplotter, Journal of Manufacturing Science and Engineering 139(8) (2017) 081002.
[162] J. Emmermacher, D. Spura, J. Cziommer, D. Kilian, T. Wollborn, U. Fritsching, J. Steingroewer, T. Walther, M. Gelinsky, A. Lode, Engineering considerations on extrusion-based bioprinting: interactions of material behavior, mechanical forces and cells in the printing needle, Biofabrication 12(2) (2020) 025022.
[163] X. Zhao, Z. Jia, W. Li, Y. Li, Numerical simulation of micro droplet formation combined with pneumatic and piezoelectric drive, Microsystem Technologies 25(7) (2018) 2727-2734.
[164] J. Qu, C. Dou, B. Xu, J. Li, Z. Rao, A. Tsin, Printing quality improvement for laser-induced forward transfer bioprinting: Numerical modeling and experimental validation, Physics of Fluids 33(7) (2021) 071906.
[165] H. Ebrahimi Orimi, S. Narayanswamy, C. Boutopoulos, Hybrid analytical/numerical modeling of nanosecond laser-induced micro-jets generated by liquid confining devices, Journal of Fluids and Structures 98 (2020) 103079.
[166] Y. Gong, Z. Bi, X. Bian, A. Ge, J. He, W. Li, H. Shao, G. Chen, X. Zhang, Study on linear bio-structure print process based on alginate bio-ink in 3D bio-fabrication, Bio-Design and Manufacturing 3(2) (2020) 109-121.
[167] I. Arango, L. Bonil, D. Posada, J. Arcila, Prediction of a flying droplet landing over a non-flat substrates for ink-jet applications, International Journal on Interactive Design and Manufacturing (IJIDeM) 13(3) (2019) 967-980.
[168] M. Monteferrante, A. Montessori, S. Succi, D. Pisignano, M. Lauricella, Lattice Boltzmann multicomponent model for direct-writing printing, Physics of Fluids 33(4) (2021) 042103.
[169] C. Zhang, J. Hao, W. Shi, Y. Su, K. Mitchell, W. Hua, W. Jin, S. Lee, L. Wen, Y. Jin, D. Zhao, Sacrificial scaffold-assisted direct ink writing of engineered aortic valve prostheses, Biofabrication 15(4) (2023) 045015.
[170] A. Goyanes, A.B. Buanz, G.B. Hatton, S. Gaisford, A.W. Basit, 3D printing of modified-release aminosalicylate (4-ASA and 5-ASA) tablets, European journal of pharmaceutics and biopharmaceutics 89 (2015) 157-62.
[171] A. Goyanes, A.B. Buanz, A.W. Basit, S. Gaisford, Fused-filament 3D printing (3DP) for fabrication of tablets, International journal of pharmaceutics 476(1-2) (2014) 88-92.
[172] M. Duranovic, S. Obeid, M. Madzarevic, S. Cvijic, S. Ibric, Paracetamol extended release FDM 3D printlets: Evaluation of formulation variables on printability and drug release, International journal of pharmaceutics 592 (2021) 120053.

[173] P. Xu, J. Li, A. Meda, F. Osei-Yeboah, M.L. Peterson, M. Repka, X. Zhan, Development of a quantitative method to evaluate the printability of filaments for fused deposition modeling 3D printing, International journal of pharmaceutics 588 (2020) 119760.
[174] R. Chand, B.S. Muhire, S. Vijayavenkataraman, Computational Fluid Dynamics Assessment of the Effect of Bioprinting Parameters in Extrusion Bioprinting, Int J Bioprint 8(2) (2022) 545.
[175] J.C. Gomez-Blanco, J.B. Pagador, V.P. Galvan-Chacon, L.F. Sanchez-Peralta, M. Matamoros, A. Marcos, F.M. Sanchez-Margallo, Computational simulation-based comparative analysis of standard 3D printing and conical nozzles for pneumatic and piston-driven bioprinting, Int J Bioprint 9(4) (2023) 730.
[176] J. Gohl, K. Markstedt, A. Mark, K. Hakansson, P. Gatenholm, F. Edelvik, Simulations of 3D bioprinting: predicting bioprintability of nanofibrillar inks, Biofabrication 10(3) (2018) 034105.
[177] A. Gosset, D. Barreiro-Villaverde, J.C. Becerra Permuy, M. Lema, A. Ares-Pernas, M.J. Abad Lopez, Experimental and Numerical Investigation of the Extrusion and Deposition Process of a Poly(lactic Acid) Strand with Fused Deposition Modeling, Polymers 12(12) (2020) 2885.
[178] L. Friedrich, M. Begley, Corner accuracy in direct ink writing with support material, Bioprinting 19 (2020) e00086.
[179] L. Friedrich, M. Begley, Printing direction dependent microstructures in direct ink writing, Additive Manufacturing 34 (2020) 101192.
[180] L. Friedrich, M. Begley, Changes in Filament Microstructures During Direct Ink Writing with a Yield Stress Fluid Support, ACS Applied Polymer Materials 2(7) (2020) 2528-2540.
[181] J. Sun, Y. Gong, M. Xu, H. Chen, H. Shao, R. Zhou, Coaxial 3D Bioprinting Process Research and Performance Tests on Vascular Scaffolds, Micromachines (Basel) 15(4) (2024) 463.
[182] X. Zhou, M. Nowicki, H. Sun, S.Y. Hann, H. Cui, T. Esworthy, J.D. Lee, M. Plesniak, L.G. Zhang, 3D Bioprinting-Tunable Small-Diameter Blood Vessels with Biomimetic Biphasic Cell Layers, ACS Appl Mater Interfaces 12(41) (2020) 45904-45915.
[183] M. Temirel, S.R. Dabbagh, S. Tasoglu, Shape Fidelity Evaluation of Alginate-Based Hydrogels through Extrusion-Based Bioprinting, J Funct Biomater 13(4) (2022) 225.
[184] L. Lemarié, A. Anandan, E. Petiot, C. Marquette, E.-J. Courtial, Rheology, simulation and data analysis toward bioprinting cell viability awareness, Bioprinting 21 (2021) e00119.
[185] G. Ukpai, B. Rubinsky, A three-dimensional model for analysis and control of phase change phenomena during 3D printing of biological tissue, Bioprinting 18 (2020) e00077.
[186] Y. Yuan, C. Abeykoon, W. Mirihanage, A. Fernando, Y.-C. Kao, J.A.W. Harings, Prediction of temperature and crystal growth evolution during 3D printing of polymeric materials via extrusion, Materials & Design 196 (2020) 109121.
[187] A. Antony Samy, A. Golbang, E. Harkin-Jones, E. Archer, A. McIlhagger, Prediction of part distortion in Fused Deposition Modelling (FDM) of semi-crystalline polymers via COMSOL: Effect of printing conditions, CIRP Journal of Manufacturing Science and Technology 33 (2021) 443-453.
[188] M. Moretti, A. Rossi, N. Senin, In-process monitoring of part geometry in fused filament fabrication using computer vision and digital twins, Additive Manufacturing 37 (2021) 101609.
[189] C. Karavasili, K. Tsongas, Andreadis, II, E.G. Andriotis, E.T. Papachristou, R.M. Papi, D. Tzetzis, D.G. Fatouros, Physico-mechanical and finite element analysis evaluation of 3D printable alginate-methylcellulose inks for wound healing applications, Carbohydrate polymers 247 (2020) 116666.
[190] M. Altunbek, S.F. Afghah, A. Fallah, A.A. Acar, B. Koc, Design and 3D Printing of Personalized Hybrid and Gradient Structures for Critical Size Bone Defects, ACS Appl Bio Mater 6(5) (2023) 1873-1885.
[191] P. Ravi, Understanding the relationship between slicing and measured fill density in material extrusion 3D printing towards precision porosity constructs for biomedical and pharmaceutical applications, 3D printing in medicine 6(1) (2020) 10.
[192] S. Garzon-Hernandez, D. Garcia-Gonzalez, A. Jérusalem, A. Arias, Design of FDM 3D printed polymers: An experimental-modelling methodology for the prediction of mechanical properties, Materials & Design 188 (2020) 108414.

[193] P. Kumar Mishra, S. P, Prediction of in-plane stiffness of multi-material 3D printed laminate parts fabricated by FDM process using CLT and its mechanical behaviour under tensile load, Materials Today Communications 23 (2020) 100955.
[194] R. Choe, E. Devoy, B. Kuzemchak, M. Sherry, E. Jabari, J.D. Packer, J.P. Fisher, Computational investigation of interface printing patterns within 3D printed multilayered scaffolds for osteochondral tissue engineering, Biofabrication 14(2) (2022) 025015.
[195] E.L. Zoudani, M. Soltani, A new computational method of modeling and evaluation of dissolving microneedle for drug delivery applications: Extension to theoretical modeling of a novel design of microneedle (array in array) for efficient drug delivery, Eur J Pharm Sci 150 (2020) 105339.
[196] H.M. Jeong, K.Y. Weon, B.S. Shin, S. Shin, 3D-Printed Gastroretentive Sustained Release Drug Delivery System by Applying Design of Experiment Approach, Molecules 25(10) (2020) 2330.
[197] N. Decker, M. Lyu, Y. Wang, Q. Huang, Geometric Accuracy Prediction and Improvement for Additive Manufacturing Using Triangular Mesh Shape Data, Journal of Manufacturing Science and Engineering 143(6) (2021).
[198] P. Schaechtl, B. Schleich, S. Wartzack, Statistical Tolerance Analysis of 3D-Printed Non-Assembly Mechanisms in Motion Using Empirical Predictive Models, Applied Sciences 11(4) (2021) 1860.
[199] N. Hooda, J.S. Chohan, R. Gupta, R. Kumar, Deposition angle prediction of Fused Deposition Modeling process using ensemble machine learning, ISA transactions (2021).
[200] A. Cerro, P.E. Romero, O. Yiğit, A. Bustillo, Use of machine learning algorithms for surface roughness prediction of printed parts in polyvinyl butyral via fused deposition modeling, The International Journal of Advanced Manufacturing Technology 115(7-8) (2021) 2465-2475.
[201] S. Obeid, M. Madzarevic, M. Krkobabic, S. Ibric, Predicting drug release from diazepam FDM printed tablets using deep learning approach: Influence of process parameters and tablet surface/volume ratio, International journal of pharmaceutics 601 (2021) 120507.
[202] M. Elbadawi, T. Gustaffson, S. Gaisford, A.W. Basit, 3D printing tablets: Predicting printability and drug dissolution from rheological data, International journal of pharmaceutics 590 (2020) 119868.
[203] M. Elbadawi, B. Muniz Castro, F.K.H. Gavins, J.J. Ong, S. Gaisford, G. Perez, A.W. Basit, P. Cabalar, A. Goyanes, M3DISEEN: A novel machine learning approach for predicting the 3D printability of medicines, International journal of pharmaceutics 590 (2020) 119837.
[204] F.Q. Pires, I. Alves-Silva, L.A.G. Pinho, J.A. Chaker, L.L. Sa-Barreto, G.M. Gelfuso, T. Gratieri, M. Cunha-Filho, Predictive models of FDM 3D printing using experimental design based on pharmaceutical requirements for tablet production, International journal of pharmaceutics 588 (2020) 119728.
[205] Y. Li, Q. Mao, X. Li, J. Yin, Y. Wang, J. Fu, Y. Huang, High-fidelity and high-efficiency additive manufacturing using tunable pre-curing digital light processing, Additive Manufacturing 30 (2019) 100889.
[206] Y. Li, Q. Mao, J. Yin, Y. Wang, J. Fu, Y. Huang, Theoretical prediction and experimental validation of the digital light processing (DLP) working curve for photocurable materials, Additive Manufacturing 37 (2021) 101716.
[207] S.M. Montgomery, C.M. Hamel, J. Skovran, H.J. Qi, A reaction–diffusion model for grayscale digital light processing 3D printing, Extreme Mechanics Letters 53 (2022) 101714.
[208] Y. Dong, T. Dong, Z. Yang, A. Luo, Z. Hong, G. Lao, H. Huang, B. Fan, The influences of light scattering on digital light processing high-resolution ceramic additive manufacturing, Ceramics International 50(6) (2024) 9556-9562.
[209] S. You, Y. Xiang, H.H. Hwang, D.B. Berry, W. Kiratitanaporn, J. Guan, E. Yao, M. Tang, Z. Zhong, X. Ma, D. Wangpraseurt, Y. Sun, T.-y. Lu, S. Chen, High cell density and high-resolution 3D bioprinting for fabricating vascularized tissues, Sci Adv 9 (2023) eade7923.

[210] Z. Liu, W. Pan, K. Wang, Y. Matia, A. Xu, J.A. Barreiros, C. Darkes-Burkey, E.P. Giannelis, Y. Menguc, R.F. Shepherd, T.J. Wallin, Acoustophoretic Liquefaction for 3D Printing Ultrahigh-Viscosity Nanoparticle Suspensions, Adv Mater 34(7) (2022) e2106183.
[211] S.H. Kim, Y.B. Seo, Y.K. Yeon, Y.J. Lee, H.S. Park, M.T. Sultan, J.M. Lee, J.S. Lee, O.J. Lee, H. Hong, H. Lee, O. Ajiteru, Y.J. Suh, S.H. Song, K.H. Lee, C.H. Park, 4D-bioprinted silk hydrogels for tissue engineering, Biomaterials 260 (2020) 120281.
[212] S. Li, M. Hu, L. Xiao, W. Song, Compressive properties and collapse behavior of additively-manufactured layered-hybrid lattice structures under static and dynamic loadings, Thin-Walled Structures 157 (2020) 107153.
[213] G. Stanojevic, D. Medarevic, I. Adamov, N. Pesic, J. Kovacevic, S. Ibric, Tailoring Atomoxetine Release Rate from DLP 3D-Printed Tablets Using Artificial Neural Networks: Influence of Tablet Thickness and Drug Loading, Molecules 26(1) (2020) 111.
[214] Y. LeCun, Y. Bengio, G. Hinton, Deep learning, Nature 521(7553) (2015) 436-44.
[215] B. Dou, Z. Zhu, E. Merkurjev, L. Ke, L. Chen, J. Jiang, Y. Zhu, J. Liu, B. Zhang, G.W. Wei, Machine Learning Methods for Small Data Challenges in Molecular Science, Chemical reviews 123(13) (2023) 8736-8780.
[216] J.R. Cerda, T. Arifi, S. Ayyoubi, P. Knief, M.P. Ballesteros, W. Keeble, E. Barbu, A.M. Healy, A. Lalatsa, D.R. Serrano, Personalised 3D Printed Medicines: Optimising Material Properties for Successful Passive Diffusion Loading of Filaments for Fused Deposition Modelling of Solid Dosage Forms, Pharmaceutics 12(4) (2020).
[217] N. Hooda, J.S. Chohan, R. Gupta, R. Kumar, Deposition angle prediction of Fused Deposition Modeling process using ensemble machine learning, ISA transactions 116 (2021) 121-128.
[218] J.M. Bone, C.M. Childs, A. Menon, B. Poczos, A.W. Feinberg, P.R. LeDuc, N.R. Washburn, Hierarchical Machine Learning for High-Fidelity 3D Printed Biopolymers, ACS Biomater Sci Eng 6(12) (2020) 7021-7031.
[219] Y. Yuan, Y. Han, C.W. Yap, J.S. Kochhar, H. Li, X. Xiang, L. Kang, Prediction of drug permeation through microneedled skin by machine learning, Bioengineering & Translational Medicine 8(6) (2023) e10512.
[220] G. Stanojevic, D. Medarevic, I. Adamov, N. Pesic, J. Kovacevic, S. Ibric, Tailoring Atomoxetine Release Rate from DLP 3D-Printed Tablets Using Artificial Neural Networks: Influence of Tablet Thickness and Drug Loading, Molecules 26(1) (2020).
[221] Y. Zhang, C. Ling, A strategy to apply machine learning to small datasets in materials science, npj Computational Materials 4(1) (2018).
[222] G.E. Karniadakis, I.G. Kevrekidis, L. Lu, P. Perdikaris, S. Wang, L. Yang, Physics-informed machine learning, Nature Reviews Physics 3(6) (2021) 422-440.
[223] S. Pawar, O. San, B. Aksoylu, A. Rasheed, T. Kvamsdal, Physics guided machine learning using simplified theories, Physics of Fluids 33(1) (2021).

Chapter 3 Controlled Release of Vancomycin From PEGylated Fibrinogen Polyethylene Glycol Diacrylate Hydrogel

This chapter contains the following publication:

D.V. Nguyen, **Y. Yuan** (co-first author), M. Kukumberg, L. Wang, S.H. Lim, A.M. Hassanbhai, M. Chong, T. Kofidis, E.C.K. Tan, D. Seliktar, L. Kang, A.J. Rufaihah, Controlled release of vancomycin from PEGylated fibrinogen polyethylene glycol diacrylate hydrogel, Biomaterials Advances 161, 213896. https://doi.org/10.1016/j.bioadv.2024.213896

The published paper format is attached in **Appendix 1**.

Abstract

Surgical site infection (SSI) is a common issue post-surgery which often prolongs hospitalization and can lead to serious complications such as sternal wound infection following cardiac surgery via median sternotomy. Controlled release of suitable antibiotics could allow maximizing drug efficacy and safety, and therefore achieving a desired therapeutic response. In this study, we have developed a vancomycin laden PEGylated fibrinogen–polyethylene glycol diacrylate (PF-PEGDA) hydrogel system that can release vancomycin at a controlled and predictable rate to be applied in SSI prevention. Two configurations were developed to study effect of the hydrogel on drug release, namely, vancomycin laden hydrogel and vancomycin solution on top of blank hydrogel. The relationship between the rigidity of the hydrogel and drug diffusion was found to comply with a universal power law, i.e., softer hydrogels result in a greater diffusion coefficient hence faster release rate. Besides, vancomycin laden hydrogels exhibited burst release, whereas the vancomycin solution on top of blank hydrogel exhibited lag release. A mathematical model was developed to simulate vancomycin permeation through the hydrogel. The permeation of vancomycin can be predicted accurately by using the mathematical model, which provided a useful tool to customize drug loading, hydrogel thickness and stiffness for personalized medication to manage SSI. To evaluate the potential of hydrogels for bone healing applications in cardiovascular medicine, we performed a proof-of-concept median sternotomy in rabbits and applied the hydrogels. The hydrogel formulations accelerated the onset of osteo-genetic processes in rabbits, demonstrating its potential to be used in human.

Keywords

Hydrogel, Vancomycin, Surgical infection, Drug delivery, Controlled release, Fick’s law

3.1 Introduction

Surgical site infection (SSI) is a common issue post-surgery and accounts for 3% of surgical mortality in the United States [1]. For median sternotomy, which is a technique used in open-heart surgery, a rare but serious complication known as sternal wound infection including deep sternal wound infection (DSWI) is often associated with this procedure [2]. The incidence of sternal wound infection is around 1-4% of all cardiac surgeries [3]. It can

prolong hospital stay and may lead to requiring a second surgery increasing the risk of morbidity and mortality [2, 4, 5]. Therefore, surgical prophylaxis is indicated for all cardiac surgeries to prevent SSI. According to the Society of Thoracic Surgeons Practice Guideline [3, 6], cephalosporin and glycopeptide are the antibiotics of choice for cardiac surgery.

Cephazolin, a □-lactam agent, is the recommended first-line preoperative antibiotic due to its broad spectrum covering both gram-positive and gram-negative bacteria. Vancomycin, a glycopeptide antibiotic, has a narrower therapeutic range (gram-positive only); however, it is the most effective antibiotic against methicillin-resistant Staphylococcus aureus (MRSA). Hence, vancomycin is reserved for patients at higher risk of MRSA infection and is the drug of focus in this study. Vancomycin can also be used as the primary prophylaxis in combination with gentamicin (gram-negative coverage) for patients who have severe hypersensitivity to □-lactam agents. The recommended route of administration is intravenous for all three antibiotics. However, systemic administration of vancomycin requires therapeutic drug monitoring to maintain therapeutic effect while minimizing nephrotoxicity and ototoxicity caused by the drug concentration exceeding the therapeutic range. Therefore, topical antibiotics are thought to be the solution to allow high concentrations of vancomycin at the target site without causing systemic side effects [7].

Vancomycin paste is an example of topical antibiotics that has been used by surgeons for many years as SSI prophylaxis [3, 8, 9]. It can be prepared by simply mixing vancomycin powder in normal saline [7] and then applied to the cut sternal edges. Lazar et al. [3] and Vander Salm et al. [9] both concluded that topical vancomycin could further reduce the incidence of sternal wound infection. However, Lander and colleagues [8, 10, 11] suggested otherwise, arguing that the evidence found in Lazar et al.'s study for reduced incidence of DSWI did not directly correlate with topical vancomycin use and could just be due to advances in post-operative care and glycemic control [8, 11]. The conflicting and limited evidence restricted the use of vancomycin paste as standard prophylaxis.

To advance the use of topical antibiotics for SSI, recent studies investigated hydrogels as drug delivery systems for antibiotics. Hydrogels are three-dimensional networks composed of crosslinked, hydrophilic polymers [12]. In recent years, its use as a drug delivery system has been widely studied due to its ability to encapsulate drugs for controlled release [13]. Localized, controlled drug delivery is especially useful for drugs like vancomycin with poor absorption and fast elimination [4]. By loading vancomycin in the hydrogel, it enables sustained release of vancomycin at the surgical site for antibacterial effect.

To encapsulate vancomycin in hydrogels, several polymers have been tested to form hydrogels with different physicochemical properties and release mechanisms [1, 4, 14, 15]. Some are injectable hydrogels while others require invasive implantation. Nonetheless, there are still distances from an ideal hydrogel for drug delivery purposes, i.e., biocompatible, injectable, stable, and tunable for drug release. Particularly, there is no guidance regarding the amount of drug released from the hydrogel as a function of hydrogel properties.

To bridge the gap, we propose a vehicle we developed previously by crosslinking fibrinogen (PF) and polyethylene glycol diacrylate (PEGDA) using ultraviolet (UV) light [16]. This hydrogel has found its applications mainly in tissue engineering [16-20], encapsulation of cells [21] and growth factors [22, 23]. Its advantages as an injectable vehicle [24] with good biocompatibility [23], low immunogenicity, and malleable mechanical property [16] also made it an ideal candidate vehicle to deliver small chemical drugs such as vancomycin. Particularly, to deliver the drug locally at the target site, it requires only a small incision to allow the precursor solution to be injected and then gelled using UV light [25].

In this study, we develop two configurations of vancomycin laden PF-PEGDA hydrogel, namely, vancomycin laden hydrogel and a blank hydrogel with vancomycin solution loaded on top serving as a drug depot. We first measure the rheological properties of these hydrogels and then evaluate their effects on drug release. It was shown that drug release from the hydrogel is correlated with the rigidity of the hydrogels. Subsequently, we interpret the drug release kinetics of the PF-PEGDA hydrogels using mathematical modelling [26] for both vancomycin laden hydrogel and a blank hydrogel with a vancomycin depot [27]. We demonstrated that the two configurations could be used to accurately control the release of vancomycin with burst or lag releasing profiles. To test the potential of the hydrogels for clinical applications, we performed a proof-of-concept median sternotomy in rabbits and applied the hydrogels of varying PEGDA concentrations. It was found that the hydrogels can accelerate the osteo-genetic processes following the operation.

3.2 Materials and Methods

3.2.1 Materials

Phosphate-buffered saline (PBS), fibrinogen, acetone, ethanol, sodium hydroxide (NaOH), phosphoric acid, vancomycin powder, Mueller Hinton agar and broth, were purchased from Sigma-Aldrich (Merck KGaA, Darmstadt, Germany). Irgacure® 2959 photoinitiator was purchased from CIBA (Basel, Switzerland). *Staphylococcus aureus* (*S. aureus*, ATCC 25923) was purchased from Oxoid (Singapore). Acetonitrile was obtained from Tedia (Fairfield, OH, USA). Dipotassium phosphate (K_2HPO_4) was obtained from Alfa Aesar (Ward Hill, MA, USA). PEGDA powder was a gift from Technion – Israel Institute of Technology (Haifa, Israel). All materials were used as supplied without further purification.

3.2.2 PEGylated-fibrinogen material preparation

The PEGylated-fibrinogen (PF) was synthesized as described previously [17]. Briefly, in solution A, fibrinogen (4 g) was added into 86 mL of PBS, which contains urea (8 M). In solution B, 280 mg/mL PEGDA (10 kDa) was added into PBS, which contains urea (8 M). Solution A was added into solution B to react for 3 hours. Then the mixture was added in 4× volume of acetone to precipitate the PF. Next, the precipitates were collected and redissolved into the PBS urea solution. The solution was filtrated to purify and concentrate the PF, which is photocurable, with the photoinitiator, namely, Irgacure 2959. After curing, further addition of PEGDA is to adjust the stiffness of the gel. The stiffness of the gel can be determined by measuring its rheological properties, i.e., the storage modulus (G').

3.2.3 PF-PEGDA hydrogel preparation

To prepare the hydrogels, 20% PEGDA stock solution (w/w) was prepared by dissolving PEGDA powder in PBS solution. PEGDA stock solution was mixed with PF solution to create PF hydrogels with varying PEGDA concentrations of 0, 2 and 6% (v/v). One gram of Igacure 2959 photoinitiator powder was mixed with 1 mL of 70% ethanol to make the stock solution. The PF-PEGDA precursor solutions were mixed with 1% (v/v) of photoinitiator stock solution before UV curing. The hydrogel precursor solutions were cured under UV using either Omnicure 2000 (Waltham, MA, USA) or a portable UV lamp (VL-6-L Vilber Lourmat 6W 365nm, Eberhardzell, Germany) depending on the experiment. The hydrogel preparation process is illustrated in **Fig. 1a**.

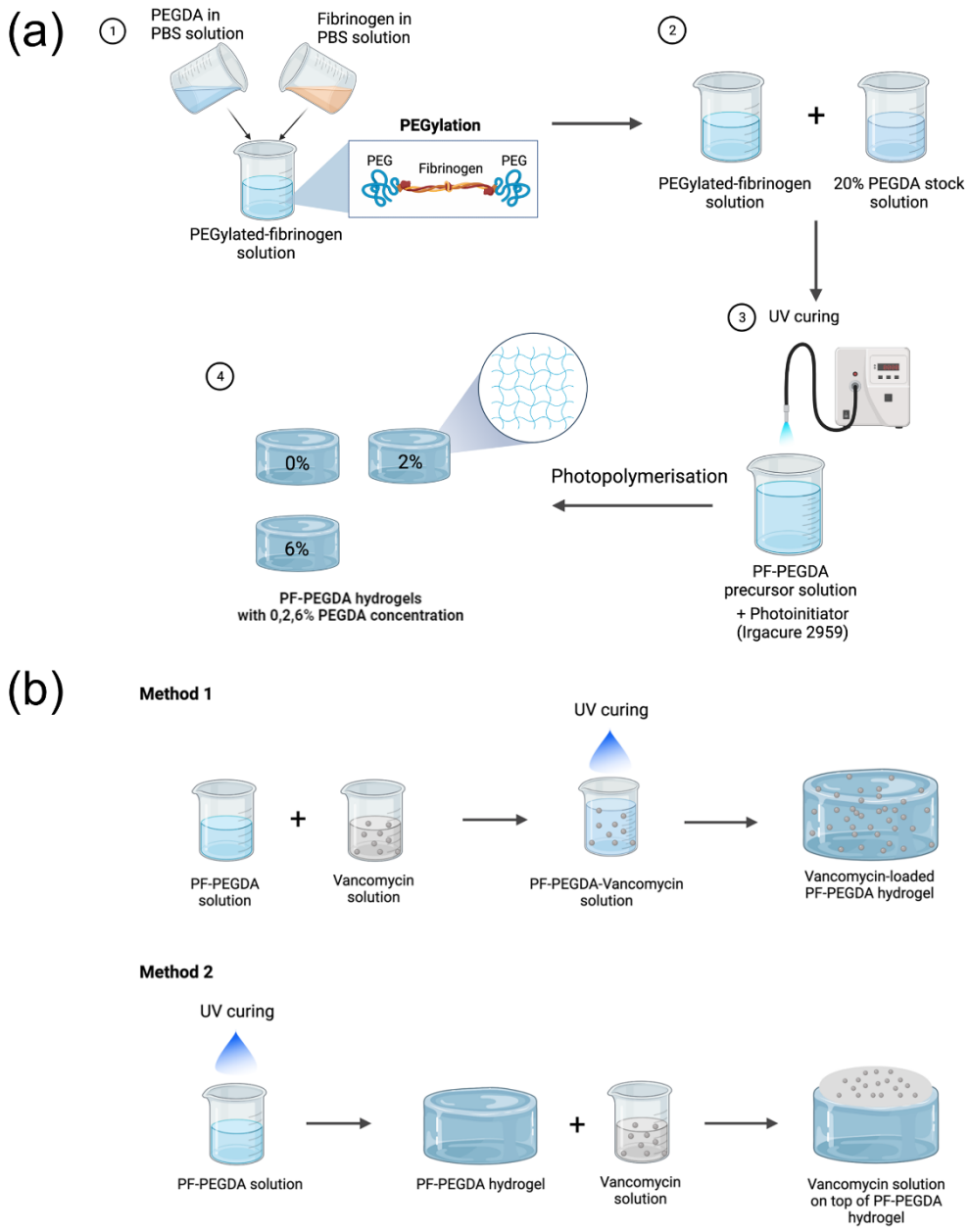


Fig. 1. (**a**) Schematic of the PF-PEGDA hydrogel fabrication process. (1) PF solution is prepared by mixing PEGDA and fibrinogen in PBS. (2) 20% PEGDA stock solution was prepared for further addition into the PF solution to control the stiffness of the hydrogel. (3) The PF solution was mixed with the photoinitiator and exposed to UV light. This enabled crosslinking of polymers via photopolymerization to produce hydrogels. (4) Multiple hydrogels with varied PEGDA concentrations were created. (**b**) Schematic of the drug loading methods used to develop the two hydrogel configurations. Method 1 is by adding vancomycin solution to the PF-PEGDA precursor solution and then curing under UV to form the vancomycin laden hydrogel. Method 2 is by curing a PF-PEGDA hydrogel first, then loading the vancomycin solution on top of the blank hydrogel. Created with Biorender.com

3.2.4 Rheological properties of the hydrogel

To determine the rheological properties of hydrogel, we measured storage modulus (G') and complex modulus (G^*) of the hydrogel. The gelation of the hydrogel with varied PEGDA content was measured using an Ares G2 rheometer (TA instrument, New Castle, DE, USA) under time sweep mode with frequency f = 1Hz, strain $\gamma = 0.001$. The PF-PEGDA hydrogel precursor solution was sandwiched between the two plates with a controlled gap. The lower plate was fixed and coupled with the Omnicure UV system. The upper plate (20 mm plane plate geometry) was connected to the measuring system. The gap between the geometry and the lower plate was fixed at 0.5 – 0.7 mm. The UV light turned on at 100s to start forming the hydrogel, and UV intensity was set at 5 mW/cm^2.

3.2.5 Formulation and vancomycin release from the hydrogel

The vancomycin stock solution of 300 mg/mL was prepared using 40 mM NaOH. Then 30 mg/mL vancomycin was added into the PF-PEGDA precursor solution. Vertical Franz diffusion cells coupled with an automated stirring temperature chamber were used for the diffusion study. Nylon filter (0.45 µm pore size) was sandwiched between two cell compartments, and then the two compartments were sealed using parafilm and clamped together. Two configurations were used to study the effect of PF hydrogel on vancomycin release and diffusion: (a) Vancomycin laden hydrogel and (b) vancomycin solution on top of blank hydrogel. The drug loading methods are illustrated in **Fig. 1b**.

In method 1, i.e., the vancomycin laden hydrogel configuration, the donor compartments were loaded with 1.5 mL of hydrogel precursor solution containing vancomycin, and then subjected to UV irradiation (Omnicure 2000) for 10 min. When the loaded hydrogels were completely cured, 4.8 mL of PBS solutions were gently put into receptor compartments and in contact with cured hydrogel through a nylon filter.

In method 2, i.e., the vancomycin on top of blank hydrogel configuration, 1 mL of hydrogel precursor solutions containing no vancomycin was put in the donor compartment, and then subjected to UV irradiation (Omnicure 2000) for 10 min. When hydrogels were completely cured, 4.8 mL of the PBS solution was gently put into receptor compartments, and then 1 mL of 30 mg/mL vancomycin was put on top of cured PF hydrogel.

All loaded cells were placed into the diffusion chamber for the vancomycin release study. 1 mL of receptor solutions was collected at fixed intervals, and then replaced by 1 mL of fresh PBS solutions to maintain sink condition and constant volume of 4.8 mL.

Vancomycin concentration was measured using high performance liquid chromatography (HPLC), equipped with a 100-5-C18 column (4.6 µm × 250 mm) from Kromasil (Sigma-Aldrich, Merck KGaA, Darmstadt, Germany). The mixture of 10% acetonitrile and 90 % 0.05 M K_2HPO_4 solution was used as mobile phase (pH adjusted to 4 using phosphoric acid), the flow rate was set at 1 mL/min. The absorbance was measured at 230 nm.

3.2.6 Relationship between gel rigidity and drug release

To examine the relationship between gel rigidity and drug release parameters, the steady flux, i.e., J ($\mu g \cdot cm^{-2} \cdot h^{-1}$), was calculated using the rate of vancomycin permeation through unit area of the hydrogel over time. Then the steady state flux was plotted against complex modulus, i.e., G*max (Pa), which is a measure of rigidity. Besides, the diffusion coefficient of vancomycin D (m2·s-1), obtained from literature[28], was also plotted against the complex modulus. Regression analysis was applied to fit the relationships between steady flux or diffusion coefficient vs the complex modulus, respectively, by using Origin Pro 2022.

3.2.7 Bacterial culture and antimicrobial activity

For the testing, *S. aureus* (ATCC 25923) was grown on both Mueller Hinton agar and broth at 37 °C in a humidified incubator. The optical density at 600 nm (OD 600) was taken using a SpectraMax microplate reader (Molecular Devices, San Jose, CA, USA). The culture was diluted accordingly to obtain a final OD of 0.15. 100 µL of the culture broth was then spread evenly over the agar plate. Vancomycin was loaded into PF-PEGDA hydrogel at 15 mg/mL. 60 µL of vancomycin loaded solutions were put into cut syringe molds and cured under a UV lamp (VL-6-L Vilber Lourmat 6W 365 nm) for 10 min. The cylindrical hydrogel was later pushed out of the mold and placed onto the surface of the agar and the plate was incubated overnight. The next day, the zone of inhibition (ZOI; defined as the diameter of the circular zone where bacterial growth was inhibited) was measured.

3.2.8 Mathematical modelling

To simulate the vancomycin release profiles, Fick's second law, as shown in **Eq. 1**, was applied to quantify the amount of drug released as a function of time.

$$\frac{\partial c}{\partial t} = D \frac{\partial^2 c}{\partial x^2} \quad (1)$$

where c is the concentration of the drug; x is the distance travelled by the diffusant; t is time; and D is the diffusion coefficient. Hadgraft [26] derived the mathematical solutions to **Eq. 1**, to describe the burst release (**Eq. 2**) and lag release (**Eq. 3**).

$$\frac{M_t}{M_\infty} = 1 - \frac{8}{\pi^2}\left(\sum_{n=1}^{\infty} \frac{1}{(2n-1)^2} \exp\left(-\frac{(2n-1)^2\pi^2 Dt}{4l^2}\right)\right) \quad (2)$$

$$\frac{M_t}{M_\infty} = \frac{\alpha Dt}{l^2} - \frac{1}{6} - \frac{2}{\pi^2}\sum_{n=1}^{\infty} \frac{(-1)^n}{n^2} \exp\left(-\frac{n^2\pi^2\alpha Dt}{l^2}\right) \quad (3)$$

where M_t is the amount of vancomycin released from the hydrogel at time t; M_∞ is the amount of drug released after an infinite amount of time; D is the diffusion coefficient; l is the thickness of the hydrogel. For lag release, the vancomycin solution is placed on top of hydrogel, hence two phases exist. When vancomycin permeates from the solution to the gel the diffusion rate decreases. Hence, a diffusion loss factor, namely, α, has been added, as shown in **Eq. 3**, to account for the phase change[26, 29-31].

3.2.9 Programming

C language in Microsoft Visual Studio 2022 was used for coding to simulate drug release profile over time, based on **Eq.2** and **Eq.3**. The codes can be found in Supplementary Information (**SI**)1. The parameters were obtained from the experimental measurement and literature (**Tab.1**). The experimental data were compared with the simulated results to validate the mathematical models.

3.2.10 Animal experiments

To evaluate the potential of PF-PEGDA hydrogel for bone healing applications in cardiovascular medicine, we performed a proof-of-concept median sternotomy in rabbits. All animal experiments were approved and performed in compliance with the NUS Institutional Animal Care and Use Committee protocol R15-0409 and carried out in accordance with the National Advisory Committee for Laboratory Animal Research (NACLAR) Guidelines. White New Zealand rabbits (n=13, age 4 months, weight 3.2±0.7 kg, Charles River Laboratories, Wilmington, MA, USA) were randomly assigned to treatment groups: a) no treatment (Control, n=3), treatment with surgical bone wax (Bonewax, n=3) or with PF-PEGDA hydrogel with varying concentrations of additional PEGDA (0%, n=1; 2%, n=2; 6%, n=4) and underwent a modified median sternotomy adapted from previous studies [32, 33].

Briefly, animals were anesthetized with a mixture of 35mg/kg ketamine (Ceva Ketamine, Ceva Animal Health Australia, Glenorie, NSW, Australia), 5.0mg/kg xylazine (ilium Xylazil 20, Troy Laboratories Australia, Sydney, NSW, Australia), and 0.1mg/kg glycopyrrolate (Glycopyrronium bromide, Martindale Pharmaceuticals, Brentwood, Essex, UK) via intramuscular injection and intubated. Anesthesia maintenance and oxygenation was performed with isoflurane (1-3%, Isoflurane B.P., Pharmachem, Eagle Farm, QLD, Australia) with a ventilator. Each rabbit received an intravenous catheter placed in the marginal ear vein for intravenous supplementation of lactated Ringer's solution (5-15 mL/h, B. Braun, Melsungen, Germany) and was operated in a supine position, hair was removed, with skin disinfected with iodine-ethanol solution. Hypothermia was prevented with a surgical warming pad. The sternum was exposed by a midline incision and dissection of both pectoralis major muscles. Each sternal vertebra was separated with a surgical chisel and surgical scissors while the sternum was lifted to avoid pleural and pericardial injury. Xiphoid was excluded from the surgical procedure and the presternum was separated only partially to secure cranio-sternal stability. Hemostasis was performed using sterile sponges. Exposed sternal vertebrae were treated with bone wax (n=1, Bone wax, B. Braun, Melsungen, Germany), PF-PEGDA hydrogel (0%, 2%, or 6%), or no treatment was applied. The sternum was closed with simple interrupted sutures using 2.0 polyamid (2-0 Ethilon Polyamide 6, Ethicon, Johnson&Johnson, New Brunswick, NJ, USA). All remaining tissue layers including the skin were closed using 4-0 polyglactin (4-0 Vicryl Polyglactin 910, Ethicon, Johnson&Johnson, New Brunswick, NJ, USA) with simple continuous suture. Animals received buprenorphine 0.05 mg/kg (ilium Temvet, Troy Laboratories Australia, Sydney, NSW, Australia) and 4mg/kg carprofen (Rimadyl, Inovat Industria Farmaceutica, Sao Paulo, Brazil) subcutaneously for five days. Additionally, the animals received 5 mg/kg enrofloxacin (Baytril, Elanco Animal Health Korea, Seoul, South Korea) subcutaneously for seven days. Daily inspection of the wound was performed for seven days. Any remaining sutures were gently removed on the tenth day. A short anesthesia was performed at Week 3 for the PET-CT evaluation and the animals were euthanized with 150 mg/kg pentobarbital (Valabarb, Jurox, Rutherford, NSW, Australia) intravenously before the PET-CT evaluation at Week 6. The evaluation of sternal osteogenesis was performed with an mCT PET/CT system (128-slice Siemens Biograph, Siemens, Munich Germany). All animals undergoing CT evaluation were under anesthesia depending on the evaluation time point. Reconstruction was performed with a slice thickness of 0.44 mm and a reconstruction increment of 0.6 mm. The field of view was adapted to the sternum size (FOV 50 mm), and a convolution kernel

dedicated to bone was adopted. All datasets gathered by the mCT PET/CT system were transferred to CD-R discs. Bone density (BD) was calculated, in Hounsfield units (HU), on transversal images (perpendicular to the long axis of the sternum) utilizing a dedicated medical imagining data examiner (AMIDE, 64-bit version, SourceForge). The circular region of interest (ROI) was determined by the manual outlying of the whole of each of the sternal vertebrae on every transversal slice. Five evenly spaced slices per vertebra were evaluated by measuring HU values in ROI. BD was determined by calculating the average of the collected HU values. To evaluate the different tissue composition during the bone healing hematoxylin-eosin (H&E), Safranin (Safranin-O), and Masson-Goldner trichome staining was performed. Selected samples were fixed in 10% neutral buffered formalin (NBF, Sigma-Aldrich, St. Louis, MO, USA), embedded in paraffin (Surgipath Paraplast Plus, Leica Biosystems, Nussloch, Germany), and sectioned at 5μm for H&E, Safranin-O and Masson-Goldman trichome staining following standard procedures and manufacturer's instructions. Histological sections were imaged with an upright brightfield microscope (Evos XL Core, ThermoFisher Scientific, Waltham, MA, USA). Acquired images were processed with ImageJ (version 1.52q, Rasband WS, National Institutes of Health, Bethesda, MA, USA).

3.2.11 Statistical treatment

Results were presented as mean ± standard deviation. The data normal distribution was checked by using Shapiro-Wilk test. Analysis for nonparametric data was determined by Kruskal-Wallis analysis of variance (ANOVA) test using Origin Pro 2022. Statistical evaluation of multiple animal data groups was performed using one-way or two-way ANOVA with Tukey's post-hoc test as appropriate, which was performed using QuickCalcs and GraphPad Prism (version 10.2.0., GraphPad Software, San Diego, CA, USA, graphpad.com). Statistically significant p-values are indicated as ****$P < 0.0001$; ***$P < 0.001$; **$P < 0.01$; *$P < 0.05$. NSD represents no significant difference.

3.3 Results

3.3.1 Rheological properties of the hydrogel

PF-PEGDA hydrogel networks are formed via UV crosslinking of prepolymer solutions. The rigidity of the hydrogel is affected by this gelation process and the degree of crosslinking. **Fig. 2** shows the typical gelation curve of PF hydrogel with varied PEGDA concentrations, with and without vancomycin. Right after being exposed to UV light from 100 seconds onwards on the gelation curve, a hydrogel network was formed, resulting in the rise of storage modulus (G') and loss modulus (G"). The hydrogel was completely formed when G' and G" reaches constant, i.e., the plateau on the gelation curve. The time during which G' and G" starts increasing and reaches plateau is known as the gelation time.

As shown in **Fig. 2(a)**, the storage modulus was the highest for PF hydrogel with 6% PEGDA (blue), followed by 2% (red) and the lowest for 0% PEGDA (green). This shows that higher PEGDA concentrations result in stiffer hydrogels, as higher gelator concentration can result in denser network in the gel. Besides, the PF hydrogels containing vancomycin show longer gelation time as compared to PF hydrogels without vancomycin. This suggests that the presence of ingredients other than the gelators in the prepolymer solution can interfere with the gelation process.

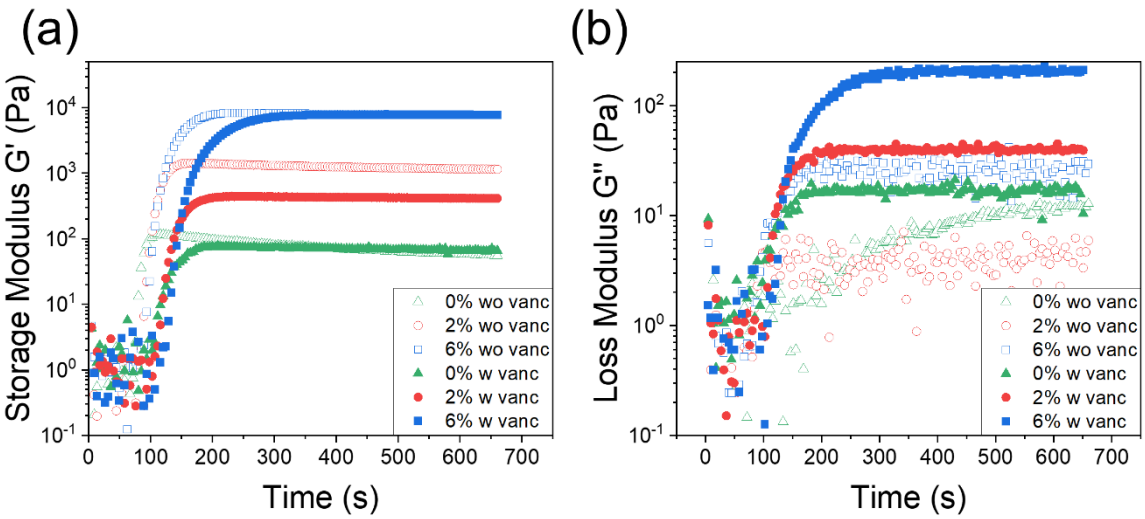


Fig. 2. Hydrogels with 0%, 2% and 6% PEGDA concentrations with and without vancomycin. Rigidity of the hydrogel is measured by (a) storage modulus (Pascals), (b) loss modulus and plotted against time (seconds) to represent the gelation process. The gelation curves show, the higher the PEGDA concentration, the more rigid the hydrogel; and the addition of vancomycin slows down the gelation process. (w: with; wo: without; vanc: vancomycin) (n = 3)

3.3.2 Vancomycin release from the hydrogel

Cumulative release of vancomycin from PF hydrogel with varied PEGDA concentration was shown in **Fig. 3**. The cumulative curve in **Fig. 3a** shows typical burst release for vancomycin laden gel configuration and **Fig. 3b** shows lag release for vancomycin solution on top of blank hydrogel configuration. The results show that for hydrogels with higher PEGDA concentrations, drug release is slower. In other words, the harder the hydrogel is, the slower the drug release, for both configurations.

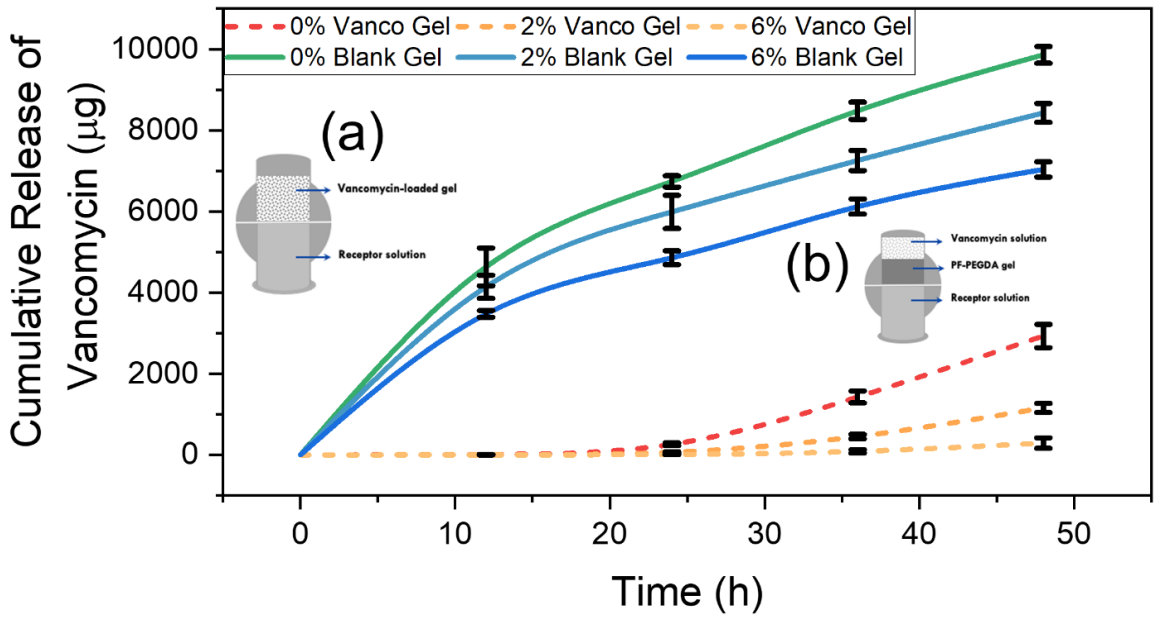


Fig. 3. Cumulative release of vancomycin from PF hydrogels with varied PEGDA concentrations over time: (a) Vancomycin laden PF-PEGDA hydrogel, (b) Vancomycin solution on top of PF-PEGDA hydrogel. Harder hydrogels with higher PEDGA concentrations have slower drug release for both configurations. (**a**) displays burst release and (**b**) displays lag release. Vanco: vancomycin. (n=3)

In **Fig. 3b**, 1 mL of 30 mg/mL vancomycin was put on top of cured hydrogel at the beginning of the experiment, hence the total amount of drug was 30mg. After 48 hours of experiment, the amount of drug accumulated in the receptor solution was determined to be ~3 mg for the 0% vancomycin gel, as shown in **Fig. 3b**. So, the amount of drug remains in the solution and the 1ml gel together was ~27 mg. Besides, the permeation curves, as shown in **Fig. 3b**, are typical of the condition of a constant reservoir. Taken together, the Hadgraft's condition of constant reservoir in the donor compartment was met for the lag release experiments as described in **Fig. 3b**.

3.3.3 Relationship between gel rigidity and drug release

To further explore this relationship between rigidity and drug release, the steady flux, J (µg cm^{-2} h^{-1}) and diffusion coefficient, D (m^2 s^{-1}), were plotted against complex modulus, G^*_{max} (Pa). The linear regression and exponential regression from the graph (**Fig. 4a and b**) with R^2 = 0.99867 and R^2=0.99982 show a strong correlation between $\ln G^*_{max}$ and ln(1/J) as well as D, respectively, highlighting the inverse relationship between gel rigidity and drug release rate. From the previous findings, gel rigidity can be controlled by altering the PEGDA concentration, hence, by altering the PEGDA concentration, drug release rate can also be controlled.

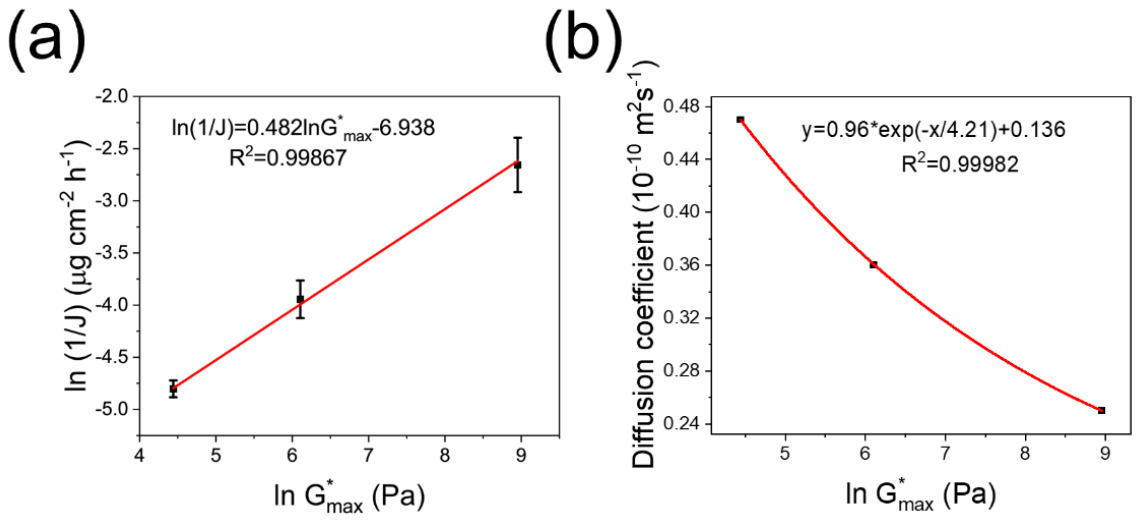


Fig. 4. The relationship between rigidity and drug release, represented by complex modulus, G^*_{max} (Pa) with steady flux, J (µg cm^{-2} h^{-1}) and diffusion coefficient, D (m^2 s^{-1}). (**a**) The inverse correlation between G^*_{max} and J implies the more rigid the gel, the lower the drug release. (**b**) The inverse correlation between G^*_{max} and D implies the more the rigid the gel, the lower the drug diffusion rate in the hydrogel.

3.3.4 Antibacterial activity of vancomycin laden hydrogel

Molds modified from a 1 mL syringe as shown in **Fig. 5a** were used to prepare hydrogel cylinders (**Fig. 5b**). Then the hydrogels were placed at the center of the *S. aureus* culture plates (**Fig. 5c**). Vancomycin laden hydrogels inhibit *S. aureus* growth as indicated by ZOI (mm) on the culture plates. ZOI appears at the center of the plates with hydrogels containing 0%, 2%, and 6% PEGDA. The diameter of ZOI varied depending on the PEGDA concentration. As the PEGDA concentration increases, ZOI decreases (**Fig. 5d)**. The result agrees well with the vancomycin release study, i.e., higher PEGDA concentration results in slower drug release.

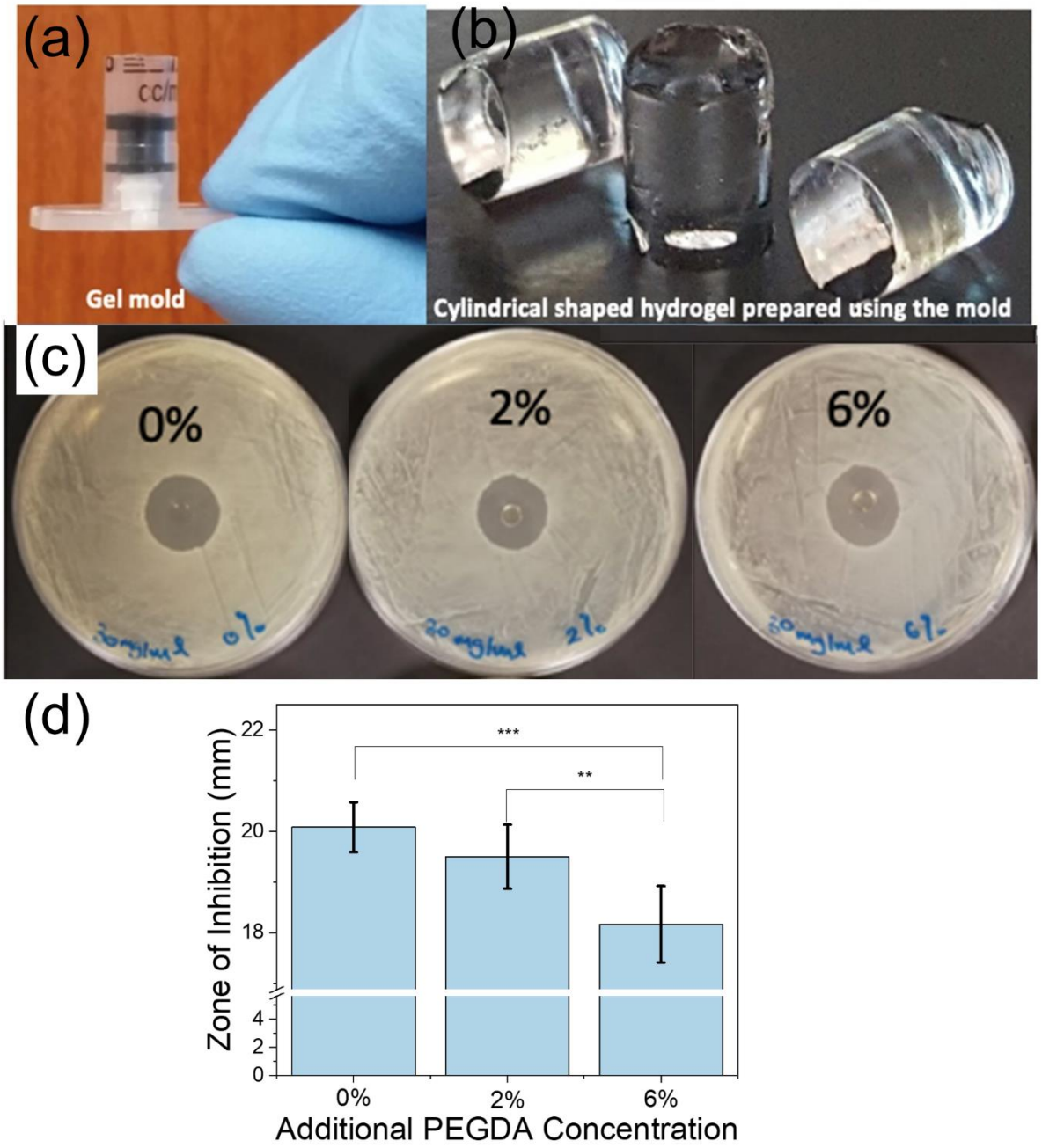


Fig. 5. (**a**) The mold to make hydrogel blocks. (**b**) Hydrogel cylinders made using the mold. (**c**) Zone of inhibition (ZOI) appears at the center of the *S. aureus* culture plate where the vancomycin laden PF-PEGDA hydrogel cylinder is located. (**d**) ZOI for vancomycin laden hydrogels with varied PEGDA concentrations.

3.3.5 Fickian diffusion of vancomycin from hydrogel

Diffusion is the major mechanism of drug release from hydrogel. Increased rigidity of the hydrogel caused a decreased drug release rate. As illustrated in **Fig. 3**, vancomycin laden hydrogel undergoes a burst release, i.e., initially, there is a fast release of drug from the

hydrogel then the rate of drug release decreases and becomes steady. In the hydrogel, vancomycin is dispersed throughout the gel matrix. When it meets the receptor solution, the drug cumulated at the surface is released hence the initial burst effect.

This is different from the blank hydrogel with vancomycin solution on top as a drug depot. It undergoes a lag release instead of a burst release, i.e., the drug release rate starts slow and then reaches a steady state after a period. The lag time is approximately 24 hours before the drug is released at a steady rate, as it takes time for the drug to first diffuse into the hydrogel and then into receptor solution.

Table 4. The related values of hydrogel and its properties used in modeling.

Property (Units)	**Value**	**Property (Units)**	**Value**
Hydrogel thickness: burst release (m)	0.015	Drug in hydrogel: burst release (μg)	45000
Hydrogel thickness: lag release (m)	0.01	Drug in solution: lag release (μg)	30000
Diffusion coefficient in 6%, 2% and 0% PEGDA hydrogel ($10^{-10} m^2/s$)	0.25, 0.36, 0.47	The experience factor α	0.68
Time step (s)	100		

The diffusion coefficient of vancomycin in aqueous solution was 3.25×10^{-10} m^2/s at 25 °C [34], and 2.83×10^{-10} m^2/s at 37 °C [35]. However, there is no report of diffusion coefficient of vancomycin inside PF-PEGDA hydrogels. To find D value of vancomycin in the hydrogels, the experimental results in burst release were used to fit the equation by using the least-square method. The D values were found to be 0.47×10^{-10}, 0.36×10^{-10}, and 0.25×10^{-10} m^2/s for 0%, 2% and 6% PEGDA hydrogel, respectively, as shown in **Tab. 1**.

An alternative method to estimate the values of D is by the slop of the initial linear part of the experimental cumulative release data versus square root of time in the burst release study, as shown in **Fig. 6b**, through fitting with Equation 20 of Hadgraft's paper [26]. As shown in **SI2**, the D values were found to be 0.56×10^{-10}, 0.37×10^{-10}, and 0.26×10^{-10} m^2/s for 0%, 2% and 6% PEGDA hydrogels, respectively. The D values are very close to those obtained above, showing both methods are valid to estimate the diffusion coefficient .

The calculated D values in the hydrogel are ~10 times smaller than those in the aqueous solutions, likely because the porous structures of the hydrogels hinder drug diffusion. Afterwards these calculated D values were used in the lag release simulation to predict the parameter of α, the best-of-fit of which was found to be 0.68.

3.3.5.1 Mathematical modelling of burst release

In this study, vancomycin was encapsulated inside the hydrogel and the receptor solution was maintained in sink condition. This is to simulate the *in vivo* conditions, in which the drug laden hydrogel will be applied to the surgical site. The drug concentration in the tissue is negligible, as the permeated drug will reach blood circulation and then be cleared from the surgical site. The parameters and their values used in the modelling are listed in **Table 4.**

The cumulative amount M_t represents the theoretical burst release, as shown in **Fig. 6a**. The predicted curve matched with the experimental data, where the R-squared values for 0%, 2% and 6 % PF-PEGDA hydrogels are 0.967, 0.973 and 0.968. It shows that the simulation is an accurate representation of the actual drug release.

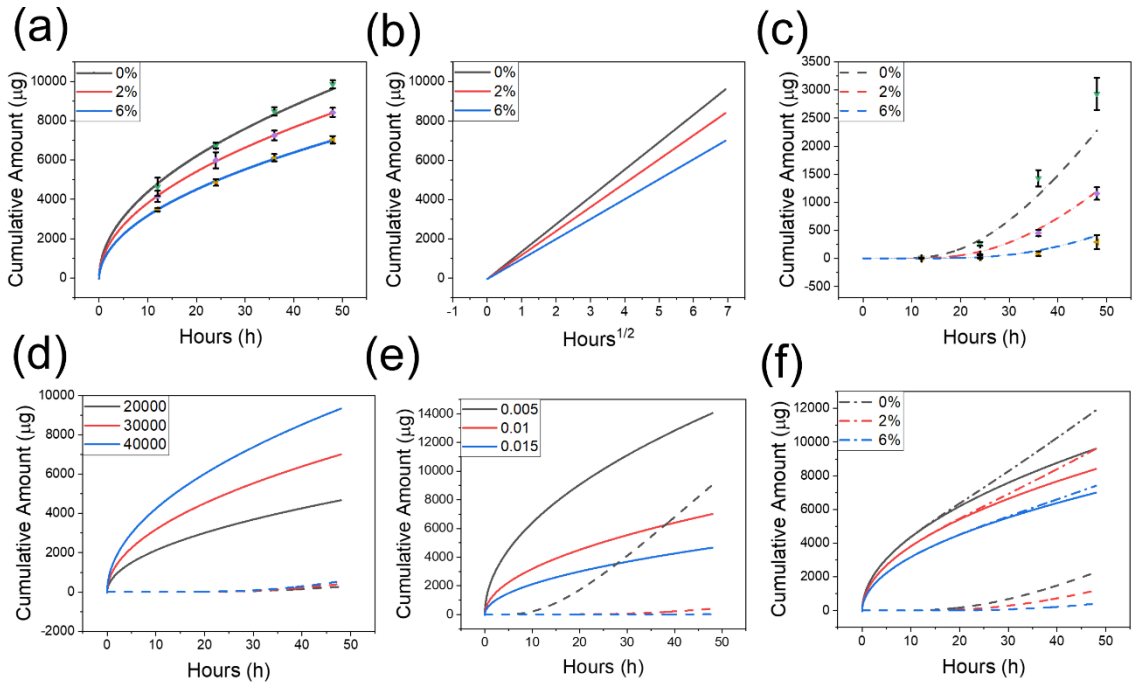


Fig. 6. (**a**) Experimental and simulated vancomycin release profiles from vancomycin laden hydrogels containing 0%, 2% and 6% PEGDA. (**b**) Cumulative drug release from drug laden hydrogel against the square root of time. **(c)** Experimental and simulated drug release of vancomycin solution through blank hydrogel. **(d**) Effect of drug loading on drug release. **(e)** Effect of hydrogel thickness on drug release. (**f**) Theoretical drug release profile, obtained by combing burst and lag release. (Solid lines represent vancomycin laden hydrogels releasing profile, dash line represents vancomycin solution on top of blank hydrogel, and dash dot line indicate the combined release profile of two configurations)

In addition, the cumulative drug release from vancomycin laden hydrogel was also graphed against the square root of time (**Fig. 6b**). The linear correlation shows that the drug release follows a 'square root of time' release kinetic, dictated by Fick's Law [36].

3.3.5.2 Mathematical modelling of lag release

In contrast to the vancomycin laden hydrogel, for the configuration of vancomycin solution on blank hydrogel, no drug was loaded inside the hydrogel. The drug release was drawn by dash line in **Fig. 6c**. The theoretical and the experimental drug release follow a similar profile, i.e., the initial time lag and subsequent steady state. The R-squared values for 0%, 2% and 6 % PF-PEGDA hydrogels are 0.963, 0.982 and 0.937, respectively, showing satisfactory data fitting. In addition, the numerical value of factor α was found to be 0.68, showing that the diffusion rate of vancomycin decreased from the solution to the hydrogel.

3.3.5.3 The effect of parameters on vancomycin releasing from hydrogel.

It was found that rigidity of the hydrogel significantly affects the vancomycin diffusion coefficient in hydrogel, i.e., stiffer hydrogels result in slower release (**Fig. 6a**). Apart from gel rigidity, we also performed simulation to investigate two additional parameters, namely, drug loading in hydrogel for burst release and the thickness of the hydrogel for lag release. **Fig. 6d** shows that higher drug loading results in faster drug release for burst release, suggesting that high drug loading is needed to achieve fast drug release. **Fig. 6e** shows that thinner hydrogels result in faster drug release, as determined by the slope of the linear portion for lag release.

3.3.5.4 Mathematical modelling of combined release

Hypothetically the burst release and lag release can be combined, to achieve fast onset of action, resultant from the loaded drug inside the hydrogel and subsequent sustained drug release, resultant from the drug depot, to maintain continual pharmacotherapy. The actual configuration is to place the drug depot on top of the drug-laden hydrogel, which is then placed on the surgical site.

Fig. 6f shows the simulation results of combinatory release profile. Initially, the release is dictated by the burst release from the drug laden hydrogel, with minimal contribution from the drug depot. Subsequently, as the time exceeds 12 hrs, the drug depot on top of the

hydrogel begins to contribute to the combined drug release profile, eventually becomes the main contributor in the combinatory drug release, to provide sustained release of vancomycin into the receptor.

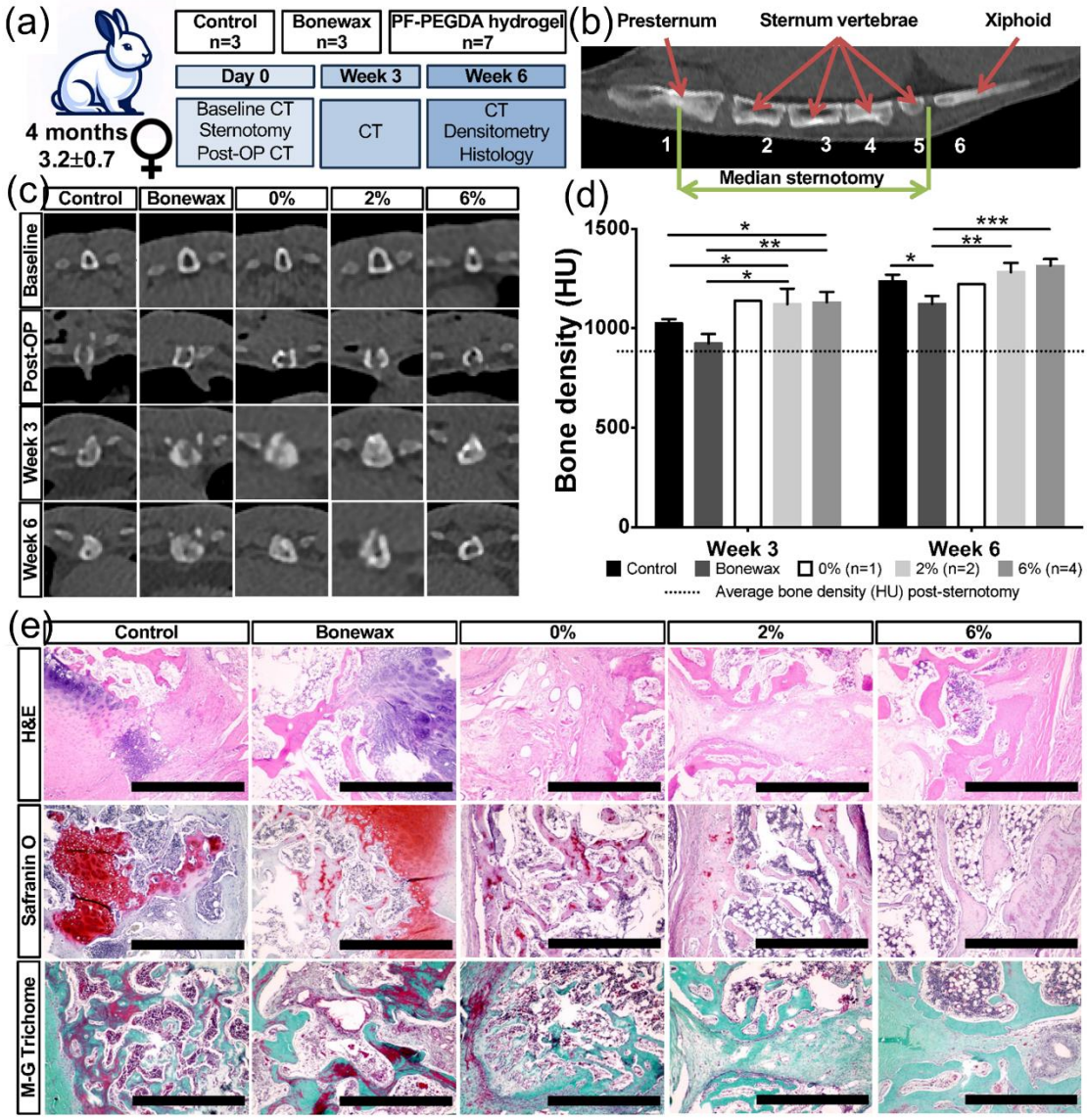


Fig. 7 PF-PEGDA hydrogel increases osteo-induction and osteogenesis in a median sternotomy rabbit model. (a) Schematic diagram of the animal study workflow. Female White New Zealand rabbits (4 months old, 3.2±0.7 kg) were treated with surgical bone wax (Bonewax, n=3), PF-PEGDA hydrogel (PF-PEGDA hydrogel, n=7) or received no additional treatment (Control, n=3) during a median sternotomy. Computed tomographic (CT) assessment was performed pre- (Baseline) and post-surgery (Post-OP), at Week 3 and Week 6 time points. Bone healing was evaluated by bone densitometric (Densitometry) and histopathological (Histology) assessment. **(b)** Anatomical visualization of median sternotomy of sternal vertebrae 1-5. **(c)** Representative transversal CT images illustrate varying degrees of radiographic density across sternal vertebrae (1-5) at selected time points (Baseline, Post-OP, Week 3, Week 6). **(d)** Bone densitometry. CT images quantification of sternal bone of

non-treated animals (Control), animals treated with bone wax (Bonewax), and PF-PEGDA (0%, 2% and 6% PEGDA concentration) evaluated at Week 3 and Week 6 post sternotomy. Multiple images per sternal vertebrae (1-5) were assessed. Bone density quantified with Hounsfield Units (HU). Mean bone density post-sternotomy is represented as a dotted line. All results are represented as mean±SD. **(e)** Histopathological evaluation of sternal vertebrae showed a higher presence of maturing and mature bone tissue over immature bone, fibrotic, and cartilage tissue. Histological sections were evaluated across all treatment (Control, Bonewax, 0%, 2% and 6% PF-PEGDA hydrogel) groups. Representative images of hematoxylin-eosin (purple – cartilage tissue, dark pink – bone tissue), Safranin-O (Safranin-O, red – cartilage tissue), and Masson-Goldman Trichome (M-G Trichome, green – mature bone matrix, red – immature bone matrix) staining of sternal vertebrae. Scale bar = 1mm.

3.3.6 The effect of PF-PEGDA hydrogel on median sternotomy in rabbits

To evaluate the customizability and toxicity of the PF-PEGDA hydrogel, we assessed the hydrogel performance in a median sternotomy in rabbits (**Fig. 7a**). Hypothermia was prevented with a surgical warming pad. The sternum was exposed by a midline incision and dissection of both pectoralis major muscles. Each sternal vertebra was separated with a surgical chisel and surgical scissors while the sternum was lifted to avoid pleural and pericardial injury. Xiphoid was excluded from the surgical procedure and the pre-sternum was separated only partially to secure cranio-sternal stability (**Fig. 7b and Fig. S1a and b**).

PF-PEGDA hydrogels with the additional PEGDA concentrations of 0%, 2%, and 6% were used to evaluate the influence of stiffness material in bone healing. No obvious adverse effects were observed during the sternotomy and the wound healing post-sternotomy. The evaluated PF-PEGDA hydrogel with additional 0%, 2% and 6% PEGDA showed different levels of applicability. Although the 0% additional PEGDA PF-PEGDA hydrogel was friable during manipulation and application, the material demonstrated a high degree of exudate absorption (**Fig. S1c and d**). The 2% and 6% PF-PEGDA hydrogel as a material with a higher stiffness, have shown also easier manipulation during application and suturing between the sternal vertebrae albeit with a lower exudate absorption (**Fig. S1 e-h**). None of the PF-PEGDA hydrogels demonstrated hemostatic properties when compared to bone wax.

Hyper-density with a hypertrophic callus was observed 3 weeks postoperatively in all animal groups (**Fig. 7c**). Six weeks postoperatively, a higher density in the cortical zones with respect to the inner cancellous bone was observed in all groups but the group treated with bone wax. PF-PEGDA hydrogel (2% and 6%) treated animals showed increased sternal vertebrae bone density (1120±79 HU and 1130±53 HU respectively) when compared to control and bone wax-treated animals (1025±21 HU and 924±47 HU respectively) three

weeks postoperatively (**Fig. 7d and Fig. S2**). Although higher bone density was observed across all animal groups six weeks postoperatively, no significant difference was observed between the PF-PEGDA-treated and control groups. Notably, the bone wax-treated animals showed lower bone density than the PF-PEGDA-treated and control groups across both time points. Evaluation of bone density of individual sternal vertebrae across groups and time points showed fluctuations in bone density values without any trends and statistically significant differences (**Fig. S3**).

Histological examination showed typical bone morphology across all animal groups albeit with differences (**Fig. 7e**). Evidence of cartilaginous and immature bone tissue was observed in animals treated with bone wax and controls observationally larger patches than in animals treated with PF-PEGDA hydrogels. Despite the foreign origin of the biomaterial used, minimal mononuclear infiltration was observed. Furthermore, no traces of the PF-PEGDA materials were found in histological samples.

3.4 Discussion

3.4.1 Vancomycin laden hydrogels

Hydrogels are three-dimensional network structures composed of hydrophilic polymers immobilizing a large amount of liquid. It provides a porous structure that permits the transfer of gas and small molecules to the wound [37]. These characteristics render hydrogels suitable for antibacterial applications and promote tissue regeneration [38]. Controlled release of vancomycin can be achieved by varying the concentration of PF-PEGDA in the hydrogel. Moreover, different drug loading methods also provide different drug release kinetics, such as burst release or lag release.

The vancomycin laden hydrogel with burst release allows high concentrations of vancomycin to be delivered at the initial stage, hence may be more desirable for surgical prophylaxis purposes to prevent rapid onset infections (**Fig. 3a and 6a**). For this configuration, it can either be implanted or injected [39]. The PF-PEGDA precursor solution mixed with vancomycin can be cured by UV irradiation to form the hydrogel first and then implanted in the surgical site. The other option is by injecting the PF-PEGDA-vancomycin precursor solution into the surgical site then using UV light for *in situ* photopolymerization of the hydrogel.

As discussed in a previous study by Nguyen and colleagues, rheological data is important in the development of controlled release hydrogel systems as it can be used to predict steady flux for drug permeation using an empirical formula, known as the universal power law [29]. According to the fractional Stokes-Einstein relation, $D(G^*)^{\varepsilon}$ = constant. In addition, the Stokes Law for steady state condition is $J = C_0 / (R_{gel} + R_{nylon})$, where R_{gel} and R_{nylon} are the resistance of the gel and nylon membrane, respectively.

In the current study, the PF-PEGDA gels were placed over a nylon filter membrane with pore size of 0.45 µm in diameter, in place of the rat skin membrane used in the previous study [29]. As the filter membrane is very permeable compared with the hydrogel, and its diffusional resistance is much smaller compared with the hydrogel's diffusional resistance, i.e., $R_{gel} >> R_{nylon.}$ As a result, $J = C_0/R_{gel}$ where $R_{gel} = l/D_{gel} = a(G^*)^{\varepsilon}$. It can be easily deduced that $1/J = a(G^*)^{\varepsilon}/C_0$, where J is the flux of the diffusants through a membrane, C_0 is the initial concentration of the diffusants in the gel, while a and ε are constants depending on diffusant-gel types. Hence, $Ln(1/J) = Ln(a) + Ln(G^*)^{\varepsilon} - Ln(C_0) = \varepsilon\, Ln(G^*) + constant$.

In the current study it was found that drug permeation and gel rigidity was strongly correlated (**Fig. 4a and b**). This relationship is represented by the equation $Ln(1/J) = 0.482\ lnG^*_{max} - 6.938$. The result showed, for the first time, that PF-PEGDA gels, as a polymeric gel, follow the universal power law as well, with the power $\varepsilon = 0.482$. This finding is important owing to the following two reasons. First, unlike the previous study where organo-gels were used [29], hydrogels were used in the current study. This has demonstrated that universal power law is applicable to both organo-gels and hydrogels. Second, rat skin samples were used in the previous study while nylon filter membranes were used in the current study. Compared with the rat skin membrane, the filter membrane poses little or no diffusion resistance to the diffusants. However, the drastic change of diffusion membranes did not affect the applicability of the universal power law, which depends solely on the diffusant-gel system.

When designing the drug delivery system, it is important to consider both gel rigidity and drug release rate. Excessive rigidity can retard drug release from hydrogel, potentially compromising the therapeutic efficacy of the hydrogel formulation. On the other hand, a gel that is too soft may not be stable to be applied onto the surgical sites.

3.4.2 Vancomycin depot on top of hydrogel

In this study, the vancomycin solution is envisaged as a drug depot, which facilitates a constantly and slowly release of the carried drugs. The blank hydrogel pad is envisaged as a hydrogel dressing, widely used in wound healing for hydration purposes. Placing a drug depot on top of hydrogel dressing can provide a means of adding antimicrobial agents onto the wound to facilitate wound healing. Compared with the first configuration, namely, drug laden hydrogel, this approach may be easier to implement in clinical settings.

In a recent report which used a similar setting to the lag release in the current study, it was found that the lag time is inversely related to the diffusion coefficient of the diffusant [40]. In the current study, similar results were obtained, i.e., greater diffusion coefficient resulted in shorter lag time, as shown in **Fig. 3b**. Besides, it was reported that the lag time is proportional to the squared thickness of the hydrogel [16, 40]. Hence, the drug releasing profile can be customized by changing the characteristics of the hydrogel. For example, softer and thinner gels can be used if shorter lag time is needed.

3.4.3 Combinatory configuration

The two configurations can be combined, although experiments were not conducted in the current study. When burst release and lag release are combined, the drug release profile exhibits an initial burst release, which is followed by a near zero-order continual drug release (**Fig. 6f**). This approach may offer a fast onset of action and sustained drug release, preferable for wound healing.

In addition, two different drugs may be loaded into the hydrogel and drug depot respectively. The drug inside the hydrogel can be used for fast release to inhibit onset of microbial infections. The other drug, e.g., growth factors or other active ingredients, can be added in the depot placed on top of the hydrogel, which is to be released after a time lag, to aid in long term tissue regeneration and/or post-operative infections [41]. It should be noted that vancomycin may be unsuitable to treat multidrug-resistant bacteria caused infections [42, 43]. In this case alternative antibiotics should be used. In addition, long-term exposure to a single antibiotic agent may cause antimicrobial resistance. To address this issue, the concurrent use of multiple antimicrobial agents may be considered [44].

Using this approach, clinicians may tailor treatment plans based on individual patient needs, for example, drug loading of 12 mg to release 6mg within the first 12 hours to inhibit the onset of microbial infections, and further 6 mg within 24 hours for sustained microbial infection suppression. The mathematical model allows for customized design of hydrogels to fine-tune key parameters such as gel rigidity/dimension and drug loading.

3.4.4 Median sternotomy in rabbit model

As the use of PF-PEGDA hydrogel formulations may be advantageous in clinical applications, we evaluated the hydrogel in an animal model using rabbits. We selected median sternotomy (MS) as our model of choice, as MS has been shown with a complication rate of up to 5%, a mortality rate approaching 80%, and a high secondary infection during repeated sternotomies [45-47].

We included in our comparison bone wax, a known hemostatic agent widely used in MS for clinical applications [48]. PF-PEGDA hydrogels can be easily prepared off-site and kept surgically sterile before application. Several other materials have been evaluated previously for their osteogenic and osteoconductive capabilities in MS but with less customizability than PF-PEGDA hydrogels [32, 48, 49].

Notably, customizing the PEGDA concentration demonstrated beneficial properties during surgical manipulation albeit with a lower hemostatic function. However, it has been shown that hemostatic material, such as surgical bone wax, inhibits osteogenesis, increases inflammation, and may increase infection risk [48]. Although higher cellularity, fuzzy hyper-density, and enlarged callus formation, at the third week postoperatively, indicated a degree of inflammation and misalignment of sternal halves in some of the animals, an increased bone density with lower cellular infiltration in all PF-PEGDA treated animal groups confirmed faster onset of osteo-genetic processes, when compared to control and bone wax-treated animals. The porous structure of hydrogel may have provided a cellular guidance leading to faster bone healing [32, 48, 49]. The PF-PEGDA hydrogel has been previously shown to facilitate cell invasion, migration, and tissue remodelling. Fibrin degradation products can promote angiogenesis by enhancing the proliferation, migration, and differentiation of endothelial cells. Consequently, the PF-PEGDA hydrogel, regardless of the varying concentrations of vancomycin, does not demonstrate a significant difference in bone regeneration.

3.4.5 Applicability of the hydrogels in clinical settings

The first formulation, designed for direct application to the cut sternal edges, can provide localized antibiotic delivery while minimizing systemic toxicity. To mitigate concerns regarding tissue regeneration, the formulation strategy included optimizing the hydrogel's mechanical properties to support, rather than hinder, the healing process. Furthermore, the UV-initiation process is designed to be rapid and conducted at a wavelength that minimizes tissue damage, a consideration that is critical for applications involving open wounds.

Crucially, we emphasize the hydrogel's customizability, which is a significant advantage in its clinical applications. The PF-PEGDA hydrogel's composition can be varied to produce materials with different stiffness levels, thereby allowing for tailored application depending on the nature of the surgical site or skin wound.

Additionally, we have conducted thorough examinations of the material's UV-crosslinking characteristics prior to surgical applications. This step is essential to confirm the hydrogel's stability and performance in a surgical environment, ensuring that it meet the stringent requirements for both safety and efficacy in wound management.

Regarding the second configuration, which involves a vancomycin solution applied atop the hydrogel, one concern is about the practicality of maintaining the solution on the gel. However, with the development of carefully designed secondary dressings, the maintenance of the vancomycin solution atop the hydrogel becomes a viable option. These specially designed wound dressings would not only retain the solution but also ensure that it remains in effective contact with the hydrogel. This formulation was developed as an alternative strategy for scenarios where direct hydrogel application may not be feasible or in cases where additional vancomycin delivery is required after the initial application.

3.4.6 Limitations and future study

In the current study, the mathematical models based on Fick's second law was used, which could only describe drug release from isotropic hydrogels with uniform drugs distribution. With this method, the simulation of drug diffusion within non-uniform hydrogels is challenging, as local variation in gel rigidity and diffusion characteristics impact drug distribution. The issue can be addressed by using finite element methods, which use integration, instead of differential methods [30, 50]. Finite element methods, when assisted by high-performance computing, could yield more accurate predictions, accounting for intricate structural variations and boundary conditions.

Second, the combinatory configuration, as simulated based on burst release and lag release, can be tested by performing drug release experiments using the hydrogels. When burst release and lag release are combined, fast onset of action plus near zero-order continual drug release can be achieved, which may be preferable for clinical applications, especially when multiple antibiotics need to be administrated.

In addition, a more detailed characterization of osteogenic, osteo-inductive, and/or osteoconductive properties is necessary to parse the mechanisms of PF-PEGDA hydrogels' effects on bone remodeling and regeneration. Furthermore, in vivo studies of PF-PEGDA hydrogel formulations containing antibiotics, such as vancomycin, are needed to demonstrate its translatability into a clinical application to manage SSI.

3.5 Conclusion

PF-PEGDA hydrogel is a promising drug delivery system to administer vancomycin *in situ* to manage surgical site infection. As an injectable hydrogel, it offers quick gelation in minutes

via photopolymerization for use in the clinical setting. Additionally, the drug release rate can be easily adjusted using the simulation methods to suit different therapeutic needs. The proof-of-concept animal testing showed the potential of the hydrogel formulations to be used in clinical settings.

References

[1] C.H. Liao, C.S. Chen, Y.C. Chen, N.E. Jiang, C.J. Farn, Y.S. Shen, M.L. Hsu, C.H. Chang, Vancomycin-loaded oxidized hyaluronic acid and adipic acid dihydrazide hydrogel: Bio-compatibility, drug release, antimicrobial activity, and biofilm model, J Microbiol Immunol Infect, 53 (2020) 525-531,https://doi.org/10.1016/j.jmii.2019.08.008.
[2] Y.D. Shi, F.Z. Qi, Y. Zhang, Treatment of sternal wound infections after open-heart surgery, Asian J Surg, 37 (2014) 24-29,https://doi.org/10.1016/j.asjsur.2013.07.006.
[3] H.L. Lazar, T.V. Salm, R. Engelman, D. Orgill, S. Gordon, Prevention and management of sternal wound infections, J Thorac Cardiovasc Surg, 152 (2016) 962-972,https://doi.org/10.1016/j.jtcvs.2016.01.060.
[4] C.T. Gustafson, F. Boakye-Agyeman, C.L. Brinkman, J.M. Reid, R. Patel, Z. Bajzer, M. Dadsetan, M.J. Yaszemski, Controlled delivery of vancomycin via charged hydrogels, PLoS One, 11 (2016) e0146401,https://doi.org/10.1371/journal.pone.0146401.
[5] A. Pradeep, J. Rangasamy, P.K. Varma, Recent developments in controlling sternal wound infection after cardiac surgery and measures to enhance sternal healing, Med Res Rev, 41 (2021) 709-724,https://doi.org/10.1002/med.21758.
[6] R. Engelman, D. Shahian, R. Shemin, T.S. Guy, D. Bratzler, F. Edwards, M. Jacobs, H. Fernando, C. Bridges, The society of thoracic surgeons practice guideline series: antibiotic prophylaxis in cardiac surgery, part II: Antibiotic choice, Ann Thorac Surg, 83 (2007) 1569-1576,https://doi.org/10.1016/j.athoracsur.2006.09.046.
[7] H.L. Lazar, A. Ketchedjian, M. Haime, K. Karlson, H. Cabral, Topical vancomycin in combination with perioperative antibiotics and tight glycemic control helps to eliminate sternal wound infections, J Thorac Cardiovasc Surg, 148 (2014) 1035-1040,https://doi.org/10.1016/j.jtcvs.2014.06.045.
[8] H.L. Lander, J.I. Ejiofor, S. McGurk, K. Tsuyoshi, P. Shekar, S.C. Body, Vancomycin paste does not reduce the incidence of deep sternal wound infection after cardiac operations, Ann Thorac Surg, 103 (2017) 497-503,https://doi.org/10.1016/j.athoracsur.2016.10.020.
[9] T.J. Vander Salm, O.N. Okike, M.K. Pasque, A.T. Pezzella, R. Lew, V. Traina, R. Mathieu, Reduction of sternal infection by application of topical vancomycin, J Thorac Cardiovasc Surg, 98 (1989) 618-622,https://doi.org/10.1016/S0022-5223(19)34366-1.
[10] H.L. Lazar, H.L. Lander, Vancomycin paste and sternal wound infections, Ann Thorac Surg, 105 (2018) 335-336,https://doi.org/10.1016/j.athoracsur.2017.02.062.
[11] M. Servito, A. Khani-Hanjani, K.M. Smith, R.T. Tsuyuki, J.C. Mullen, Topical vancomycin and risk of sternal wound infections: a double-blind randomized controlled trial, Ann Thorac Surg, 114 (2022) 1555-1561,https://doi.org/10.1016/j.athoracsur.2021.11.012.
[12] A. Mandal, J.R. Clegg, A.C. Anselmo, S. Mitragotri, Hydrogels in the clinic, Bioeng Transl Med, 5 (2020) e10158,https://doi.org/10.1002/btm2.10158.
[13] R. Narayanaswamy, V.P. Torchilin, Hydrogels and their applications in targeted drug delivery, Molecules, 24 (2019) 603,https://doi.org/10.3390/molecules24030603.
[14] A.L. Lakes, R. Peyyala, J.L. Ebersole, D.A. Puleo, J.Z. Hilt, T.D. Dziubla, Synthesis and characterization of an antibacterial hydrogel containing covalently bound vancomycin, Biomacromolecules, 15 (2014) 3009-3018,https://doi.org/10.1021/bm5006323.
[15] J. Hoque, B. Bhattacharjee, R.G. Prakash, K. Paramanandham, J. Haldar, Dual function injectable hydrogel for controlled release of antibiotic and local antibacterial therapy, Biomacromolecules, 19 (2018) 267-278,https://doi.org/10.1021/acs.biomac.7b00979.
[16] L. Almany, D. Seliktar, Biosynthetic hydrogel scaffolds made from fibrinogen and polyethylene glycol for 3D cell cultures, Biomaterials, 26 (2005) 2467-2477,https://doi.org/10.1016/j.biomaterials.2004.06.047.
[17] D. Dikovsky, H. Bianco-Peled, D. Seliktar, The effect of structural alterations of PEG-fibrinogen hydrogel scaffolds on 3-D cellular morphology and cellular migration, Biomaterials, 27 (2006) 1496-1506,https://doi.org/10.1016/j.biomaterials.2005.09.038.

[18] I. Frisman, D. Seliktar, H. Bianco-Peled, Nanostructuring PEG-fibrinogen hydrogels to control cellular morphogenesis, Biomaterials, 32 (2011) 7839-7846,https://doi.org/10.1016/j.biomaterials.2011.06.078.
[19] B.A.G. de Melo, Y.A. Jodat, E.M. Cruz, J.C. Benincasa, S.R. Shin, M.A. Porcionatto, Strategies to use fibrinogen as bioink for 3D bioprinting fibrin-based soft and hard tissues, Acta Biomater, 117 (2020) 60-76,https://doi.org/10.1016/j.actbio.2020.09.024.
[20] M. Samberg, R. Stone, 2nd, S. Natesan, A. Kowalczewski, S. Becerra, N. Wrice, A. Cap, R. Christy, Platelet rich plasma hydrogels promote in vitro and in vivo angiogenic potential of adipose-derived stem cells, Acta Biomater, 87 (2019) 76-87,https://doi.org/10.1016/j.actbio.2019.01.039.
[21] C. Fuoco, M.L. Salvatori, A. Biondo, K. Shapira-Schweitzer, S. Santoleri, S. Antonini, S. Bernardini, F.S. Tedesco, S. Cannata, D. Seliktar, G. Cossu, C. Gargioli, Injectable polyethylene glycol-fibrinogen hydrogel adjuvant improves survival and differentiation of transplanted mesoangioblasts in acute and chronic skeletal-muscle degeneration, Skelet Muscle, 2 (2012) 24,https://doi.org/10.1186/2044-5040-2-24.
[22] C.T. Drinnan, G. Zhang, M.A. Alexander, A.S. Pulido, L.J. Suggs, Multimodal release of transforming growth factor-β1 and the BB isoform of platelet derived growth factor from PEGylated fibrin gels, J Control Release, 147 (2010) 180-186,https://doi.org/10.1016/j.jconrel.2010.03.026.
[23] C.A. Joseph, C.W. McCarthy, A.G. Tyo, K.R. Hubbard, H.C. Fisher, J.A. Altscheffel, W. He, R. Pinnaratip, Y. Liu, B.P. Lee, R.M. Rajachar, Development of an injectable nitric oxide releasing poly(ethylene) glycol-Fibrin adhesive hydrogel, ACS Biomater Sci Eng, 5 (2019) 959-969,https://doi.org/10.1021/acsbiomaterials.8b01331.
[24] D. Ben-David, S. Srouji, K. Shapira-Schweitzer, O. Kossover, E. Ivanir, G. Kuhn, R. Müller, D. Seliktar, E. Livne, Low dose BMP-2 treatment for bone repair using a PEGylated fibrinogen hydrogel matrix, Biomaterials, 34 (2013) 2902-2910,https://doi.org/10.1016/j.biomaterials.2013.01.035.
[25] Q. Lu, M. Pandya, A.J. Rufaihah, V. Rosa, H.J. Tong, D. Seliktar, W.S. Toh, Modulation of dental pulp stem cell odontogenesis in a tunable PEG-Fibrinogen hydrogel system, Stem Cells Int, 2015 (2015) 525367,https://doi.org/10.1155/2015/525367.
[26] J. Hadgraft, Calculations of drug release rates from controlled release devices, Int J Pharm, 2 (1979) 177-194,https://doi.org/10.1016/0378-5173(79)90019-X.
[27] E. Tsakalozou, A. Babiskin, L. Zhao, Physiologically-based pharmacokinetic modeling to support bioequivalence and approval of generic products: A case for diclofenac sodium topical gel, 1%, CPT: Pharmacomet Syst Pharmacol, 10 (2021) 399-411,https://doi.org/10.1002/psp4.12600.
[28] K. O'Donnell, A. Boyd, B.J. Meenan, Controlling fluid diffusion and release through mixed-molecular-weight poly(ethylene) glycol diacrylate (PEGDA) hydrogels, Materials, 12 (2019),https://doi.org/10.3390/ma12203381.
[29] D.V. Nguyen, F. Li, H. Li, B.S. Wong, C.Y. Low, X.Y. Liu, L. Kang, Drug permeation through skin is inversely correlated with carrier gel rigidity, Mol Pharm, 12 (2015) 444-452,https://doi.org/10.1021/mp500542a.
[30] Y. Yuan, C. Abeykoon, W. Mirihanage, A. Fernando, Y.-C. Kao, J.A.W. Harings, Prediction of temperature and crystal growth evolution during 3D printing of polymeric materials via extrusion, Mater Des, 196 (2020) 109121.,https://doi.org/10.1016/j.matdes.2020.109121.
[31] C. Emoto, T.N. Johnson, B.T. McPhail, A.A. Vinks, T. Fukuda, Using a vancomycin PBPK model in special populations to elucidate case-based clinical PK observations, CPT Pharmacometrics Syst Pharmacol, 7 (2018) 237-250,https://doi.org/10.1002/psp4.12279.
[32] A. Rainer, C. Spadaccio, P. Sedati, F. De Marco, S. Carotti, M. Lusini, G. Vadala, A. Di Martino, S. Morini, M. Chello, E. Covino, V. Denaro, M. Trombetta, Electrospun hydroxyapatite-functionalized PLLA scaffold: potential applications in sternal bone healing, Ann Biomed Eng, 39 (2011) 1882-1890,https://doi.org/10.1007/s10439-011-0289-2.
[33] T. Kamitani, H. Masumoto, H. Kotani, T. Ikeda, S.H. Hyon, R. Sakata, Prevention of retrosternal adhesion by novel biocompatible glue derived from food additives, J Thorac Cardiovasc Surg, 146 (2013) 1232-1238,https://doi.org/10.1016/j.jtcvs.2013.02.001.
[34] S. Miyamoto, K. Shimono, Molecular modeling to estimate the diffusion coefficients of drugs and other small molecules, Molecules, 25 (2020),https://doi.org/10.3390/molecules25225340.
[35] Q. Zhu, X. Gao, M.D. Brown, F. Eismont, W. Gu, Transport of vancomycin and cefepime into human intervertebral discs: quantitative analyses, Spine, 44 (2019) E992-E999,https://doi.org/10.1097/BRS.0000000000003028.
[36] J. Siepmann, N.A. Peppas, Higuchi equation: derivation, applications, use and misuse, Int J Pharm, 418 (2011) 6-12,https://doi.org/10.1016/j.ijpharm.2011.03.051.
[37] I. Firlar, M. Altunbek, C. McCarthy, M. Ramalingam, G. Camci-Unal, Functional hydrogels for treatment of chronic wounds, Gels, 8 (2022),https://doi.org/10.3390/gels8020127.

[38] H. Chen, Y. Cheng, J. Tian, P. Yang, X. Zhang, Y. Chen, Y. Hu, J. Wu, Dissolved oxygen from microalgae-gel patch promotes chronic wound healing in diabetes, Sci Adv, 6 (2020) eaba4311,https://doi.org/10.1126/sciadv.aba4311.
[39] J.D. Caplin, A.J. Garcia, Implantable antimicrobial biomaterials for local drug delivery in bone infection models, Acta Biomater, 93 (2019) 2-11,https://doi.org/10.1016/j.actbio.2019.01.015.
[40] G. Kalosakas, E. Panagopoulou, Lag time in diffusion-controlled release formulations containing a drug-free outer layer, Processes, 10 (2022),https://doi.org/10.3390/pr10122592.
[41] Z. Lv, T. Hu, Y. Bian, G. Wang, Z. Wu, H. Li, X. Liu, S. Yang, C. Tan, R. Liang, X. Weng, A MgFe-LDH nanosheet-incorporated smart thermo-responsive hydrogel with controllable growth factor releasing capability for bone regeneration, Adv Mater, 35 (2023) e2206545,https://doi.org/10.1002/adma.202206545.
[42] Y. Cong, S. Yang, X. Rao, Vancomycin resistant Staphylococcus aureus infections: A review of case updating and clinical features, J Adv Res, 21 (2020) 169-176,https://doi.org/10.1016/j.jare.2019.10.005.
[43] R.P.J. Willems, K. van Dijk, M. Vehreschild, L.M. Biehl, J.C.F. Ket, S. Remmelzwaal, C. Vandenbroucke-Grauls, Incidence of infection with multidrug-resistant Gram-negative bacteria and vancomycin-resistant enterococci in carriers: a systematic review and meta-regression analysis, Lancet Infect Dis, 23 (2023) 719-731,https://doi.org/10.1016/S1473-3099(22)00811-8.
[44] L. Yang, A.A. Yergeshov, Y. Al-Thaher, S. Avdokushina, E. Statsenko, T.I. Abdullin, P. Prokopovich, Nanocomposite orthopaedic bone cement combining long-acting dual antimicrobial drugs, Biomater Adv, 153 (2023) 213538,https://doi.org/10.1016/j.bioadv.2023.213538.
[45] P. Hota, C. Dass, C. Erkmen, A. Donuru, M. Kumaran, Poststernotomy complications: a multimodal review of normal and abnormal postoperative imaging findings, AJR Am J Roentgenol, 211 (2018) 1194-1205,https://doi.org/10.2214/AJR.18.19782.
[46] J.E. Losanoff, B.W. Richman, J.W. Jones, Disruption and infection of median sternotomy: a comprehensive review, Eur J Cardiothorac Surg, 21 (2002) 831-839,https://doi.org/10.1016/s1010-7940(02)00124-0.
[47] C. Heilmann, R. Stahl, C. Schneider, T. Sukhodolya, M. Siepe, M. Olschewski, F. Beyersdorf, Wound complications after median sternotomy: a single-centre study, Interact Cardiovasc Thorac Surg, 16 (2013) 643-648,https://doi.org/10.1093/icvts/ivs554.
[48] T. Wellisz, J.K. Armstrong, J. Cambridge, Y.H. An, X. Wen, C.M. Hill, T.C. Fisher, The effects of a soluble polymer and bone wax on sternal healing in an animal model, Ann Thorac Surg, 85 (2008) 1776-1780,https://doi.org/10.1016/j.athoracsur.2007.11.042.
[49] M. Shibata, G. Takagi, M. Kudo, J. Kurita, Y. Kawamoto, Y. Miyagi, M. Kanazashi, T. Sakatani, Z. Naito, Y. Tabata, M. Miyamoto, T. Nitta, Enhanced sternal healing through platelet-rich plasma and biodegradable gelatin hydrogel, Tissue Eng Part A, 24 (2018) 1406-1412,https://doi.org/10.1089/ten.TEA.2017.0505.
[50] Y. Yuan, Y. Han, C.W. Yap, J.S. Kochhar, H. Li, X. Xiang, L. Kang, Prediction of drug permeation through microneedled skin by machine learning, Bioeng Transl Med, (2023) e10512.,https://doi.org/10.1002/btm2.10512.
[51] Bootle-Wilbraham CA, Tazzyman S, Thompson WD, Stirk CM, Lewis CE, Fibrin fragment E stimulates the proliferation, migration and differentiation of human microvascular endothelial cells in vitro, Angiogenesis 4 (2001) 269–275,https://doi.org/10.1023/a:1016076121918.

Supplementary Information

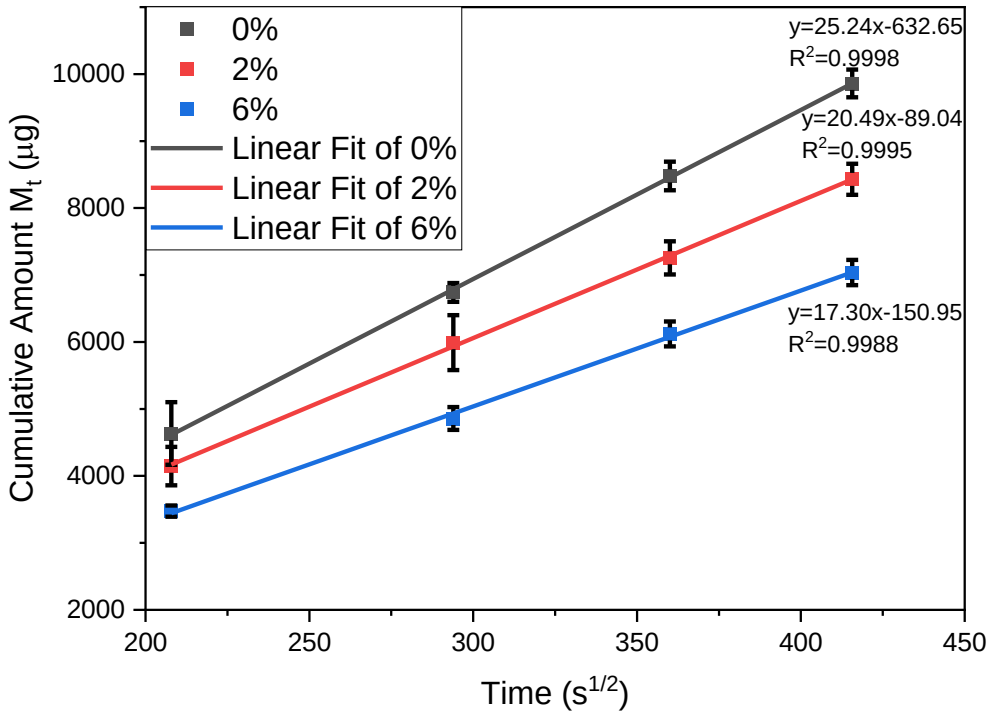
An Alternative Method to Calculate the Diffusion Coefficients in Burst Release

To verify the calculation of the diffusion coefficient as described in the main text, an alternative method has been used to calculate the values of D with the least-square method. According to Eq. (20) in Hadgraft's paper, the time-dependent M_t is proportional to $t^{1/2}$:

$$M_t = 2M_\infty(\tau/\pi)^{1/2}, \tau = \frac{Dt}{l^2}$$

$$M_t = 2M_\infty(\frac{D}{l^2 \cdot \pi})^{1/2} \cdot t^{1/2}$$

Therefore, the experimental data was plotted with $t^{1/2}$ to acquire the slope value (k), as shown in the graph below:



The slope of fitted lines between M_t with $t^{1/2}$ are 25.24, 20.49 and 17.30 for 0%, 2% and 6% PEGDA hydrogel, respectively. So, the diffusion coefficient could be calculated by:

$$D = \left(\frac{kl}{2M_\infty}\right)^2 \cdot \pi$$

With this method, the D values were found to be 0.56×10^{-10}, 0.37×10^{-10}, and $0.26\times10^{-10}\,m^2/s$ for 0%, 2% and 6% PEGDA hydrogels. The D values are very close to those obtained from the method described in the main text, i.e., 0.47×10^{-10}, 0.36×10^{-10}, and 0.25×10^{-10}.

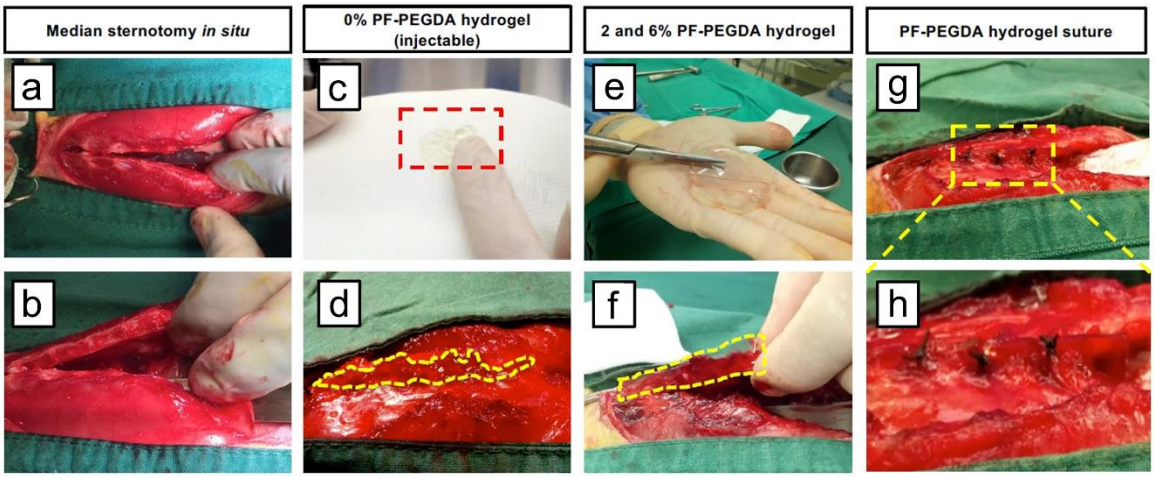


Figure S1. Representative images of PF-PEGDA hydrogel application in median sternotomy in a rabbit model – a pilot study. a), b) Median sternotomy in situ. c) Demonstration of the spreadability of the injectable 0% PF-PEGDA hydrogel d) Application of 0% PF-PEGDA hydrogel in median sternotomy. e) Demonstration of material (2 and 6% PF-PEGDA hydrogel) preparation before application. f) Application of 2 and 6% PF-PEGDA hydrogel in median sternotomy. g), h) PF-PEGDA hydrogel sternal vertebrae suture.

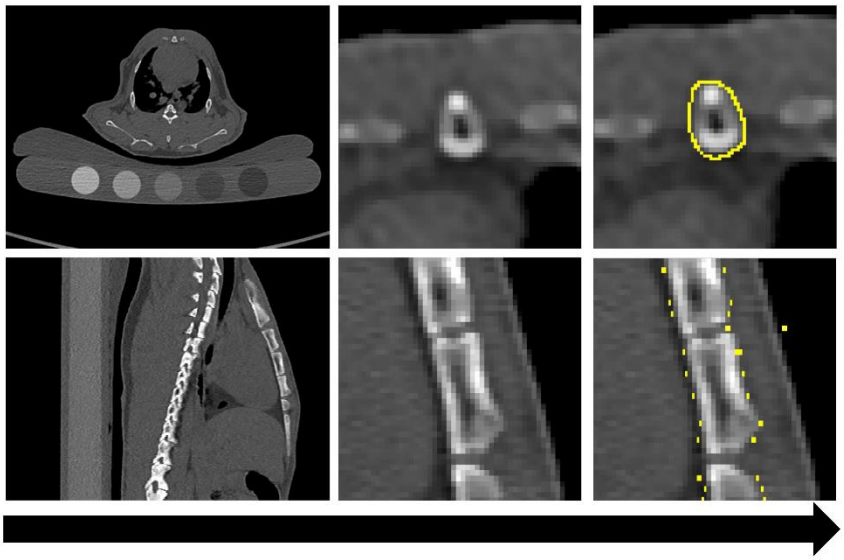


Figure S2. Representative computed tomography images of bone density quantification. The arrow represents the workflow. Yellow lines and dots represent the transversal sectioning in two perpendicular planes and the area of bone densitometric assessment.

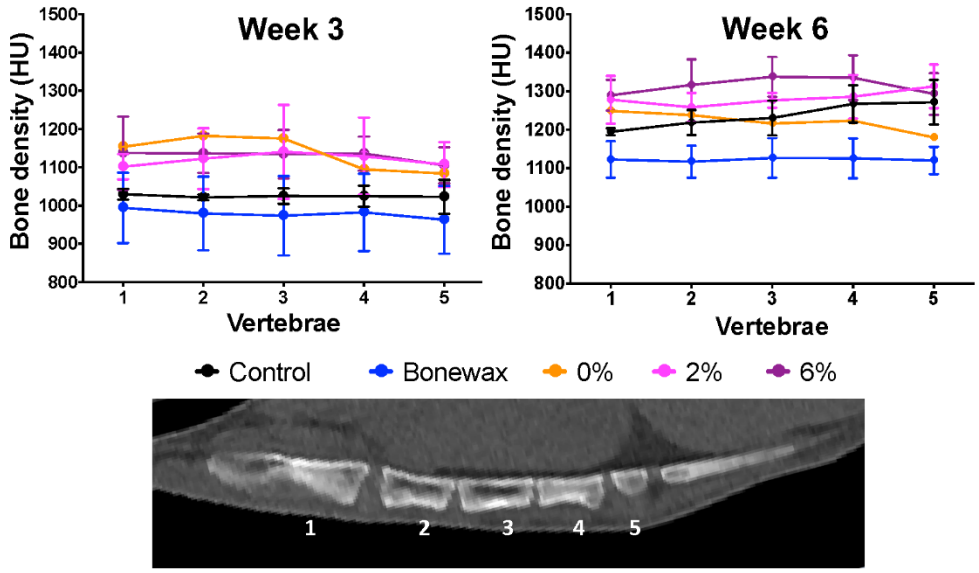


Figure S3. No observable trend in healing between individual vertebrae and treatment shown by bone densitometry. Computed tomography (CT) images quantification of sternal bone of non-treated animals (Control), animals treated with bone wax (Bonewax) and PF-PEGDA (0%, 2% and 6% PEGDA concentration) evaluated at Week 3 and Week 6 post sternotomy. Multiple images per sternal vertebrae were assessed and plotted for individual vertebrae.

Chapter 4 Manufacture Hydrogel Microwells Using Optical 3D Printers for Human Spheroids Culture in Vitro

Abstract

Microwell array has proven to be an effective tool for generating uniform and scalable spheroids, making them invaluable for high throughput drug screening. However, conventional microwells, often fabricated from polydimethylsiloxane (PDMS), face limitations in transporting small molecule, thereby restricting the nutrition supply to the bottom of the spheroids. To address these limitations, a 3D printed polyethylene glycol diacrylate (PEGDA) hydrogel-based microwell device is proposed that enhances small molecule permeability. The PEGDA hydrogel microwell device provides a high flux of nutrition mimicking an in vivo vascular supply. This enhanced nutrition supply plays a vital role in creating a conducive environment for the generation of viable and functional spheroids. Consequently, the generated spheroids benefit from a replication of in vivo conditions, exhibiting reduced cell apoptosis and necrosis. Besides, the mechanical properties of 3D-printed PEGDA hydrogel are adjustable, allowing cells to inhabit an environment that more accurately represents physiological conditions and diverse tissue environments. A 2D simulation model has been proposed to simulate the diffusion and consumption of small molecules within the microwell system. This model enables the aiding in the optimization of the 3D-printed microwell structure and guiding the addition of chemicals, growth factors, and peptides at appropriate times. Overall, the cells cultured in 3D printed PEGDA hydrogel microwell present a promising model to observe single cell, early stage spheroids and organs development. Besides, it is also well-suited for high-throughput drug screening. The combination of small molecule permeability, enhanced nutrition supply, and adjustable mechanical properties positions the 3D printed PEGDA hydrogel microwell as a cutting-edge tool for advancing research in cellular biology and drug development.

Keywords: Microwell, Biomaterials, 3D printing, Simulation

4.1 Introduction

Microwell chip consists of hundred small wells, typically ranging from tens to hundreds of micrometres in diameter. This microwell platform provides simple, inexpensive, and applicable in standard biological laboratories. Microwell enables the generation of high throughput, homogenous, and easily retrievable spheroid, which provides in situ analysis alongside swift and direct sample retrieval [1-3]. The integration of cell culturing within microwells emerges in the spatiotemporal monitoring of cell dynamics, which is challenging to achieve with other methods [4, 5]. Microwell has been widely applied in biomedical research, including single cell analysis [6-8], cell interaction studies [9], tissue regenerations [10], cancer therapy [11], and drug screening [12-14]. Most microwells were fabricated with PDMS via photolithography or moulding methods, which lack design flexibility and cost efficiency [15]. Functionalizing the microwell structure typically requires multiple steps. For instance, Kim et al. proposed a 3 steps methods to fabricate a sigma shape microwell with a roof to avoid cell loss and external interference [16]. Udomluck et al. used pin array mould to fabricate a goblet shaped microwell that enhance the supply of biochemical molecules. This microwell contained hydrogel between the bottom liquid and cells enabling the culture of spheroids in two different media [17]. Similarly, multimedia culturing can be achieved by adding a semi-permeable membrane at the bottom of the microwell [18]. To enhance nutrition supply, a step motor controlled rocking system was applied in spheroids culture within microwell [19]. Besides, it is important to consider the volume and aspect ratio when designing the morphology of microwell to prevent hindered diffusion, which would otherwise deplete nutrients or enzymatic substrates [20]. Despite these advancements, the current functional microwell system grapples with limitations due to the complex and time consuming geometry fabrications. Addressing these challenges is essential for developing more efficient and effective microwell platforms for biomedical research.

The advent of 3D bioprinting bears immense potential. 3D bioprinting permits the mixture of distinct inks and cell types and building up heterogeneous structures for comprehension of disease biology [21-23]. Using 3D bioprinting could achieve the manufacturing of the optimized microwell structure, enhancing cell metabolism and the transfer of nutrients and enzymes, which is not possible or not economical via conventional manufacturing processes [24]. This optimization can be validated through fluid dynamics analysis. Besides, the mechanical properties of 3D printed hydrogel are highly customizable [25]. The adjustable

mechanical properties of microwells offer a unique opportunity to replicate an in vivo environment for cells. This ability to fine-tune the mechanical characteristics of microwells allows for the creation of conditions that closely mimic the complexities and nuances of the cellular microenvironment in living organisms. By manipulating factors such as stiffness, elasticity, and rigidity, a more accurate representation of the physiological surroundings can be engineered, providing cells with conditions that closely resemble those they experience within tissues. The reliable 3D printed microwell addresses challenges such as low multiplexing feasibility, reactant recovery, and inability to perform multistep assays. The transition between different well plate formats (e.g., 24/96-well plates) becomes seamless, exhibiting the flexibility of this approach. Moreover, the application of pharmacokinetics and pharmacodynamics models has revolutionized new drug development and administration of personalized medicine. 3D printed microwell based model holds promise for acquiring crucial metabolism data of tissues tumours, which are typically viewed as bulk compartments with time-varying concentrations of drug response [26]. Moreover, to date, the time dependent evolution of small molecule in the microwell have not been thoroughly investigated, which hinder the optimization of the microwell structure design, metabolism, and quality of cells cultured in the microwell. Addressing this gap is essential for maximizing the potential of 3D-printed microwells in biomedical research and drug development.

In this study, we propose using PEGDA based bioink to 3D print a muti-microwell chip for culturing cancer spheroids. By varying the concentrations of PEGDA, the mechanical properties and rheological properties of the microwell could be tailored to replicate the in vivo environment for cells. With the capabilities of 3D printing, versatile structure can be designed and manufactured in a single step. Combining this with computational fluid dynamics (CFD) methods, we have built a two-dimensional model to simulate the time-dependent small molecule evolution in the microwell culturing system. Our proposed microwell fabrication and simulation methodology is intended to serve as a useful tool for designing, analysing, optimizing, and generating spheroids, which can be further applied in developing diseases model and conducting drug screening.

4.2 Methods

4.2.1 Materials

All materials used in this manuscript were purchased from Sigma-Aldrich except the specified otherwise.

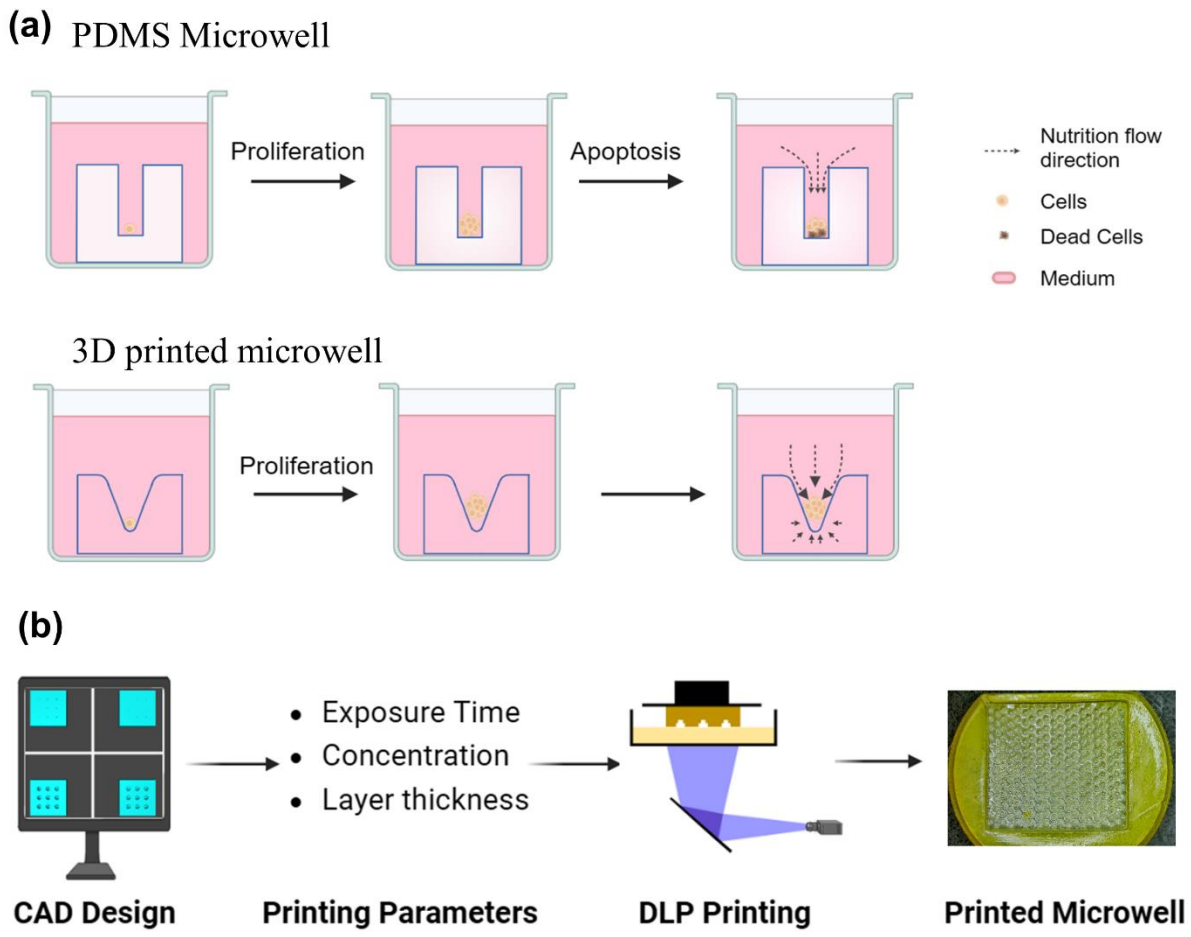


Fig. 1 a) Schematic illustrating the difference of cell culture in PDMS microwell and printed enhanced microwell. b) The schematic of the process to print microwell.

4.2.2 Characterizations

Scanning electron microscopy (SEM) was performed using a benchtop scanning electron microscope (JCM-7000 NeoScope Tabletop SEM, JEOL Ltd., Japan). Optical and fluorescent images were taken using an inverted microscope with imaging software (Olympus CKX53, Olympus Co., Japan) and 3D fluorescent microscope images were scanned using a THUNDER imaging systems (Leica Microsystems Pty Ltd, Australia). OriginPro 2022 software was used for data plotting. ImageJ was used to analyse and modify pictures.

4.2.3 Physical Properties of Hydrogel

The 4 × 4 × 1 - mm^3 rectangular shape samples were printed for water uptake ability measurement. All printed samples were completely dried to remove the water before experiments. Then, samples were hydrated for 0.25, 0.5, 1, and 2 h in 1 × PBS (pH = 7.4) at 37 °C. The ratio of water uptake from dried printed samples can be calculated as the following equation:

$$Q = \frac{W_i - W_0}{W_0} \times 100\%$$

Where, Q is the ratio of PBS uptake in the hydrogel, W_i is the weight of the hydrogel at the ith time, and W_0 is the dried weight of the hydrogel.

The expansion rate from the dried sample by water was calculated by measuring the length of the X and Y axes based on the dried status of the microwell. The rate of expansion from the dried sample can be calculated by the following equation:

$$R = \frac{L_i - L_0}{L_0} \times 100\%$$

Where, R is the expansion rate of a microwell in PBS, L_i is the length of hydrogel at the ith time, and L_0 is the dried status length of the hydrogel.

The compressive stress-strain measurements were performed on water-filled hydrogel using a tensile-compressive tester (DMA 2980, TA Instruments, USA). The cylindrical hydrogels were 3D printed via the DLP printer. The printing parameters were set as: printing thickness, 50 μm; the number of base layers, 1; bottom exposure time, 8 s, and normal exposure time, 3 s. The dimensions of samples were prepared in 8 mm diameter and 2 mm thickness with different concentrations: 20%, 30%, 40% and 50%. The samples were set on the lower plate and compressed by the upper plate at room temperature in air, which was connected to a loading and distance detector. The loading stress rate was set at 1 N/min and the maximum applied force was set as 10 N. The output stress results did not include the effects of dynamic change in the radius of samples. Therefore, the acquired stress should be modified with the dynamic change of the cross-section area:

$$\sigma_i = \frac{F}{\pi R_i^2}$$

Where, σ_i, R_i and T_i are the applied stress on the hydrogel, radius, and thickness of the hydrogel at ith time, respectively. F is applied force at the axial direction. Then, the modified stress and strain could be used to draw the curve. The compression modulus (E) of the sample could be calculated via the linear part of the stress-strain ($\triangle\sigma - \triangle\varepsilon$) curve:

$$E = \frac{\triangle\sigma}{\triangle\varepsilon}$$

Poisson's ratio (υ) can be calculated by the ratio of horizontal strain ($d\varepsilon_{trans}$) to vertical strain ($d\varepsilon_{axial}$):

$$\upsilon = -\frac{d\varepsilon_{trans}}{d\varepsilon_{axial}}$$

4.2.4 Rheological Properties

The rheological properties of samples were measured at room temperature and 37 °C using an Anton Paar MCR 301 and 702e rheometer (Anton Paar, Zofingen, Switzerland). Peltier element and a thermostatic hood for temperature control were equipped in the rheometer. For the UV gelation test, varied PEGDA content with Lithium phenyl-2,4,6-trimethylbenzoylphosphinate (LAP) (0.25% w/v) and tartrazine (0.25 μg/mL) was measured under time sweep mode with frequency 1 Hz, strain 0.001 to measure storage modulus (G') and loss modulus (G''). The PEGDA ink was sandwiched between two plates with a 0.5 mm gap. The lower plate was fixed and assembled with a UV system. The upper plate (20 mm plane plate) was connected to the measuring system. The UV light was turned on at 30 s to start forming the hydrogel, and the UV intensity was applied at 5 mW/cm^2. The measurement lasted for 500 s recording per data point every seconds. For the non-UV time sweep test, the measurements were performed utilizing a sandblasted-type geometry (CP50-1, 50 mm in diameter, 1-degree angle) with a humidified atmosphere in the measuring chamber. The formulation of PEGDA inks were prepared same as above. Angular frequency was set constant as 6.28 rad s^{-1} and strain was set as 1% all the time. The measurement lasted for 2 hours recording per data point every 10s. For the amplitude sweep and frequency sweep tests, the measurements were performed utilizing a sandblasted-type geometry (PP25 s^{-1}, 25 mm in diameter) with a humidified atmosphere with controlled temperature in the measuring chamber. Disc-shaped specimens with 25 mm in diameter and 1.2 mm thickness were 3D printed for rheological analysis. The materials' storage modulus (G') and loss modulus (G'') were measured in oscillatory mode at 37 ºC. In the amplitude sweep measurement, the

frequency was set as constant at 10 rad s^{-1} while strain values varied from 0.01 to 100%. In the case of the frequency sweep measurement, the hydrogel materials were tested from 0.1 to 100 rad s^{-1} frequency range by keeping the shear strain constant at 0.3%.

4.2.5 DLP 3D Printing Microwell

To produce the best-quality 3D printed microwell and reduce the waste of bioinks. A high-quality DLP printer of laboratory scale was designed and assembled. UV Digital Micro-mirror Device with a resolution of 40 μm (4,096 x 2,560 pixels; Hongkong Anycubic Technology Co., China) 405 nm UV-LED with average 30,735 lux light intensity. The build area is I.D. × H 60 mm × 180 mm with an adjustable layer thickness ranging from 25 to 200 mm. PEGDA (Mn = 575) was dissolved in water at various concentrations of 20-50% v/v and the photoinitiator was added and mixed until fully dissolved. LAP was used in experiments and the concentration was set as 0.25% w/v. Tartrazine was used as the photoinhibitor and the concentration was set as 0.25 μg/mL.

Specimens were designed by Solidworks2022 (Dassault Systèmes SolidWorks Co., Waltham, USA) and were saved as a Stereolithography (STL) file. Then, the STL files were inserted into the slicing software Anycubic Photon Workshop (Hongkong Anycubic Technology Co., China) to slice in the vertical direction. Finally, the sliced models were saved as 3D printer readable files and input into the DLP printer to create the designed 3D models. Printing parameters were used as follows: printing thickness, 50μm; the number of base layers, 1; bottom exposure time, 10 s, 8 s, and 6 s and normal exposure time, 3.5 s, 3 s, and 2.5 s for controlled long (L), medium (M), and short (S) exposure experiments, respectively. After printing, the printed specimens were placed in deionized water and stored at 4 ^{o}C. The printed microwell for in vitro cell culture studies were sterilized with 80% ethanol before application.

4.2.6 The Actual Resolution and Accuracy of 3D Printed Microwell

To check the actual resolution and similarity of printed microwell, the designed microwell had been fabricated via different exposure time. The actual microwell size was pictured under the microscope (Zongyuanweiye Tech Co., Shenzheng, China). Then, the images were input into ImageJ to measure and calculate the diameters of the printed microwell in pixels:

$$D_{actual} = \frac{D_{pixel}}{L_{pixel}} \cdot L_{actual}$$

Where, D_{scale} was the actual diameter of the printed microwell, L_{actual} was the actual length of the scale bar. D_{pixel} was the measured diameter of printed microwell in pixel, and L_{pixel} was the measured length of the scale bar in pixel.

4.2.7 High Performance Liquid Chromatography (HPLC)

To measure the residual LAP and tartrazine in the 3D printed microwell, HPLC (Shimadzu Scientific Instruments (Oceania) Pty Ltd, New Zealand) was used to detect the concentration of the analyte with an autosampler, a binary solvent pump. The separation was achieved by employing an Agilent™ Eclipse Plus C18 (3.5 μm particle size, I.D. × L 2.1 mm × 100 mm). The mobile phase consisted of a 0.1 M Phosphate Buffer (PH = 6.8) (solvent A) and pure Acetonitrile (solvent B). The flow rate was set at 1.0 mL/min, and the injection volume was 10 μL. The column temperature was set as room temperature. The wavelength for the fluorescence detector was set as 365 nm and 430 nm for LAP and tartrazine, respectively.

Different concentrations of LAP and tartrazine solutions (10 μg/mL, 4 μg/mL, 2.5 μg/mL, 0.8 μg/mL, 0.5 μg/mL and 0.1 μg/mL) were prepared to draw the standard calibration curve. Afterwards, the printed microwells were dialysed in a 50 mL centrifuge tube. The samples were collected by taking out 1 mL of dialysed solution each time on days 1, 3, and 7 and replenishing with the same amount of pure water. The amount of LAP and tartrazine was detected by the HPLC with the mentioned parameters.

4.2.8 Stability of 3D Printed Microwell

The 3D printed microwells were washed with deionized water and then placed in the PBS solution (pH = 7.4) at 37 ^{o}C. The samples were taken out and observed on days 1, 3, and 7 under microscopy to figure out the stability.

4.2.9 Simulation of Small Molecule Dynamic Flow Through the Microwell

A general two-dimensional finite element model was proposed to calculate the dynamic flow profile of small molecule in the microwell. Two domains were considered in the proposed model: a centre cross-section designed microwell and a surrounding cylinder (14 mm × 10 mm), representing the culture medium in a well of 24 microwell plates. To imitate the

experimental set up, the top edge of the culture medium domains was set as an open environment, where the culture medium could free flow in this surface. All other edges of the culture medium domain were set as fixed boundary conditions, and there was no flux of the culture medium or small molecule implemented due to the solution could not permeate through the plastic well plate. The molecular weight of small molecule we choose is 480 Da in the proposed test, which can represent small to moderately sized organic molecules, such as drugs, metabolites, or small peptides, studying the diffusion properties of therapeutic agents within 3D spheroids or artificial tissues. The small molecule was released at the left of the microwell to imitate the pipetting of small molecule into the well plate process. In the microwell domain, the microwell was seen as the porosity structure, which allowed small molecule and culture median to penetrate it. All the edges of the microwell domain allowed the median solution flow in and out. At the bottom of each well, a circle area was set to represent the cell. These circle cells will constantly consume the small molecule with time during the simulation process. These cells won't have proliferation or morphology change during the simulation. The transient concentration of small molecule in each domain was solved by the Navier–Stokes equation combined with Fick's second law:

$$\rho\frac{\partial \mathbf{u}}{\partial t}+\rho(\mathbf{u}\cdot\nabla)\mathbf{u}=\nabla\cdot[-\mathbf{P}+\mathbf{T}]+\rho\mathbf{g} \tag{1}$$

$$\rho\nabla\mathbf{u}=0 \tag{2}$$

$$\frac{\partial c_i}{\partial t}+\nabla\cdot\mathbf{J}_i+\mathbf{u}\cdot\nabla c_i=R_i \tag{3}$$

$$\mathbf{J}_i=-D_i\nabla c_i \tag{4}$$

where, ρ is the density of the medium, $\mathbf{u}$ is the liquid velocity, $\mathbf{P}$ is the pressure inside the liquid, $\mathbf{T}$ is the viscous stress tensor, $\mathbf{g}$ is the gravity acceleration, c is the concentration, $\mathbf{J}$ is the flux, R is the external source, and D is the diffusion coefficient of small molecules. For the small molecule transporting in porous structures, the Eq. (3) and (4) will be modified into Eq. (5) and (6):

$$\frac{\partial(\varepsilon_p c_i)}{\partial t}+\frac{\partial(\rho c_{P,j})}{\partial t}+\nabla\cdot\mathbf{J}_i+\mathbf{u}\cdot\nabla c_i=R_i+S_i \tag{5}$$

$$\mathbf{J}_i=-(D_j+D_{e,j})\nabla c_i \tag{6}$$

$$D_{e,j}=\frac{\varepsilon_p}{\tau_{F,j}}D_{F,j},\ \tau_{F,j}=\varepsilon_p^{-1/3} \tag{7}$$

where, ε_p is the porosity ratio, S is the external source in porosity structure, D_F is the liquid diffusion coefficient in the porosity structure. A time-dependent study simulated over 10ks was performed with a time step of 10s.

The model was solved in COMSOL Multiphysics. For the calculations, a general size of mesh was applied in the COMSOL program with the following settings: maximum element size of 500 μm, minimum element size of 1 μm, curvature factor of 0.3, resolution of narrow domains of 1, and maximum growth rate of 1.13. All results were independent of the mesh.

4.2.10 Cell Culture

Human glioblastoma cell line (U87MG) was cultured in Minimum Essential Medium (MEM) and the mouse melanoma cell line (B16F10) was cultured in Dulbecco's Modified Eagle Medium (DMEM) supplemented with 10% fetal bovine serum (FBS) and 1% penicillin/streptomycin. Cells were incubated at 37 °C in a humidified 5% CO_2 atmosphere and passaged every 3 days.

To seed cells in the microwell, cells were cultured in 6 well plates at passage 3 before transferring the cell to the printed microwell. The stored microwell was placed in 80% ethanol for 24 hours to sterilise. Then, the sterilised microwell will be washed with sterilised PBS 3 times for 15 mins and then immersed it into the complete medium for 10 mins. 1.2×10^7/mL cells were prepared in the complete medium and 100 μL well-mixed medium with cells were added into the microwell. The cell-seeded microwell was placed in a 12 well plate and incubated at 37 °C in a humidified 5% CO_2 atmosphere for 1 day. After that, 1 mL complete medium were added and change the half medium every 3 days.

4.2.11 Live/dead assay

The 3D printed microwell with spheroids were washed with PBS 3 times. The 100 μL 2.5 μg/mL calcium acetoxymethyl ester (Calcein-AM) and 2.5 μg/mL propidium iodide (PI) were added into the microwell incubating at 37 °C for 40 mins. Then, using sterilised PBS washed samples 3 times for 5 mins and placed under inversed fluorescent microscope to observe.

4.2.12 Scanning Electron Microscopy (SEM)

Surface patterns of the printed microwell and cross-section of the vertical cut area were imaged with a SEM. The printed microwell was rinsed with deionised water for 3 times for 15 mins and then frozen it in the -80 ^{o}C fridge for 24 hours. The frozen microwell was transferred to the freeze drier for 24 hours to acquire lyophilised microwell. A scalpel was used to vertically cut the middle of the microwell to show the cross-section area. The freeze-dried microwell was coated with gold by a sputter coater prior to SEM imaging.

4.2.13 Data Analysis

All results were presented as mean ± standard deviation ($n \geq 3$). The data normal distribution was checked by using the Shapiro-Wilk test. Statistical analysis for normal distribution data was determined by the one-way ANOVA test with Tukey's post-hoc analysis and for non-distribution data was determined by the Kruskal-Wallis ANOVA test with Tukey's post-hoc analysis using Origin Pro 2022. Statistically significant P values are indicated in the figures and/or legends as ****$P < 0.0001$; ***$P < 0.001$; **$P < 0.01$; *$P < 0.05$. N.S. represents no significant difference. Linear fitting was performed via Origin Pro 2022.

4.3 Results

4.3.1 Physical Properties of PEGDA Hydrogel

PEGDA hydrogel for physical testing was fabricated by the DLP printer. The hydrogel composition included photoinitiator (0.25% LAP) and photoinhibitor (0.25 μg/mL tartrazine). The UV light intensity was set at 30,735 lux for 3 seconds, which was sufficient to solidify each printed layer. The swelling properties of the printed microwell are shown in **Fig. 2**a. The weights of the specimens increased with the hydration time, reaching a constant weight after approximately 1 hour. PEGDA hydrogel demonstrated a water uptake ratio that varied with its concentration: 4 times greater with 20% PEGDA hydrogel, 2.6 times greater with 30% PEGDA hydrogel, 2.1 times greater with 40% PEGDA hydrogel and 1.3 times greater with 50% PEGDA hydrogel compared to its dry weight. Additionally, the expansion measurements of the microwells in PBS indicated size increases of 28.66 ± 0.05%, 44.5 ± 0.01%, 52.90 ± 0.02%, and 71.27 ± 0.01% for 50%, 40%, 30% and 20% PEGDA microwell, respectively (**Fig. 2**b).

The mechanical properties of PEGDA hydrogel were evaluated through compression testing. The stress-strain curves were analysed to determine the compression modulus of the PEGDA hydrogel (**Fig. 2**c). Results showed that the compressive modulus increased with higher PEGDA concentrations. Specifically, every 10% increment in PEGDA concentration resulted in a 1.9-fold increase in the compressive modulus (**Fig. 2**d). Poisson's ratio in the vertical direction increased with the strain, regardless of the PEGDA concentration, and the values were slightly larger than 0.5. This value indicated that when the specimens were under pressure, the volume of the printed hydrogels increased (**Fig. 2**e). The average Poisson's ratio under a 10 N force decreased with increasing PEGDA concentrations (**Fig. 2**f).

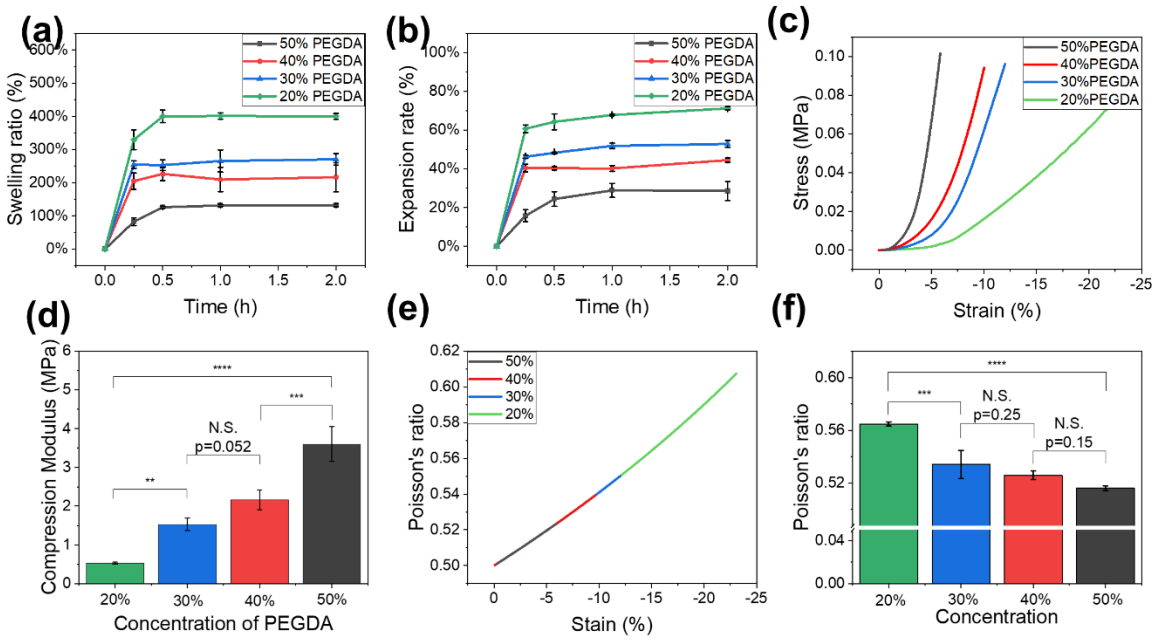


Fig. 2 Characteristics of printed different concentrations PEGDA hydrogel ranging from 20-50%: **Swelling properties**. **a)** water taken rate; **b)** Expansion rate; **Mechanical properties**. **c)** stress – strain curve in compression test; **d)** Compression modulus; **e)** Poisson's ratio varied with strain; **f)** Averaged Poisson's ratio under 10 N force. Data are presented as mean ± s.d. The black line/dot (/bar), red line/dot (/bar), blue line/dot (/bar), and green line/dot (/bar) indicate 50%, 40%, 30% and 20% of PEGDA hydrogel, respectively. (n = 3)

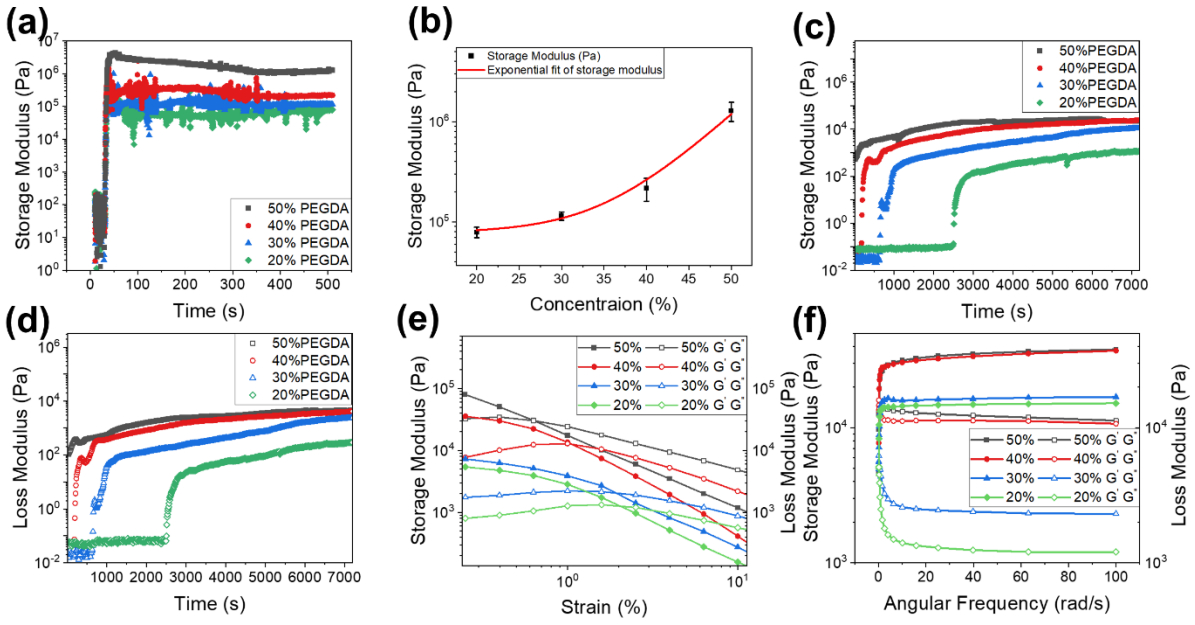


Fig. 3 Rheological properties of different concentrations PEGDA inks/printed hydrogel ranging from 20-50%: **a)** Photorheological storage modulus; **b)** The relationship between photorheological storage modulus and PEGDA concentrations; **c)** Storage modulus under time sweep; **d)** Loss modulus under time sweep; **e)** Amplitude sweep at 37 ^{o}C; and **f)** Frequency sweep of storage and loss modulus. Data are presented as mean ± s.d. The black line/dot (/bar), red line/dot (/bar), blue line/dot (/bar), and green line/dot (/bar) indicate 50%, 40%, 30% and 20% of PEGDA hydrogel, respectively. (n=3)

4.3.2 Rheological Properties of PEGDA Hydrogel

Rheological characterization of PEGDA bioinks was conducted using oscillatory rheological measurements to assess the curing process and rheological properties under various conditions. In photorheological time sweep, storage modulus (G') and loss modulus (G'') of PEGDA hydrogels with varying concentrations under constant photoinitiator and photoinhibitor conditions were exhibited in **Fig. 3**a and **Fig. S1a.** Both G' and G'' increased with PEGDA concentration. Notably, G' exhibited an exponential relationship with PEGDA concentration between 20% to 50%, 20% to 50%, which is $y = 145.05 * \exp(x / 5.59) + 77538.04$ with $R^2 = 0.9547$. In time sweep tests, the gelation onset time increased from 10s to 170s, 650s, and 2430s as PEGDA concentration decreased from 50% to 40%, 30%, and 20%, respectively (**Fig. 3**c and d). After gelation onset, both G' and G'' increased gradually until reaching the maximum measuring time, indicating increased stiffness with higher PEGDA concentrations. In the amplitude sweep tests, the strain varied from 0.01% to 100%, with a constant angular frequency of 10 rad/s. The cross point of G' and G'' indicated the transition between elastic and plastic deformation ranges of the printed PEGDA disks under different strains (**Fig. S1**b). PEGDA hydrogels exhibited elastic deformation below 1% strain, while irreversible, plastic deformation occurred above 1% strain. Up to 0.3% strain, PEGDA hydrogels of various concentrations showed linear viscoelastic and then G' started to decrease due to the large deformation (**Fig. S1**c). G'' initially increased with strain until reaching a peak value, after which it decreased, and the area under G'' decreased with the concentration (**Fig. S1**d). The cross point of G' and G'' increased with decreasing PEGDA concentration, indicating a greater elastic range at lower concentrations (**Fig. 3**e). Temperature and frequency sweep tests further characterized the viscoelastic behaviour of PEGDA hydrogels. The cross point of G' and G'' under amplitude sweep shifted to higher strains with increasing temperature, indicating increased resistance to deformation (**Fig. 3**e and **Fig. S1**e). In the sweep frequency test, G' remained consistently higher than G'' across all frequencies and PEGDA concentrations, indicating that the printed PEGDA hydrogels behaved predominantly as elastomeric materials with stable viscoelastic properties (**Fig. 3**f).

4.3.3 Morphology of the 3D Printed Microwell

A variety of microwell has been designed and 3D printed, allowing for customization of area, density, shape, and thickness within a single microwell chip (**Fig. S2**a - c). To minimize edge light scattering that could affect printing accuracy, a hole structure was incorporated into the

design and printed using consistent printing settings. Layer-by-layer analysis revealed minimal impact of edge light scattering on the circular shape within the first 4 layers. However, photopolymerization affecting the inner printed hole began noticeably at the 8th layer, altering the intended structure with further printing. Therefore, a maximum depth of 8 printing layers, equivalent to 400 μm, was identified to achieve high fidelity while minimizing edge light scattering effects. (**Fig. S3**). Optimal depth for microwells was crucial to accommodate formed spheroids without compromising fidelity. Thus, a depth of 250 μm was finalized in the design to strike a balance between fidelity and functionality.

To enhance cell culture operations within the microwells, a curved cone structure was designed, optimized, and printed (**Fig. 4**a and b). This structure featured a top opening diameter of 400 μm tapering down to 100 μm at the bottom, facilitating easy movement of cells to the well's base. The smooth curve linking the edge and microwell enabled efficient cell placement. Each printed microwell sheet contained a density of 260 microwells (20 × 13) per chip, optimizing the use of space for high-throughput applications.

The accuracy of the 3D printed microwells was assessed by measuring the actual sizes under a microscope and analysing images using ImageJ software. Microwells with designed diameters of 100 μm and 400 μm were printed using different light exposure times: Long (L), Medium (M), and Short (S). Due to inconsistencies in short exposure condition, measurements included only medium and long exposure conditions. Results indicated diameters of 72.19 ± 7.11 μm (designed 100 μm L), 98.56 ± 9.52 μm (designed 100 μm M), 363.37 ± 13.11 μm (designed 400 μm L), and 426.64 ± 18.01 μm (designed 400 μm M) (**Fig. 4**c). Prolonged light exposure strengthened microwells but also narrowed them due to over-exposure and light scattering at the edges. Consequently, medium light exposure parameters were chosen for subsequent experiments due to their superior fidelity.

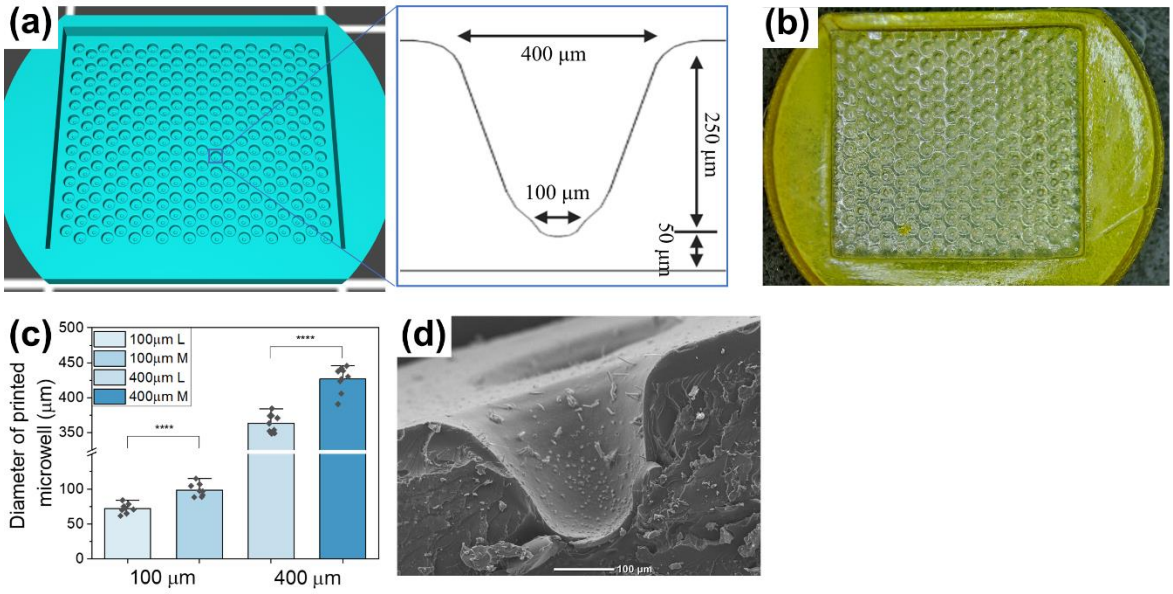


Fig. 4 a) The designed microwell. The diameter of the outer well is 400 µm and the diameter of the inner well is 100 µm; **b)** The picture of 3D printed microwell under microscope; **c)** The diameter of printed microwell with different design and printing parameters (n = 8); **d)** The cut cross section of the printed microwell under SEM. Data are presented as mean ± s.d.

Fig. 4d showed the cross-sectional morphology of printed microwell chips via SEM. To investigate the influence of photomonomer concentration, various concentrations of PEGDA were used to print microwells under identical printing parameters. After printing, the microwells were lyophilised and examined using SEM (**Fig. S4**a - d). The results demonstrated that lower concentrations of photomonomer led to inadequate crosslinking between layers **(Fig. S4**a), compromising the structural integrity of the printed microwells. Conversely, higher concentrations of photomonomer resulted in over-photocrosslinking, which adversely affected fidelity by causing structural distortion and reduced resolution (**Fig. S4**c and d).

4.3.4 The Amount of Residuals in 3D Printed Microwell

The removal of chemical residues from 3D printed microwells and the subsequent sample collection for HPLC testing are illustrated in **Fig. 5**a. The 3D printed microwells were subjected to dialysis, significantly reducing the yellow coloration and resulting in non-coloured, semi-transparent microwells (**Fig. 5**b). Using the proposed HPLC protocol, the retention times for LAP and tartrazine were 3.4 minutes and 0.8 minutes, respectively. A linear regression calibration curve for tartrazine was constructed by plotting the peak area against different concentrations, resulting in the equation y=95861.48x-5249.68 (R^2 = 0.995)

in the range of 0.1 to 10 μg/mL, suitable for quantitative analysis. The concentrations of LAP and tartrazine in the collected samples over days 1, 3, and 7 are shown in **Fig. 5**c and d. Most of the LAP has been reacted during the printing process. As a photoinhibitor, tartrazine did not participate in the photopolymerization reaction, resulting in its presence as a residual substance. The concentration of tartrazine slightly decreased over time, indicating that it was fully released into pure water by day 1 and subsequently degraded under normal light conditions. The stability of the 3D printed microwells' morphology during dialysis was also examined. **Fig. 5**e shows the diameter evolution of the printed microwells over 7 days. No significant changes were observed, demonstrating that the printed microwells maintained their structural integrity and stability throughout the dialysis process.

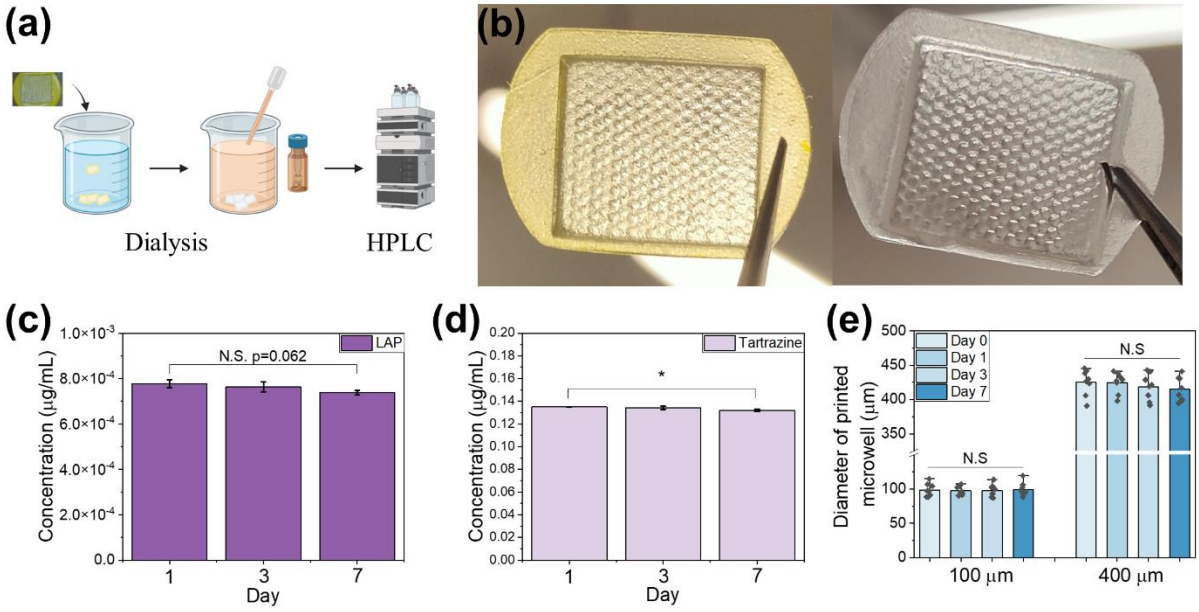


Fig. 5 a) The schematic of the using HPLC to test small molecule removal. **b)** The printed microwell before and after dialysis; The concentration of **c)** LAP and **d)** Tartrazine in the collected sample on days 1, 3 and 7; and **e)** The stability of the printed microwell under dialysis process. Data are presented as mean ± s.d. (n=3)

4.3.5 Simulation of Small Molecule Dynamic Flow Through the Microwell

Table 1 The related parameters and values used in the simulation.

Properties (Unit)	Value	Properties (Unit)	Value
Porosity ratio of the microwell	0.3	Time step (h)	0.1
Permeability rate of printed PEGDA microwell (m^2)	1e-12 [27]	Temperature (K)	310.15
Diffusion coefficient of printed PEGDA microwell (m^2 / s)	7e-11 [27]	Density of culture medium (kg / m^3)	1000
Diffusion coefficient of small molecule in PDMS microwell (m^2 / s)	1e-13 [28]	Dynamic viscosity ($Pa \cdot s$)	1e-3
Diffusion coefficient of small molecule in water (m^2 / s)	3.6e-10 [29]	Gravity acclerator (m / s^2)	9.8
The diameter of cells (μm)	100	The outer and inner diameter of microwell (μm)	400, 100

The comsuption rate in cell surface ($mol/(m^2 \cdot s)$)	1e-5	The initial amount of small molecule pipetted in (mol)	5e-12
Liquid velocity (m/s)	0		

A computational model was proposed to simulate the time-dependent dynamic of small molecule flow in both PDMS and 3D printed microwell. The parameters used in the model are detailed in **Table 1**. The small molecule were released at the left side of the microwell to mimic the pipetting process. Cells, represented by circles, were drawn at the bottom of the microwell consuming the small molecule at a constant rate (**Fig. 6**a). To assess the ability of small molecule transporting through the microwell, the flux of small molecule at the microwell bottom was recorded (**Fig. 6**a). The results showed that 3D printed microwell exhibited significantly better capabilities to transport small molecules compared to PDMS microwells (**Fig. 6**b). The concentration of small molecules in 3D printed microwells remained consistently higher than in PDMS microwells throughout the observation period (**Fig. 6**c). The small molecule flux profile was divided into five distinct periods. First, Upon release, small molecules passively diffused from the release point into the entire culture medium (**Fig. 6**d and e). Simultaneously, small molecules began to flow into the microwell, reaching maximum flux when the concentration difference between the medium and microwell was greatest at the observed point (**Fig. 6**f). Then, the flux of small molecule decreased due to the concentration difference between microwell and culture medium decreased. The concentration of the small moleule in the well would reach to the maximum point (**Fig. 6**g). After that, as cells continued to consume small molecules, the flux decreased further. Small molecules flowed back from the microwell to the cell area due to lower concentrations near the cells compared to the surrounding environment (**Fig. 6**h). In the end, the concentration of small molecule in the culture medium and microwell system gradually decreased as cells consumed them. The small molecule flux was directed towards the cell area (**Fig. 6**i). Nevertheless, the small molecule barely flow into PDMS microwell due to the low diffusion coefficient of PDMS than that in PEGDA (**Fig. S5**a-d).

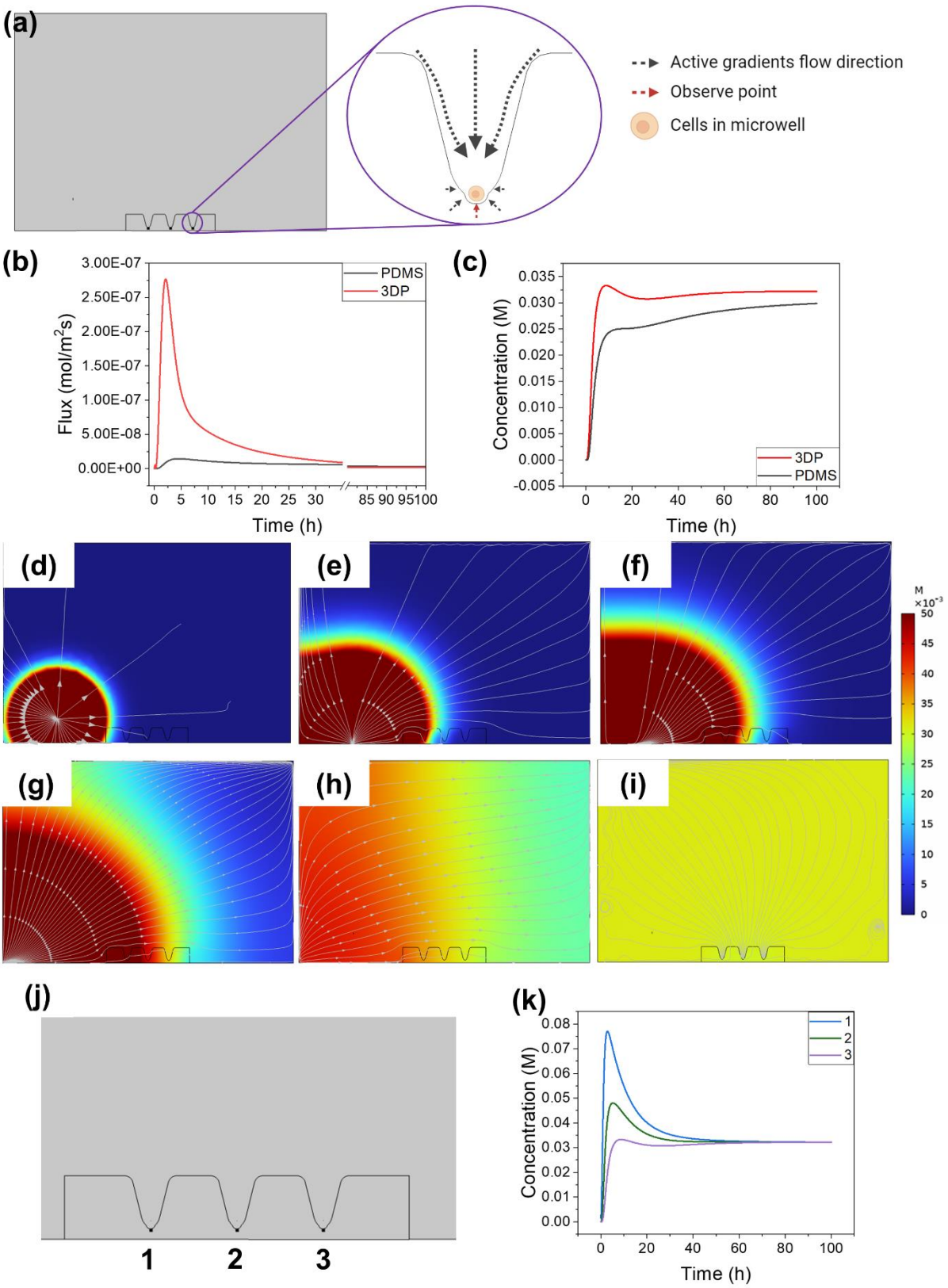


Fig. 6 a) The proposed model to represent the microwell-culture medium system. (Dash arrows indicate the small molecule flow direction). **b)** the flux evolution of small molecule at the observed points varied with time; **c)** the concentration of small molecule at the observed point varied with time; Key point of small molecule distribution in the 3D print microwell system: **d)** t=0h, **e)** t=1h; **f)** t=2.1h; **g)** t=8.8h; **h)** t=24h, and **i)** t=72h; **j)** three selected point inside the microwell to see the spatial evolution pf concentration distribution varied with

time in the microwell **k)** the simulation data showing concentration distribution profiles over time at selected points in the microwell

To observe the spatial distribution of small molecule in the microwell, 3 points inside the microwell were selected to record the time dependent evolution of concentration (**Fig. 6**j). The concentration of small molecule increased sharply following their release into the microwell (**Fig. 6**k). The proximity to the release point influenced the concentration levels, with points closer to the release point exhibiting higher concentrations, peaking at around 8 hours post-release. Following the peak, the concentration began to decrease. the concentrations at the recorded points within the microwell gradually converged, indicating a more uniform distribution of small molecules as equilibrium was approached.

4.3.6 Formation of Cell Spheroids in Microwell Arrays

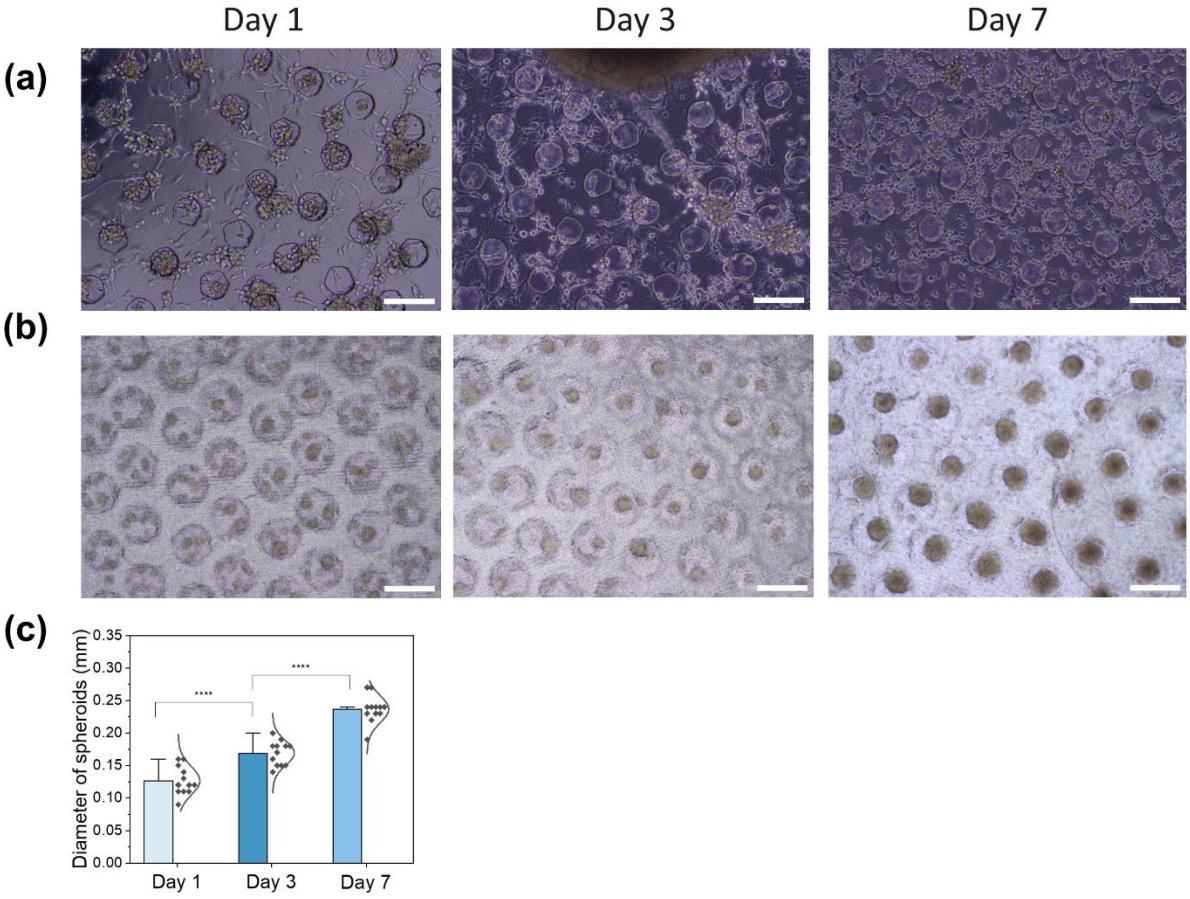


Fig. 7 Contrast in size variation of U87MG spheroids cultured in **a)** PDMS microwell and **b)** 3D printed microwell; **c)** statistical bar chart with normal distribution analysis illustrate the variation in size of the U87MG spheroids culturing in 3D printed microwell at day 1, 3, and 7. (n = 12) Scale bar, a) 200μm and b) 500 μm.

The behaviour of U87MG cells within PDMS microwells and 3D printed microwells exhibited marked differences over a seven-day observation period (**Fig. 7**a and b). In PDMS

microwell, cells initially aggregated upon settling on day 1. 2 days after incubation, the cells crawled out of PDMS microwells, adopting a spreading morphology that is typically observed in two-dimensional cultures. This trend continued, and the cells had proliferated and extended out, connecting with adjacent cells but failing to form spheroids at day 7. In contrast to the PDMS microwell, cells within the 3D printed microwells exhibited a more desirable behaviour for tissue engineering applications. The cells formed small, suspended spheroids, with two to three spheroids per microwell at day 1 (**Fig. 7**b). 2 days later, the small spheroids dismissed reorganized into larger spheroids. This process of proliferation and spheroid growth continued significantly, resulting in average spheroid diameters of 126.67 ± 21.88, 169.17 ± 18.81, and 236.67 ± 21.03 μm at day 1, 3, and 7, respectively (**Fig. 7**c).

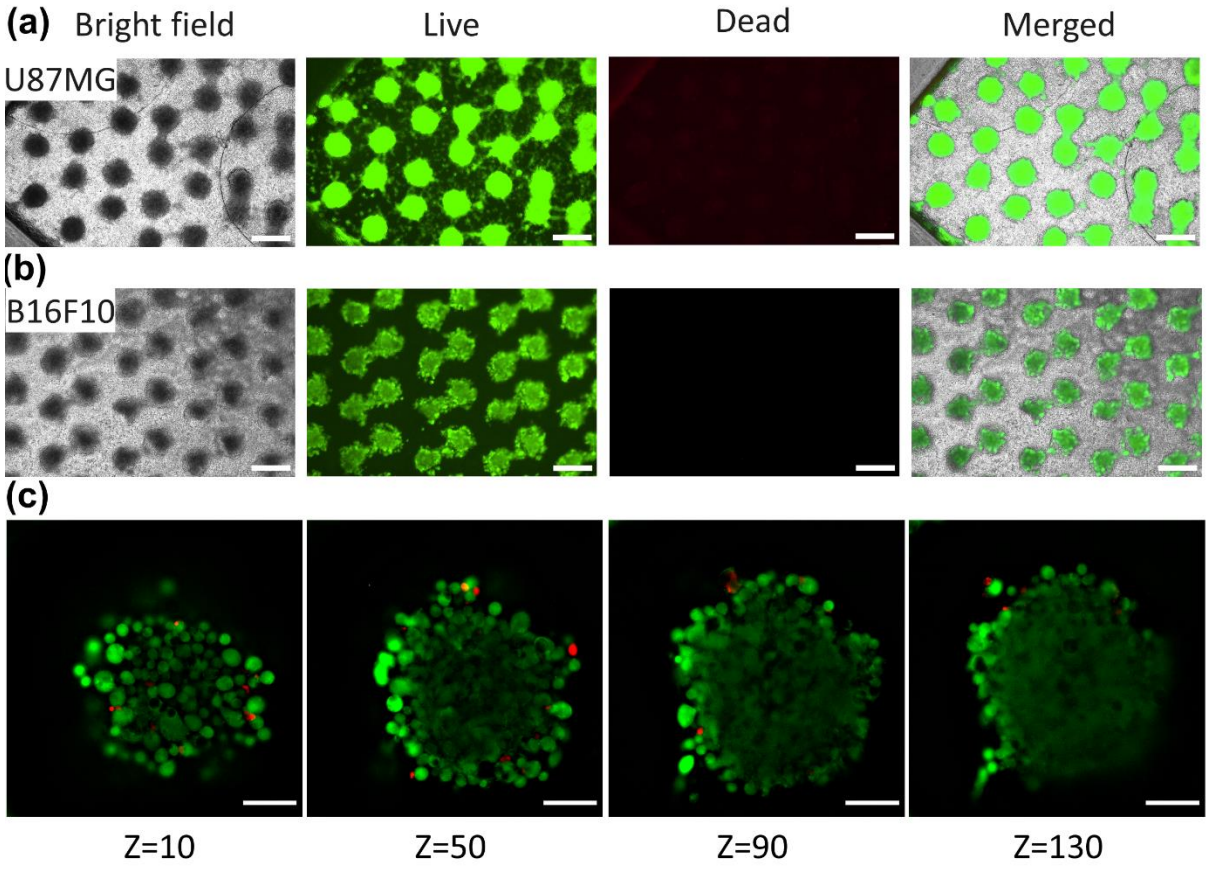


Fig. 8 Fluorescent images of **a)** U87MG and **b)** B16F10 with live/dead staining at day 21. Scale bar, 500 μm; **c)** Sliced 3D images of 3D printed microwell cultured U87MG spheroids at day 21 in different height sections: 10 μm, 50 μm, 90 μm, and 130 μm from top surface. Scale bar, 200 μm.

To further evaluate the versatility of the 3D printed microwell system for spheroid culture, a mouse skin cell line, B16F10, was also tested in the microwell. Both U87MG and B16F10 were cultured in the 3D printed microwell and stainied at day 21. The live/dead staining results (**Fig. 8**a and b) showed few dead cells in the spheroids, indicating high cell viability

within the 3D printed microwells. A 3D scan of a single stained spheroid revealed a height of approximately 260 μm, demonstrating the capacity of the microwell to support substantial spheroid growth. Additionally, 4 layers of sliced U87MG spheroids were imaged at different heights: 10 μm, 50 μm, 90 μm, and 130 μm from the top surface, respectively (**Fig. 8**c). These images confirmed high cell viability from the surface to the centre of the spheroids, highlighting the microwell's ability to support large-diameter spheroid cultures over an extended period without the need for vascularisation.

4.4 Discussion

4.4.1 Physical Properties of PEGDA Hydrogel

The physical properties of the tissue-engineered product significantly influence cellular morphology, proliferation, differentiation, and interaction [30, 31]. Water contents in artificially manufactured materials is crucial for tissue culture. Lower PEGDA concentration resulted in larger pore size and higher swelling ratio (**Fig. 2**a) [32]. The stability of the shape is also necessary for the cell culture. The water taken time of printed microwell was less than 1 hour and after that, the shape was stable (**Fig. 2**b). Resistance to fatigue loading is also important due to the frequent biological forces exerted by cells. In this study, increasing PEGDA concentration enhanced the mechanical properties of PEGDA microwell (**Fig. 2**c and d). All concentrations of PEGDA hydrogel could withstand compressive stresses exceeding 100 kPa. The compressive modulus of PEGDA ranges from 0.53 to 3.60 MPa, about 15 times higher than that in GelMA or SilMA [33]. Previous research has exhibited that the stiffness drives the cell behaviour. For example, endothelial cells tend to migrate to the edge and form ring like structure in soft environment compared in harder ones [34]. Based on the measured compressive modulus, the printed microwell appear suitable to culture human radial artery (~1 MPa), muscular tissue (~2 MPa), cartilage (0.02 – 6.44 MPa) [35-38]. Poisson’s ratio, another key parameter, indicates a material's ability to resist various loading conditions [39]. Most natural materials, which are isotropic yet incompressible, have a Poisson’s ratio ranging from 0.25 to 0.49. However, with topological design, Poisson’s ratio can extend from -1 to greater than 0.5 in specific directions. Besides, the Poisson's ratio is also influenced by the dynamic strain [40]. In this study, the vertical Poisson's ratio of printed microwell was slightly larger than 0.5 and increased with dynamic strain (**Fig. 2**e and f). This phenomenon might be due to the layer-by-layer porous structure formed by

photopolymerisation. The overlapped curves showed that the Poisson's ratio was not affected with the PEGDA concentration.

4.4.2 Rheological Properties of PEGDA Hydrogel

Rheological properties of DLP-printed PEGDA hydrogel, including storage (G') and loss modulus (G''), as well as the gelation process with and without UV light, amplitude sweep, and frequency sweep, were measured across various concentrations (**Fig. 3**a-f and **Fig. S1**a-e). Typically, the strength of hydrogel can be determined by comparing G' with G''. In strong hydrogels, G' is 1-2 orders of magnitude higher than G''. Meanwhile, G' is independent of frequencies in strong hydrogel [41]. As expected, PEGDA is a strong hydrogel, and increasing its concentration leads to the printed hydrogel microwell harder, which in turn slowed down small molecular diffusion [42]. The light exposure can maximise the efficiency of the initiator, promoting PEGDA monomer crosslinking to form a more stable and stronger hydrogel. Additionally, the heat generated from friction during the time sweep can also trigger the initiator to create free radicals, commencing the PEGDA crosslinking process [43]. In amplitude sweep, the cross point between G' and G'' plays a significant role in designing materials. Data showed that the PEGDA hydrogel performed elastic behaviour under small strain (< 1%). Reducing concentration or increasing temperature could extend the elastic range of PEGDA hydrogel. Besides, the storage modulus of printed hydrogel does not vary with frequency, suggesting that the printed hydrogel does not contain non-covalent bonds, which demonstrates the strong stability of the printed microwell [44-46].

4.4.3 Morphology of the 3D Printed Microwell

The fabrication of microwell was achieved via a DLP printer (**Fig. 4**b). The photocrosslinkable material, PEGDA, was combined with a photoinitiator, LAP, and a photoinhibitor, tartrazine. LAP has greater water solubility, higher efficiency, and low cell cytotoxicity [47]. Tartrazine was used as a safe lemon yellow azo dye in the food industry, and was mixed in the PEGDA solution to avoid overexposure to light [48]. The photocrosslinkable reaction was initiated when the LAP and tartrazine mixed PEGDA solution was exposed to 405 nm light. Under the light, LAP decomposed into two free radicals that initiate the opening of PEGDA's double bonds, starting the crosslinking process

essential for chain polymerization [31]. By optimising the light exposure time, the diameter of the microwell could be adjusted (**Fig. 4**c). However, this adjustment is not under controlled. excessive exposure time can cause light scattering at the edges, which may lead to inaccuracies and potential damage to the desired structures [48]. After the printing process, it is significant to remove the residual monomers to avoid adverse effects on cell cultures (**Fig. 5**c and d). Tartrazine, LAP and unreacted PEGDA monomers all exhibit high water solubility, and the porous structure of the 3D printed microwell facilitates the washing out of these small molecules. The stable chemical crosslinking ensures that the microwell maintains its shape during the cleaning process. Therefore, the effective removal of chemical residues from 3D printed microwells and confirm their morphological stability, ensuring their suitability for biological applications.

4.4.4 Simulation of Small Molecule Dynamic Flow Through the Microwell

The proposed 2D simulation model provides insights into the passive diffusion of small molecules throughout the entire microwell culture system. The molecular weight of the 480 Da drug used in the simulation corresponds to rhodamine B, which is commonly employed in *in vitro* assays for small to moderately sized organic molecules, including drugs, metabolites, and small peptides. It is particularly useful for studying the diffusion properties of therapeutic agents within 3D spheroids or artificial tissues. The strong fluorescence of rhodamine B facilitates the easy and accurate tracking of its diffusion into and around the spheroids within the microwell system, making it ideal for visualizing and quantifying drug penetration. The proposed simulation model is highly adaptable and can be easily modified by adjusting the input parameters for different drugs to suit various testing scenarios. Compared with PDMS microwell, the 3D printed microwell demonstrate the superior ability in transporting small molecules, which is crucial for cell culture applications requiring efficient nutrient and drug delivery (**Fig. 6**b and c). The simulation highlights how material properties influence passive diffusion rates and small molecule concentrations within the microwell system, as well as directing flow dynamics adjacent to the microwell (**Fig. 6**g and h and **Fig. S**5c). The position of small molecule release directly impacts its concentration within the microwell (**Fig. 6**k), potentially leading to gradient cell morphology or behaviours. With this model, it becomes feasible to monitor the distribution and consumption of additives like chemicals, growth factors, and peptides within microwell-based spheroid culture systems, which significantly influence cell morphology and motility [5]. However, the proposed model still has certain

limitations. The proposed model was operated under idealized conditions without external disturbances such as cell culture operations like shaking or pipetting, which can affect small molecule diffusion. Besides, the cells were assumed as constant in both volume and molecular consumption rate, whereas in reality, cells formed small spheroids first, and then aggregated into a bigger size (**Fig. 7**b) [49]. Cells proliferate change in size, and alter their metabolic demands, affecting the distribution of molecules within spheroids. Future models should address these limitations to better reflect real-world scenarios and improve the predictive accuracy of microwell-based culture systems.

4.4.5 Formation of Cell Spheroids in Microwell Arrays

The two cell lines used in this study are glioblastoma cells and melanoma cells. Glioblastoma cells represent an aggressive form of brain cancer characterized by a high degree of heterogeneity. Testing this cell line allows for the evaluation of how the microwell system can facilitate the formation of spheroids with complex growth characteristics, which are essential for drug testing and personalized medicine in cancer research. Melanoma spheroids are commonly used in drug delivery research, making them a relevant model for assessing drug diffusion and penetration within solid tumors. Additionally, the melanoma model helps evaluate the versatility of the microwell system in supporting different cancer types for future applications.

PEGDA does not have arginine-glycine-aspartic acid, and PEGDA based hydrogel are nonadhesive to the cells, which provide a versatile platform for incorporating biologically or chemically functional components. This characteristic allows for the creation of various geometries to guide cellular alignment and pattern. The ability of cells to aggregate into spheroids is primarily driven by cell-cell adhesion proteins and extracellular matrix (ECM) interactions [50]. Cells express surface proteins (such as cadherins and integrins) that allow them to adhere to each other or to the ECM, promoting the formation of stable 3D structures [51]. The spheroid structure is stable in a 3D environment, providing protection to the cells by distributing environmental stress uniformly, rather than concentrating it at any single point. When cells were seeded into the microwell, the total volume of cells was much smaller than the single microwell. Therefore, they initially form small clusters based on their proximity to neighbouring cells (**Fig. 7**b).

As the cells proliferated, moved, and interacted with other cell spheroids, smaller spheroids merged into larger ones. This process illustrates the dynamic nature of cell interactions within a 3D environment, where cells aim to minimize surface tension and maximize internal stability. To regulate the size of the spheroids from the outset, we hypothesize that adjustments to parameters related to microwell design and cell seeding density can influence outcomes. For instance, reducing the cross-sectional area of the microwell may enhance the likelihood of seeded cells coming into contact and aggregating into a small spheroid by day 1. Conversely, if larger spheroids are desired from the beginning, increasing the seeding density in the microwell would also elevate the chances of cell contact, leading to the formation of bigger spheroids.

While it may be feasible to use the Monte Carlo model to predict the potential size of the formed small spheroids based on initial conditions (such as microwell geometry, cell number, and cell type), controlling the size, movement, and reorganization of spheroids remains challenging with the current 3D-printed microwell platform. Future modifications, such as integrating microfluidics, could provide a means to better manage spheroid size and reorganization. This would allow for the control of nutrient flow, chemical gradients, and mechanical forces, all of which could be regulated through microfluidics to enhance spheroid formation and maintain consistent sizes over time.

The cell cultured in the 3D printed PEGDA microwell readily form spheroids with high growth rates and viability (**Fig. 7**b and c and **Fig. 8**a and b). Typically, spheroids larger than 200 μm in diameter without vascularisation would gradient display three concentric zones: an outer region with rapidly dividing and moving cells, a middle region with inactive cells, and an inner region with dying cells [14, 52, 53]. However, the spheroids cultured in the proposed 3D printed microwell did not face this problem. The spheroids grew up to 400 μm at day 21 and the 3D scanning live/dead staining showed the high cell viability in the core of the spheroids. With this advanced functionality, researcher can easily build high throughput large spheroids and explore drug screening effects involving gradient diffusion within complex cell tissues. The tunability of 3D printed PEGDA microwells allows them to replicate in vivo microenvironment, offering opportunities for developing disease models and testing various drugs to solidify their applications. Future advancements could focus on designing more

complex structures to investigate bi-cellular interactions and cell migration. The versatility of the system and its compatibility with various requirements can pave the way towards comprehensive applications in biomedical research, spanning from basic research to drug development and personalised cell therapy.

4.5 Conclusion

We have demonstrated the utility of 3D printing for single-step fabrication of anisotropic microwell chips designed for culturing cell spheroids. By adjusting the formulation of bioinks and printing parameters, we successfully tailored the mechanical properties of the printed microwells to mimic the in vivo microenvironment required for cell replication. The proposed two-dimensional model can be a useful tool to analysis the cell-microwell culturing system, providing insights into optimal timing for supplying various small molecules. In the 3D printed microwell, cells can grow up to around 400 μm in diameter and 260 in height maintaining high cell viability without requiring vascularization. This simple, flexible, versatile, and cost-effective device can be convenient to be applied in a wide range of tissue engineering and biomedical applications. Moving forward, further advancements in design and application could enhance its capabilities in replicating complex cellular environments and advancing biomedical research.

Reference

[1] K. Ravikumar, C. Wiegand, I. Banerjee, High Throughput Generation of Spherical and Nonspherical Stem-cell Tissue Constructs using 3D Printed Templates, Trends Biomater. Artif. 35(5) (2021) 461-470.
[2] Y. Zhang, I. Naguro, A.E. Herr, In Situ Single-Cell Western Blot on Adherent Cell Culture, Angew Chem Int Ed Engl 58(39) (2019) 13929-13934.
[3] X. Xu, J. Wang, L. Wu, J. Guo, Y. Song, T. Tian, W. Wang, Z. Zhu, C. Yang, Microfluidic Single-Cell Omics Analysis, Small 16(9) (2020) e1903905.
[4] P. Zhang, N. Shao, L. Qin, Recent Advances in Microfluidic Platforms for Programming Cell-Based Living Materials, Adv Mater 33(46) (2021) e2005944.
[5] S. Ansaryan, Y.C. Liu, X. Li, A.M. Economou, C.S. Eberhardt, C. Jandus, H. Altug, High-throughput spatiotemporal monitoring of single-cell secretions via plasmonic microwell arrays, Nature biomedical engineering 7(7) (2023) 943-958.
[6] D.K. Wood, D.M. Weingeist, S.N. Bhatia, B.P. Engelward, Single cell trapping and DNA damage analysis using microwell arrays, PNAS 107(22) (2010) 10008-13.
[7] X. Han, R. Wang, Y. Zhou, L. Fei, H. Sun, S. Lai, A. Saadatpour, Z. Zhou, H. Chen, F. Ye, D. Huang, Y. Xu, W. Huang, M. Jiang, X. Jiang, J. Mao, Y. Chen, C. Lu, J. Xie, Q. Fang, Y. Wang, R. Yue, T. Li, H. Huang, S.H. Orkin, G.C. Yuan, M. Chen, G. Guo, Mapping the Mouse Cell Atlas by Microwell-Seq, Cell 172(5) (2018) 1091-1107 e17.
[8] S. Wiedenmann, M. Breunig, J. Merkle, C. von Toerne, T. Georgiev, M. Moussus, L. Schulte, T. Seufferlein, M. Sterr, H. Lickert, S.E. Weissinger, P. Moller, S.M. Hauck, M. Hohwieler, A. Kleger, M. Meier, Single-cell-resolved differentiation of human induced pluripotent stem cells into pancreatic duct-like organoids on a microwell chip, Nature biomedical engineering 5(8) (2021) 897-913.

[9] Y. Zhou, N. Shao, R. Bessa de Castro, P. Zhang, Y. Ma, X. Liu, F. Huang, R.F. Wang, L. Qin, Evaluation of Single-Cell Cytokine Secretion and Cell-Cell Interactions with a Hierarchical Loading Microwell Chip, Cell Rep 31(4) (2020) 107574.
[10] J. Pan, S. Yung Chan, J.E. Common, S. Amini, A. Miserez, E. Birgitte Lane, L. Kang, Fabrication of a 3D hair follicle-like hydrogel by soft lithography, Journal of biomedical materials research. Part A 101(11) (2013) 3159-69.
[11] T. Man, X. Zhu, Y.T. Chow, E.R. Dawson, X. Wen, A.N. Patananan, T.L. Liu, C. Zhao, C. Wu, J.S. Hong, P.S. Chung, D.L. Clemens, B.Y. Lee, P.S. Weiss, M.A. Teitell, P.Y. Chiou, Intracellular Photothermal Delivery for Suspension Cells Using Sharp Nanoscale Tips in Microwells, ACS Nano 13(9) (2019) 10835-10844.
[12] C.H. Kim, I.R. Suhito, N. Angeline, Y. Han, H. Son, Z. Luo, T.H. Kim, Vertically Coated Graphene Oxide Micro-Well Arrays for Highly Efficient Cancer Spheroid Formation and Drug Screening, Advanced healthcare materials 9(7) (2020) e1901751.
[13] Y. Hu, X. Sui, F. Song, Y. Li, K. Li, Z. Chen, F. Yang, X. Chen, Y. Zhang, X. Wang, Q. Liu, C. Li, B. Zou, X. Chen, J. Wang, P. Liu, Lung cancer organoids analyzed on microwell arrays predict drug responses of patients within a week, Nature communications 12(1) (2021) 2581.
[14] J. He, C. Zhou, X. Xu, Z. Zhou, M. Danoy, M. Shinohara, W. Xiao, D. Zhu, X. Zhao, X. Feng, Y. Mao, W. Sun, Y. Sakai, H. Yang, Y. Pang, Scalable Formation of Highly Viable and Functional Hepatocellular Carcinoma Spheroids in an Oxygen-Permeable Microwell Device for Anti-Tumor Drug Evaluation, Advanced healthcare materials 11(18) (2022) e2200863.
[15] C. Chen, V. Rengarajan, A. Kjar, Y. Huang, A matrigel-free method to generate matured human cerebral organoids using 3D-Printed microwell arrays, Bioactive materials 6(4) (2021) 1130-1139.
[16] D. Kim, K. Kim, J.Y. Park, Novel microwell with a roof capable of buoyant spheroid culture, Lab on a chip 21(10) (2021) 1974-1986.
[17] N. Udomluck, S.H. Kim, H. Cho, J.Y. Park, H. Park, Three-dimensional cartilage tissue regeneration system harnessing goblet-shaped microwells containing biocompatible hydrogel, Biofabrication 12(1) (2019) 015019.
[18] S. Lee, S. Kim, J. Ahn, J. Park, B.Y. Ryu, J.Y. Park, Membrane-bottomed microwell array added to Transwell insert to facilitate non-contact co-culture of spermatogonial stem cell and STO feeder cell, Biofabrication 12(4) (2020) 045031.
[19] D. Tian, Z. Mao, L. Wang, X. Huang, W. Wang, H. Luo, J. Peng, Y. Chen, Rocking- and diffusion-based culture of tumor spheroids-on-a-chip, Lab on a chip 24(9) (2024) 2561-2574.
[20] H. Li, K. Hsieh, P.K. Wong, K.E. Mach, J.C. Liao, T.-H. Wang, Single-cell pathogen diagnostics for combating antibiotic resistance, Nature Reviews Methods Primers 3(1) (2023).
[21] L. Neufeld, E. Yeini, S. Pozzi, R. Satchi-Fainaro, 3D bioprinted cancer models: from basic biology to drug development, Nat Rev Cancer 22(12) (2022) 679-692.
[22] B. Ladoux, R.M. Mege, Mechanobiology of collective cell behaviours, Nat Rev Mol Cell Biol 18(12) (2017) 743-757.
[23] A. Saraswathibhatla, D. Indana, O. Chaudhuri, Cell-extracellular matrix mechanotransduction in 3D, Nat Rev Mol Cell Biol 24(7) (2023) 495-516.
[24] A.P. Zhang, X. Qu, P. Soman, K.C. Hribar, J.W. Lee, S. Chen, S. He, Rapid fabrication of complex 3D extracellular microenvironments by dynamic optical projection stereolithography, Advanced materials 24(31) (2012) 4266-70.
[25] K.S. Lim, J.H. Galarraga, X. Cui, G.C.J. Lindberg, J.A. Burdick, T.B.F. Woodfield, Fundamentals and Applications of Photo-Cross-Linking in Bioprinting, Chemical reviews 120(19) (2020) 10662-10694.
[26] M.A. Miller, R. Weissleder, Imaging of anticancer drug action in single cells, Nat Rev Cancer 17(7) (2017) 399-414.
[27] K. O'Donnell, A. Boyd, B.J. Meenan, Controlling Fluid Diffusion and Release through Mixed-Molecular-Weight Poly(ethylene) Glycol Diacrylate (PEGDA) Hydrogels, Materials (Basel) 12(20) (2019).
[28] J. Grant, A. Ozkan, C. Oh, G. Mahajan, R. Prantil-Baun, D.E. Ingber, Simulating drug concentrations in PDMS microfluidic organ chips, Lab on a chip 21(18) (2021) 3509-3519.
[29] P.O. Gendron, F. Avaltroni, K.J. Wilkinson, Diffusion coefficients of several rhodamine derivatives as determined by pulsed field gradient-nuclear magnetic resonance and fluorescence correlation spectroscopy, J Fluoresc 18(6) (2008) 1093-101.
[30] L. Polonchuk, L. Surija, M.H. Lee, P. Sharma, C. Liu Chung Ming, F. Richter, E. Ben-Sefer, M.A. Rad, H. Mahmodi Sheikh Sarmast, W.A. Shamery, H.A. Tran, L. Vettori, F. Haeusermann, E.C. Filipe, J. Rnjak-Kovacina, T. Cox, J. Tipper, I. Kabakova, C. Gentile, Towards engineering heart tissues from bioprinted cardiac spheroids, Biofabrication 13(4) (2021).
[31] C. Yu, J. Schimelman, P. Wang, K.L. Miller, X. Ma, S. You, J. Guan, B. Sun, W. Zhu, S. Chen, Photopolymerizable Biomaterials and Light-Based 3D Printing Strategies for Biomedical Applications, Chemical reviews 120(19) (2020) 10695-10743.

[32] K.H. Son, J.W. Lee, Synthesis and Characterization of Poly(Ethylene Glycol) Based Thermo-Responsive Hydrogels for Cell Sheet Engineering, Materials 9(10) (2016).
[33] S.H. Kim, Y.K. Yeon, J.M. Lee, J.R. Chao, Y.J. Lee, Y.B. Seo, M.T. Sultan, O.J. Lee, J.S. Lee, S.I. Yoon, I.S. Hong, G. Khang, S.J. Lee, J.J. Yoo, C.H. Park, Precisely printable and biocompatible silk fibroin bioink for digital light processing 3D printing, Nature communications 9(1) (2018) 1620.
[34] G.J. Pahapale, J. Tao, M. Nikolic, S. Gao, G. Scarcelli, S.X. Sun, L.H. Romer, D.H. Gracias, Directing Multicellular Organization by Varying the Aspect Ratio of Soft Hydrogel Microwells, Advanced science 9(17) (2022) e2104649.
[35] R. Akhtar, M.J. Sherratt, J.K. Cruickshank, B. Derby, Characterizing the elastic properties of tissues, Mater Today (Kidlington) 14(3) (2011) 96-105.
[36] S. Huang, D. Lei, Q. Yang, Y. Yang, C. Jiang, H. Shi, B. Qian, Q. Long, W. Chen, Y. Chen, L. Zhu, W. Yang, L. Wang, W. Hai, Q. Zhao, Z. You, X. Ye, A perfusable, multifunctional epicardial device improves cardiac function and tissue repair, Nat Med 27(3) (2021) 480-490.
[37] G. Singh, A. Chanda, Mechanical properties of whole-body soft human tissues: a review, Biomed Mater 16(6) (2021).
[38] Y. Zhang, P. Habibovic, Delivering Mechanical Stimulation to Cells: State of the Art in Materials and Devices Design, Advanced materials 34(32) (2022) e2110267.
[39] Y. Javanmardi, H. Colin-York, N. Szita, M. Fritzsche, E. Moeendarbary, Quantifying cell-generated forces: Poisson's ratio matters, Commun Phys 4 (2021) 237.
[40] P. Soman, J.W. Lee, A. Phadke, S. Varghese, S. Chen, Spatial tuning of negative and positive Poisson's ratio in a multi-layer scaffold, Acta biomaterialia 8(7) (2012) 2587-94.
[41] A. Martínez-Ruvalcaba, E. Chornet, D. Rodrigue, Viscoelastic properties of dispersed chitosan/xanthan hydrogels, Carbohydrate polymers 67(4) (2007) 586-595.
[42] D.V. Nguyen, Y. Yuan, M. Kukumberg, L. Wang, S.H. Lim, A.M. Hassanbhai, M. Chong, T. Kofidis, E.C.K. Tan, D. Seliktar, L. Kang, A.J. Rufaihah, Controlled release of vancomycin from PEGylated fibrinogen polyethylene glycol diacrylate hydrogel, Biomater Adv 161 (2024) 213896.
[43] X. Kuang, Q. Rong, S. Belal, T. Vu, A.M.L. López, N. Wang, M.O. Arıcan, C.E. Garciamendez-Mijares, M. Chen, J. Yao, Y.S. Zhang, Self-enhancing sono-inks enable deep-penetration acoustic volumetric printing, Science 382 (2023) 1148-1155.
[44] Y. Yang, K. Shi, K. Yu, F. Xing, H. Lai, Y. Zhou, P. Xiao, Degradable Hydrogel Adhesives with Enhanced Tissue Adhesion, Superior Self-Healing, Cytocompatibility, and Antibacterial Property, Advanced healthcare materials 11(4) (2022) e2101504.
[45] J. George, C.C. Hsu, L.T.B. Nguyen, H. Ye, Z. Cui, Neural tissue engineering with structured hydrogels in CNS models and therapies, Biotechnology advances 42 (2020) 107370.
[46] G. Stojkov, Z. Niyazov, F. Picchioni, R.K. Bose, Relationship between Structure and Rheology of Hydrogels for Various Applications, Gels 7(4) (2021).
[47] C.G. Williams, A.N. Malik, T.K. Kim, P.N. Manson, J.H. Elisseeff, Variable cytocompatibility of six cell lines with photoinitiators used for polymerizing hydrogels and cell encapsulation, Biomaterials 26(11) (2005) 1211-8.
[48] H. Goodarzi Hosseinabadi, D. Nieto, A. Yousefinejad, H. Fattel, L. Ionov, A.K. Miri, Ink material selection and optical design considerations in DLP 3D printing, Applied Materials Today 30 (2023).
[49] M. McCune, A. Shafiee, G. Forgacs, I. Kosztin, Predictive modeling of post bioprinting structure formation, Soft Matter 10(11) (2014) 1790-800.
[50] B. Honig, L. Shapiro, Adhesion Protein Structure, Molecular Affinities, and Principles of Cell-Cell Recognition, Cell 181(3) (2020) 520-535.
[51] S. SenGupta, C.A. Parent, J.E. Bear, The principles of directed cell migration, Nat Rev Mol Cell Biol 22(8) (2021) 529-547.
[52] B. Pinto, A.C. Henriques, P.M.A. Silva, H. Bousbaa, Three-Dimensional Spheroids as In Vitro Preclinical Models for Cancer Research, Pharmaceutics 12(12) (2020).
[53] S. Gunti, A.T.K. Hoke, K.P. Vu, N.R. London, Jr., Organoid and Spheroid Tumor Models: Techniques and Applications, Cancers (Basel) 13(4) (2021).

Supplementary information

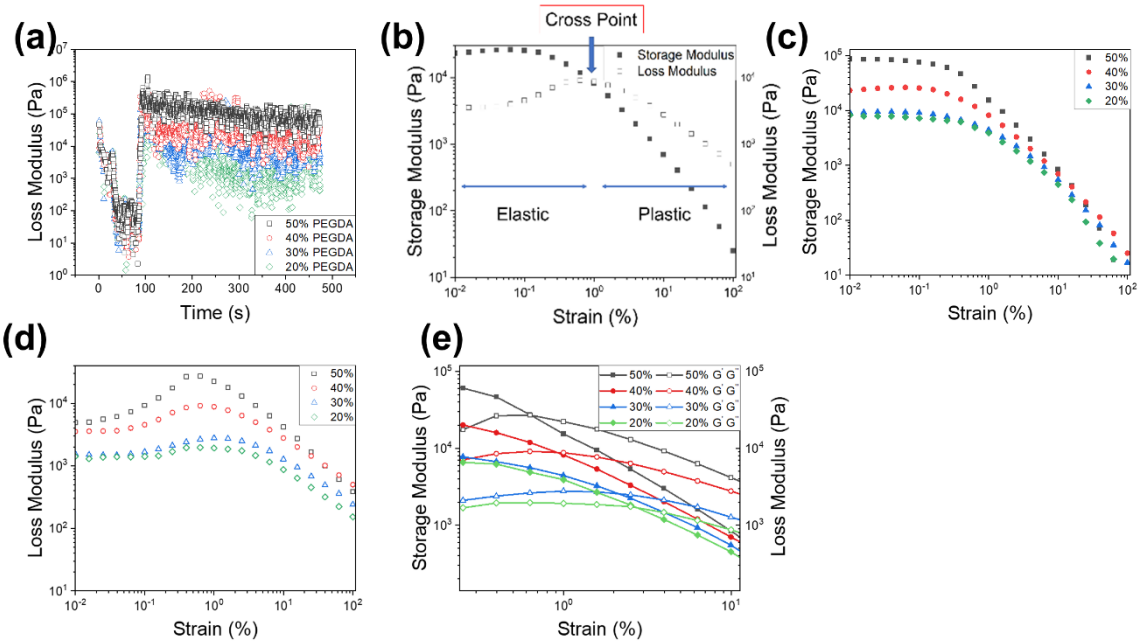


Fig. S1 Rheological properties of different concentrations PEGDA inks/printed hydrogel ranging from 20-50%: **a)** Photorheological loss modulus; **b)** Amplitude sweep of 30% PEGDA hydrogel; **c)** Amplitude sweep storage modulus; **d)** Amplitude sweep loss modulus **e)** Amplitude sweep at 25 ^{o}C.

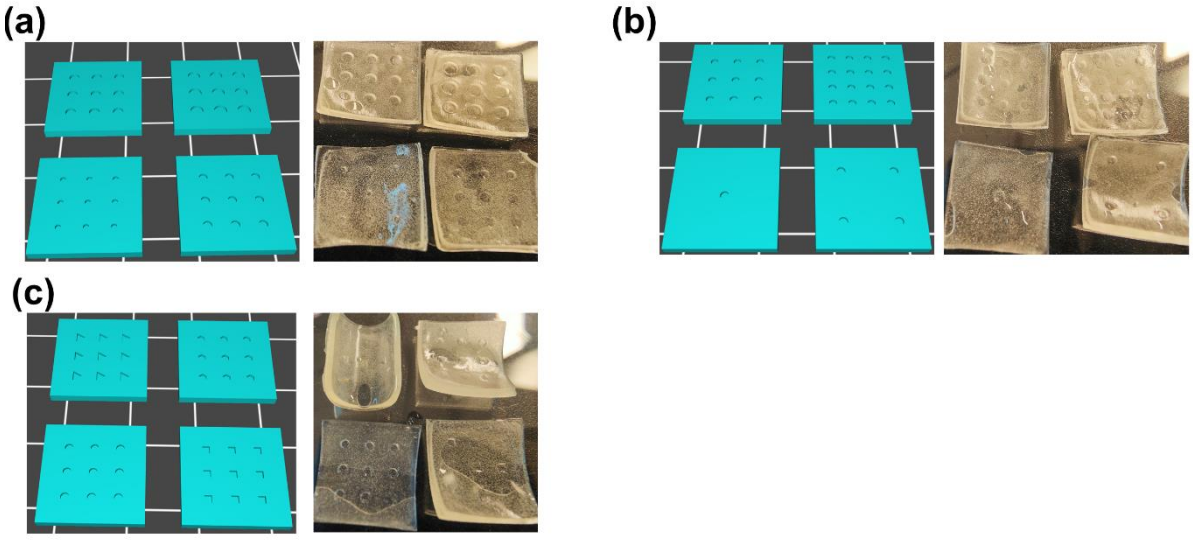


Fig. S2 3D printed microwell with different **a)** Area size, **b)** well density per chip; **c)** shape type: triangle, hexagon, circle, and square.

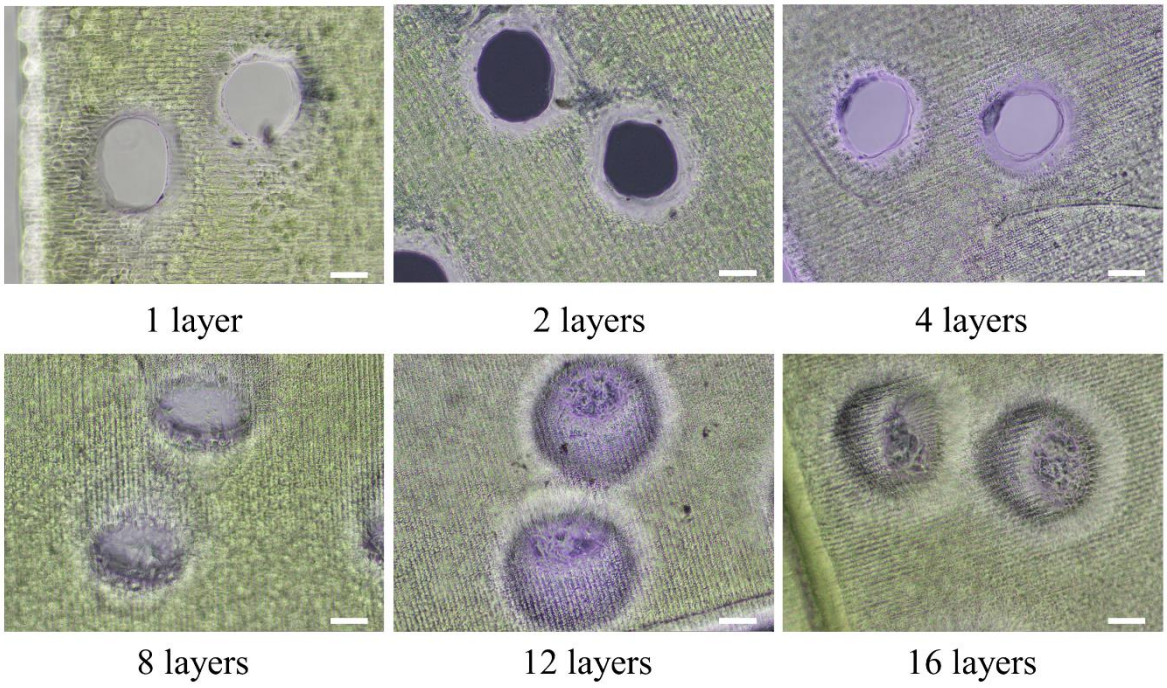


Fig. S3 Edge light scattering effects: Layer-by-layer analysis revealed minimal impact of edge light scattering on the circular shape: 1, 2, 4, 8, 12, and 16 layers.

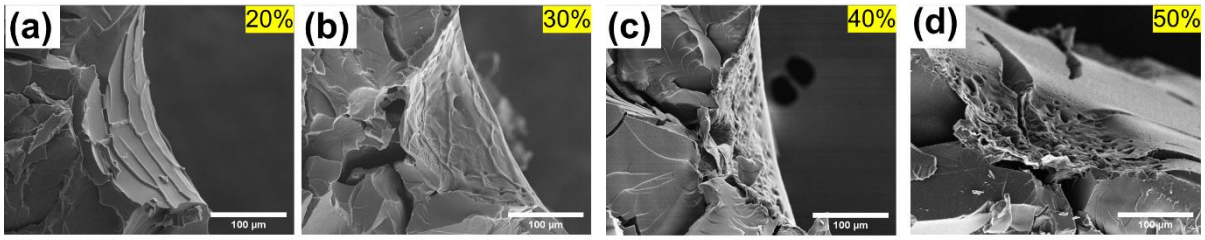


Fig. S4 SEM image about lyophilised different concentrations printed microwell under identical printing parameters: a)20% PEGDA, b) 30% PEGDA, c) 40% PEGDA, and d) 50% PEGDA.

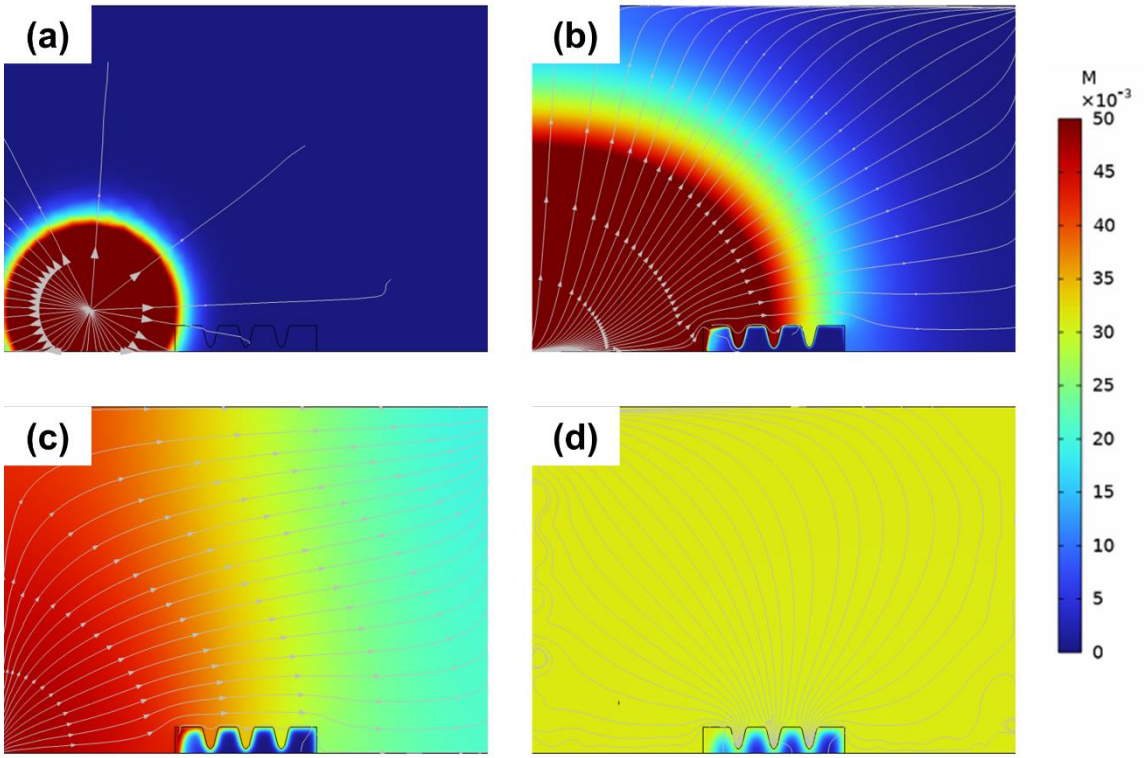


Fig. S5 Concentration distribution of small molecule passive diffusion in PDMS microwell system: **a)** t=0h, **b)** t=8h, **c)** t=24h, and **d)** t= 72h.

Chapter 5 Oxygen Penetration Through Full-Thickness Skin by Oxygen-Releasing Sutures for Skin Graft Transplantation

This chapter contains the following publication:

> W Zai, **Y Yuan** (co-first author), L Kang, J Xu, Y Hu, L Kang, J Wu, Oxygen Penetration Through Full-Thickness Skin by Oxygen-Releasing Sutures for Skin Graft Transplantation, Engineering 29, 83-94. https://doi.org/10.1016/j.eng.2023.05.006.

Engineering 29 (2023) 83–94

Contents lists available at ScienceDirect

Engineering

journal homepage: www.elsevier.com/locate/eng

Research
Medical Engineering—Article

Oxygen Penetration Through Full-Thickness Skin by Oxygen-Releasing Sutures for Skin Graft Transplantation

Wenjing Zai [a,c,#], Yunong Yuan [b,#], Lin Kang [a,f,#], Jialong Xu [a], Yiqiao Hu [a], Lifeng Kang [b], Jinhui Wu [a,d,e,*]

[a] State Key Laboratory of Pharmaceutical Biotechnology, Medical School, Nanjing University, Nanjing 210093, China
[b] School of Pharmacy, Faculty of Medicine and Health, University of Sydney, Sydney, NSW 2006, Australia
[c] School of Biomedical Engineering, Shanghai Jiao Tong University, Shanghai 200240, China
[d] Chemistry and Biomedicine Innovation Center, Nanjing University, Nanjing 210023, China
[e] Jiangsu Provincial Key Laboratory for Nano Technology, Nanjing University, Nanjing 210093, China
[f] Jiangsu Food & Pharmaceutical Science College, Huai'an 223003, China

ARTICLE INFO

Article history:
Received 28 January 2023
Revised 11 April 2023
Accepted 6 May 2023
Available online 29 May 2023

Keywords:
Wound
Skin graft transplantation
Oxygen-releasing sutures
Full-thickness oxygen delivery

ABSTRACT

The transplantation of full-thickness skin grafts (FTSGs) is important for reconstructing skin barrier and promoting wound healing. Sufficient oxygen supply is closely related to the success of skin grafting. However, full-thickness oxygen delivery is limited by the poor oxygen permeability of skin. Oxygen-releasing sutures (O_2 sutures) were developed to facilitate oxygen penetration through full-thickness skin. The O_2 sutures delivered 100 times more oxygen than topical gaseous oxygen therapy at a 15 mm depth in the skin model. Under extreme hypoxia (< 0.5% O_2, v/v), O_2 sutures could also promote endothelial cell proliferation. After the transplantation of FTSGs in mice, O_2 sutures accelerated blood re-perfusion and increased the survival area of the skin graft. It is expected that O_2 sutures will be adopted in clinical applications to increase the success rate of full-thickness skin transplantation.

© 2023 THE AUTHORS. Published by Elsevier LTD on behalf of Chinese Academy of Engineering and Higher Education Press Limited Company. This is an open access article under the CC BY-NC-ND license (http://creativecommons.org/licenses/by-nc-nd/4.0/).

1. Introduction

Skin graft transplantation involves the transplantation of skin from a healthy site to a wound site to promote wound healing [1]; it has significant value in the treatment of surgical incisions including abdominal wall defects and hernias [2–4], thermal burns [5,6], and chronic ulcers [1]. Full-thickness skin grafts (FTSGs) exhibit numerous advantages over split-thickness skin grafts and have an important role in exposed wounds [7,8]. However, the success rate of FTFGs is severely restricted by the local oxygen concentration in the wound tissue, as anoxia (< 0.5% O_2, v/v) leads to cell death [9–11]. Local oxygen concentration depends on the speed of revascularization, which can take 1–2 d post operation [12,13]. Additional oxygen supply immediately after an FTSG procedure can effectively improve graft survival and increase the success of the skin grafting.

To increase the supply of oxygen to wound tissue, several approaches can be applied; these are based on either of two principles: inhalation of gaseous oxygen via the airway and topical delivery of oxygen to the wound tissue [14,15]. After patients breathe 100% oxygen at normal or higher pressures, oxygen can be delivered to the wound site via blood circulation. However, because blood microcirculation requires 1–2 d to reconstruct post-operative FTSGs, oxygen delivery is limited and insufficient for cell proliferation [12,16,17].

To overcome delayed revascularization, oxygen can be delivered topically using either topical gaseous oxygen (TGO) therapy or an oxygen dressing. During TGO therapy, the wound site is directly exposed to 100% gaseous oxygen. Gaseous oxygen first dissolves in the moisture in the epidermis and then diffuses into the skin graft [18–20]. Oxygen dressing is another strategy for topically delivering oxygen to wounds, where dissolved oxygen is produced by peroxide or photosynthetic microbes and then diffuses into the epidermis [21–23]. However, epidermis is virtually impermeable to oxygen and the maximal diffusion distance of oxygen in dermis is between 300 and 700 μm, which is considerably less than the 2–4 mm that FTSGs require [15,24,25]. Therefore, there is an urgent requirement to devise a new approach to effectively deliver oxygen for wound healing after skin graft transplantation. Surgical sutures could be useful in these cases.

* Corresponding author.
E-mail address: wuj@nju.edu.cn (J. Wu).
# These authors contributed equally to this work.

https://doi.org/10.1016/j.eng.2023.05.006
2095-8099/© 2023 THE AUTHORS. Published by Elsevier LTD on behalf of Chinese Academy of Engineering and Higher Education Press Limited Company.
This is an open access article under the CC BY-NC-ND license (http://creativecommons.org/licenses/by-nc-nd/4.0/).

Sutures are surgical threads commonly used to hold body tissues together and approximate wound edges after injury, including FTSG operations. Recent progress in materials and fabrication techniques has enabled the development of a variety of sutures with added functions including monitoring deep wounds [26], antibacterial [27] and anti-inflammatory properties, and wound healing promotion [28]. The added functions capitalize on the fact that sutures are pervious and intimately integrated into the wound tissue upon application. This inspired us to develop a functionalized suture to enhance oxygen delivery to deep skin layers.

In this study, we construct oxygen-releasing sutures (O_2 sutures) for *in-situ* wound oxygen production to promote the success of FTSGs (Fig. 1). The sutures are made from a double-layer hydrogel containing CaO_2 and catalase (CAT). The inner layer of CaO_2 reacts with water to produce H_2O_2; then, the H_2O_2 diffuses to the outer layer and reacts with the CAT to produce oxygen. When used in FTSG operations, O_2 sutures promote the proliferation of endothelial cells in an anoxic environment and accelerate the restoration of blood perfusion of the graft, thereby increasing the success rate of the FTSGs.

2. Materials and methods

2.1. Animal experiments

All animal experiments were performed in compliance with guidelines approved by the Institutional Animal Care and Use Committee of Nanjing University. BALB/c and C57BL/6 mice were purchased from Yangzhou University (China). Human umbilical vein endothelial cells (HUVECs) were purchased from American Type Culture Collection (ATCC).

2.2. Fabrication of O_2 suture

An O_2 suture was fabricated using a double-layer hydrogel wrapping method based on commercial silk sutures. A 4# silk suture (Changchun Shiji Bairuida Pharmacy Co., Ltd., China) was inserted into a conical die with holes at both ends and 8% (w/v) sodium alginate solution (pH 6.7; Sinopharm Chemical Reagent Co., Ltd., China) containing 30 $mg{\cdot}mL^{-1}$ CaO_2 (China Pharmaceutical Group Chemical Reagents Company Ltd.) was added to the die. The silk core was then pulled from the small hole and immersed in 3% (w/v) calcium chloride solution (pH 7.1; China Pharmaceutical Group Chemical Reagents Company Ltd.) to form an outer CaO_2 hydrogel sheath. Subsequently, the CaO_2 modified suture was inserted into another conical die with sodium alginate solution containing 4.5 $mg{\cdot}mL^{-1}$ CAT (Beyotime Biotechnology, China) and coated with a CAT hydrogel layer using the previous treatment. CaO_2, CAT, and calcium alginate hydrogel (Alg) sutures were constructed using the same method, however with different hydrogels. The fabrication was performed at room temperature. Sutures were used immediately after they were fabricated; they could be stored at 4 °C by wrapping in plastic wrap and using within 24 h in a special situation.

2.3. Fluorescence labeling of double-layer structure

The double-layer structure of the O_2 suture was labeled with rhodamine B and 123 poly(lactic-*co*-glycolic acid) (PLGA) nanoparticles. The nanoparticles were fabricated using a double emulsion (water/oil/water) solvent evaporation process, as described in our previous study [29]. The nanoparticles were centrifuged at 8000 revolutions per minute (rpm) for 40 min to remove the free dyes. These two fluorescent nanoparticles were mixed in sodium alginate solution and wrapped with silk sutures. The fabricated fluorescence-labeling sutures were embedded in an optimal cutting temperature compound for frozen sections and observed under a fluorescence microscope (FV3000; Olympus Corporation, Japan).

2.4. Suture–sheath bonding test

The bonding between the suture and sheath was tested as previously described [30]. A blank suture was embedded in CaO_2 containing hydrogel. Subsequently, the hydrogel was fixed and the suture was pulled out using a universal tensile-testing machine (68SC-2; Instron, USA). The force and pullout distances were recorded. The adhesion energy between the blank suture and CaO_2 sheath was calculated based on a published equation. The adhesion energy between the blank suture and Alg sheath, and that between the CaO_2 suture and CAT sheath, were calculated using the same method.

2.5. Mechanical characterization of sutures

Suture strength was investigated using the universal tensile-testing machine. Tension strength was determined by the maximal force that the sutures could bear.

2.6. Oxygen-releasing effect of O_2 suture in vitro

The O_2 suture was immersed in phosphate-buffered saline (PBS) (pH 7.4) and the oxygen generation effect of the suture was detected using an oxygen microelectrode (OX-N; Unisence, Denmark). At 6 and 24 h post reaction, the suture was removed from the previous solution and fresh PBS was added to evaluate the continuous oxygen-releasing effect.

The experimental fitting algorithm of the O_2 generating curve was used with Origin Pro 2022 software (v9.9.0.225).

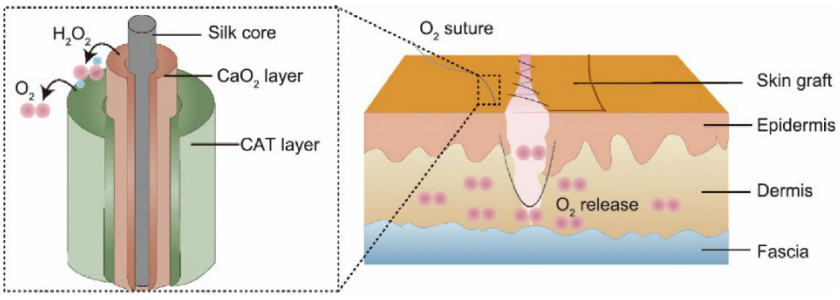


Fig. 1. Schematic of O_2 suture and mechanism to deliver oxygen in skin. CAT: catalase.

2.7. The gelatin hydrogel construction

The gelatin solution (30% w/v) was prepared by water bath at 50 °C for 30 min. The solution was then added to an open plastic pipe (diameter: 13 mm, length: 40 mm) to a height of 20 mm. The solution was held at 4 °C overnight to form the gelatin hydrogel.

2.8. Determination of oxygen transmission efficiency

The oxygen transmission of the porcine skin and gelatin hydrogel at different depths was calculated in a device composed of large and small beakers (volume: 200 and 50 mL). The large beaker was covered with parafilm and filled with pure oxygen to maintain a near-saturated oxygen atmosphere (oxygen flow rate: 1 $L{\cdot}min^{-1}$ for 1 min and then continuously at 30 $mL{\cdot}min^{-1}$). The small beaker was placed inside the large beaker and sealed with parafilm. The gelatin hydrogel containing the plastic pipe or plastic pipe covered with porcine skin was inserted through the parafilm to ensure that oxygen could only enter the small beaker through the gelatin hydrogel or skin. The oxygen electrode was inserted into the small beaker to monitor the oxygen curves inside the small beaker.

2.9. Oxygen penetration in gelatin hydrogel tested by oxygen microelectrode

The oxygen penetration effects of the O_2 sutures and TGO therapy were monitored using the oxygen microelectrode. O_2 sutures were inserted into the center of the gelatin hydrogel and the oxygen curves at different sites were detected by inserting an oxygen microelectrode into different sites. For the TGO therapy test, the gelatin hydrogel was placed in a 200 mL beaker and the oxygen microelectrode was inserted at different sites in the gelatin hydrogel. Pure oxygen was continuously added to the beaker to maintain a nearly maturated oxygen atmosphere. The oxygen curves in the gelatin hydrogel after the TGO therapy were monitored using an oxygen electrode.

2.10. Fick's law with domain discretization

To predict time-dependent oxygen diffusion in the gelatin hydrogel, a two-dimensional model was proposed. In the proposed model, Fick's second law was combined with domain discretization to predict the oxygen evolution of the O_2 suture and TGO system in the gelatin hydrogel. The two-dimensional model represented the central cross-section of the gelatin hydrogel. Owing to the symmetry of the system, half of the entire construction was simulated to conserve computational time and resources. Four hypotheses were assumed in the proposed two-dimensional model to simplify the problems of time and space.

(1) The gelatin hydrogel was assumed incompressible. Gelatin hydrogels are considered nondegradable during oxygen permeation. In addition, the effect of the compression force resulting from the airflow and oxygen probe insertion was neglected.

(2) The oxygen creation rate was assumed to be consistent and uniform in a unit length of the O_2 suture, and the oxygen concentration in each meshed element was assumed to be uniform and perpendicular to the cross-sectional direction. The diffusion of oxygen was assumed to occur only in the x- and y-directions.

(3) The diffusion coefficient was assumed to be constant throughout the entire gelatin hydrogel, and the effect of oxygen pressure on the diffusion coefficient to be neglectable.

(4) The side and bottom edges were wrapped using a sealed film, and it was assumed that no oxygen exchange occurred at these interfaces. Oxygen exchange with the surroundings occurred only at the top edge of both the suture and TGO systems.

In the proposed model, the oxygen concentration evolution was calculated as follows:

$$\frac{\partial C_{i,j}^{t-\Delta t}}{\partial t} = D \cdot \left(\frac{\partial^2 C_{i,j}^{t}}{\partial x^2} + \frac{\partial^2 C_{i,j}^{t}}{\partial y^2} \right) \tag{1}$$

where t is the time, Δt is the time step, $C_{i,j}^{t}$ is the concentration of the oxygen in the i, j position at time t, and D is the oxygen diffusion coefficient in the gelatin hydrogel. In Eq. (1), the left part represents the oxygen exchange of that element at time t; the right part represents the oxygen exchange with its neighboring elements. The Taylor formula was used to solve this equation.

$$\frac{C_{i,j}^{t-\Delta t} - C_{i,j}^{t}}{\Delta t} = D \cdot \left(\frac{C_{i+1,j}^{t} + C_{i-1,j}^{t} - 2C_{i,j}^{t}}{\mathrm{d}x^2} + \frac{C_{i,j+1}^{t} + C_{i,j-1}^{t} - 2C_{i,j}^{t}}{\mathrm{d}y^2} \right) \tag{2}$$

Because the O_2 suture and TGO system were enclosed by a sealed film, the left and right edges were fixed in the model. Therefore, there were five types of boundary conditions: corner, bottom corner, edge, bottom edge, and internal elements, as indicated in Fig. S1 in Appendix A. For example, the internal elements could exchange oxygen with the top, bottom, left, and right elements. The entire meshed element was updated at each calculation time step. Both proposed models were coded using C in Visual Studio 2022 (v17.0.6).

2.11. Live/dead tests of HUVECs (adherent HUVECs and HUVECs in three-dimensional (3D) hydrogel)

HUVECs were cultured in a 1640 medium supplemented with 10% fetal bovine serum (FBS) and 1% penicillin/streptomycin at 37 °C with 5% CO_2.

For the adherent HUVECs test, the HUVECs were seeded in 24-well plates at a density of 150 000 $cells{\cdot}well^{-1}$. After attachment, the cells were divided into seven groups: normoxia (21% O_2), hypoxia (2% O_2), anoxia (<0.5% O_2; blank), anoxia + O_2 suture, anoxia + TGO, anoxia + CaO_2 suture, and anoxia + CAT suture. Different sutures were co-cultured with the HUVECs on the transwell inserts with 8 μm pore-sized filters. For the anoxia + TGO group, the HUVECs were cultured in pure oxygen for 30 min and then cultured in the anoxic chamber (5% CO_2, < 0.5% O_2) at 37 °C. For the hypxia group, the HUVECs were cultured in the hypoxic chamber (5% CO_2, 2% O_2) at 37 °C. These treatments were repeated 24 h after the initial treatment. The HUVECs were stained with calcein-acetoxymethyl ester (AM) (live) and propidium iodide (dead) to evaluate the live/dead status 48 h after the first treatment.

For the HUVECs in 3D hydrogel, a 2% (w/v) sodium alginate solution was sterilized and mixed with a 1640 medium, FBS, and penicillin/streptomycin after cooling to 42 °C. HUVECs were added to the prepared sodium alginate solution at a density of 300 000 $cells{\cdot}mL^{-1}$. HUVEC-sodium alginate solution (1 mL) was added to a confocal cell culture dish (20 mm) and solidified with 250 μL 2% $CaCl_2$ solution to form a 3D hydrogel. The cells were divided into four groups: normoxic, anoxic, anoxic + O_2 suture, and anoxic + TGO. The sutures were embedded in the center of the hydrogel. The HUVECs were stained with calcein-AM (live) and propidium iodide (dead) to evaluate the live/dead status 24 h after treatment.

2.12. Proliferation of HUVECs

HUVECs were cultured in 1640 medium supplemented with 10% FBS and 1% penicillin/streptomycin at 37 °C with 5% CO_2. The cells were seeded into 24-well plates at a density of 50 000 $cells{\cdot}well^{-1}$. After attachment, the cell viability was evaluated using a cell counting kit-8 (CCK-8) test. The cells were then divided

into seven groups, similar to those used in the live/dead test for adherent HUVECs. This treatment was repeated 24 h later. Cell viability was evaluated using the CCK-8 test again 48 h after the first treatment. HUVEC proliferation were analyzed by comparing the CCK-8 results on days 0 and 2.

2.13. Autologous skin graft transplantation

Autologous skin graft transplantation was performed on the backs of mice (BALB/c or C57BL/6). A rectangle of skin (1 cm × 2 cm) was cut on three edges (with one short edge connected), lifted to disconnect the blood supply, and carefully sutured. For graft survival research, the mice were randomly divided into six groups: blank suture, O_2 suture, TGO, alginate suture, CaO_2 suture, and CAT suture. Typically, we sewed approximately ten stitches per flap. For the TGO group, grafts received pure oxygen at a flow of 0.25 L·min ^{1} for 30 min. Images of the transplanted grafts were obtained daily. On days 3 and 6, the mice were euthanized and grafts were collected for further research. For blood perfusion and angiogenesis studies, the mice were randomly divided into four groups: blank suture, O_2 suture, TGO, and alginate. Blood flow was detected using a MoorFLPI (Moor Instruments, UK).

2.14. Histology and immunohistochemistry

Mice were euthanized three or six days post treatment and the skin grafts were embedded in paraffin. Paraffin-embedded tissue was used for the immunohistochemical analysis. Slices of the graft were observed on day 6 using hematoxylin and eosin staining. Graft slices on day 3 were observed using Masson's staining and cluster of differentiation 31 (CD31) incubation. For CD31 incubation, slices were dehydrated and incubated with 3% H_2O_2 to block endogenous peroxidases. After antigen retrieval and blocked with serum, the slices were incubated with anti-CD31 antibody at 4 °C overnight and then incubated with horseradish peroxidase-conjugated secondary goat anti-rat antibody at room temperature for 30 min. Sections were observed and photographed using a microscope connected to a digital camera.

2.15. Statistical analysis

The statistical significance was determined using unpaired and paired two-sided student's *t*-tests for two groups and one-way analysis of variance (ANOVA) for more than three groups; data were presented as single measurements with bars as means ± standard error (SE). Statistically significant *P* values are indicated in the figures and/or legends as $^{****}P < 0.0001$, $^{***}P < 0.001$, $^{**}P < 0.01$, and $^{*}P < 0.05$. NSD indicated no significant differences.

2.16. Data availability

All data supporting the findings of this study are available within the article and Appendix A and from the corresponding author upon reasonable request.

3. Results

3.1. Fabrication and characterization of O_2 sutures

We constructed O_2 sutures through a double-layer wrapping method with commercially available surgical silk sutures. Specifically, we inserted the silk thread core into a conical die with holes at both ends and added a sodium alginate solution containing CaO_2 to the die. The silk core was then removed from the small hole and immersed in a calcium chloride solution to form an outer CaO_2 hydrogel sheath. Subsequently, the CaO_2-modified suture was inserted into another conical die with a sodium alginate solution containing CAT and coated with a CAT hydrogel layer with the previous treatment (Fig. 2(a)). The sutures were verified using a continuous-zoom stereomicroscope. The diameter of the O_2 suture was approximately 0.4 mm, and the hydrogel shell was evenly wrapped around the suture. The O_2 sutures were bent and knotted freely after being wrapped with the hydrogel; the knotting step did not impair the hydrogel on the surface of the O_2 sutures (Fig. 2(b)). The double-layered structure around the suture core was further confirmed by fluorescence labeling (Fig. 2(c)).

Strong bonding between the suture core and sheath is critical to guarantee the integrity of an O_2 suture during surgery. The strong bonding ensures that the hydrogel sheath does not easily fall off the suture surface during surgery. To quantify the bonding between the suture and hydrogel sheath, a pullout test was designed. The sutures were embedded in the hydrogel and pulled out using a universal tensile-testing machine. Both the forces and pullout distances were recorded to quantify the bonding (Fig. 2(d)). The adhesion energy was calculated using a previously published method [30]. The adhesion energy between the silk suture core and CaO_2 hydrogel and that between the CaO_2 suture and CAT hydrogel both exceeded 1000 J·m^{-2} (Fig. 2(e)), indicating strong bonding among all ingredients and excellent O_2 suture integrity.

We further investigated the O_2 suture tensile strength using a universal tensile-testing machine. The curves of the force change with stretching distance are displayed in Fig. S2 in Appendix A. The O_2 sutures achieved a maximum tension of 10 N, which was approximately 1.5 N greater than that of blank sutures (Fig. 2(f)). This could be because the outer sheath helped to maintain the integrity of the sutures. The multifilament sutures were united and jointly counteracted the pulling force, thus exhibiting superior maximum tension.

To detect the oxygen generation, O_2 sutures were immersed in PBS (Fig. 2(g)). The O_2 sutures generated O_2 rapidly after being immersed in the PBS, and the O_2 concentration increased from 280 to approximately 900 μmol·L^{-1} (approaching the saturation of dissolved oxygen) in 2 h. The sutures were removed from the original PBS and reimmersed in fresh PBS. It was found that the O_2 sutures generated oxygen for more than 24 h. In addition, a large number of small bubbles were observed around the sutures after 10 min of immersion, and the sutures floated after 2 h of immersion (Fig. 2(h)), likely owing to the buoyancy provided by the large number of generated oxygen bubbles. The O_2 sutures swelled during water absorption and oxygen production. The diameter of the swollen sutures was approximately 0.8 mm. The O_2 sutures maintained similar oxygen producing ability for 24 h after storage at 4 °C (Fig. S3 in Appendix A).

O_2 sutures were fabricated through double-layer wrapping of the CaO_2- and CAT-containing hydrogels. CAT in the outer layer catalyzes H_2O_2 relieved from the inner layer to provide O_2 and avoids H_2O_2 release. The H_2O_2 release content of the O_2 sutures was maintained at zero in solution. The sutures modified with CaO_2 containing hydrogel released a large amount of H_2O_2 (Fig. S4 in Appendix A). The double-layer wrapping design can prevent cell damage due to the potential oxidative stress caused by H_2O_2.

3.2. Oxygen penetration capability of O_2 sutures

We used a gelatin hydrogel to simulate skin to investigate the oxygen penetration capability of the O_2 sutures. Gelatin is the product of the partial hydrolysis of collagen, which is the main component of skin. A device for measuring the oxygen diffusion was developed (Figs. S5(a)–(c) in Appendix A). The device consisted of internal and external containers. The oxygen concentration in the

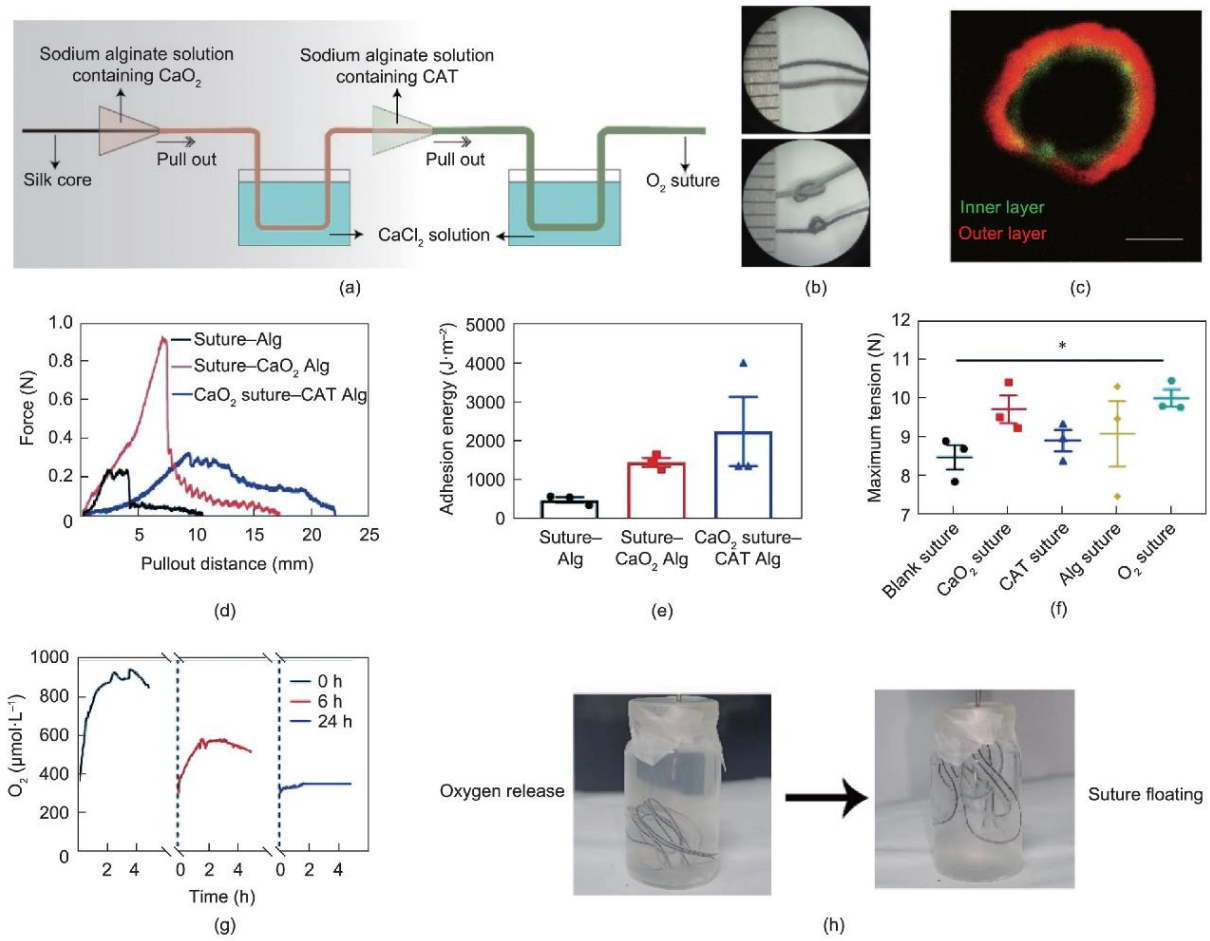


Fig. 2. Fabrication and characterization of O_2 sutures. (a) Schematic of fabrication of O_2 sutures. Hydrogel sheath containing CaO_2 and that containing CAT are in turn coated onto a silk suture core. (b) Microscopic images of blank sutures and O_2 sutures. Upper: unfolded sutures; lower: folded sutures. Minimum scale of ruler is 1 mm. (c) Fluorescence labeling of two-layer sheath of CAT–CaO_2 sutures. Scale bar: 150 μm. (d) Representative force–displacement curves between sutures and hydrogel sheaths tested by pullout tests. Suture represents blank silk suture and CaO_2 suture represents silk suture coated with Alg containing CaO_2 (CaO_2 Alg). (e) Adhesion energy between different sutures and hydrogel sheaths calculated from pullout tests in (d). (f) Maximum tension of sutures with different modification tested by tensile tests. (g) Oxygen production curves of O_2 suture. O_2 suture was taken from original solution and added to fresh PBS at different time points to investigate its long-term oxygen generating effect. (h) Representative images of O_2 sutures in PBS. The image on the left is the appearance ten minutes post O_2 suture insertion, there are a large number of bubbles around the sutures. The image on the right is the appearance 2 h post O_2 suture insertion; the sutures are floating upwards.

internal container was used to represent the oxygen penetration of the skin and gelatin hydrogel. After calibration, a gelatin hydrogel with a thickness of 20 mm was used as the optimal model to simulate actual skin (Figs. S5(d) and (e) in Appendix A). TGO therapy was used as a control for comparison with the O_2 sutures.

It was hypothesized that O_2 sutures could provide deeper oxygen penetration than TGO therapy because the O_2 sutures could pass through the skin (Fig. 3(a)). To test this hypothesis, the oxygen penetration was evaluated using a gelatin-hydrogel skin model. The O_2 sutures were inserted into gelatin hydrogel with a thickness of 20 mm and diameter of 13 mm. Different positions in the gelatin hydrogel were defined using x and y, where x represented the horizontal distance from the O_2 suture (or the center of the hydrogel in the TGO group), and y represented the vertical distance from the surface of the gelatin hydrogel. The oxygen concentrations at different positions in the gelatin hydrogel were then tested (Figs. 3(b)–(g)). At 3600 s post insertion, the oxygen concentration at all positions of the O_2 sutures was greater than 50 $\mu mol·L^{-1}$, which was considerably higher than that at the same positions in the TGO control group. In particular, at positions 2 and 3, the oxygen concentration through the O_2 sutures at 3600 s post insertion was greater than 200 $\mu mol·L^{-1}$, which was considerably higher than that in the TGO control group (< 10 $\mu mol·L^{-1}$). To further evaluate the oxygen diffusion profile of the O_2 sutures, positions with the same x or y values were compared (Figs. 3(h) and (i)). At positions 2 and 3 (same x value), O_2 sutures delivered 50 and 100 times more O_2 than the TGO therapy, respectively. At positions 3, 6, and 7 (same y value), the O_2 sutures delivered 100 times more O_2 than the TGO therapy. These results indicate that O_2 sutures can achieve full-thickness delivery of oxygen to the skin. In particular, O_2 sutures can promote oxygen penetration deeper into gelatin gels, which is not possible with TGO therapy.

3.3. Computational digital simulation of oxygen penetration of O_2 sutures

To further verify our hypothesis that O_2 sutures can achieve full-thickness oxygen penetration and enhance oxygen delivery efficiency in deep skin layers, we compared oxygen distribution in the gelatin hydrogel using a computational simulation method.

Fick's law of diffusion was combined with the domain discretization model to simulate the spatial and temporal evolution

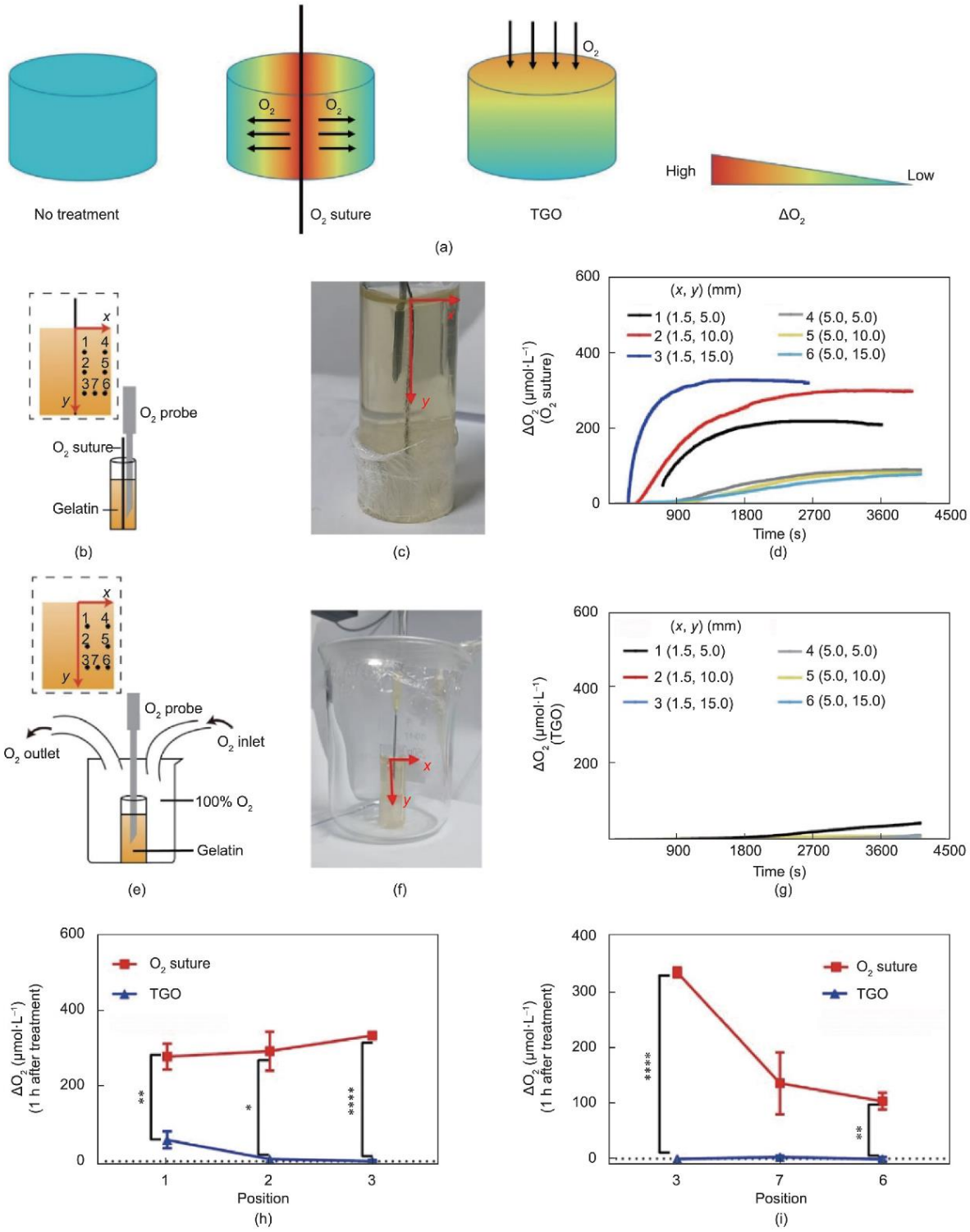


Fig. 3. Comparison of oxygen penetration between O_2 sutures and TGO therapy. (a) Schematic illustration of speculation for oxygen permeability through O_2 suture or TGO therapy in the gelatin hydrogel. (b) Schematic illustration of device to monitor oxygen diffusion through O_2 suture therapy. Oxygen microelectrode was inserted at different positions of the gelatin hydrogel and sutures were inserted in the center of the gelatin hydrogel. Different positions (1, 2, 3, 4, 5, 6, 7) in gelatin hydrogel were defined using x and y, where x represents horizontal distance from O_2 suture and y represents vertical distance from gelatin-hydrogel surface. (c) Image of device to monitor oxygen diffusion through O_2 suture therapy. (d) Oxygen concentration curves for O_2 suture therapy at different positions of gelatin hydrogel. (e) Schematic illustration of device to monitor oxygen diffusion through TGO therapy. Gelatin hydrogel was placed in a container that was continuously filled with oxygen. (f) Image of device to monitor oxygen diffusion through TGO therapy. (g) Oxygen concentration curves for TGO therapy at different positions of gelatin hydrogel. (h) Changes of oxygen concentration (ΔO_2) at different depths of the gelatin hydrogel with the same x value 1 h post treatment. (i) Changes of oxygen concentration (ΔO_2) at different widths of the gelatin hydrogel with the same y value 1 h post treatment. Gelatin hydrogel was used as the simulated skin model. $n = 3$ in (h) and (i).

of the oxygen concentration through O_2 sutures and TGO therapy, respectively (Fig. S1). The parameters used in the proposed model are listed in Table 1 [31]; the rate of O_2 suture-produced oxygen was calculated using Eq. (3). The oxygen production rates of the O_2 sutures and their exponential fitting curves are displayed in Fig. S6 in Appendix A. Representative points in the gelatin hydrogel were selected to validate the proposed model for predicting the evolution of the oxygen concentration (Figs. 4(a)–(c)). The predicted results agreed well with the experimental results obtained using O_2 sutures and TGO therapy, thus validating the reliability of the proposed simulation model.

$$y = -622.51 \cdot \exp\left(-\frac{x}{2387.76}\right) + 597.64 \quad (3)$$

Table 1
The related values of parameters in the proposed model.

Parameters	Values
Gelatin hydrogel depth and width (mm)	H = 20, W = 6.5
Suture length and width (mm)	L_{sur} = 20, W_{sur} = 0.4
Grid size (mm)	dx = 0.1, dy = 0.1
Diffusion coefficient ($m^2 \cdot s^{-1}$)	D = 0.0027 [31]
Convection coefficient ($m \cdot s^{-1}$)	h = 0.005
Time step (s)	Δt = 0.1

After validating the simulation model, the distribution dynamics of released oxygen in the gelatin hydrogel were calculated (Fig. 4(d)). An O_2 suture with a length of 20 mm was inserted into the gelatin hydrogel and compared with TGO therapy. Oxygen in the O_2 suture diffused horizontally, indicating that the concentration of oxygen at positions with the same x value was similar. In the TGO group, oxygen diffused vertically, indicating that the concentrations of oxygen at positions with the same y values were similar. In the O_2 suture group, from 500 to 5000 s, the oxygen concentration increased from 200 to 300 $\mu mol \cdot L^{-1}$ at all positions with x = 1 mm. At 5000 s, the oxygen concentration reached 100 $\mu mol \cdot L^{-1}$ at all positions with x = 5 mm, which is sufficiently high for cell growth and proliferation. In the TGO group, because the oxygen diffused vertically, the concentration of oxygen at positions with y > 10 mm was zero from start to finish. Taken together, these results demonstrate that the O_2 suture had acceptable oxygen perfusion, especially for thick skin tissue.

3.4. Survival and proliferation of anoxic endothelial cells mediated by O_2 sutures

Transplanted tissues experience hypoxia (< 5% O_2, v/v) and anoxia (< 5% O_2, v/v) owing to the poor blood supply and oxygen consumption. Anoxia environments further hamper cell proliferation, cause

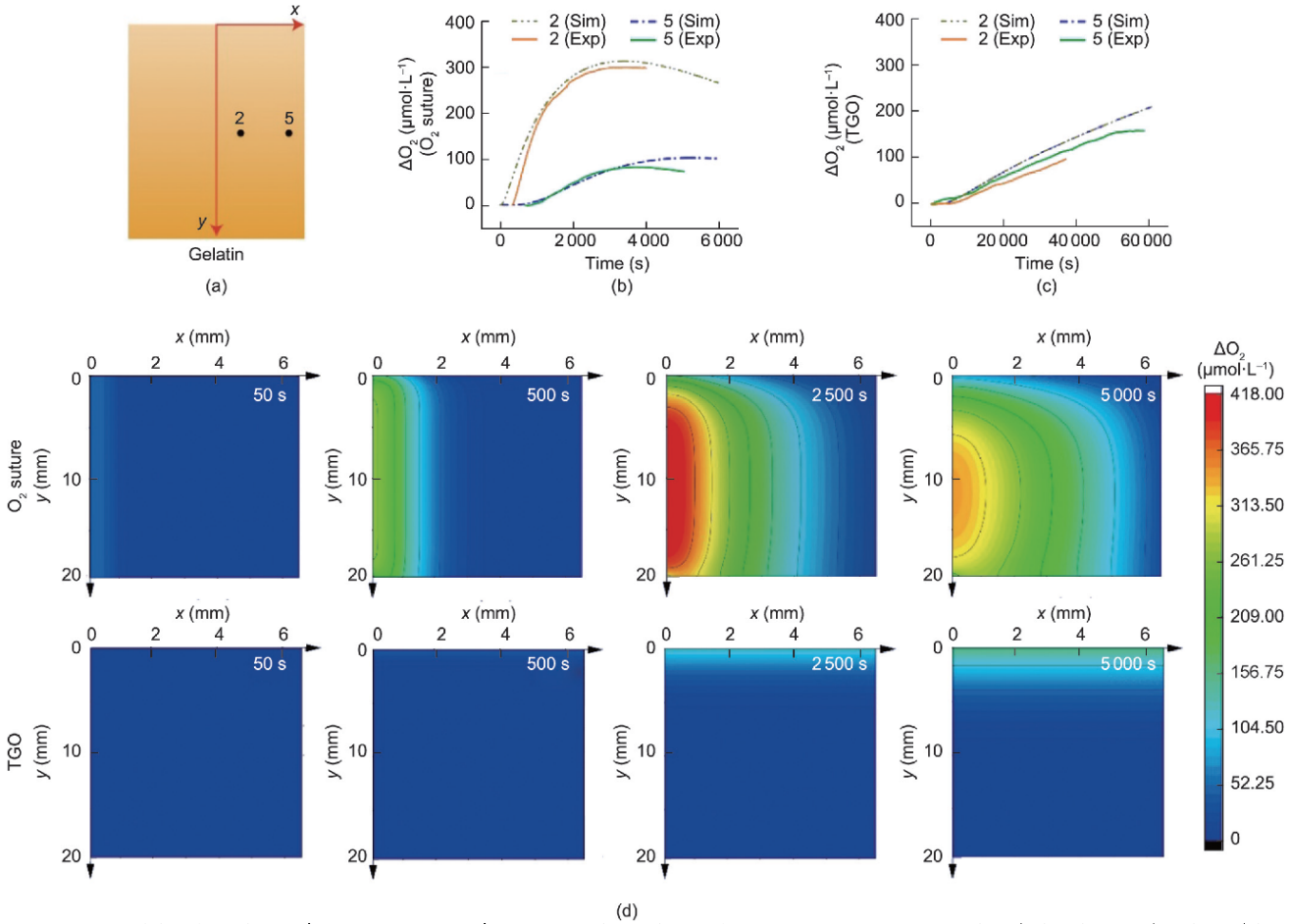


Fig. 4. Computational digital simulation of oxygen penetration of O_2 sutures and TGO therapy. (a) Representative positions in gelatin hydrogel were selected to validate proposed model. Position 2: x = 1.5 mm, y = 10.0 mm; position 5: x = 5.0 mm, y = 10.0 mm. (b) Experimental oxygen curves (Exp) and simulated oxygen curves (Sim) at positions 2 and 5 using O_2 sutures. (c) Experimental oxygen curves (Exp) and simulated oxygen curves (Sim) at positions 2 and 5 using TGO therapy. (d) Simulation results of oxygen distribution in gelatin hydrogel through O_2 sutures (top) and TGO therapy (bottom) varied with time (50, 500, 2500, and 5000 s).

cell death, and limit angiogenesis, both leading to transplantation failure [11,31]. Therefore, we investigated the effects of O_2 sutures on the survival and proliferation of HUVECs under anoxic conditions.

HUVECs were cultured under normoxic, hypoxic, and anoxic conditions. Anoxic HUVECs were divided into different groups and treated with O_2 sutures, CaO_2 sutures, CAT sutures, or TGO therapy separately. Cell survival and death were detected using live/dead tests 48 h after co-culturing (Fig. 5(a)). The HUVEC live/dead rate declined approximately 70% under anoxic conditions, whereas the O_2 suture group maintained cell survival at a live/dead rate similar to that of the normoxic group (Fig. 5(b)). Cell proliferation was also evaluated (Fig. 5(c)). O_2 sutures also promoted HUVEC proliferation under anoxic conditions. To emulate true skin conditions, we seeded HUVECs in 3D hydrogel (2% calcium

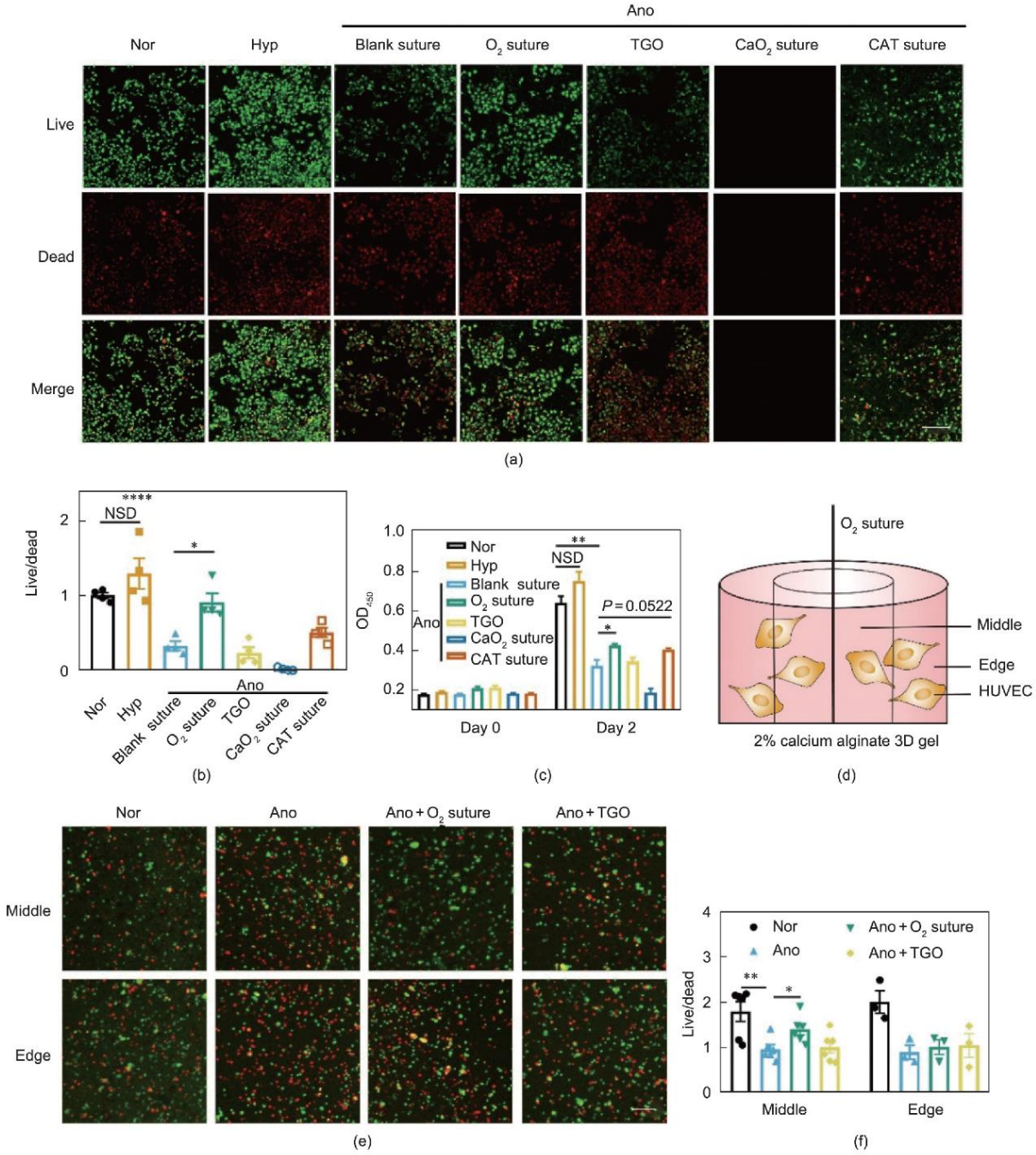


Fig. 5. Promotion of HUVEC survival and proliferation under anoxic conditions induced by O_2 sutures. (a) Representative fluorescent images of adherent HUVECs with different treatments stained with calcein-AM (green, live) and propidium iodide (red, dead). TGO therapy was operated for 0.5 h before culturing cells in anoxia environment. Sutures were put above the trans-well inserts for co-culture with HUVECs. Scale bar: 300 μm. (b) Semi-quantification of relative live/dead rates for HUVECs as displayed in (a). (c) HUVECs proliferation tested by CCK-8 tests. (d) Schematic illustration of HUVECs cultured in 3D hydrogel. O_2 suture was inserted in center. The region with a 5 mm radius around the sutures was considered as the middle and the remaining area was the edge. (e) Representative fluorescent images of HUVECs in 3D hydrogel with different treatments stained with calcein-AM (green, live) and propidium iodide (red, dead). Scale bar: 200 μm. (f) Semi-quantification of live/dead rates for HUVECs as displayed in (e). Nor: normoxia; Hyp: hypoxia; Ano: anoxia; OD_{450}: optical density at 450 nm.

alginate) and inserted O_2 sutures into the hydrogel center (Fig. 5(d)). HUVEC 3D hydrogels were cultured under different O_2 conditions and live/dead rates were detected (Fig. 5(e)). Similar to the case of the adherent cells, the O_2 sutures promoted HUVEC survival in the 3D hydrogels, and the promotion effect was maintained within a radius of 5 mm around the O_2 sutures (Fig. 5(f)).

3.5. Effect of O_2 sutures on the survival, blood perfusion, and angiogenesis of transplanted FTSGs

To investigate whether O_2 sutures could benefit FTSG survival, we evaluated the effects of O_2 sutures in an autologous skin graft transplantation model in BALB/c mice. Rectangular grafts (2 cm long and 1 cm wide) were cut from the backs of the mice, with one short side connected, peeled from the subcutaneous tissue, and sewn with sutures (Fig. 6(a)). The mice were divided into six groups: blank sutures (sewn up with commercial silk sutures), Alg sutures (silk sutures coated with Alg), O_2 sutures, TGO, CaO_2 sutures, and CAT sutures. Owing to the disrupted blood supply and oxygen consumption of the skin grafts from the recipients, the grafts were prone to necrosis, especially at the site distal to the connected edge (Fig. 6(b)). We quantified the necrosis rate of the skin grafts six days after treatment (Fig. 6(c)). The average necrosis rates in blank sutures, Alg sutures, TGO, CaO_2, and CAT sutures were 27.2%, 32.0%, 24.4%, 40.0%, and 30.4%, respectively. Specifically, the necrosis rate in the O_2 suture group declined to

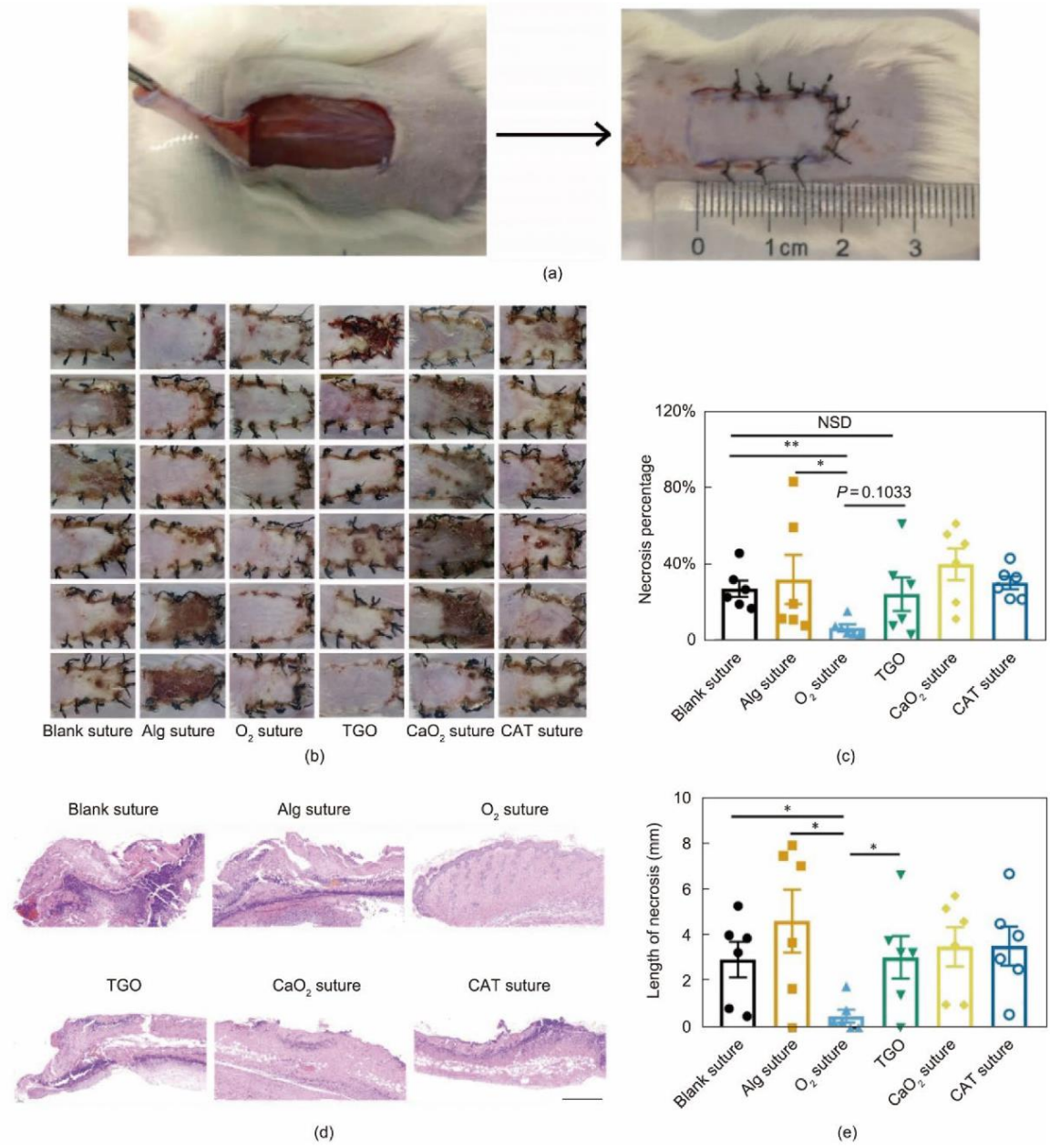


Fig. 6. Transplanted skin graft survival induced by O_2 sutures. (a) Images illustrate progress of autologous skin graft transplantation. (b) Representative images of transplanted skin grafts six days post operation. (c) Quantification of graft necrosis percentage as displayed in (b). (d) Representative hematoxylin and eosin (H&E) images of skin grafts six days later. Scale bar: 500 μm. (e) Quantification of necrosis length of skin graft as displayed in (d), $n = 6$.

only 6.6%, which was considerably less than other groups. We found that the TGO treatment marginally reduced the necrosis rate, which could have been due to poor oxygen delivery efficiency. The CaO_2 sutures exacerbated necrosis, which could have been due to the oxidative stress caused by the released H_2O_2. The deposition of collagen decreased on day 3, whereas that with O_2 suture treatment was maintained (Fig. S7 in Appendix A). On day 6, the necrotic graft lost its intact epithelial structure, and the number of hair follicles decreased. It was confirmed that the O_2 suture treatment preserved the intact epithelial structure and hair follicles (Fig. 6(d)). Moreover, the O_2 sutures decreased necrosis length, with the average necrosis length of 0.52 mm, which was considerably less than the 2.98 mm in the blank suture group (Fig. 6(e)). This positive role in promoting skin graft survival was further confirmed in C57BL/6 mice (Fig. S8 in Appendix A).

We investigated the blood perfusion of skin grafts daily using laser Doppler flowmetry (Fig. 7(a)). Blood flow was plentiful before the experiment; however, it decreased sharply after the experiment owing to the disruption of blood vessels. In particular, limited blood perfusion was more prominent distant from the connected site of the skin. We divided the skin graft into three regions: proximal (near the connected site), middle, and distal (distant from the connected site) (Fig. 7(b)). The relative blood flux at the middle and distal sites relative to that at the proximal sites was quantified (Figs. 7(c)–(e)). Middle and distal blood fluxes in the blank suture group both decreased for approximately 30% post operation and did not recover over the next six days. TGO therapy improved the blood perfusion of the middle site slowly by approximately 10%; however, it could not increase blood flux at the distal site. Surprisingly, we found that the O_2 suture treatment had a positive effect on blood perfusion at both the middle and distal sites. O_2 sutures lightened the reduction in blood flow at the middle sites one day post treatment and maintained this over next time. For the distal sites, although blood flow decreased one day later, it returned to near normal after two days in the O_2 suture group. These results indicate that O_2 suture treatment improved blood re-perfusion in transplanted skin grafts.

To investigate whether O_2 sutures promoted angiogenesis of skin grafts, we quantified blood vessel densities in the blank suture, O_2 suture, TGO, and Alg suture groups using CD31 immunohistochemical staining at three days post treatment. CD31 is a platelet/endothelial cell adhesion molecule widely used to label endothelial cells and evaluate angiogenesis during wound healing [21]. O_2 suture treatment significantly increased the number of CD31 positive vessels. The average vessel density in the O_2 suture group was 2.4 times of that in the blank suture group, 2.2 times

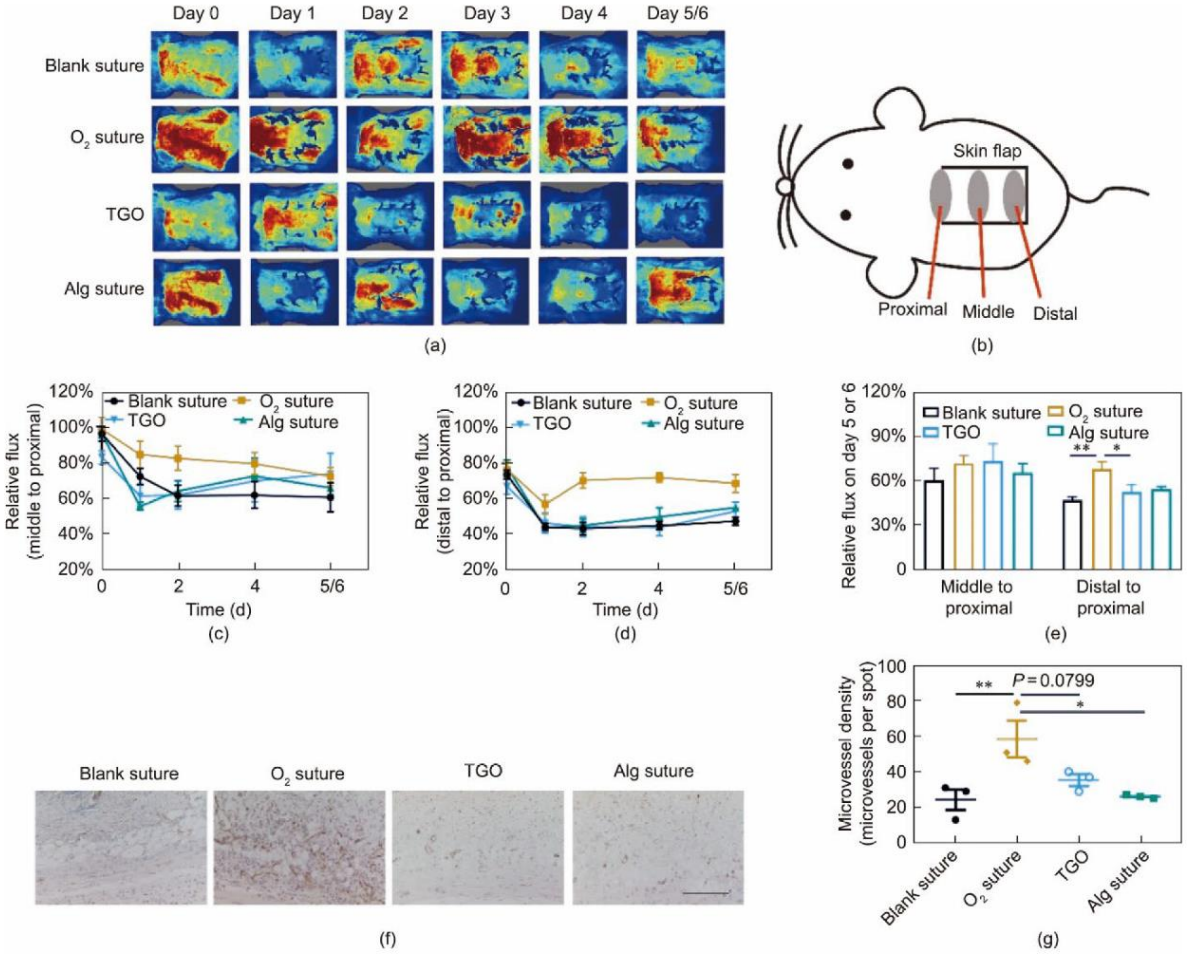


Fig. 7. Re-perfusion and angiogenesis promotion of transplanted skin graft mediated by O_2 sutures. (a) Representative blood flow images captured by laser Doppler flowmetry. (b) Schematic illustration of proximal, middle, and distal sites of skin graft. (c) Curves of relative flux in middle site of grafts. (d) Curves of relative flux in distal site of grafts. (e) Quantification of relative flux five or six days post operation in middle and distal sites. (f) Representative images of CD31 staining three days post operation. Scale bar: 100 μm. (g) Microvessel density of skin grafts three days post operation. In (c)–(e), n = 8 in O_2 suture group, and n = 7 in blank suture, TGO, and Alg suture groups. In (g), n = 3 for each group.

that in the Alg suture group, and 1.6 times that in the TGO group (Figs. 7(f) and (g)). In recent years, the von Willebrand factor (VWF), a hemostatic protein, has been demonstrated to regulate blood vessel formation. The loss of VWF in endothelial cells results in dysfunctional angiogenesis and vascular malformations [33,34]. We investigated VWF expression to evaluate the angiogenesis-promoting effects of the O_2 sutures. The expression of VWF was significantly higher in this group than in the other groups. In particular, VWF expression in the O_2 suture group was 3.9 times that in the blank suture group and twice that in the TGO group (Fig. S9 in Appendix A). These results indicate that O_2 sutures could accelerate angiogenesis after graft transplantation, thus benefiting blood re-perfusion and skin graft survival.

4. Discussion

O_2 sutures were designed to achieve full-thickness oxygen penetration during FTSG transplantation. The oxygen supply in FTSGs is limited by the excessive thickness. It is difficult for new blood vessels to pass through grafts thicker than 0.4 mm quickly and the grafts can suffer from poor oxygen transportation [35]. Thus, FTSG transplantation is restricted by the stringent requirements for an acceptable blood bed [7,36]. Additional oxygen delivery through the skin is important to promote the success of FTSG transplantation, especially for patients in the inferior blood bed group. Existing oxygen delivery strategies such as TGO therapy deliver oxygen from the surface to the deep skin, and their efficiency is hampered by poor oxygen penetration into the skin. O_2 sutures pass through the entire skin layer and remain at the wound site. Unlike existing strategies, they deliver oxygen horizontally throughout the skin. Thus, O_2 sutures can overcome the obstacle of skin thickness and realize full-thickness oxygen delivery, especially by improving oxygen penetration in deep skin.

In particular, O_2 sutures can provide significant benefits in the treatment of abdominal hernias repaired with FTSGs. The recurrence rate of hernia is up to 33% when treated with conventional mesh reinforcement [37]. FTSGs have recently gained attention in large incisional hernia repair. Serious complications in abdominal surgeries, including the incarceration of abdominal contents, impair blood supply, and further limit oxygen delivery [3]. Thus, it is more meaningful to relieve deep anoxia in abdominal FTSGs using O_2 sutures for abdominal hernia repair.

A clinical retrospective study of 1142 free graft procedures indicated that 91% of graft failures occur within a 48 h window, emphasizing the importance of blood perfusion recovery at the early stage of transplantation [35]. Extreme hypoxia (anoxia) inhibits revascularization, which hampers cell metabolism and proliferation [9,10]. The O_2 suture treatment improves endothelial cell survival and promotes endothelial cell proliferation in anoxic environments (Fig. 5). O_2 sutures promoted angiogenesis and blood re-perfusion in the autologous skin graft transplantation models of mice (Fig. 7 and Fig. S9). This is important for skin grafting because it guarantees sustained transport of oxygen and nutrients post transplantation and thus promotes the long-term survival of skin grafts.

Fick's second law combined with domain discretization has been extensively used to predict oxygen or drug diffusion in skin and other tissue [31,38,39]. The proposed 2D oxygen diffusion model using Fick's second law proved effective in predicting the time-dependent oxygen evolution in gel, as evidenced by the successful matching of the experimental results (Figs. 4(b) and (c)). However, the accuracy of the model is somewhat limited owing to the simplified assumptions made in the model, including a constant diffusion coefficient and neglecting the effect of oxygen pressure on the diffusion coefficient. Moreover, the largest deviation observed in the model was less than 19.6 $\mu mol \cdot L^{-1}$ (< 6.3%), which could be due to differences in the oxygen creation rate between the O_2 sutures submerged in PBS and in the gel. Despite these limitations, the proposed model demonstrated promising potential; incorporating more complex factors such as the effect of verifying the diffusion coefficient and oxygen pressure on the diffusion coefficient could improve the model's reliability. In addition, to simulate the entire process in the skin accurately, it is essential to add the oxygen consumption component to the oxygen evolution equation because skin cells consume a portion of oxygen during metabolism while diffusing over distance.

O_2 sutures are expected to realize efficient oxygen delivery along the entire wound edge and induce revascularization between grafts and hosts in clinical applications. We evaluated the maximum oxygen delivery radius of O_2 sutures further to determine the recommended distance between stitches. The effective distance was defined as the point at which the oxygen concentration was greater than 50 $\mu mol \cdot L^{-1}$ in the gelatin hydrogel. As indicated in Fig. S10 in Appendix A, the effective distance for oxygen delivery through the O_2 sutures was approximately 14 mm. Converting to actual skin (3 mm skin being approximately 20 mm gelatin hydrogel), the effective distance was approximately 2.1 mm in the skin. Thus, to ensure sufficient oxygen penetration between the suturing edges, the distance between the stitches should be less than 4.2 mm. In general, the distance between stitches is approximately 5–10 mm in clinical suturing [40]. Thus, the 4.2 mm distances between the stitches of the O_2 sutures would be barely sufficient to ensure oxygenation alongside the wound edge. The O_2 sutures could be further optimized to extend their oxygen delivery distance by optimizing the loaded CaO_2. Moreover, the effect of O_2 sutures on large grafts could be further investigated in the future.

5. Conclusions

We demonstrated that O_2 sutures, which can deliver oxygen deep into the skin, promoted skin graft revascularization and survival. The deep oxygen delivery of the O_2 sutures was examined by combining experimental measurements with a microelectrode and computational digital simulation. O_2 sutures delivered 100 times more oxygen than TGO therapy to the deep skin. Effective oxygen delivery promotes endothelial cell survival and proliferation in anoxic environments. *In vivo* studies demonstrated that O_2 sutures alleviated necrosis in transplanted skin grafts and stimulated angiogenesis and blood re-perfusion, hence improving the success of skin grafting. Our design provides a new approach for deep oxygen delivery in skin grafting, and O_2 sutures should have an excellent possibility to be adopted in clinical applications.

Acknowledgments

This paper was supported by the National Key Research and Development Program of China (2022YFC3401600), the National Natural Science Foundation of China (32171372), the Program A for Outstanding PhD Candidate of Nanjing University (202102A004), the Logistics Research Projects (BWS20J017), and the University of Sydney–China Scholarship Council (USYD-CSC) scholarship (202008320366). We would like to thank Editage (www.editage.cn) for English language editing.

Compliance with ethics guidelines

Wenjing Zai, Yunong Yuan, Lin Kang, Jialong Xu, Yiqiao Hu, Lifeng Kang, and Jinhui Wu declare that they have no competing interests.

Appendix A. Supplementary data

Supplementary data to this article can be found online at https://doi.org/10.1016/j.eng.2023.05.006.

References

[1] Sun BK, Siprashvili Z, Khavari PA. Advances in skin grafting and treatment of cutaneous wounds. Science 2014;346(6212):941–5.
[2] Sen CK, Gordillo GM, Roy S, Kirsner R, Lambert L, Hunt TK, et al. Human skin wounds: a major and snowballing threat to public health and the economy. Wound Repair Regen 2009;17(6):763–71.
[3] Clay L, Stark B, Gunnarsson U, Strigård K. Full-thickness skin graft vs. synthetic mesh in the repair of giant incisional hernia: a randomized controlled multicenter study. Hernia 2018;22(2):325–32.
[4] Winsnes A, Falk P, Gunnarsson U, Strigård K. Full-thickness skin grafts to reinforce the abdominal wall: a cross-sectional histological study comparing intra- and extraperitoneal onlay positions in mice. J Wound Care 2022;31(1):48–55.
[5] Peck MD. Epidemiology of burns throughout the world. Part I: distribution and risk factors. Burns 2011;37(7):1087–100.
[6] Butler KL, Goverman J, Ma H, Fischman A, Yu YM, Bilodeau M, et al. Stem cells and burns: review and therapeutic implications. J Burn Care Res 2010;31(6):874–81.
[7] Andreassi A, Bilenchi R, Biagioli M, D'Aniello C. Classification and pathophysiology of skin grafts. Clin Dermatol 2005;23(4):332–7.
[8] Silva ITS, Menezes HF, Souza Neto VL, Sales JRP, Sousa PAF, et al. Terminological subset of the international classification for nursing practice for patients hospitalized due to burns. Rev Esc Enferm. In press.
[9] Smith MK, Mooney DJ. Hypoxia leads to necrotic hepatocyte death. J Biomed Mater Res A 2007;80(3):520–9.
[10] Malda J, Rouwkema J, Martens DE, Le Comte EP, Kooy FK, Tramper J, et al. Oxygen gradients in tissue-engineered PEGT/PBT cartilaginous constructs: measurement and modeling. Biotechnol Bioeng 2004;86(1):9–18.
[11] Semenza GL. Life with oxygen. Science 2007;318(5847):62–4.
[12] Marks H, Bucknor A, Roussakis E, Nowell N, Kamali P, Cascales JP, et al. A paintable phosphorescent bandage for postoperative tissue oxygen assessment in DIEP flap reconstruction. Sci Adv 2020;6(51):eabd1061.
[13] Lin SJ, Nguyen MD, Chen C, Colakoglu S, Curtis MS, Tobias AM, et al. Tissue oximetry monitoring in microsurgical breast reconstruction decreases flap loss and improves rate of flap salvage. Plast Reconstr Surg 2011;127(3):1080–5.
[14] Al-Waili NS, Butler GJ. Effects of hyperbaric oxygen on inflammatory response to wound and trauma: possible mechanism of action. Sci World J 2006;6:425–41.
[15] Reading SA, Yeomans M, Levesque C. Skin oxygen tension is improved by immersion in oxygen-enriched water. Int J Cosmet Sci 2013;35(6):600–7.
[16] Heyboer 3rd M, Sharma D, Santiago W, McCulloch N. Hyperbaric oxygen therapy: side effects defined and quantified. Adv Wound Care 2017;6(6):210–24.
[17] Chen CY, Wu PW, Hsu MC, Hsieh CJ, Chou MC. Adjunctive hyperbaric oxygen therapy for healing of chronic diabetic foot ulcers. J Wound Ostomy Cont 2017;44(6):536–45.
[18] Dissemond J, Kröger K, Storck M, Risse A, Engels P. Topical oxygen wound therapies for chronic wounds: a review. J Wound Care 2015;24(2):53–4,56–60,62–3.
[19] Gordillo GM, Sen CK. Evidence-based recommendations for the use of topical oxygen therapy in the treatment of lower extremity wounds. Int J Low Extrem Wounds 2009;8(2):105–11.
[20] Tawfick WA, Sultan S. Technical and clinical outcome of topical wound oxygen in comparison to conventional compression dressings in the management of refractory nonhealing venous ulcers. Vasc Endovascular Surg 2013;47(1):30–7.
[21] Chen H, Cheng Y, Tian J, Yang P, Zhang X, Chen Y, et al. Dissolved oxygen from microalgae-gel patch promotes chronic wound healing in diabetes. Sci Adv 2020;6(20):eaba4311.
[22] Ochoa M, Rahimi R, Zhou J, Jiang H, Yoon CK, Maddipatla D, et al. Integrated sensing and delivery of oxygen for next-generation smart wound dressings. Microsyst Nanoeng 2020;6(1):46.
[23] Lewis AS. Eliminating oxygen supply limitations for transplanted microencapsulated islets in the treatment of type 1 diabetes [dissertation]. Cambridge: Massachusetts Institute of Technology; 2008.
[24] Davis SC, Cazzaniga AL, Ricotti C, Zalesky P, Hsu LC, Creech J, et al. Topical oxygen emulsion: a novel wound therapy. Arch Dermatol 2007;143(10):1252–6.
[25] Li J, Zhang YP, Zarei M, Zhu L, Sierra JO, Mertz PM, et al. A topical aqueous oxygen emulsion stimulates granulation tissue formation in a porcine second-degree burn wound. Burns 2015;41(5):1049–57.
[26] Kalidasan V, Yang X, Xiong Z, Li RR, Yao H, Godaba H, et al. Wirelessly operated bioelectronic sutures for the monitoring of deep surgical wounds. Nat Biomed Eng 2021;5(10):1217–27.
[27] Liu M, Zhang Y, Liu K, Zhang G, Mao Y, Chen L, et al. Biomimicking antibacterial opto-electro sensing sutures made of regenerated silk proteins. Adv Mater 2021;33(1):e2004733.
[28] Zhu J, Jin Q, Zhao H, Zhu W, Liu Z, et al. Reactive oxygen species scavenging sutures for enhanced wound sealing and repair. Small struct 2021;2(7):2100002.
[29] Zai W, Kang L, Dong T, Wang H, Yin L, Gan S, et al. *E. coli* membrane vesicles as a catalase carrier for long-term tumor hypoxia relief to enhance radiotherapy. ACS Nano 2021;15(9):15381–94.
[30] Ma Z, Yang Z, Gao Q, Bao G, Valiei A, Yang F, et al. Bioinspired tough gel sheath for robust and versatile surface functionalization. Sci Adv 2021;7(15):eabc3012.
[31] Wang LH, Ernst AU, An D, Datta AK, Epel B, Kotecha M, et al. A bioinspired scaffold for rapid oxygenation of cell encapsulation systems. Nat Commun 2021;12(1):5846.
[32] Farzin A, Hassan S, Teixeira LSM, Gurian M, Crispim JF, Manhas V, et al. Self-oxygenation of tissues orchestrates full-thickness vascularization of living implants. Adv Funct Mater 2021;31(42):2100850.
[33] Ishihara J, Ishihara A, Starke RD, Peghaire CR, Smith KE, McKinnon TAJ, et al. The heparin binding domain of von Willebrand factor binds to growth factors and promotes angiogenesis in wound healing. Blood 2019;133(24):2559–69.
[34] Randi AM, Laffan MA. von Willebrand factor and angiogenesis: basic and applied issues. J Thromb Haemost 2017;15(1):13–20.
[35] Chen KT, Mardini S, Chuang DCC, Lin CH, Cheng MH, Lin YT, et al. Timing of presentation of the first signs of vascular compromise dictates the salvage outcome of free flap transfers. Plast Reconstr Surg 2007;120(1):187–95.
[36] Davis JS. Address of the president: the story of plastic surgery. Ann Surg 1941;113(5):641–56.
[37] Holmdahl V, Stark B, Clay L, Gunnarsson U, Strigård K. Long-term follow-up of full-thickness skin grafting in giant incisional hernia repair: a randomised controlled trial. Hernia 2022;26(2):473–9.
[38] Willemen NGA, Hassan S, Gurian M, Jasso-Salazar MF, Fan K, Wang H, et al. Enzyme-mediated alleviation of peroxide toxicity in self-oxygenating biomaterials. Adv Healthc Mater 2022;11(13):e2102697.
[39] Yuan Y, Han Y, Yap CW, Kochhar JS, Li H, Xiang X, et al. Prediction of drug permeation through microneedled skin by machine learning. Bioeng Transl Med 2023;10512:e10512.
[40] Kudur MH, Pai SB, Sripathi H, Prabhu S. Sutures and suturing techniques in skin closure. Indian J Dermatol Ve 2009;75(4):425–34.

Supplementary Information

Oxygen Penetration through Full-Thickness Skin by Oxygen-Releasing Sutures for Skin Graft Transplantation

Wenjing Zai [a,c,#], Yunong Yuan [b,#], Lin Kang [a,f,#], Jialong Xu [a], Yiqiao Hu [a], Lifeng Kang [b], Jinhui Wu [a,d,e,*]

[a] *State Key Laboratory of Pharmaceutical Biotechnology, Medical School, Nanjing University, Nanjing 210093, China*

[b] *School of Pharmacy, Faculty of Medicine and Health, University of Sydney, Sydney, NSW 2006, Australia*

[c] *School of Biomedical Engineering, Shanghai Jiao Tong University, Shanghai 200240, China*

[d] *Chemistry and Biomedicine Innovation Center, Nanjing University, Nanjing 210023, China*

[e] *Jiangsu Provincial Key Laboratory for Nano Technology, Nanjing University, Nanjing 210093, China*

[f] *Jiangsu Food & Pharmaceutical Science College, Huai'an 223003, China*

[#] These authors contributed equally to this work.

* Corresponding author.

E-mail address: wuj@nju.edu.cn (J. Wu)

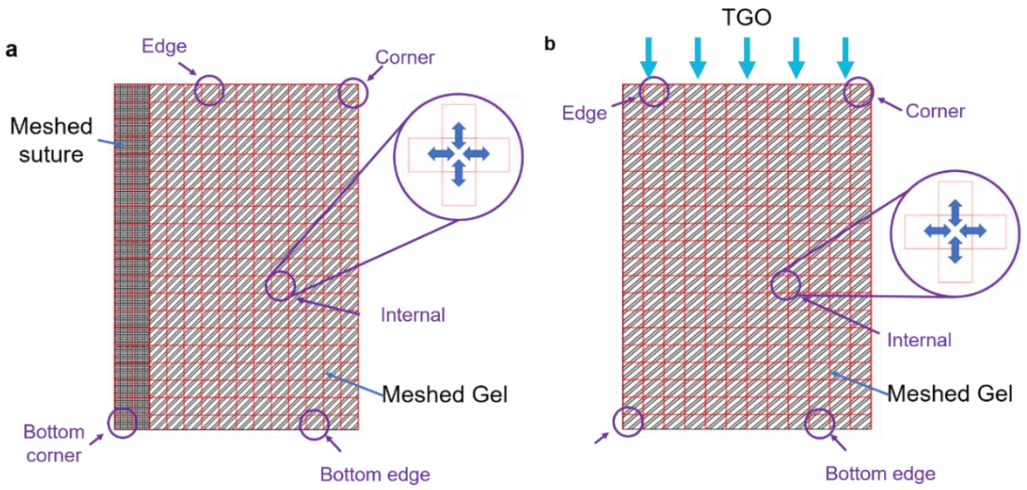


Fig. S1. (a) Meshed suture and gelatin-hydrogel (Gel) system with different boundary conditions. (b) Meshed TGO system with different boundary conditions.

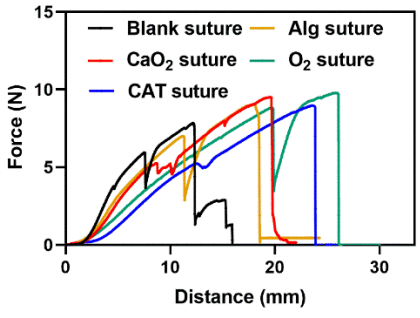


Fig. S2. Curves of force with tensile displacement.

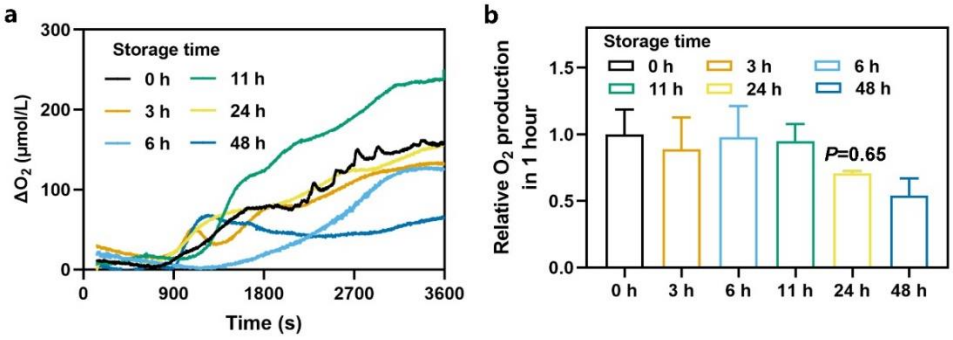


Fig. S3. Oxygen production of O_2 sutures after storage at 4 °C for different time. (a) Oxygen production curves of O_2 sutures stored in plastic wrap at 4 °C for different time. (b) Relative oxygen production in one hour of O_2 sutures stored for different time (relative to oxygen producing amount of O_2 suture stored for zero hour), n = 3 for each group.

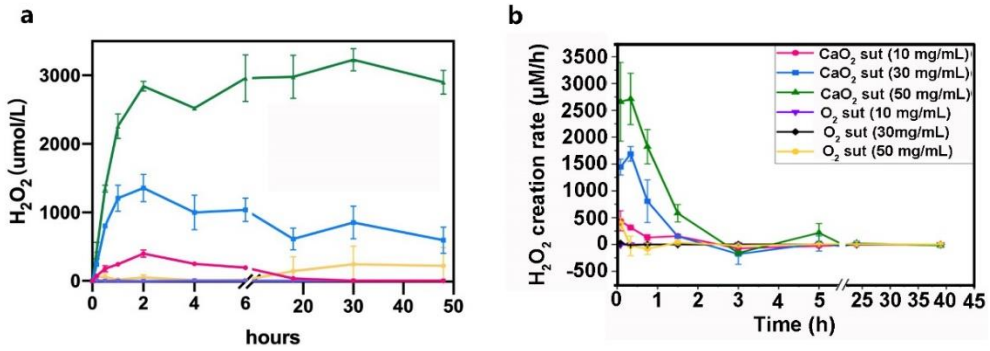


Fig. S4. Hydrogen peroxide concentration curves (a) and creation rate curves (b) of CaO_2 sutures and O_2 sutures.

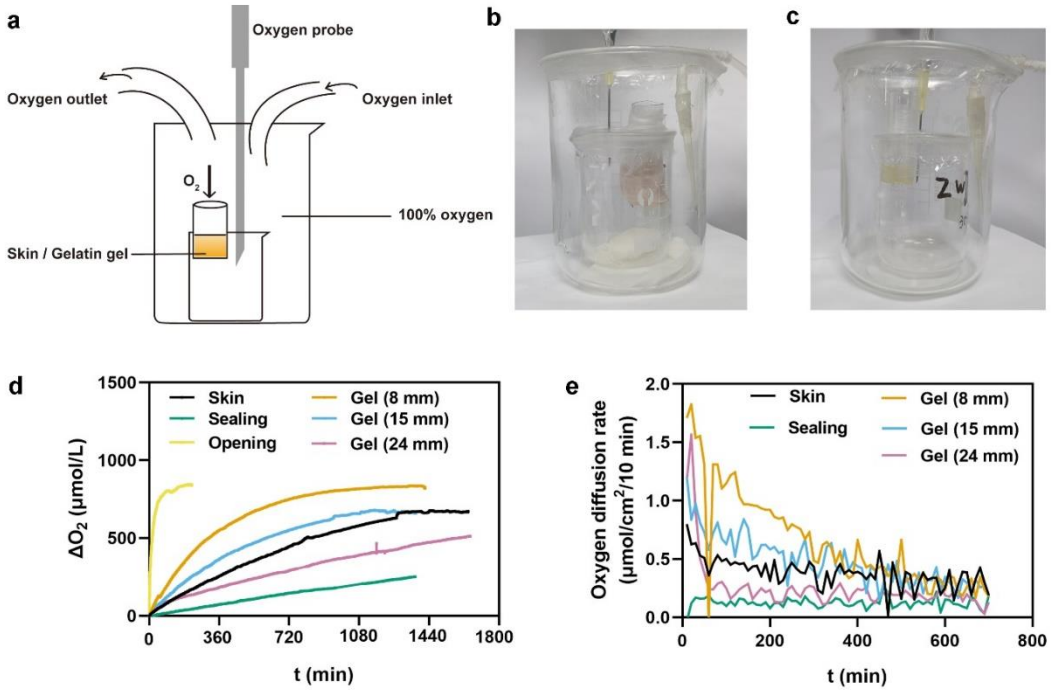


Fig. S5. Oxygen diffusion rates of real skin and the gelatin hydrogel (Gel) with different thicknesses. (a) Schematic illustration of equipment to measure oxygen diffusion rate. (b) Image of equipment to measure oxygen diffusion rate through skin. (c) Image of equipment to measure oxygen diffusion rate through Gel. (d) Oxygen curves in inside container. (e) Oxygen diffusion rate curves.

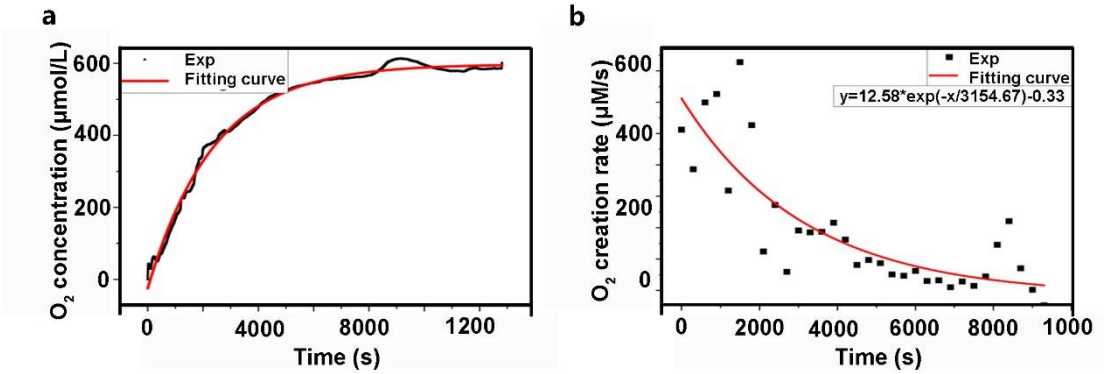


Fig. S6. (a) Oxygen concentration (black) and exponential fitting (red) curves of O_2 suture. (b) Oxygen creation rate of O_2 suture.

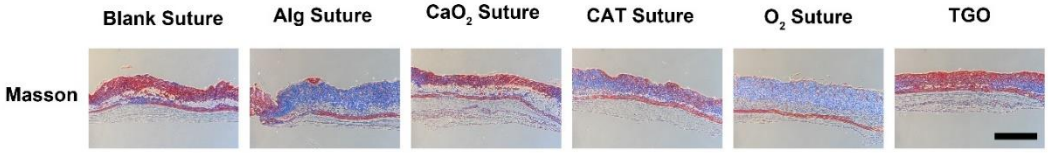


Fig. S7. Masson staining of skin grafts on Day 3. Scale bar = 1000 μm.

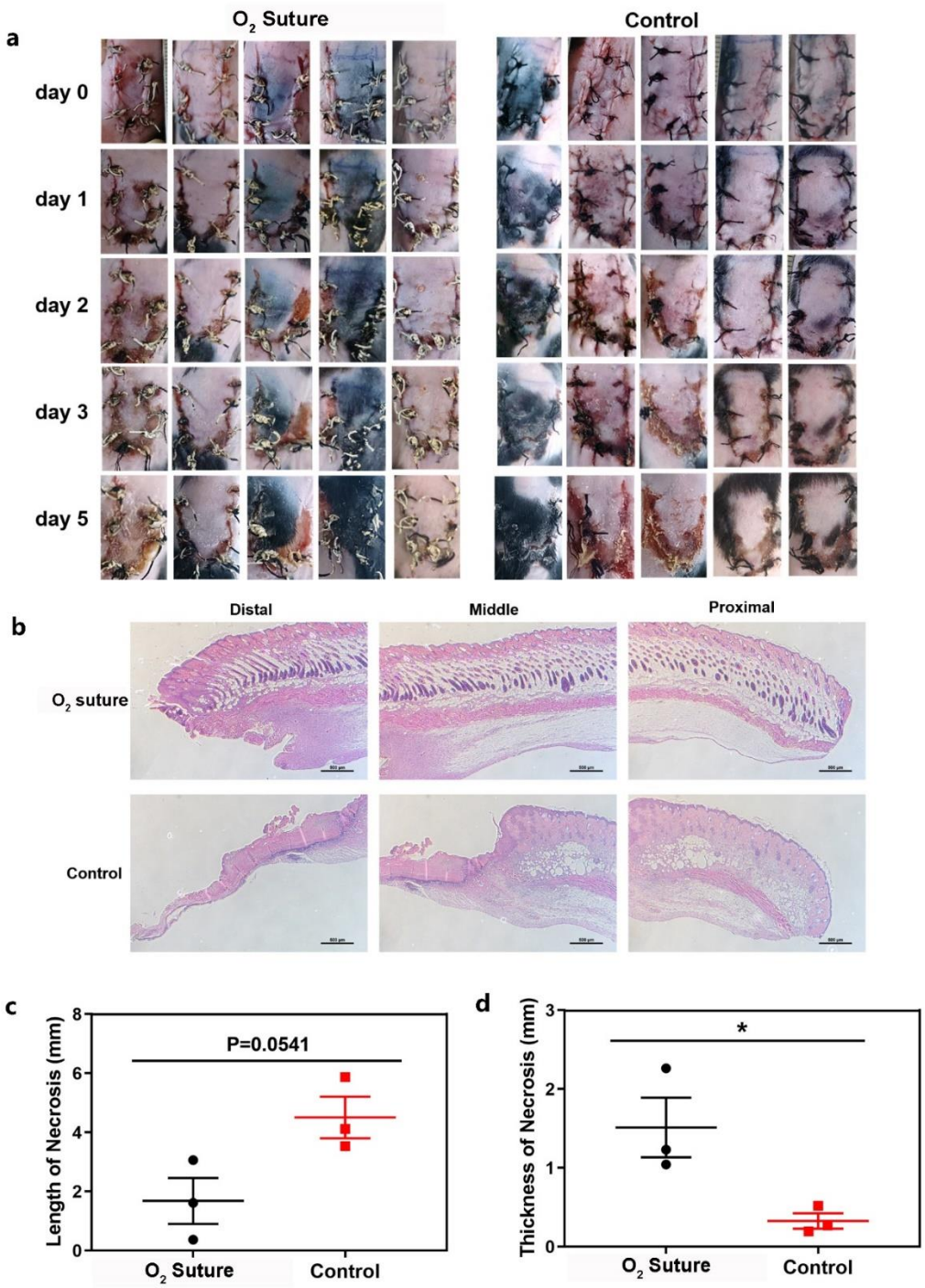


Fig. S8. Skin graft survival in C57BL/6 mice. (a) Images of transplanted skin grafts on C57BL/6 mice. (b) Representative H&E images of skin grafts. Scale bar: 500 μm. (c) Quantification of necrosis length of skin graft as displayed in (b). (d) Quantification of thickness of necrosis skin grafts as displayed in (b), $n = 3$ in (c) and (d).

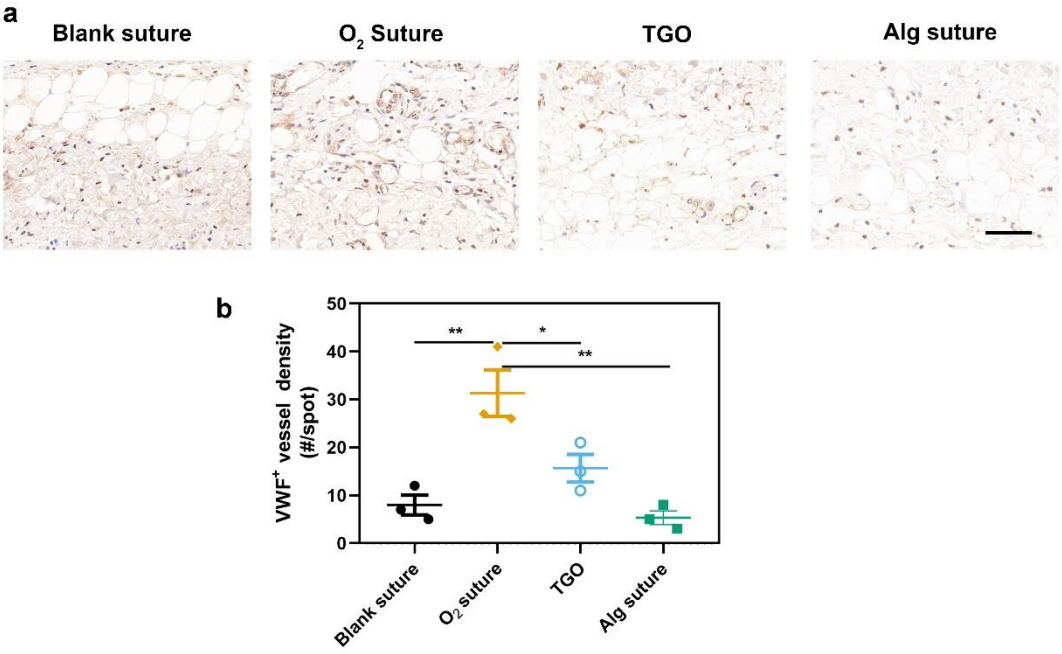


Fig. S9. (a) Representative images of VWF staining of skin grafts. Scale bar: 60 μm. (b) Quantification of VWF positive vessel densities of skin grafts, $n = 3$.

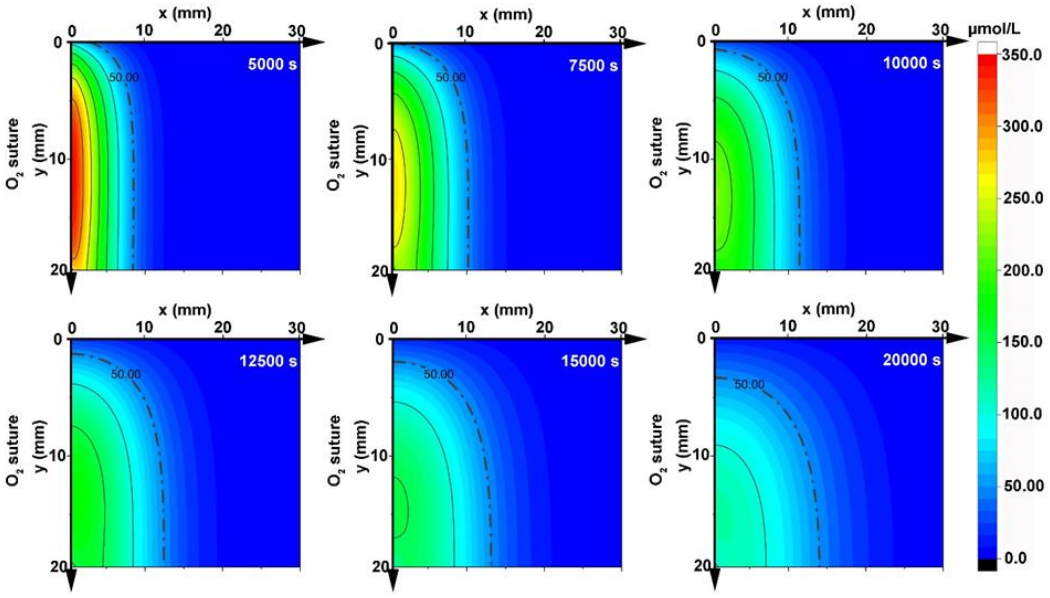


Fig. S10. Simulation results of oxygen distribution in Gel through O_2 sutures varied with time: 5000 s (top left); 7500 s (top middle); 10000 s (top right); 12500 s (bottom left); 15000 s (bottom middle); 20000 s (bottom right). Dotted line represents O_2 concentrations of 50 μmol·L^{-1}.

Chapter 6 Prediction of Drug Permeation Through Microneedled Skin by Machine Learning

This chapter contains the following publication:

> **Y Yuan**, Y Han, CW Yap, JS Kochhar, H Li, X Xiang, L Kang, Prediction of drug permeation through microneedled skin by machine learning, Bioengineering & Translational Medicine 8 (6), e10512. https://doi.org/10.1002/btm2.10512

Check for updates

Received: 11 November 2022 | Revised: 22 February 2023 | Accepted: 8 March 2023

DOI: 10.1002/btm2.10512

RESEARCH ARTICLE

BIOENGINEERING & TRANSLATIONAL MEDICINE

Prediction of drug permeation through microneedled skin by machine learning

Yunong Yuan[1] | Yiting Han[2,3] | Chun Wei Yap[4] | Jaspreet S. Kochhar[5] | Hairui Li[6] | Xiaoqiang Xiang[2] | Lifeng Kang[1]

[1]School of Pharmacy, Faculty of Medicine and Health, University of Sydney, New South Wales, 2006, Australia

[2]Department of Clinical Pharmacy and Pharmacy Administration, School of Pharmacy, Fudan University, Shanghai, 201203, China

[3]Harvard T.H. Chan School of Public Health, 677 Huntington Avenue, Boston, Massachusetts 02115, USA

[4]National Healthcare Group, 1 Fusionopolis Link, Singapore 138542, Singapore

[5]Procter & Gamble, 70 Biopolis Street, Singapore 138547, Singapore

[6]MGI Tech, 21 Biopolis Road, Nucleos, Singapore 138567, Singapore

Correspondence
Xiaoqiang Xiang, Department of Clinical Pharmacy and Pharmacy Administration, School of Pharmacy, Fudan University, Shanghai, 201203, China.
Email: xiangxq@fudan.edu.cn

Lifeng Kang, School of Pharmacy, Faculty of Medicine and Health, University of Sydney, NSW, 2006, Australia.
Email: lifeng.kang@sydney.edu.au

Funding information
China Scholarship Council, Grant/Award Number: 202008320366; University of Sydney, Grant/Award Number: PCA2019

Abstract

Stratum corneum is the outermost layer of the skin preventing external substances from entering human body. Microneedles (MNs) are sharp protrusions of a few hundred microns in length, which can penetrate the stratum corneum to facilitate drug permeation through skin. To determine the amount of drug delivered through skin, in vitro drug permeation testing is commonly used, but the testing is costly and time-consuming. To address this issue, machine learning methods were employed to predict drug permeation through the skin, circumventing the need of conducting skin permeation experiments. By comparing the experimental data and simulated results, it was found extreme gradient boosting (XGBoost) was the best among the four simulation methods. It was also found that drug loading, permeation time, and MN surface area were critical parameters in the models. In conclusion, machine learning is useful to predict drug permeation profiles for MN-facilitated transdermal drug delivery.

KEYWORDS
machine learning, microneedle, multiple linear regression, random forest, transdermal, XGBoost

1 | INTRODUCTION

A microneedle (MN) patch consists of an array of MNs of a few hundred microns in length, made of biocompatible materials, such as metals or polymers.[1] These MNs can enhance drug permeation into the skin and/or main circulation, by creating multiple micron-sized passages through skin, a formidable biological barrier preventing external substances from entering human body.[2–5] Owing to the simple concept of MN and technological feasibility of MN fabrication, MN has been extensively studied as a device to deliver into human a variety of therapeutic agents, for example, small-molecule compounds,[6,7] peptides,[8–10] mRNA,[11] proteins,[12] and extracellular vesicles.[13]

To determine the amount of drug entering human via skin, in vitro skin permeation testing can be performed. In such testings, the MN patch is mounted onto animal or human skin grafts in vitro,

This is an open access article under the terms of the Creative Commons Attribution License, which permits use, distribution and reproduction in any medium, provided the original work is properly cited.
© 2023 The Authors. *Bioengineering & Translational Medicine* published by Wiley Periodicals LLC on behalf of American Institute of Chemical Engineers.

which are then placed in a Franz-type diffusion device to monitor drug concentrations at different time points.[14] The results from the tests can reveal the amount of drug penetrating skin as a function of time, which is critical to evaluate the performance of a MN patch, in terms of drug dose and therapeutic efficacy. However, it is costly and time-consuming to perform such tests.[15]

To address this issue, simulation methods have been explored, that is, to predict drug permeation profiles using predictors, instead of conducting in vitro skin permeation experiments. In our previous study of a topical formulation, a multiple linear regression (MLR) model was constructed to link the permeability rate of the drug to the physicochemical properties of an excipient used in the formulation.[16] With the established model, it was shown that the predicted values were good fits of the experimental results. The MLR model allows the prediction of the performance of the excipient, namely, skin penetration enhancers, without the need to conduct in vitro experiments using scarce human skin samples.

The prior study has motivated us to apply this method onto MN-facilitated transdermal delivery, that is, to simulate the process and predict drug permeation through skin without performing in vitro skin permeation testing. Apart from the MLR method, additional machine learning methods were also investigated, because MN-facilitated drug permeation profiles are more complex than those found in conventional topical dosage forms, hence advanced machine learning models may offer better predictions than the MLR model.

Machine learning is a subset of artificial intelligence, which builds a model based on the training data set to make predictions or decisions. Machine learning has been studied in various areas in medicine, such as cancer diagnostics, antibiotic synthesis, chemical reaction optimization, and protein structural prediction.[17–25] In the field of drug delivery, it also found many applications. For example, a machine learning model was proposed to predict the potential drug–drug interactions, in terms of pharmacokinetic parameter changes of the patients.[26] It can be used to evaluate drug–drug interactions before clinical trials, potentially useful for drug discovery and development.

Recently, machine learning has been used to optimize MN design and fabrication. For example, a deep learning (a subset of machine learning) method was used to aid the fabrication of MN patches. The model can be used to find efficient procedures for MN fabrication prior to actual production, saving materials and resources.[27] In another example, drug diffusion from a polymeric MN patch was simulated, using surface erosion theory and Fick's law.[28] The model allows users to optimize the MN design without fabricating the MN patch. Considering these recent developments, we hypothesize this approach can be used to predict drug permeation through skin.

In this study, machine learning was used to simulate the process of MN facilitated transdermal drug delivery and predict drug permeation through skin. The parameters in the models include MN features and the physicochemical properties of the drugs. The data points used in model training were collected from our previous studies on MN facilitated transdermal drug delivery, ensuring data consistency. Three machine learning methods were used, namely, first-order MLR, random forest (RF), and extreme gradient boosting (XGBoost). In addition, a simulation method based on Fick's law was also included as a comparison. The key parameter used in Fick's law model was not obtained by using the training data set but from literature. To our knowledge, this is the first study to predict the drug permeation through MN-treated skin using machine learning methods.

2 | METHODS

2.1 | Data collection

In our previous studies on MN-facilitated transdermal drug delivery, we performed in vitro skin permeation experiments using similar protocols and devices for six different drugs/chemicals, namely, caffeine, copper, peptide, bovine serum albumin (BSA), lidocaine, and rhodamine. During the experiments, the time course of drug permeation through skin was determined by using Franz-type of diffusion devices. The data points from those studies were compiled into a single database.

For copper[9] and peptide,[9] the data are based on plastic MNs, obtained by Li et al. For caffeine,[29] BSA,[30] and rhodamine,[31] the skin permeation data are based on hydrogel MNs, obtained by Neo and Kochhar et al. For lidocaine, the skin permeation data are based on both plastic MNs and hydrogel MNs, obtained by Kochhar[12] and Li et al.[32] The whole data set can be found in Data S1.

2.2 | Overview of the simulation methods

The four methods are illustrated in Figure 1. For Fick's law, a two-dimensional model representing the central cross-section of the MN and skin was used to predict drug permeation through skin, as shown in Figure 1a. The diagram illustrates a typical setup used for in vitro skin permeation testing, where the MN was applied onto skin. The drugs encapsulated in the MN will diffuse into the skin tissue and in turn diffuse into the receptor solution. The drug concentration inside the receptor solution was measured at different time points to obtain the cumulative amount of drug permeated through skin.

For all four methods, the dependent variable is the cumulative percentage/amount of drug permeated through skin. The descriptors, such as permeation time and MN features, were used to predict the percentage/amount of drug permeated through skin. In the first order MLR model, the dependent variable was assumed to be linearly correlated to the descriptors, as shown in Figure 1b. The linear assumption may not be valid, but MLR can provide a simple model for prediction. The RF and XGBoost methods are based on the decision trees, as shown in Figure 1c,d.

The data points collected from the in vitro skin permeation testing were randomly divided into the training set and test set. The training set was used to build the models in the machine learning algorithm, while the test set was used to verify the robustness and precision of the models, namely, MRL, RF, and XGBoost.

23806761, 2023, 6, Downloaded from https://aiche.onlinelibrary.wiley.com/doi/10.1002/btm2.10512 by University Of Sydney, Wiley Online Library on [18/06/2024]. See the Terms and Conditions (https://onlinelibrary.wiley.com/terms-and-conditions) on Wiley Online Library for rules of use; OA articles are governed by the applicable Creative Commons License

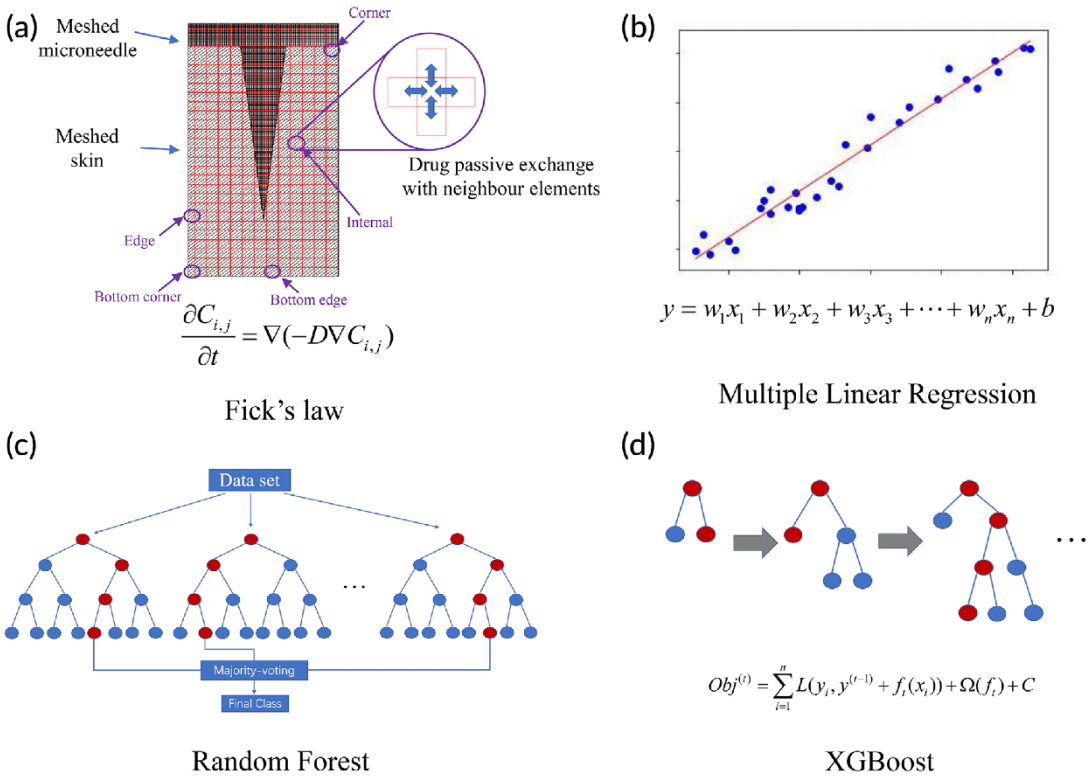


FIGURE 1 Four methods were used to predict drug permeation through skin: (a) Fick's law; (b) multiple linear regression; (c) random forest; and (d) XGBoost.

2.3 | Fick's law

During the process of drug permeation through skin, the drug concentration in the receptor compartment of the Franz diffusion device can be calculated by using Fick's second law of diffusion, as shown in Equation (1):

$$\frac{\partial C}{\partial t} = D\left(\frac{\partial^2 C}{\partial x^2} + \frac{\partial^2 C}{\partial y^2}\right). \quad (1)$$

In Equation (1), C is the concentration of the drug at time t while D is the diffusion coefficient. With initial and boundary conditions given, as those in skin permeation experiments, an analytical solution can be obtained from Equation (1), for non-MN facilitated drug permeation through skin.[33,34] However, the drug permeation process becomes complex when MNs were inserted into skin membrane. In this case, it is challenging and/or unnecessary to obtain an analytical solution, as drug concentrations inside skin depend not only on skin depth but also the geometry of the MNs. To this end, numerical solutions based on domain discretization can be useful, as they approximate the differential equation's solution and calculate each subdomain rather than over the entire domain. Recently a study reported numerical solutions for MN-facilitated drug permeation through skin method, using a commercial software (COMSOL Multiphysics).[35] In this study, we use C language to write the model to obtain a numerical solution to Equation (1) for MN-facilitated drug permeation.

To simplify the modeling process, we used a two-dimensional model to represent the 3D MN-skin system, as shown Figure 1a. The 2D model shows the cross-section of the MN and the total amount of drug in the 3D MN is evenly distributed on the 2D surface. An MN patch normally consists of multiple identical MNs with fixed spacing between each MN. For modeling purpose, we assume that each MN-skin unit, as shown in Figure 1a, is independent of other MN-skin units in the mesh and considered as a repeating unit. Hence, there are five types of mesh elements, namely, corner, bottom corner, edge, bottom edge, and internal elements, as shown in Figure 1a. For each type of element, their boundary conditions are different. For instance, the internal element shown in Figure 1a will exchange the drug with its top, down, left, and right elements while the edge element will exchange the drug with its top, down, and right element, but there is no left element to exchange with. The exchange of drug can be calculated with concentration gradient multiplied by diffusion coefficient.

Based on this model, the left part of Equation (1) represents the drug concentration in an arbitrary element varied with time. The right part of Equation (1) represents the drug exchange of that element with its neighbor elements. Equation (1) can be solved by using Taylor's formula to calculate drug concentration in each element.[36] The drug concentration in each element of whole meshed MN-skin system can be updated with every time step. Once the drug molecules gradually permeate through skin and reach the receptor liquid, the amount of drug in the receptor, at a certain time point, can be calculated by multiplying the volume of the receptor solution with the drug

23806761, 2023, 6, Downloaded from https://aiche.onlinelibrary.wiley.com/doi/10.1002/btm2.10412 by University Of Sydney, Wiley Online Library on [18/06/2024]. See the Terms and Conditions (https://onlinelibrary.wiley.com/terms-and-conditions) on Wiley Online Library for rules of use; OA articles are governed by the applicable Creative Commons License

concentration at that time point. Afterwards, the total amount of drug in the receptor solution can be obtained by multiplying the amount of drug from one MN with the total number of MNs on one MN patch.

The cumulative amount of permeated drug was defined as the amount of drug through an area of 1 cm^2, which refers to the diffusion window between the donor compartment and receptor compartment in the diffusion device. In our previous in vitro skin permeation experiments, two types of Franz diffusion devices were used, that is, vertical diffusion device and horizontal diffusion device. In the vertical diffusion device,[9] the diffusion area is 1 cm^2 and the horizontal diffusion area[12] is 1.13 cm^2. So, the experimental cumulative amount of drug was normalized to be through an area of 1 cm^2.

The cumulative drug permeation percentage is calculated by the cumulative amount of permeated drug from time zero to t (m_t), divided by the total amount of drugs impregnated inside the MN (m_{total}), as shown in Equation (2):

$$\text{Permeation percentage} = \frac{m_t}{m_{total}} \times 100\%. \quad (2)$$

In this model, five assumptions were made to simplify the modeling process. First, the shape of the MN is incompressible. The MN is seen as nondegradable and not compressible after it is inserted into skin. Second, the drugs in MN are uniformly distributed. Moreover, the drug concentration in each element is uniform. The drug diffuses in X and Y directions only, as this is a 2D model. Third, the diffusion coefficient of the drug is constant in skin, and the temperature effect is neglectable, as the skin permeation study is normally held at human body temperature. Fourth, the permeated drugs will not block the interface between skin and the receptor solution in the Franz device. The drugs will be instantly distributed to the receptor solution after they penetrate the skin membrane, as stirring is always provided in the receptor compartment in our drug permeation experiments. Fifth, the skin thickness is assumed to be 1 mm for all experiments. This is reasonable as the MN is of a few hundred microns in length while the skin membrane is ~1 mm thick.

2.4 | Multiple linear regression (MLR)

MLR is a regression model estimating a dependent variable based on multiple independent variables (Figure 1b). For a simple linear regression model, the formulation includes a response (y) and one variable (x), a slope (k) and an intercept (b), as shown in Equation (3). MLR extends one variable in linear regression to multiple variables. All variables contribute to the response. The formula of MLR is given in Equation (4).

$$y = kx + b, \quad (3)$$

$$y = k_1x_1 + k_2x_2 + \cdots + k_nx_x + b. \quad (4)$$

2.5 | Random forest (RF)

RF is based on the decision tree method, as shown in Figure 1c. The RF model consists of multiple trees, and each tree is independent of other trees. A decision tree starts to build from the root node to the sub-nodes until it meets the maximum layer, or no features can be used. During the process of construction of a decision tree, several critical experimental features are selected by the model. This process is repeated several times, producing multiple trees. The output result of an RF model is the majority voting for classification or the average value for regression. The contribution of each feature to the RF model is different. The greater the importance of a feature, the more frequently it would be selected by the decision trees in the RF model.

2.6 | Extreme gradient boosting (XGBoost)

The XGBoost is also based on the decision tree method, as shown in Figure 1d. However, unlike the RF, the trees in XGBoost are related to one another. The former tree results are used to guide the development of the next tree. The objective formula in the XGBoost is shown in Equation (5):

$$Obj = \sum_{i=1}^{n} l(y_i, \hat{y}_i) + \sum_{k=1}^{K} \Omega(f_k). \quad (5)$$

The objective formula is made up of two parts, the first part $\sum_{i=1}^{n} l(y_i, \hat{y}_i)$ is the training loss, and the second part $\sum_{k=1}^{K} \Omega(f_k)$ represents the complexity of the trees. The $\Omega(f_k)$ could be expressed as Equation (6):

$$\Omega(f_k) = \gamma T + \frac{1}{2}\lambda \sum_{j=1}^{T} w_j^2. \quad (6)$$

In Equation (6), γ represents the minimum loss reduction required to make a further partition on a leaf node of the tree, T the number of the leaves, w the score on the leaf, and λ is the weight for w. Adjusting the complexity of the trees could reduce model overfitting when trying to minimize the objective formula.

2.7 | Model evaluation

The predicted results and the actual experimental data were compared using two parameters, that is, the root mean square error (RMSE) and R-squared (R^2), as shown in Equations (7) and (8).

$$RMSE = \sqrt{\frac{1}{n}\sum_{i=1}^{n} (y_i - \hat{y}_i)^2}, \quad (7)$$

23806761, 2023, 6, Downloaded from https://aiche.onlinelibrary.wiley.com/doi/10.1002/btm2.10512 by University Of Sydney, Wiley Online Library on [18/06/2024]. See the Terms and Conditions (https://onlinelibrary.wiley.com/terms-and-conditions) on Wiley Online Library for rules of use; OA articles are governed by the applicable Creative Commons License

$$R^2 = 1 - \frac{\sum_{i}^{n} (\hat{y}_i - y_i)^2}{\sum_{i-1}^{n} (\bar{y}_i - y_i)^2}. \quad (8)$$

The smaller the RMSE value, the better the prediction is. For R^2, a value closer to 1 indicates a better prediction.

2.8 | Simulation process

The simulation process is illustrated in Figure 2. After the manual data cleaning process, a data set containing 191 experimental data points was obtained, as shown in Data S1. The 191 data points were randomly split into training set and test set, at a ratio of 7:3. Afterwards, the models were subjected to the training process to obtain the final models. The model based on Fick's law did not undergo the training process, as the key parameter (diffusion coefficient) for each drug was found in literature. After the four models were obtained, the data points in the test set were used to verify the accuracy of the predicted numerical values. The prediction accuracy of the four methods, that is, how close the simulated results to the experimental data, was compared using both RMSE and R^2.

The codes of MLR, XGBoost, and RF were written with the R language (R version 4.1.2) in R Studio. The version of XGBoost and RF were 1.5.0.2 and 4.7.1, respectively. The code of Fick's law was written using the C language in Microsoft Visual Studio 2022. The codes of all four methods can be found in Data S2.

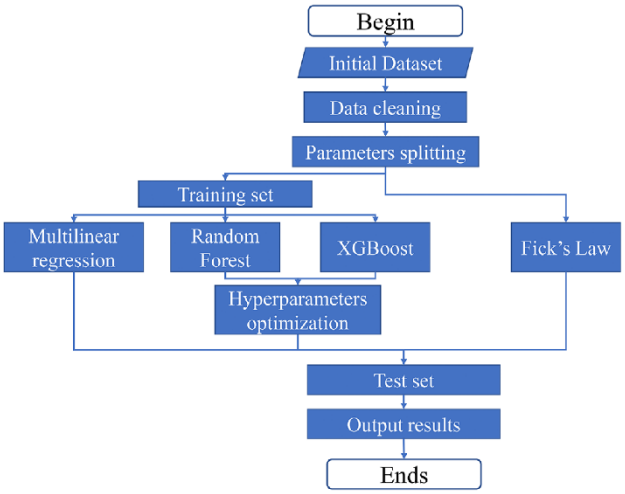


FIGURE 2 A flowchart showing the model training and prediction process of all four models: Fick's law, MLR, RF, and XGBoost. MLR, multiple linear regression; RF, random forest.

3 | RESULTS

3.1 | Data collection

The experimental data consist of six different drugs, namely, BSA, copper ions, a tripeptide glycyl-L-histidyl-L-lysine (GHK), rhodamine B, lidocaine, and caffeine, as shown in Data S1. Compared with others in this study, BSA is a relatively large molecule, with a molecular weight (MW) of 66,000.[30] GHK is a naturally occurring carrier tripeptide with high affinity for copper ions.[9] The total number of data points is 191, of which each drug contributes at a percentage as shown in Figure 3.

In the data set, lidocaine has 73 data points, accounting for 38% of all data points. Followed are BSA (33%), GHK (24%), and copper (24%). Lastly, rhodamine B and caffeine have relatively smaller number of data points, accounting for 10% each. There are four small molecules (GHK, rhodamine, lidocaine, caffeine), one metal ion (copper), and one big molecule (BSA), representing different classes of permeants, with the majority being small

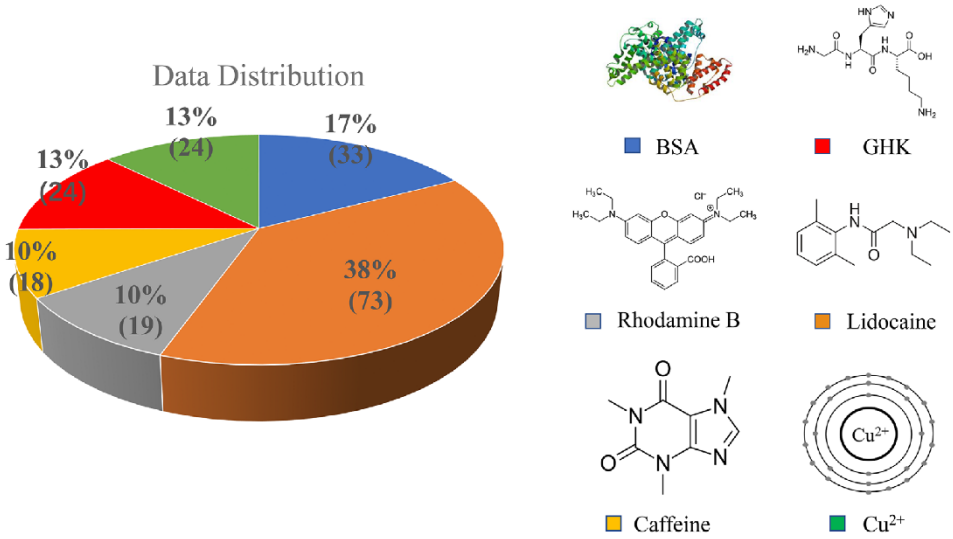


FIGURE 3 The data distribution and molecular structure of the drugs delivered using MNs in the skin permeation study.[9,12,30,31] MNs, microneedles.

23806761, 2023, 6, Downloaded from https://aiche.onlinelibrary.wiley.com/doi/10.1002/btm2.10512 by University Of Sydney, Wiley Online Library on [18/06/2024]. See the Terms and Conditions (https://onlinelibrary.wiley.com/terms-and-conditions) on Wiley Online Library for rules of use; OA articles are governed by the applicable Creative Commons License

molecules. Overall, the total number of data points is small, which is a limitation of this study.

3.2 | Fick's law

The parameters used in Fick's law are listed in Table 1. The diffusion coefficient of each drug was found in literature.[37–40]

The left panel of Figure 4a shows the setup of a typical in vitro skin permeation experiment, with the MN being inserted into skin membrane, which was then placed above a receptor compartment (blue color block) filled with receptor solution, collecting the drug molecules permeated through skin. The upper left section represents the half MN, and the lower right section represents the adjacent skin tissue. The bottom area represents the receptor compartment of a Franz type diffusion cell. Since the two-dimensional model is symmetric, only half of the model is used in calculation to save computer resources and time.[41]

On the right panel of Figure 4a, the predicted data points (black dots/line), and the experimental data points (red dots) of lidocaine permeation through skin are plotted together. At the beginning part of curve, the drug permeation rate increases, shown by the gradually increasing slope. This is resulted from the drugs released from the MNs, which then permeated into the skin tissue adjacent to the MN, as shown in Figure 4b. In the heat map, the red color indicates high drug concentration inside the MN while the green/blue color indicates the lower concentration of the drug. The dash lines in Figure 4b–f distinguish between the MN section at the upper left and the skin tissue at the lower right.

As the drug permeation from MN to skin continues, more drug molecules from the MN patch diffuse into the skin tissue gradually, as shown in Figure 4c–f. As a result, the rate of drug permeation from skin tissue into the receptor solution continues to increase, as depicted in the middle part of the curve. As the diffusion process continues, more drug molecules diffuse into the receptor solution.

After a period, the drug permeation reached a critical point where the permeation rate decreased and plateaued eventually. This is because the drug concentration in the MN, the skin and the receptor

TABLE 1 The parameters used in Fick's law simulation.[9,12,30,31]

Parameters	Values
Diffusion coefficient (*D*)	50–1000 μm^2/min[37–40]
MN number (*N*)	64, 351
Microneedle length (*L*)	700, 820, 876, 889, 999, 1250, 1063 μm
Releasing time (*t*)	15 min–48 hr
Mass of loaded drug (*m*)	50–70,940 μg
Grid size (*dx*, *dy*)	2 × 2
Time step (dt)	0.00001–0.001 min

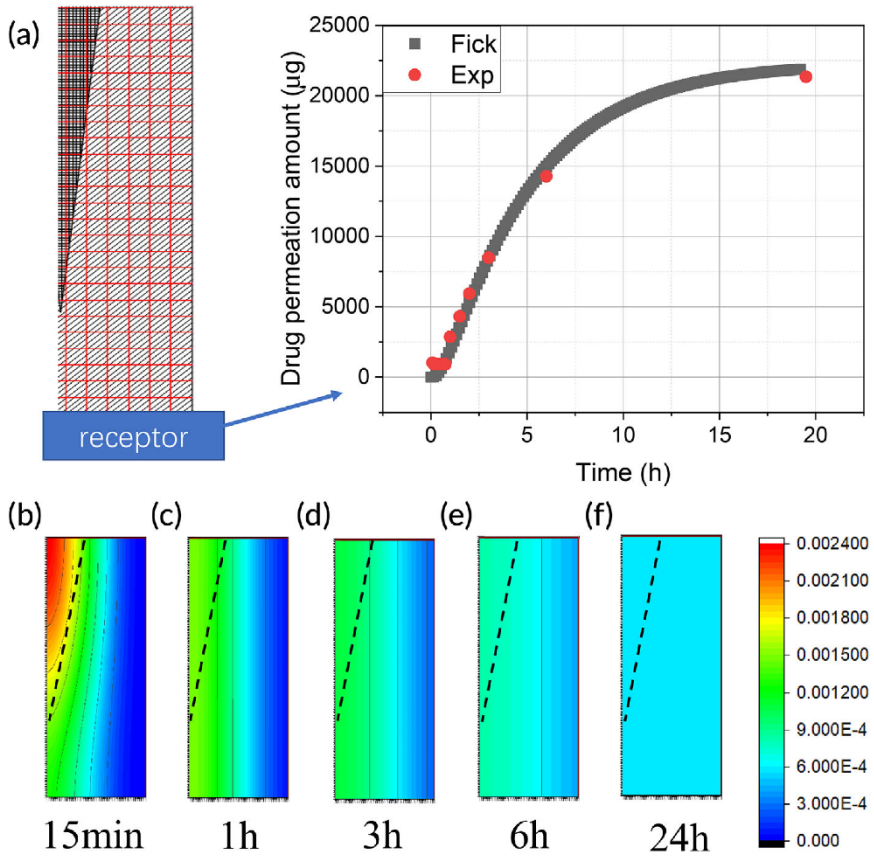


FIGURE 4 (a) An illustration of the Fick's law prediction curve compared with the experimental data. The drug distribution in the MN-skin system at (b) 15 min, (c) 1 h, (d) 3 h, (e) 6 h, and (f) 24 h. MN, microneedle.

23806761, 2023, 6, Downloaded from https://aiche.onlinelibrary.wiley.com/doi/10.1002/btm2.10512 by University Of Sydney, Wiley Online Library on [18/06/2024]. See the Terms and Conditions (https://onlinelibrary.wiley.com/terms-and-conditions) on Wiley Online Library for rules of use; OA articles are governed by the applicable Creative Commons License

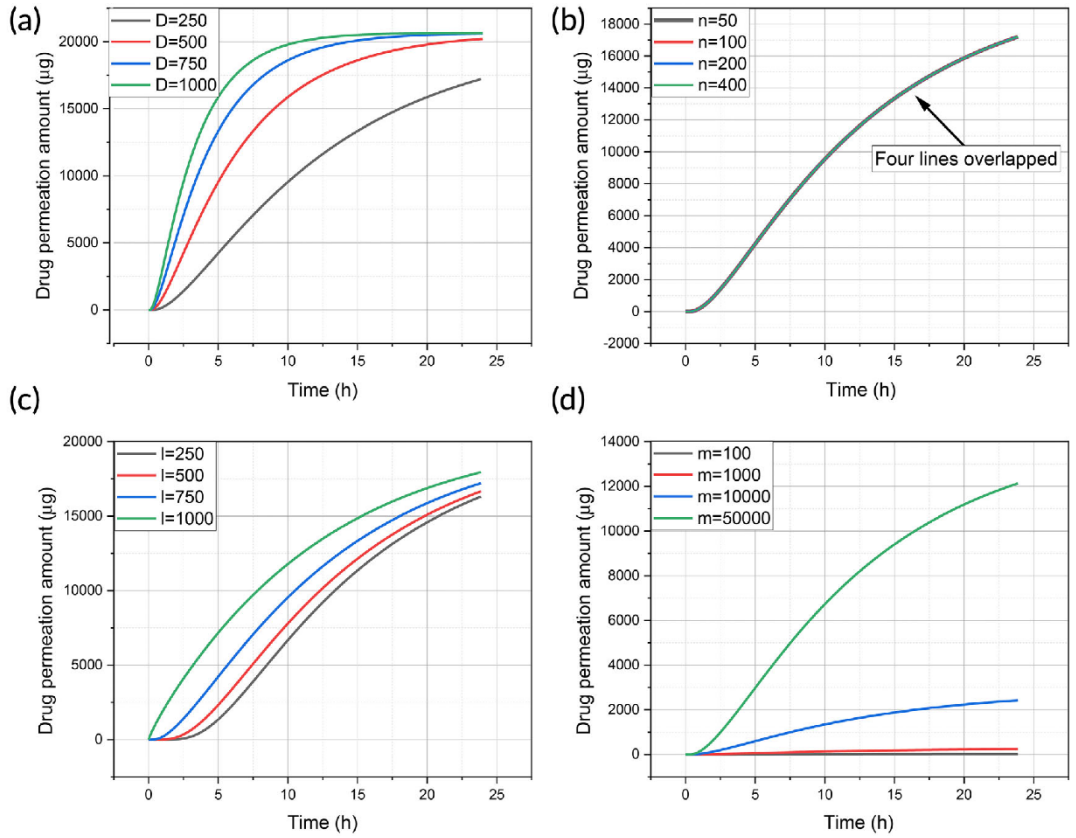


FIGURE 5 Effect of different parameters in Fick's law simulation: (a) diffusion coefficient; (b) number of MN; (c) MN length, and (d) mass of loaded drugs. MN, microneedle.

solution reached an equilibrium, such as that drug diffusion from MN to skin, or from skin to receptor solution stopped, as shown in Figure 4f.

The simulated curve fits well with the experimental points, demonstrating that the MN-facilitated drug permeation process complied with Fick's law of diffusion, that is, the MN provide a finite amount of drug reservoir and the drug continues to diffuse into skin till the concentration gradient ceases to exist.

Although the diffusion model is based on the hydrogel type of MN, that is, the MNs were inserted inside skin during the drug permeation process, the diffusion model was also used for the plastic type of MN. For the plastic MNs, the skin is pre-treated with the plastic MN patch and left with an array of micron-sized passages, complementary to the contour of the plastic MN.[9] The pre-treated skin sample is then mounted between the donor and receptor compartment of Franz-type diffusion device for drug permeation testing. The aqueous solution containing the drug in the donor compartment will fill in the micron-sized passages, to further permeate into skin tissue and subsequently the receptor compartment, resembling that of the hydrogel type of MN.

For the hydrogel MNs, the drug loading is defined as the amount of drug impregnated inside the MN patch. For plastic MNs, the drug loading is defined as the amount of drug, which is dissolved in an aqueous solution in advance, added to the donor cell in the in vitro skin permeation experiments. During the drug permeation process, the drug concentration was assumed to be homogenous inside the donor compartment and the micron-sized passages inside skin tissue. As the permeation process continues, the drug concentration inside the donor compartment and micron-sized passages decreases, which also resembles that of the hydrogel MN patch.

Based on these assumptions and approximations, we used a single mathematical model to simulate both type of MN patches for drug permeation through skin membranes. The data from in vitro permeation experiments were fitted using the model, regardless of hydrogel or plastic MN patches.

For the Fick's law model, the effect of the key parameters, namely, diffusion coefficient, the number of MNs, the length of MN, and drug loading inside the MN, on drug permeation through skin are shown in Figure 5.

The greater the diffusion coefficient, the quicker the drug permeation, as shown in Figure 5a. When the diffusion coefficient increases from 250 to 1000 μm^2/min, the drug permeation increased accordingly. Figure 5b illustrates the effect of the number of MN on a MN patch. It was shown that the number of MN

23806761, 2023, 6, Downloaded from https://aiche.onlinelibrary.wiley.com/doi/10.1002/btm2.10512 by University Of Sydney, Wiley Online Library on [18/06/2024]. See the Terms and Conditions (https://onlinelibrary.wiley.com/terms-and-conditions) on Wiley Online Library for rules of use; OA articles are governed by the applicable Creative Commons License

had no effect on the drug permeation profile, when the amounts of loaded drugs in the MN patch were the same. Therefore, all four lines overlapped to become a single curve in Figure 5b. Next, longer MN can deliver drugs into deeper skin, hence increase drug permeation, as shown in Figure 5c. Lastly, increasing the amount of drug loading results in greater drug permeation, as shown in Figure 5d. Drug loading has a greater impact on drug permeation than MN length.

3.3 | Machine learning

To build the machine learning models, seven features were selected for MLR, RF, and XGBoost, including the skin type (rat and human), type of the MN (hydrogel and plastic), MN length, surface area of the MN, drug loading in MN, drug permeation time, and the MW of the drug. Skin type,[9] drug permeation time,[33] and drug MW[42] are found affecting drug permeation through skin in our previous studies on non-MN facilitated transdermal drug delivery. The type of MN, MN length, surface area of MN, and drug loading in MN are potentially important parameters we identified for MN-facilitated transdermal drug delivery, hence included in the models in the current study.

Two types of MNs were used in the in vitro skin permeation experiments we performed previously. The first type of MN is made of a biocompatible polymer, namely, polyethylene glycol diacrylate (PEGDA), impregnated with drugs, in the shape of a frustum.[31] Upon application into skin, the PEGDA MNs will absorb moisture to form a hydrogel, and in turn release drugs into skin tissue. So, it is named as hydrogel type of MN. The other type of MN is made of plastics, in the shape of a pyramid.[9] The plastic MN is used to pre-treat skin membrane to increase skin permeability, and then removed from the skin membrane. The treated skin membrane was then mounted onto the drug permeation testing device and a small volume of aqueous solution of the drug was added into the donor compartment of the testing device where drug permeates through the pre-treated skin membrane.

MN surface area is an important parameter, as it represents the total contact surface area of a MN patch with skin tissue, where drug permeates into skin tissue. For the hydrogel MNs, it is approximately in the shape of a frustum, like a truncated cone. For the surface area of hydrogel MN, it is calculated using Equation (9), where S is the surface area of single MN, r the radius of top circle, R the radius of bottom circle, and l is the slant height of the conical frustum.

$$S = \pi r^2 + \pi(Rl + rl). \tag{9}$$

For the plastic MN, each MN is in the shape of a regular square pyramid. So, the surface area is calculated using Equation (10), where a is the length of the bottom square edge, and h is the height of a single MN from the apex of the pyramid to the base plane.

$$S = 4 \cdot \frac{1}{2} a \cdot \sqrt{\left(\frac{a}{2}\right)^2 + h^2}. \tag{10}$$

The total surface area of a MN patch is calculated using Equation (11), where S_{total} is the total surface area of all MNs on one MN patch, and n is the total number of MNs integrated on a single MN patch.

$$S_{total} = S \cdot n. \tag{11}$$

For example, the length of the bottom square edge of a plastic MN is 0.075 mm, and the height of a single MN is 0.7 mm. So, for a plastic MN patch consisting of 351 pieces of single MNs,[9] the total MN surface area is:

$$S = 4 \cdot \frac{1}{2} a \cdot \sqrt{\left(\frac{a}{2}\right)^2 + h^2} = 4 \cdot \frac{1}{2} \cdot 0.075 \cdot \sqrt{\left(\frac{0.075}{2}\right)^2 + 0.7^2} = 0.105\,\text{mm}^2,$$

$$S_{total} = S \cdot n = 0.105 \times 351 = 36.855\,\text{mm}^2.$$

The MW of drug may also influence the drug permeation and it was included as well. The features and their values are listed in Table 2. The hyperparameters used in RF and XGBoost models for drug permeation amount and percentage are shown in Table 3.

3.4 | Method comparison

To compare the four simulation methods, two parameters were used, that is, the RMSE and R^2, the definitions of which are shown in Equations (7) and (8). For RMSE, it is the root of summation of all the squared difference of the predicted result and the experimental result, divided by the number of data points. So, a smaller RMSE value indicates a better prediction, that is, the predicted results are closer to the experimental results. Although easy to understand and interpret, the numerical value of RMSE depends on the unit of the data points. Different from RMSE, R^2 does not depend on the unit of the data, hence useful to make comparisons with studies using different units.

The RMSE and R^2 results of four simulation methods are shown in Table 4. XGBoost had the lowest RMSE value and highest R^2 for both permeation amount and percentage prediction, among the four simulation methods. Between RF and Fick's law, RF showed better performance in permeation percentage prediction, while Fick's law was better in predicting permeation amount. MLR showed the poorest prediction among the four methods for both amount and percentage permeation.

The comparison of predicted results against experimental data was shown in Figure 6 (drug permeation amount) and Figure 7 (drug permeation percentage), respectively. The MLR result was excluded

23806761, 2023, 6, Downloaded from https://aiche.onlinelibrary.wiley.com/doi/10.1002/btm2.10512 by University Of Sydney, Wiley Online Library on [18/06/2024]. See the Terms and Conditions (https://onlinelibrary.wiley.com/terms-and-conditions) on Wiley Online Library for rules of use; OA articles are governed by the applicable Creative Commons License

to reduce overcrowding in the figures as it has the poorest prediction. There are six drugs permeating through human and/or rat skin, namely, BSA through rat skin (Figure 6a and Figure 7a), GHK through human skin (Figure 6b and Figure 7b), GHK through rat skin (Figure 6c and Figure 7c), rhodamine B through rat skin (Figure 6d and Figure 7d), lidocaine through human skin (Figure 6e and Figure 7e), lidocaine through rat skin (Figure 6f and Figure 7f), caffeine through human skin (Figure 6g and Figure 7g), copper through rat skin (Figure 6h and Figure 7h), and copper through human skin (Figure 6i and Figure 7i).

In each figure, the experimental points were color coded in red, while the Fick diffusion predictions were coded green, RF predictions were coded blue, and XGBoost predictions were coded black. The *x*-axis represents the permeation time in hours while the *y*-axis represents either the drug permeation amount (μg) (Figure 6) or permeation percentage (Figure 7). When the predicted result is close to the experimental point, the prediction is deemed to be better than when the predicted result is far from the experimental point. The quantified prediction results, that is, RMSE and R^2 were shown in Table 4.

For permeation amount prediction, as shown in Figure 6, the XGBoost and RF predictions matched well with experimental data points. However, there were significant deviations, when the data set was relatively small for the drug, namely, rhodamine B and caffeine, as shown in Figure 6d,g. For rhodamine B or caffeine, each drug has only less than 20 data points, accounting for only 10% of the data (Figure 3). For the permeation percentage prediction, as shown in Figure 7, the results were similar to those of permeation amount prediction, as shown in Figure 6.

TABLE 2 The parameters used in MLR, RF, and XGBoost.[9,12,30,31]

Feature	Value
Skin type	Rat (R), human (H)
MN type	Hydrogel, solid
MN length (μm)	700, 820, 889, 1250, 875.97, 998.62, 1062.97
MN surface area (mm^2)	26.76, 28.54, 29.97, 32.13, 32.43, 34.49, 36.86
Drug loading (μg)	50–70,940
Permeation time (hr)	0.08333–48
MW (Da)	64, 194, 234, 340, 479, 66,430
Drug permeation (μg)	0–30,000

Abbreviations: MLR, multiple linear regression; MN, microneedle; MW, molecular weight; RF, random forest.

TABLE 3 The hyperparameters used in the RF and XGBoost.

XGBoost parameter	Value	RF parameter	Value
Max depth[a]	4	Trees number[a]	500
Eta[a]	0.4	Mtry[a]	5
Nround[a]	100		
Max depth[b]	3	Trees number[b]	500
Eta[b]	0.2	Mtry[b]	6
Nround[b]	45		

[a]Drug permeation amount prediction.
[b]Drug permeation percentage prediction.

3.5 | Feature significance

The importance of different features used in the model in predicting drug permeation is shown in Figure 8. For RF and XGBoost, the surface area of the MN and permeation time were shown to be the key features in predicting drug permeation percentage (Figure 8a,c), while the drug loading in MN and permeation time were the key features in predicting drug permeation amount (Figure 8b,d). Hence, permeation time is a common feature for both drug permeation amount and permeation percentage prediction, which is consistent with Fick's law of diffusion. For permeation percentage, surface area of MN was found important, meaning that larger surface can result in a higher percentage drug loaded in the MN patch to be delivered into human. For permeation amount, drug loading was found important, meaning that higher drug loading can result in greater amount of drug to be delivered into human. Although both surface area and drug loading are important for drug permeation through skin, their contributions to drug permeation percentage and amount are different, as shown by the modeling results.

Besides, for RF method, the importance of drug MW, drug content, MN length, skin type, and MN type were below 12%, in predicting drug permeation percentage. The importance of MN surface area, MN length and type, skin type, and drug MW were below 7% in predicting permeation amount. These features were included in RF but have limited influence on the prediction. In XGBoost, drug content had less than 3% contribution in predicting drug permeation percentage. All other features showed little relevance in the prediction.

TABLE 4 Comparison of the four simulation methods.

RMSE and R^2	XGBoost	RF	Fick's law	MLR
RMSE of permeation amount (μg)	4447.23	7043.97	6778.17	23398.91
R^2 of permeation amount	0.98	0.95	0.95	0.46
RMSE of permeation percentage (%)	28.24	34.33	85.58	120.33
R^2 of permeation percentage	0.98	0.97	0.82	0.65

Abbreviations: MLR, multiple linear regression; RF, random forest; RMSE, root mean square error.

23806761, 2023, 6, Downloaded from https://aiche.onlinelibrary.wiley.com/doi/10.1002/btm2.10512 by University Of Sydney, Wiley Online Library on [18/06/2024]. See the Terms and Conditions (https://onlinelibrary.wiley.com/terms-and-conditions) on Wiley Online Library for rules of use; OA articles are governed by the applicable Creative Commons License

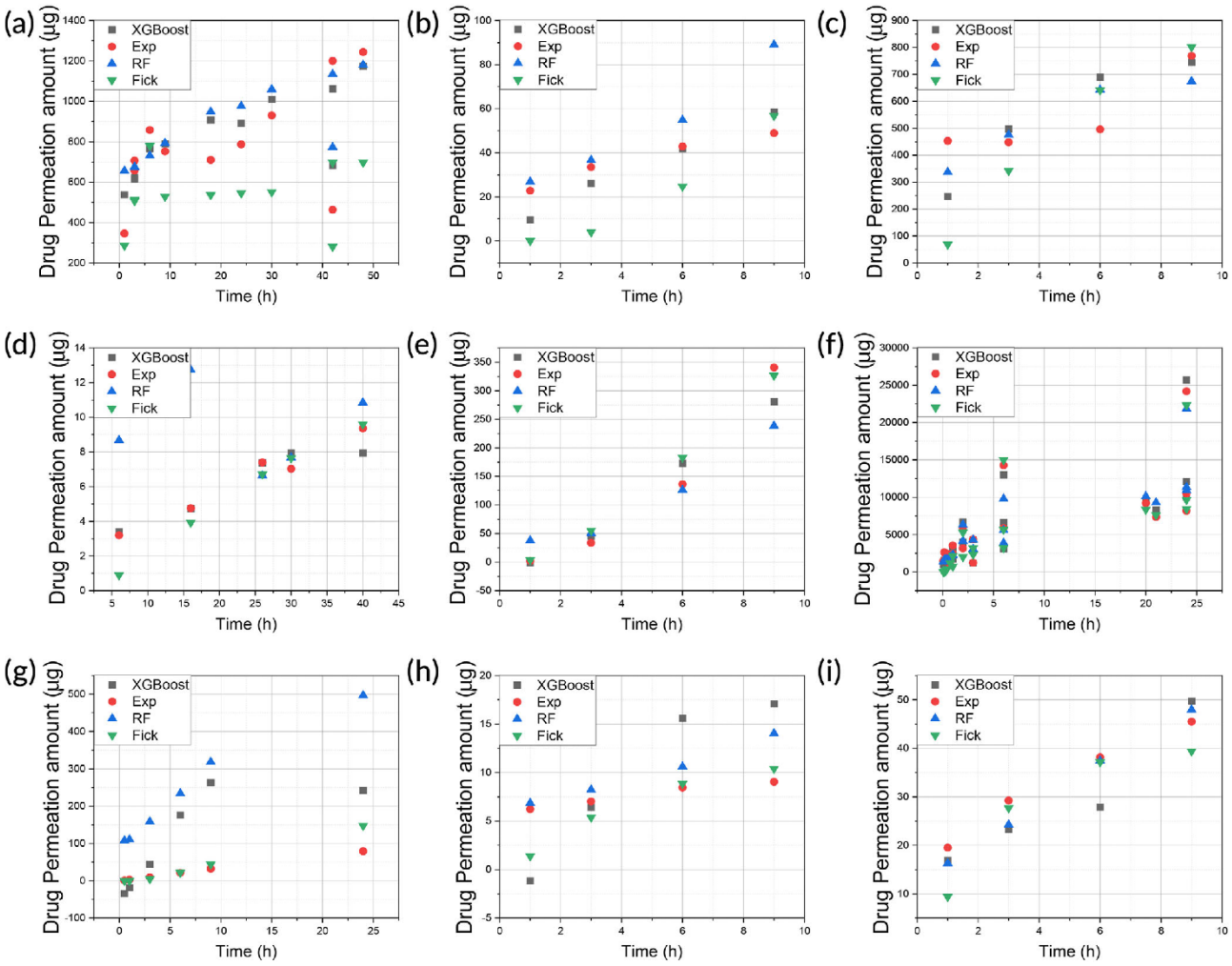


FIGURE 6 The comparison of the predicted permeation results with experimental data: (a) BSA(R); (b) GHK(H); (c) GHK(R); (d) rhodamine B(R); (e) lidocaine(H); (f) lidocaine(R); (g) caffeine(H); (h) Cu(R); and (i) Cu(H) (R: rat skin; H: human skin). BSA, bovine serum albumin; GHK, glycyl-L-histidyl-L-lysine.

4 | DISCUSSION

4.1 | Mechanistic and statistical modeling

In our previous studies, we used mechanistic modeling to predict crystal growth of materials for additive manufacturing,[41] to predict mammalian cell seeding inside microwells for tissue engineering,[43] and to count cells automatically on microscopic images for image recognition applications.[44] These methods are based on physical rules, such as the heat transfer equation and Stokes' formula of falling velocity. For such mechanistic models, the parameters in the models were obtained from the properties of the objects under investigations, for example, material crystallinity and dimension of the cells. Apart from the mechanistic models, we also studied statistical models, such as MLR, to make inferences and predictions of drug permeation through skin.[16] For statistical models, the models are not based on physical rules and the parameters in the models were obtained from experimental data, not based on the objects themselves (materials, cells, microwells, etc.).

In the current study, we used both mechanistic models (Fick's law of diffusion) and statistical models (MLR, RF, and XGboost) to predict drug permeation through MN-treated skin membrane. In comparison with MLR, RF and XGboost are more precisely defined as machine learning methods, which are focused on prediction than inference, but closely related to statistical models.[45] One of the characteristics of machine learning is that the data set is divided into training set to obtain the model, and test set to validate the model. The other characteristic of machine learning is that larger data set is needed to obtain satisfactory out-of-sample predictions. In this study, we regard all three statistical models as machine learning models.

All four methods in this study are to predict the drug permeation through the skin, in terms of the amount (μg) of drug and as a percentage of total amount of drug loaded in the MN. Among the four methods, RF is a widely used algorithm, which grows a series of

23806761, 2023, 6, Downloaded from https://aiche.onlinelibrary.wiley.com/doi/10.1002/btm2.10412 by University Of Sydney, Wiley Online Library on [18/06/2024]. See the Terms and Conditions (https://onlinelibrary.wiley.com/terms-and-conditions) on Wiley Online Library for rules of use; OA articles are governed by the applicable Creative Commons License

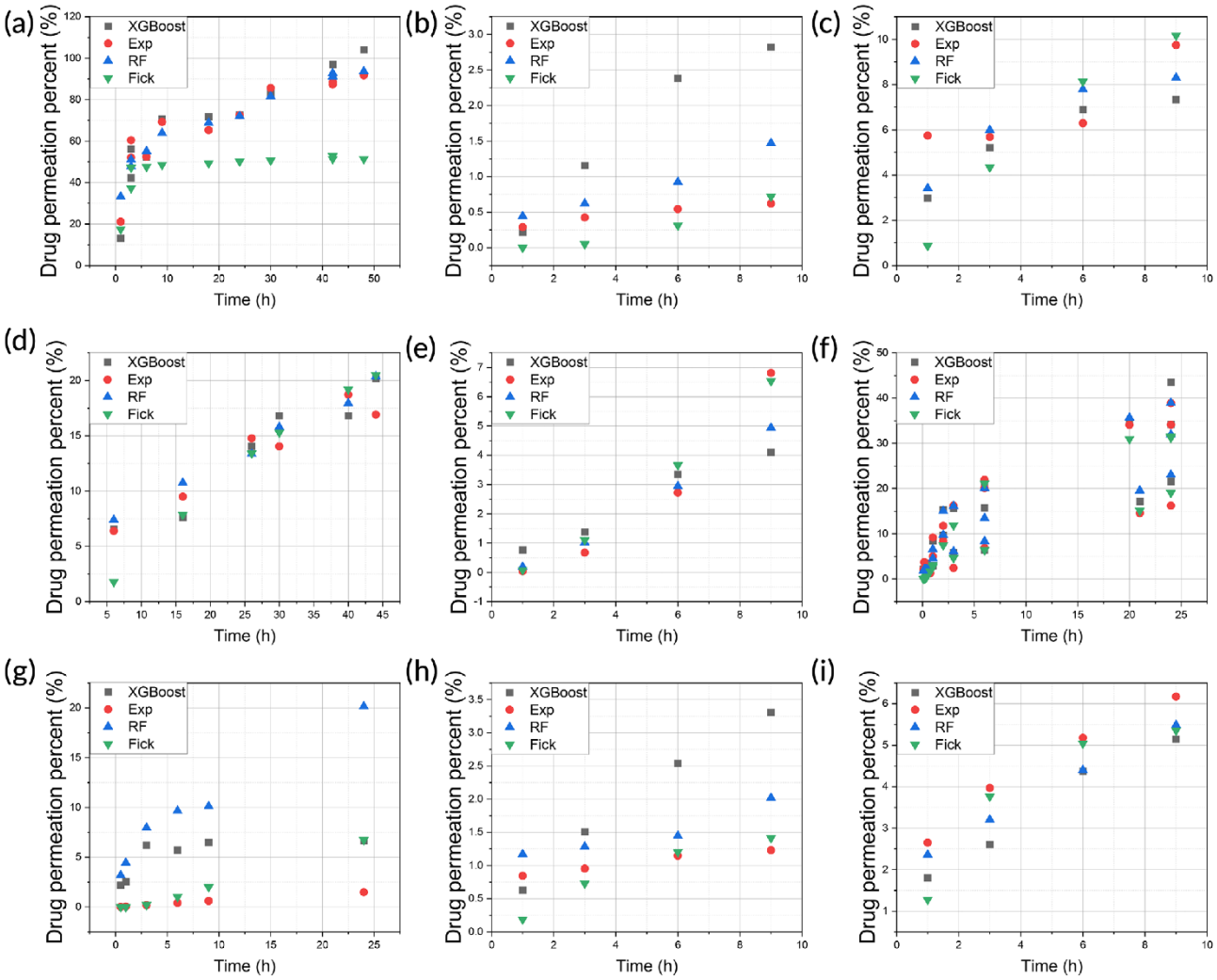


FIGURE 7 The comparison of the predicted drug permeation percentage with experimental data: (a) BSA; (b) GHK(H); (c) GHK(R); (d) rhodamine B(R); (e) lidocaine(H); (f) lidocaine(R); (g) caffeine(H); (h) Cu(R); and (i) Cu(H) (R: rat skin and H: human skin). BSA, bovine serum albumin; GHK, glycyl-L-histidyl-L-lysine.

decision trees for regression and classification. XGBoost is also based on tree model, but it provides parallel tree boosting and is the leading machine learning library for regression, classification, and ranking problems. Among the four methods, XGBoost showed the best performance, for predicting both the drug permeation amount and percentage.

4.2 | Model comparison

Fick's law is useful to understand the underlying mechanism of how drugs are released from MN and further permeate through the skin.[46–48] The drug diffusion process can be calculated at any specified time according to Fick's law (Figure 4). However, one of the key parameters, namely, the diffusion coefficient is not readily available.[37] In addition, diffusion coefficient is dependent on various factors, such as the depth of the skin, ambient temperature, and skin type.[28,35] This is the reason why machine learning methods are advantageous, since diffusion coefficient is not needed in machine learning methods, as demonstrated by the MLR, RF, and XGBoost models.

Although XGBoost produced the best predictions, the data sets were relatively small for caffeine and copper peptide, which affected the prediction precision to some extent (Figure 6d,g and Figure 7d,g). To further validate the XGBoost model, the model was used to predict the permeation of a drug which was purposely removed from the training data set. However, a large deviation was observed for both permeation amount (Figure S1) and percentage (Figure S2). The deviation may be resulted from the wide distribution of drug loading from various drugs used in the study, which is a heavily weighted parameter in XGBoost model. As a result, the predicted result for the new drug was dictated by drug loading. To address this issue, more experimental points should be obtained to cover the full range of drug

23806761, 2023, 6, Downloaded from https://aiche.onlinelibrary.wiley.com/doi/10.1002/btm2.10412 by University Of Sydney, Wiley Online Library on [18/06/2024]. See the Terms and Conditions (https://onlinelibrary.wiley.com/terms-and-conditions) on Wiley Online Library for rules of use; OA articles are governed by the applicable Creative Commons License

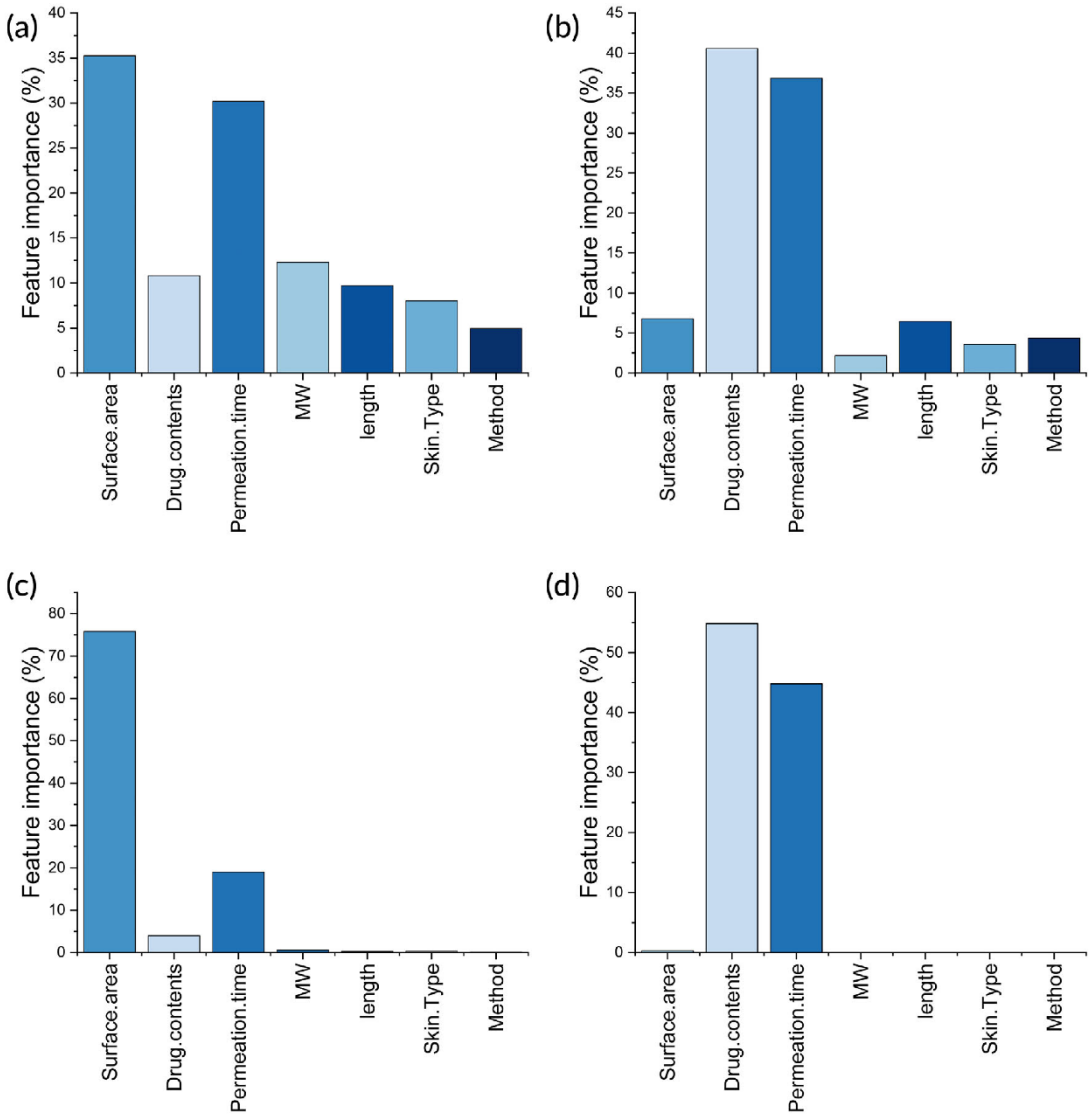


FIGURE 8 The feature significance in the RF and XGBoost models: (a) permeation percentage (RF); (b) permeation amount (RF); (c) permeation percentage (XGBoost); (d) permeation amount (XGBoost). RF, random forest.

loading (50–70,940 μg) for each drug in the training set in future studies. Besides, more experimental data are needed to increase the weight of the other parameters, such as MW of different drugs, number of needles per MN patch, and needle spacing on a MN patch. This can be achieved by increasing the number of drug candidates, which are then delivered using MN patches of different designs.

Nonetheless, the XGBoost can provide predictions if the drug is included in the training set, which is useful to evaluate the drug permeation profiles of varying MN patch designs. For example, the drug permeation profile of an MN patch with a hypothetical drug loading and surface area can be predicted by using the trained XGBoost model. This can aid the design of MN patches, without performing actual in vitro skin permeation experiments. Currently many MN devices for drug delivery are under clinical trial, for example, MN-facilitated transdermal delivery of zolmitriptan, a painkiller to treat migraine.[49] In such cases, the machine learning method may be used to generate optimal MN patch design to deliver certain doses of drugs into human, accelerating the development process of new therapeutics.

4.3 | Feature comparison

The contribution of different features used in the model was shown in Figure 8. Permeation time is important for both permeation percentage and amount, that is, longer permeation time results into higher drug permeation. This is consistent with the results obtained in the Fick's model in Figure 5. In transdermal patch formulations, the amount of drug is generally provided in excess to create a concentration gradient against skin, to ensure drug permeation from the patch into skin. With excess amount of

23806761, 2023, 6, Downloaded from https://aiche.onlinelibrary.wiley.com/doi/10.1002/btm2.10512 by University Of Sydney, Wiley Online Library on [18/06/2024]. See the Terms and Conditions (https://onlinelibrary.wiley.com/terms-and-conditions) on Wiley Online Library for rules of use; OA articles are governed by the applicable Creative Commons License

drug in the patch, more drug can permeate over extended permeation time.

In addition to permeation time, the contribution from other features varies. For permeation percentage, it was shown that larger MN surface area could result in higher drug permeation percentage (Figure 8). For permeation amount, it was found that greater drug loading in MN patch can result in more drug permeation through skin (Figure 8). Compared with permeation percentage, permeation amount is of greater importance, as it represents the dose to be delivered into human, which has always been the focus of transdermal drug delivery, that is, to enhance drug permeation through skin. On the other hand, permeation percentage represents the amount of drug being absorbed into human, as a percentage of total drug loading in the patch. Hence, it indicates the efficiency of the drug delivery system (bioavailability), and larger MN surface area is associated with greater bioavailability.

Apart from permeation time, MN surface area, and drug loading in MN, other features (drug MW, MN length, MN type, skin type), are of less relevance in the prediction, which seems to be contradicting the rules for drug permeation through skin. For example, the MW of the drug is a known parameter affecting drug permeation through skin, with lower MW being associated with higher drug permeation.[50] This discrepancy may also be ascribed to the small number of data points in this study, which put too much weight on drug loading in MNs. Hence, more data need to be generated experimentally to increase the weights of the other parameters, such as MW of drugs and MN geometries.[51]

It was also noted that MN type was not a significant feature even though the two types of MNs (hydrogel and plastic) have distinct mode of action. For hydrogel MNs, drugs are impregnated inside the polymeric materials of the MN and are gradually released into skin tissue.[31] For the plastic MNs, they are used to pre-treat the skin before drugs, which are dissolved in an aqueous solution, are applied onto the pre-treated skin.[9] Fundamentally, however, both types of MN can enhance drug permeation by piercing skin to create multiple passages for drugs to permeate through. In this regard, they share the same mechanism, hence are not very different from each other after all.

For future studies, the model can be improved by using a larger data set, including different types and shapes of MN, various drugs, and different drug loading, to reduce the deviation between the predictions and the experimental data. The model is aimed at predicting the amount of drug which permeates skin after a certain period of MN patch application onto skin. Furthermore, the model is also expected to make predictions for drugs, which are not in the training data set. This will be useful to optimize the MN formulations for a given drug and can be used to predict the skin permeation profile of new drugs.

5 | CONCLUSION

Four simulation models were established to predict drug permeation through skin. Among which the XGBoost model provided the best prediction results. The RF method ranked second in predicting drug permeation percentage, while Fick's law was in the second position in predicting drug permeation amounts. Taken together, machine learning methods were found useful in predicting drug permeation through skin treated with MNs.

AUTHOR CONTRIBUTIONS

Yunong Yuan: Formal analysis (lead); investigation (lead); methodology (lead); software (lead); validation (equal); visualization (equal); writing – original draft (equal); writing – review and editing (equal). **Yiting Han:** Conceptualization (equal); data curation (equal); investigation (equal); methodology (equal); writing – review and editing (equal). **Chun Wei Yap:** Investigation (equal); methodology (equal); supervision (equal); writing – review and editing (equal). **Jaspreet S. Kochhar:** Data curation (equal); investigation (equal); methodology (equal); writing – review and editing (equal). **Hairui Li:** Data curation (equal); investigation (equal); methodology (equal); writing – review and editing (equal). **Xiaoqiang Xiang:** Conceptualization (equal); funding acquisition (equal); investigation (equal); methodology (equal); resources (equal); writing – review and editing (equal). **Lifeng Kang:** Conceptualization (equal); data curation (equal); formal analysis (equal); funding acquisition (equal); investigation (equal); methodology (equal); project administration (equal); resources (equal); supervision (equal); visualization (equal); writing – review and editing (equal).

ACKNOWLEDGMENTS

This work is funded by the University of Sydney-Fudan University Partnership Collaboration Awards (PCA) of the year 2019. Yunong Yuan is supported by a USYD-CSC (University of Sydney-China Scholarship Council) scholarship (No. 202008320366).

CONFLICT OF INTEREST STATEMENT

The authors declare no conflicts of interest.

PEER REVIEW

The peer review history for this article is available at https://www.webofscience.com/api/gateway/wos/peer-review/10.1002/btm2.10512.

DATA AVAILABILITY STATEMENT

The data are available as supplementary materials published together with this article.

ETHICS STATEMENT

The data used in this study are experimental results from the authors' previous studies with required ethical approvals for using animal and human skin tissue samples.

ORCID

Lifeng Kang https://orcid.org/0000-0002-1676-7607

REFERENCES

1. Lim SH, Kathuria H, Amir MHB, et al. High resolution photopolymer for 3D printing of personalised microneedle for transdermal delivery of anti-wrinkle small peptide. *J Control Release*. 2021;329:907-918.

23806761, 2023, 6, Downloaded from https://aiche.onlinelibrary.wiley.com/doi/10.1002/btm2.10512 by University Of Sydney, Wiley Online Library on [18/06/2024]. See the Terms and Conditions (https://onlinelibrary.wiley.com/terms-and-conditions) on Wiley Online Library for rules of use; OA articles are governed by the applicable Creative Commons License

2. Roh H, Yoon YJ, Park JS, et al. Fabrication of high-density out-of-plane microneedle arrays with various heights and diverse cross-sectional shapes. *Nano-Micro Lett*. 2021;14:24.
3. Li J, Ma Y, Huang D, et al. High-performance flexible microneedle array as a low-impedance surface biopotential dry electrode for wearable electrophysiological recording and polysomnography. *Nano-Micro Lett*. 2022;14:132.
4. Shan J, Zhang X, Kong B, et al. Coordination polymer nanozymes-integrated colorimetric microneedle patches for intelligent wound infection management. *J Chem Eng*. 2022;444:136640.
5. Yang B, Kong J, Fang X. Programmable CRISPR-Cas9 microneedle patch for long-term capture and real-time monitoring of universal cell-free DNA. *Nat Commun*. 2022;13:3999.
6. Ohn J, Jang M, Kang BM, et al. Dissolving candlelit microneedle for chronic inflammatory skin diseases. *Adv Sci (Weinh)*. 2021;8:2004873.
7. Abd-El-Azim H, Tekko IA, Ali A, et al. Hollow microneedle assisted intradermal delivery of hypericin lipid nanocapsules with light enabled photodynamic therapy against skin cancer. *J Control Release*. 2022;348:849-869.
8. Liu S, Yeo DC, Wiraja C, Tey HL, Mrksich M, Xu C. Peptide delivery with poly(ethylene glycol) diacrylate microneedles through swelling effect. *Bioeng Transl Med*. 2017;2:258-267.
9. Li H, Low YS, Chong HP, et al. Microneedle-mediated delivery of copper peptide through skin. *Pharm Res*. 2015;32:2678-2689.
10. Chen J, Bian J, Hantash BM, et al. Enhanced skin retention and permeation of a novel peptide via structural modification, chemical enhancement, and microneedles. *Int J Pharm*. 2021;606:120868.
11. Koh KJ, Liu Y, Lim SH, et al. Formulation, characterization and evaluation of mRNA-loaded dissolvable polymeric microneedles (RNApatch). *Sci Rep* 2018;8:11842.
12. Kochhar JS, Lim WX, Zou S, Foo WY, Pan J, Kang L. Microneedle integrated transdermal patch for fast onset and sustained delivery of lidocaine. *Mol Pharm*. 2013;10:4272-4280.
13. Bui VD, Son S, Xavier W, et al. Dissolving microneedles for long-term storage and transdermal delivery of extracellular vesicles. *Biomaterials*. 2022;287:121644.
14. Mah CS, Kochhar JS, Ong PS, Kang L. A miniaturized flow-through cell to evaluate skin permeation of endoxifen. *Int J Pharm*. 2013;441:433-440.
15. Ding D, Pan J, Yeo SH, et al. A miniaturized device for biomembrane permeation analysis. *Mater Sci Eng C Mater Biol Appl*. 2019;103:109772.
16. Kang L, Yap CW, Lim PF, et al. Formulation development of transdermal dosage forms: quantitative structure-activity relationship model for predicting activities of terpenes that enhance drug penetration through human skin. *J Control Release*. 2007;120:211-219.
17. MacLeod BP, Parlane FGL, Morrissey TD, et al. Self-driving laboratory for accelerated discovery of thin-film materials. *Sci Adv*. 2020;6:eaaz8867.
18. Hosny A, Parmar C, Quackenbush J, Schwartz LH, Aerts H. Artificial intelligence in radiology. *Nat Rev Cancer*. 2018;18:500-510.
19. Zhavoronkov A, Ivanenkov YA, Aliper A, et al. Deep learning enables rapid identification of potent DDR1 kinase inhibitors. *Nat Biotechnol*. 2019;37:1038-1040.
20. McKinney SM, Sieniek M, Godbole V, et al. International evaluation of an AI system for breast cancer screening. *Nature*. 2020;577:89-94.
21. Senior AW, Evans R, Jumper J, et al. Improved protein structure prediction using potentials from deep learning. *Nature*. 2020;577:706-710.
22. Stokes JM, Yang K, Swanson K, et al. A deep learning approach to antibiotic discovery. *Cell*. 2020;180:688-702.
23. Bannigan P, Aldeghi M, Bao Z, Hase F, Aspuru-Guzik A, Allen C. Machine learning directed drug formulation development. *Adv Drug Deliv Rev*. 2021;175:113806.
24. Shin S, Austin PC, Ross HJ, et al. Machine learning vs. conventional statistical models for predicting heart failure readmission and mortality. *ESC Heart Failure*. 2021;8:106-115.
25. You Y, Lai X, Pan Y, et al. Artificial intelligence in cancer target identification and drug discovery. *Signal Transduct Target Ther*. 2022;7:156.
26. Jang HY, Song J, Kim JH, et al. Machine learning-based quantitative prediction of drug exposure in drug-drug interactions using drug label information. *npj Digit Med*. 2022;5:88.
27. Rezapour Sarabi M, Alseed MM, Karagoz AA, Tasoglu S. Machine learning-enabled prediction of 3D-printed microneedle features. *Biosensors (Basel)*. 2022;12:491.
28. Zoudani EL, Soltani M. A new computational method of modeling and evaluation of dissolving microneedle for drug delivery applications: extension to theoretical modeling of a novel design of microneedle (array in array) for efficient drug delivery. *Eur J Pharm Sci*. 2020;150:105339.
29. Neo JK. *Microneedle for Self Administration of Caffeine in Cellulite Treatment*. B.Sc. thesis. Department of Pharmacy, National University of Singapore; 2014.
30. Kochhar JS, Zou S, Chan SY, Kang L. Protein encapsulation in polymeric microneedles by photolithography. *Int J Nanomedicine*. 2012;7:3143-3154.
31. Kochhar JS, Goh WJ, Chan SY, Kang L. A simple method of microneedle array fabrication for transdermal drug delivery. *Drug Dev Ind Pharm*. 2013;39:299-309.
32. Li H. *Creation of Transport Pathways across Skin by Microneedles for Drug Delivery*. Ph.D. thesis. Department of Pharmacy, National University of Singapore; 2016 https://scholarbank.nus.edu.sg/handle/10635/129141
33. Kang L, Liu XY, Sawant PD, Ho PC, Chan YW, Chan SY. SMGA gels for the skin permeation of haloperidol. *J Control Release*. 2005;106(1–2):88–98.
34. Nguyen DV, Li F, Li H, et al. Drug permeation through skin is inversely correlated with carrier gel rigidity. *Mol Pharm*. 2015;12(2):444-452.
35. Yadav PR, Dobson LJ, Pattanayek SK, Das DB. Swellable microneedles based transdermal drug delivery: mathematical model development and numerical experiments. *Chem Eng Sci*. 2022;247:117005.
36. Nikan O, Avazzadeh Z, Tenreiro Machado JA. Numerical approach for modeling fractional heat conduction in porous medium with the generalized Cattaneo model. *Appl Math Model*. 2021;100:107-124.
37. Ellison CA, Tankersley KO, Obringer CM, et al. Partition coefficient and diffusion coefficient determinations of 50 compounds in human intact skin, isolated skin layers and isolated stratum corneum lipids. *Toxicol In Vitro*. 2020;69:104990.
38. Gajewska M, Paini A, Sala Benito JV, et al. In vitro-to-in vivo correlation of the skin penetration, liver clearance and hepatotoxicity of caffeine. *Food Chem Toxicol*. 2015;75:39-49.
39. Wood DG, Brown MB, Jones SA. Understanding heat facilitated drug transport across human epidermis. *Eur J Pharm Biopharm*. 2012;81:642-649.
40. Safranyos RGA, Caveney S. Rates of diffusion of fluorescent molecules via cell-to-cell membrane channels in a developing tissue. *Int J Cell Biol*. 1985;100:736-747.
41. Yuan Y, Abeykoon C, Mirihanage W, Fernando A, Kao Y-C, Harings JAW. Prediction of temperature and crystal growth evolution during 3D printing of polymeric materials via extrusion. *Mater Des*. 2020;196:109121.
42. Kathuria H, Handral HK, Cha S, et al. Enhancement of skin delivery of drugs using proposome depends on drug lipophilicity. *Pharmaceutics*. 2021;13(9):1457.
43. Kang L, Hancock MJ, Brigham MD, Khademhosseini A. Cell confinement in patterned nanoliter droplets in a microwell array by wiping. *J Biomed Mater Res A*. 2010;93(2):547-557.

23806761, 2023, 6, Downloaded from https://aiche.onlinelibrary.wiley.com/doi/10.1002/btm2.10412 by University Of Sydney, Wiley Online Library on [18/06/2024]. See the Terms and Conditions (https://onlinelibrary.wiley.com/terms-and-conditions) on Wiley Online Library for rules of use; OA articles are governed by the applicable Creative Commons License

44. Kachouie N, Kang L, Khademhosseini A. Arraycount, an algorithm for automatic cell counting in microwell arrays. *Biotechniques*. 2009; 47(3):x-xvi.
45. Bzdok D, Altman N, Krzywinski M. Statistics versus machine learning. *Nat Methods*. 2018;15(4):233-234.
46. Shu W, Heimark H, Bertollo N, Tobin DJ, O'Cearbhaill ED, Annaidh AN. Insights into the mechanics of solid conical microneedle array insertion into skin using the finite element method. *Acta Biomater*. 2021;135:403-413.
47. Kim KS, Ita K, Simon L. Modelling of dissolving microneedles for transdermal drug delivery: theoretical and experimental aspects. *Eur J Pharm Sci*. 2015;68:137-143.
48. Zhang R, Zhang P, Dalton C, Jullien GA. Modeling of drug delivery into tissues with a microneedle array using mixture theory. *Biomech Model Mechanobiol*. 2010;9:77-86.
49. Tepper SJ, Dodick DW, Schmidt PC, Kellerman DJ. Efficacy of ADAM zolmitriptan for the acute treatment of difficult-to-treat migraine headaches. *Headache*. 2019;59:509-517.
50. Hutton ARJ, McCrudden MTC, Larraneta E, Donnelly RF. Influence of molecular weight on transdermal delivery of model macromolecules using hydrogel-forming microneedles: potential to enhance the administration of novel low molecular weight biotherapeutics. *J Mater Chem B*. 2020;8:4202-4209.
51. Li W, Li S, Fan X, Prausnitz MR. Microneedle patch designs to increase dose administered to human subjects. *J Control Release*. 2021;339:350-360.

SUPPORTING INFORMATION

Additional supporting information can be found online in the Supporting Information section at the end of this article.

How to cite this article: Yuan Y, Han Y, Yap CW, et al. Prediction of drug permeation through microneedled skin by machine learning. *Bioeng Transl Med*. 2023;8(6):e10512. doi:10.1002/btm2.10512

23806761, 2023, 6, Downloaded from https://aiche.onlinelibrary.wiley.com/doi/10.1002/btm2.10512 by University Of Sydney, Wiley Online Library on [18/06/2024]. See the Terms and Conditions (https://onlinelibrary.wiley.com/terms-and-conditions) on Wiley Online Library for rules of use; OA articles are governed by the applicable Creative Commons License

Supplementary information

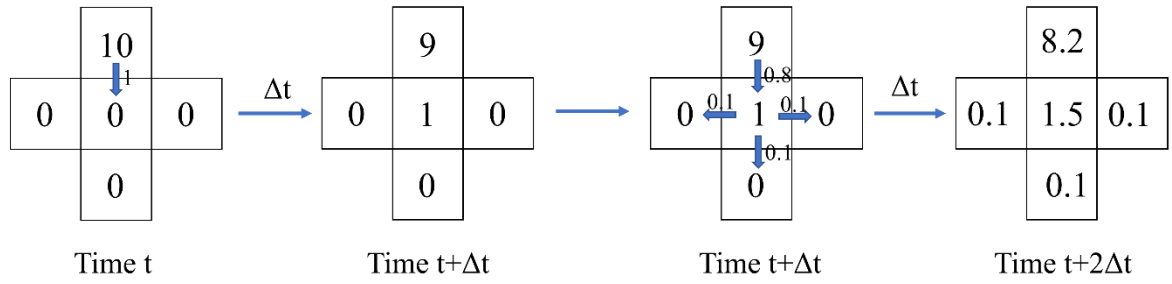


Figure S1. Illustration of the evolution of five elements' drug concentration varied with time. At time t, only the top element contained the drug. Then, after $\triangle t$ time, the centre element has the drug due to the drug inflow from top element. At $t+2\triangle t$ time, the centre element drug value slightly increased due to drugs inflow or out flow from its neighbour elements

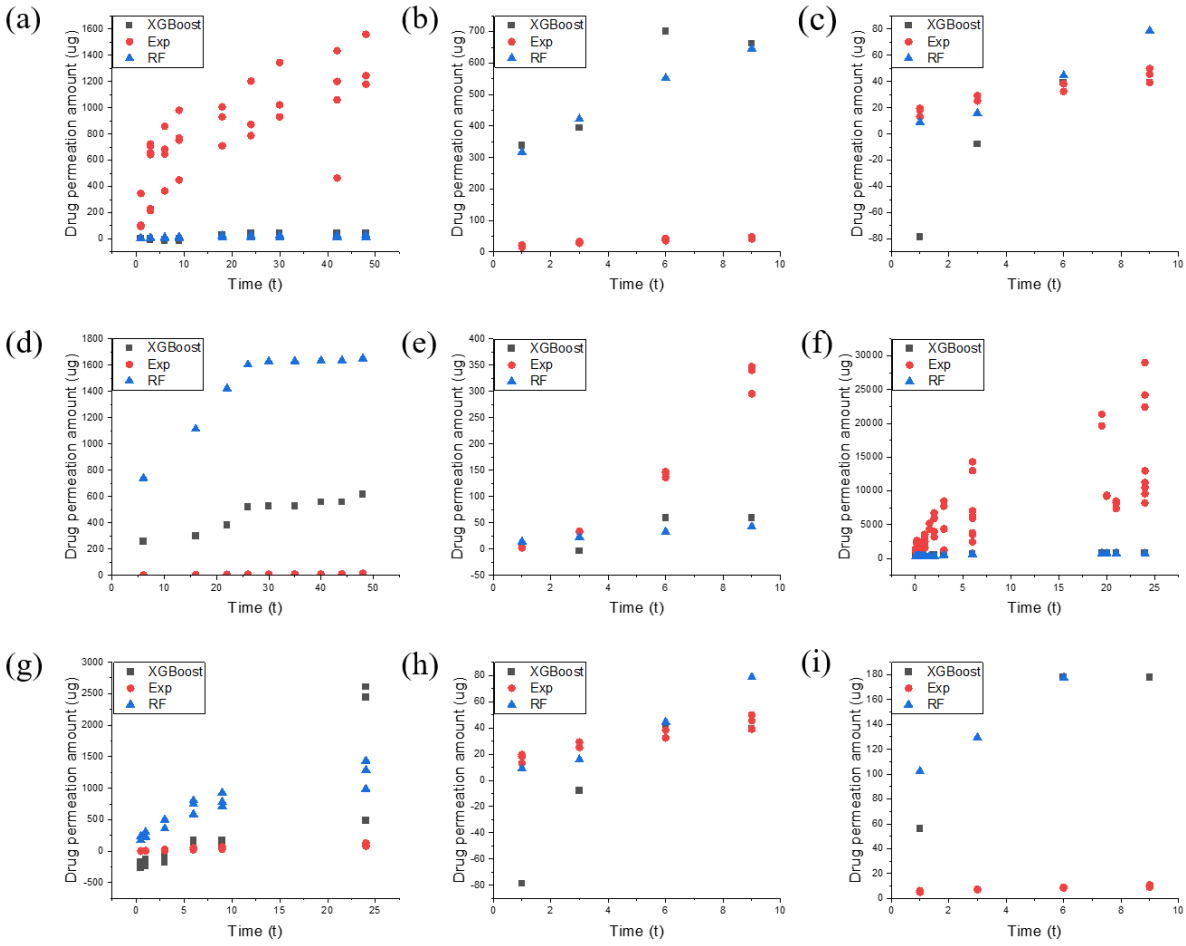


Figure S2. New drug permeation amount prediction: (a) BSA; (b) GHK(H); (c) GHK(R) (d) Rhodamine B(R); (e) Lidocaine(H); (f) Lidocaine(R); (g) Caffeine(H); (h) Cu(R); and (i) Cu(H). (R: in vitro rat skin permeation experiments, H: in vitro human skin permeation experiments

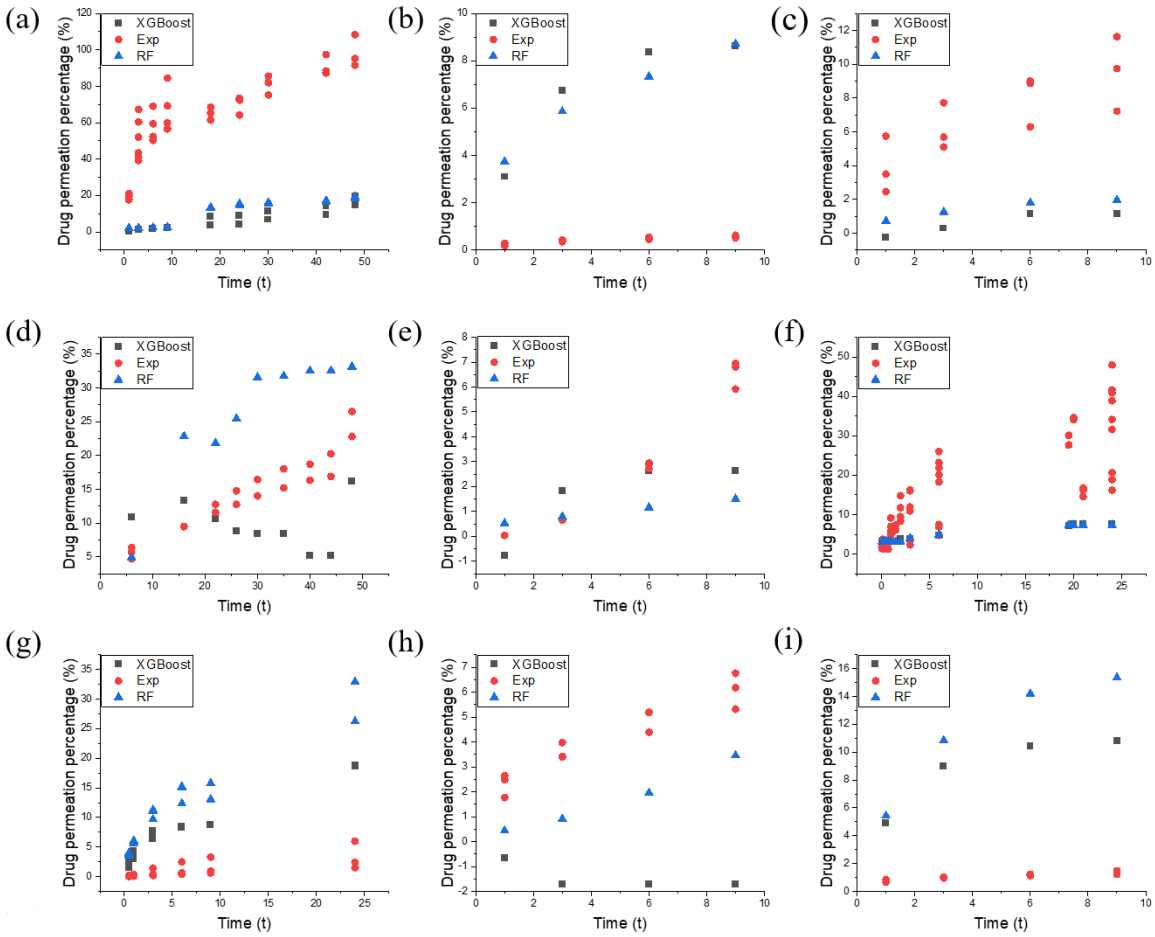


Figure S3. New drug permeation percentage prediction: (a) BSA; (b) GHK(H); (c) GHK(R) (d) Rhodamine B(R); (e) Lidocaine(H); (f) Lidocaine(R); (g) Caffeine(H); (h) Cu(R); and (i) Cu(H). (R: in vitro rat skin permeation experiments, H: in vitro human skin permeation experiments

Chapter 7 Conclusion and Future works

7.1 Conclusion

While traditional 2D cell culture models have been widely used in drug development and biological research, they are limited by insufficient cell-cell interactions and the absence of the physiological complexities in 3D environments. These models do not accurately replicate the mechanical forces (e.g., gravity) and cellular behaviour found in living tissues, which significantly limits their predictive power in drug testing [1-4]. Besides, most animal testing fails to accurately predict human response to drug metabolism, efficacy, or safety due to the species differences. Ethical concerns also arise from the potential pain, suffering, and death of animals involved in these experiments. The development of 3D spheroid/organoid cultures has emerged as a promising solution to these challenges in recent 10-15 years [5-7]. While 3D models have not yet reached the level of sophistication required to fully replicate the complexities of living organisms, they are anticipated to reduce reliance on animal models, particularly in preclinical research, thereby providing greater accuracy in predicting human outcomes for new drug development. This thesis extends beyond the conventional approaches by integrating 3D spheroid models, which better mimic the three-dimensional architecture and cellular microenvironment of human tissues, offering a more physiologically relevant platform for studying cell behaviour, drug efficacy, and tissue responses.

Modelling and simulation techniques play a crucial role in understanding mechanisms across different systems. This technology aids in reducing costs, minimizing risks, saving time, enhancing accuracy, and addressing ethical issues related to animal testing [8-11]. For instance, the time and spatial dependent concentration of oxygen or drug in the skin can be simulated via the proposed model, which is not possible via experimental way or needs huge amount of effort to complete it. They also offer valuable insights into the customized fabrication of soft materials used in drug delivery systems and tissue engineering. This thesis evaluates the potential contributions of controlled drug release, cell culture platforms, and oxygen therapy to developing soft materials-based personalized medicine via simulation methods. It also discusses the clinical significance of simulation-assisted soft materials in personalized medical treatments.

The PF-PEGDA hydrogel offers a promising solution for delivering vancomycin directly to surgical infection sites. This injectable hydrogel rapidly gels through photopolymerization,

facilitating quick application in clinical settings. Additionally, simulation methods allow the drug release rate to be easily tailored to specific treatment needs. Initial animal tests have shown promising efficacy for these hydrogel formulations, indicating their potential for future clinical use as presented in Chapter 3. (**Aim 1**)

Chapter 4 study highlights the effectiveness of 3D printing in creating anisotropic microwell chips to culture cell spheroids in a single step. By adjusting the bioink composition and printing parameters, we can customize the mechanical properties of the microwells to simulate the natural microenvironment essential for cell growth. This proposed model provides a valuable framework for analysing cell-microwell cultures, allowing for insights into the optimal timing for introducing various molecules. The 3D printed microwells can support cell growth up to 400 μm in diameter and 260 μm in height, maintaining high cell viability without the need for vascularization. This cost-effective and versatile device has the potential for widespread application in tissue engineering and biomedical research. With further refinements in design and implementation, we foresee the potential for this technology to accurately replicate complex cellular environments and drive advancements in biomedical research. (**Aim 2**)

Chapter 5 confirmed that O_2 sutures, capable of delivering oxygen deep into the skin, play a significant role in promoting the revascularization and survival of skin grafts. Combining experimental measurements with a microelectrode and computational digital simulation, we demonstrated that O_2 sutures deliver oxygen to the deep layers of the skin at a rate 100 times higher than traditional TGO therapy. This efficient oxygen delivery is crucial for enhancing the survival and proliferation of endothelial cells in oxygen-deprived environments. Furthermore, our in vivo studies showed that O_2 sutures effectively reduce necrosis in transplanted skin grafts and stimulate the growth of new blood vessels, improving the overall success of skin grafting procedures. These findings highlight the potential of O_2 sutures as a novel approach to deep oxygen delivery in skin grafting, with promising prospects for clinical applications in the future. (**Aim 3**)

Chapter 6 established four simulation models to predict drug permeation through the skin. To the best of our knowledge, this is the first time where machine learning has been employed to model drug release from microneedles, offering a new approach for identifying key features that influence this advanced drug delivery system. The XGBoost model stood out for

providing the most accurate predictions, followed by the RF method for drug permeation percentage, and Fick's law for drug permeation amounts. Overall, the findings demonstrate the effectiveness of machine learning methods in predicting drug permeation through skin treated with MNs. The proposed ML models can bring personalised pharmacotherapy, which would increase the drug efficiency and reduce the adverse effects. Meanwhile, for those who require frequent drug injections, the structure of MNs could be designed by the guidance of the proposed ML model to achieve the aimed drug releasing profile. Therefore, the adoption in clinical setting is expected to increase, leading to wider availability of minimally invasive MN-based treatments for various conditions and improving patient compliance. The range of drugs can be expanded to include biological drugs, which are not amenable to oral delivery. (**Aim 4**)

By using simulation and machine learning approaches, this thesis tackles several challenges in the realm of soft materials-based drug delivery and tissue engineering. These advancements place this thesis at the cutting edge of research focused on minimizing reliance on animal testing and enhancing the predictive accuracy of preclinical models.

7.2 Future studies

The applicability and generalisability of the models proposed in this thesis are based on certain underlying assumptions, which are necessary to simplify the models and minimize spatial and temporal complexity. These assumptions render the predicted results acceptable when compared to experimental data. However, the proposed models have several limitations, which are addressed in the corresponding chapters. Future studies might consider the following aspects:

1. Mathematical model is driven by solving the difference equation through mathematical approximation. Therefore, their use must meet certain conditions, such as isotropic hydrogels and uniform drug distribution. Modelling the release profile of gradient drug loading or from anisotropic hydrogels poses a challenge. This issue should be addressed by more advanced simulation method like FEM, which can yield more accurate predictions by accounting for intricate structural variations and boundary conditions.
2. The combinatory configuration, simulated based on burst release and lag release, should be validated by performing drug release experiments using the hydrogels.

Evaluating the potential interactions between multiple antibiotics is essential to explore the clinical benefits of these combined configurations.

3. The proposed model of cell culturing in the microwell was operated without external disturbances such as shaking or pipetting, which can affect small molecule diffusion. Besides, the cells were assumed as constant in both volume and molecular consumption rate, whereas in reality, cells proliferate change in size, and alter their metabolic demands, affecting the distribution of molecules within spheroids. Future models should address these limitations to better reflect real-world scenarios and improve the predictive accuracy of microwell-based culture systems.
4. Drug screening using 3D printed microwell is attractive due to its high throughput capability and the independent cavity for each spheroid to grow and position. Clinical trials of new drug development on this platform could be accelerated, and it has the potential to guide the optimization of dosing regimens in personalized treatments.
5. The trained ML model have limited ability in predicting the behaviour of drugs outside the current database. Generating more consistent experimental data is necessary to train the model further, enhancing its ability to predict new drugs and enabling the design of personalized treatments for patients.

Reference:

[1] A.C. Daly, M.E. Prendergast, A.J. Hughes, J.A. Burdick, Bioprinting for the Biologist, Cell 184(1) (2021) 18-32.

[2] L. Vettori, P. Sharma, J. Rnjak-Kovacina, C. Gentile, 3D Bioprinting of Cardiovascular Tissues for In Vivo and In Vitro Applications Using Hybrid Hydrogels Containing Silk Fibroin: State of the Art and Challenges, Current Tissue Microenvironment Reports 1(4) (2020) 261-276.

[3] S. Rahmani Dabbagh, M. Rezapour Sarabi, M.T. Birtek, N. Mustafaoglu, Y.S. Zhang, S. Tasoglu, 3D bioprinted organ-on-chips, Aggregate (2022) e197.

[4] D. Qi, H. Lin, B. Hu, Y. Wei, A review on in vitro model of the blood-brain barrier (BBB) based on hCMEC/D3 cells, Journal of controlled release : official journal of the Controlled Release Society 358 (2023) 78-97.

[5] M. Tang, J.N. Rich, S. Chen, Biomaterials and 3D Bioprinting Strategies to Model Glioblastoma and the Blood-Brain Barrier, Advanced materials 33(5) (2021) e2004776.

[6] N. Huebsch, B. Charrez, G. Neiman, B. Siemons, S.C. Boggess, S. Wall, V. Charwat, K.H. Jaeger, D. Cleres, A. Telle, F.T. Lee-Montiel, N.C. Jeffreys, N. Deveshwar, A.G. Edwards, J. Serrano, M. Snuderl, A. Stahl, A. Tveito, E.W. Miller, K.E. Healy, Metabolically driven maturation of human-induced-pluripotent-stem-cell-derived cardiac microtissues on microfluidic chips, Nature biomedical engineering 6(4) (2022) 372-388.

[7] M. Wang, W. Li, L.S. Mille, T. Ching, Z. Luo, G. Tang, C.E. Garciamendez, A. Lesha, M. Hashimoto, Y.S. Zhang, Digital Light Processing Based Bioprinting with Composable Gradients, Advanced materials 34(1) (2022) e2107038.

[8] H. Zhu, H. Yang, Y. Ma, T.J. Lu, F. Xu, G.M. Genin, M. Lin, Spatiotemporally Controlled Photoresponsive Hydrogels: Design and Predictive Modeling from Processing through Application, Advanced functional materials 30(32) (2020) 2000639.

[9] D.A.J. Brion, S.W. Pattinson, Generalisable 3D printing error detection and correction via multi-head neural networks, Nature communications 13(1) (2022) 4654.

[10] P. Bannigan, M. Aldeghi, Z. Bao, F. Hase, A. Aspuru-Guzik, C. Allen, Machine learning directed drug formulation development, Advanced drug delivery reviews 175 (2021) 113806.

[11] J. Qin, F. Hu, Y. Liu, P. Witherell, C.C.L. Wang, D.W. Rosen, T.W. Simpson, Y. Lu, Q. Tang, Research and application of machine learning for additive manufacturing, Additive Manufacturing 52 (2022).

Appendix 1. The Published Version of Chapter 3

D.V. Nguyen, **Y. Yuan** (co-first author), M. Kukumberg, L. Wang, S.H. Lim, A.M. Hassanbhai, M. Chong, T. Kofidis, E.C.K. Tan, D. Seliktar, L. Kang, A.J. Rufaihah, Controlled release of vancomycin from PEGylated fibrinogen polyethylene glycol diacrylate hydrogel, Biomaterials Advances 161, 213896. https://doi.org/10.1016/j.bioadv.2024.213896

Biomaterials Advances 161 (2024) 213896



Contents lists available at ScienceDirect

Biomaterials Advances

journal homepage: www.journals.elsevier.com/materials-science-and-engineering-c





Controlled release of vancomycin from PEGylated fibrinogen polyethylene glycol diacrylate hydrogel

Duc-Viet Nguyen [a,1], Yunong Yuan [b,1], Marek Kukumberg [c,d,e,1], Lingxin Wang [b,1], Seng Han Lim [f], Ammar Mansoor Hassanbhai [g], Mark Chong [h], Theodoros Kofidis [c], Edwin C.K. Tan [b], Dror Seliktar [i], Lifeng Kang [b,*], Abdul Jalil Rufaihah [c,j,**]

[a] Nusmetics Pte Ltd., 3791 Jalan Bukit Merah, E-Centre@Redhill, Singapore 159471, Singapore
[b] School of Pharmacy, Faculty of Medicine and Health, University of Sydney, Pharmacy and Bank Building A15, Science Road, NSW 2006, Australia
[c] Department of Surgery, Yong Loo Lin School of Medicine, National University of Singapore, 1E Kent Ridge Road, NUHS Tower Block, Level 8, Singapore 119228, Singapore
[d] Department of Obstetrics & Gynaecology, Yong Loo Lin School of Medicine, National University of Singapore, 1E Kent Ridge Road, NUHS Tower Block, Level 12, Singapore 119228, Singapore
[e] Healthy Longevity Translational Research Programme, Yong Loo Lin School of Medicine, National University of Singapore, Singapore 119228, Singapore
[f] Department of Pharmacy, National University of Singapore, 18 Science Drive 4, Block S4A, Level 3, Singapore 117543, Singapore
[g] Osteopore International Pte Ltd, 2 Tukang Innovation Grove #09-06, MedTech Hub, Singapore 618305, Singapore
[h] College of Design and Engineering, National University of Singapore, 5 Engineering Drive 2, Block E2A, #04-05, Singapore 117579, Singapore
[i] Department of Biomedical Engineering, Technion-Israel Institute of Technology, Haifa 32000, Israel
[j] School of Applied Science, Temasek Polytechnic, 21 Tampines Avenue 1, Block 8, Level 3, Singapore 529757, Singapore

ARTICLE INFO

Keywords:
Hydrogel
Vancomycin
Surgical infection
Drug delivery
Controlled release
Fick's law

ABSTRACT

Surgical site infection (SSI) is a common issue post-surgery which often prolongs hospitalization and can lead to serious complications such as sternal wound infection following cardiac surgery via median sternotomy. Controlled release of suitable antibiotics could allow maximizing drug efficacy and safety, and therefore achieving a desired therapeutic response. In this study, we have developed a vancomycin laden PEGylated fibrinogen–polyethylene glycol diacrylate (PF-PEGDA) hydrogel system that can release vancomycin at a controlled and predictable rate to be applied in SSI prevention. Two configurations were developed to study effect of the hydrogel on drug release, namely, vancomycin laden hydrogel and vancomycin solution on top of blank hydrogel. The relationship between the rigidity of the hydrogel and drug diffusion was found to comply with a universal power law, i.e., softer hydrogels result in a greater diffusion coefficient hence faster release rate. Besides, vancomycin laden hydrogels exhibited burst release, whereas the vancomycin solution on top of blank hydrogels exhibited lag release. A mathematical model was developed to simulate vancomycin permeation through the hydrogels. The permeation of vancomycin can be predicted accurately by using the mathematical model, which provided a useful tool to customize drug loading, hydrogel thickness and stiffness for personalized medication to manage SSI. To evaluate the potential of hydrogels for bone healing applications in cardiovascular medicine, we performed a proof-of-concept median sternotomy in rabbits and applied the hydrogels. The hydrogel formulations accelerated the onset of osteo-genetic processes in rabbits, demonstrating its potential to be used in human.

* Corresponding author at: A15 Pharmacy and Bank Building, Science Road, NSW 2006, Australia.
** Correspondence to: A. Rufaihah, Department of Surgery, Yong Loo Lin School of Medicine, National University of Singapore, 1E Kent Ridge Road, NUHS Tower Block, Level 8, Singapore 119228, Singapore.
E-mail addresses: lifeng.kang@sydney.edu.au (L. Kang), surraj@nus.edu.sg (A.J. Rufaihah).
[1] Authors made equal contributions.

https://doi.org/10.1016/j.bioadv.2024.213896
Received 22 December 2023; Received in revised form 29 April 2024; Accepted 14 May 2024
Available online 21 May 2024
2772-9508/© 2024 The Author(s). Published by Elsevier B.V. This is an open access article under the CC BY license (http://creativecommons.org/licenses/by/4.0/).

1. Introduction

Surgical site infection (SSI) is a common issue post-surgery and accounts for 3 % of surgical mortality in the United States [1]. For median sternotomy, which is a technique used in open-heart surgery, a rare but serious complication known as sternal wound infection including deep sternal wound infection (DSWI) is often associated with this procedure [2]. The incidence of sternal wound infection is around 1–4 % of all cardiac surgeries [3]. It can prolong hospital stay and may lead to a second surgery increasing the risk of morbidity and mortality [2,4,5]. Therefore, surgical prophylaxis is indicated for all cardiac surgeries to prevent SSI. According to the Society of Thoracic Surgeons Practice Guideline [3,6], cephalosporin and glycopeptide are the antibiotics of choice for cardiac surgery.

Cephazolin, a β-lactam agent, is the recommended first-line preoperative antibiotic due to its broad spectrum covering both Gram-positive and Gram-negative bacteria. Vancomycin, a glycopeptide antibiotic, has a narrower therapeutic range (Gram-positive only); however, it is the most effective antibiotic against *methicillin-resistant Staphylococcus aureus* (MRSA). Hence, vancomycin is reserved for patients at higher risk of MRSA infection and is the drug of focus in this study. Vancomycin can also be used as the primary prophylaxis in combination with gentamicin (Gram-negative coverage) for patients who have severe hypersensitivity to β-lactam agents. The recommended route of administration is intravenous for all three antibiotics. However, systemic administration of vancomycin requires therapeutic drug monitoring to maintain therapeutic effect while minimizing nephrotoxicity and ototoxicity caused by the drug concentration exceeding the therapeutic range. Therefore, topical antibiotics are thought to be the solution to allow high concentrations of vancomycin at the target site without causing systemic side effects [7].

Vancomycin paste is an example of topical antibiotics that has been used by surgeons for many years as SSI prophylaxis [3,8,9]. It can be prepared by simply mixing vancomycin powder in normal saline [7] and then applied to the cut sternal edges. Lazar et al. [3] and Vander Salm et al. [9] both concluded that topical vancomycin could further reduce the incidence of sternal wound infection. However, Lander and colleagues [8,10,11] suggested otherwise, arguing that the evidence found in Lazar et al.'s study for reduced incidence of DSWI did not directly correlate with topical vancomycin use and could just be due to advances in post-operative care and glycemic control [8,11]. The conflicting and limited evidence restricted the use of vancomycin paste as standard prophylaxis.

To advance the use of topical antibiotics for SSI, recent studies investigated hydrogels as drug delivery systems for antibiotics. Hydrogels are three-dimensional networks composed of crosslinked, hydrophilic polymers [12]. In recent years, its use as a drug delivery system has been widely studied due to its ability to encapsulate drugs for controlled release [13]. Localized, controlled drug delivery is especially useful for drugs like vancomycin with poor absorption and fast elimination [4]. By loading vancomycin in the hydrogel, it enables sustained release of vancomycin at the surgical site for antibacterial effect.

To encapsulate vancomycin in hydrogels, several polymers have been tested to form hydrogels with different physicochemical properties and release mechanisms [1,4,14,15]. Some are injectable hydrogels while others require invasive implantation. Nonetheless, there are still distances from an ideal hydrogel for drug delivery purposes, i.e., biocompatible, injectable, stable, and tunable for drug release. Particularly, there is no guidance regarding the amount of drug released from the hydrogel as a function of hydrogel properties.

To bridge the gap, we propose a vehicle we developed previously by crosslinking fibrinogen (PF) and polyethylene glycol diacrylate (PEGDA) using ultraviolet (UV) light [16]. This hydrogel has found its applications mainly in tissue engineering [16–20], encapsulation of cells [21] and growth factors [22,23]. Its advantages as an injectable vehicle [24] with good biocompatibility [23], low immunogenicity, and malleable mechanical property [16] also made it an ideal candidate vehicle to deliver small chemical drugs such as vancomycin. Particularly, to deliver the drug locally at the target site, it requires only a small incision to allow the precursor solution to be injected and then gelled using UV light [25].

In this study, we develop two configurations of vancomycin laden PF-PEGDA hydrogel, namely, vancomycin laden hydrogel and a blank hydrogel with vancomycin solution loaded on top serving as a drug depot. We first measure the rheological properties of these hydrogels and then evaluate their effects on drug release. It was shown that drug release from the hydrogel is correlated with the rigidity of the hydrogels. Subsequently, we interpret the drug release kinetics of the PF-PEGDA hydrogels using mathematical modelling [26] for both vancomycin laden hydrogel and a blank hydrogel with a vancomycin depot [27]. We demonstrated that the two configurations could be used to accurately control the release of vancomycin with burst or lag releasing profiles. To test the potential of the hydrogels for clinical applications, we performed a proof-of-concept median sternotomy in rabbits and applied the hydrogels of varying PEGDA concentrations. It was found that the hydrogels can accelerate the osteo-genetic processes following the operation.

2. Materials and methods

2.1. Materials

Phosphate-buffered saline (PBS), fibrinogen, acetone, ethanol, sodium hydroxide (NaOH), phosphoric acid, vancomycin powder, Mueller Hinton agar and broth, were purchased from Sigma-Aldrich (Merck KGaA, Darmstadt, Germany). Irgacure® 2959 photoinitiator was purchased from CIBA (Basel, Switzerland). *Staphylococcus aureus* (*S. aureus*, ATCC 25923) was purchased from Oxoid (Singapore). Acetonitrile was obtained from Tedia (Fairfield, OH, USA). Dipotassium phosphate (K_2HPO_4) was obtained from Alfa Aesar (Ward Hill, MA, USA). PEGDA powder was a gift from Technion – Israel Institute of Technology (Haifa, Israel). All materials were used as supplied without further purification.

2.2. PEGylated-fibrinogen material preparation

The PEGylated-fibrinogen (PF) was synthesized as described previously [17]. Briefly, in solution A, fibrinogen (4 g) was added into 86 mL of PBS, which contains urea (8 M). In solution B, 280 mg/mL PEGDA (10 kDa) was added into PBS, which contains urea (8 M). Solution A was added into solution B to react for 3 h. Then the mixture was added in 4× volume of acetone to precipitate the PF. Next, the precipitates were collected and redissolved into the PBS urea solution. The solution was filtrated to purify and concentrate the PF, which is photocurable, with the photoinitiator, namely, Irgacure 2959. After curing, further addition of PEGDA is to adjust the stiffness of the gel. The stiffness of the gel can be determined by measuring its rheological properties, i.e., the storage modulus (G`).

2.3. PF-PEGDA hydrogel preparation

To prepare the hydrogels, 20 % PEGDA stock solution (*w*/w) was prepared by dissolving PEGDA powder in PBS solution. PEGDA stock solution was mixed with PF solution to create PF hydrogels with varying PEGDA concentrations of 0, 2 and 6 % (v/v). One gram of Igacure 2959 photoinitiator powder was mixed with 1 mL of 70 % ethanol to make the stock solution. The PF-PEGDA precursor solutions were mixed with 1 % (v/v) of photoinitiator stock solution before UV curing. The hydrogel precursor solutions were cured under UV using either Omnicure 2000 (Waltham, MA, USA) or a portable UV lamp (VL-6-L Vilber Lourmat 6 W 365 nm, Eberhardzell, Germany) depending on the experiment. The hydrogel preparation process is illustrated in Fig. 1a.

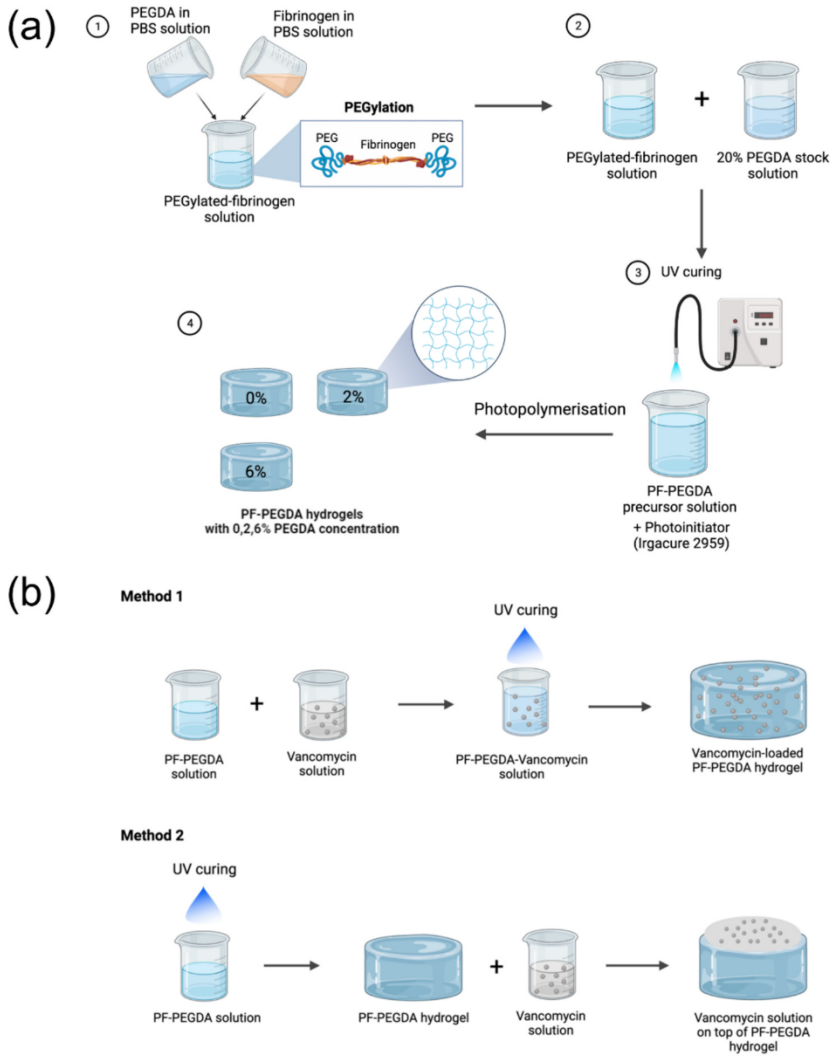


Fig. 1. (a) Schematic of the PF-PEGDA hydrogel fabrication process. (1) PF solution is prepared by mixing PEGDA and fibrinogen in PBS. (2) 20 % PEGDA stock solution was prepared for further addition into the PF solution to control the stiffness of the hydrogel. (3) The PF solution was mixed with the photoinitiator and exposed to UV light. This enabled crosslinking of polymers via photopolymerization to produce hydrogels. (4) Multiple hydrogels with varied PEGDA concentrations were created. (b) Schematic of the drug loading methods used to develop the two hydrogel configurations. Method 1 is by adding vancomycin solution to the PF-PEGDA precursor solution and then curing under UV to form the vancomycin laden hydrogel. Method 2 is by curing a PF-PEGDA hydrogel first, then loading the vancomycin solution on top of the blank hydrogel. Created with Biorender.com

2.4. Rheological properties of the hydrogel

To determine the rheological properties of hydrogel, we measured storage modulus (G`) and complex modulus (G*) of the hydrogel. The gelation of the hydrogel with varied PEGDA content was measured using an ARES G2 rheometer (TA instrument, New Castle, DE, USA) under time sweep mode with frequency f − 1 Hz, strain γ − 0.001. The PF-PEGDA hydrogel precursor solution was sandwiched between the two plates with a controlled gap. The lower plate was fixed and coupled with the Omnicure UV system. The upper plate (20 mm plane plate geometry) was connected to the measuring system. The gap between the geometry and the lower plate was fixed at 0.5–0.7 mm. The UV light was turned on at 100 s to start forming the hydrogel, and UV intensity was set at 5 mW/cm^2.

2.5. Formulation and vancomycin release from the hydrogel

The vancomycin stock solution of 300 mg/mL was prepared using 40 mM NaOH. Then 30 mg/mL vancomycin was added into the PF-PEGDA precursor solution. Vertical Franz diffusion cells coupled with an automated stirring temperature chamber were used for the diffusion study. Nylon filter (0.45 μm pore size) was sandwiched between two cell compartments, and then the two compartments were sealed using parafilm and clamped together. Two configurations were used to study the effect of PF hydrogel on vancomycin release and diffusion: (a) Vancomycin laden hydrogel and (b) vancomycin solution on top of blank hydrogel. The drug loading methods are illustrated in Fig. 1b.

In method 1, i.e., the vancomycin laden hydrogel configuration, the donor compartments were loaded with 1.5 mL of hydrogel precursor solution containing vancomycin, and then subjected to UV irradiation

(Omnicure 2000) for 10 min. When the loaded hydrogels were completely cured, 4.8 mL of PBS solutions were gently put into receptor compartments and in contact with cured hydrogel through a nylon filter.

In method 2, i.e., the vancomycin on top of blank hydrogel configuration, 1 mL of hydrogel precursor solutions containing no vancomycin was put in the donor compartment, and then subjected to UV irradiation (Omnicure 2000) for 10 min. When hydrogels were completely cured, 4.8 mL of the PBS solution was gently put into receptor compartments, and then 1 mL of 30 mg/mL vancomycin was put on top of cured PF hydrogel.

All loaded cells were placed into the diffusion chamber for the vancomycin release study. 1 mL of receptor solutions was collected at fixed intervals, and then replaced by 1 mL of fresh PBS solutions to maintain sink condition and constant volume of 4.8 mL.

Vancomycin concentration was measured using high performance liquid chromatography (HPLC), equipped with a 100–5-C18 column (4.6 μm × 250 mm) from Kromasil (Sigma-Aldrich, Merck KGaA, Darmstadt, Germany). The mixture of 10 % acetonitrile and 90 % 0.05 M K_2HPO_4 solution was used as mobile phase (pH adjusted to 4 using phosphoric acid), the flow rate was set at 1 mL/min. The absorbance was measured at 230 nm.

2.6. Relationship between gel rigidity and drug release

To examine the relationship between gel rigidity and drug release parameters, the steady flux, i.e., J ($\mu g \cdot cm^{-2} \cdot h^{-1}$), was calculated using the rate of vancomycin permeation through unit area of the hydrogel over time. Then the steady state flux was plotted against the maximum complex modulus, i.e., G^*_{max} (Pa), which is a measure of gel rigidity. Besides, the diffusion coefficient of vancomycin D ($m^2 \cdot s^{-1}$), likely affected by gel rigidity [28], was also plotted against the complex modulus. Regression analysis was applied to fit the relationships between steady flux or diffusion coefficient vs the complex modulus, respectively, by using Origin Pro 2022.

2.7. Bacterial culture and antimicrobial activity

For the testing, *S. aureus* (ATCC 25923) was grown on both Mueller Hinton agar and broth at 37 °C in a humidified incubator. The optical density at 600 nm (OD 600) was taken using a SpectraMax microplate reader (Molecular Devices, San Jose, CA, USA). The culture was diluted accordingly to obtain a final OD of 0.15. 100 μL of the culture broth was then spread evenly over the agar plate. Vancomycin was loaded into PF-PEGDA hydrogel at 15 mg/mL. 60 μL of vancomycin loaded solutions were put into cut syringe molds and cured under a UV lamp (VL-6-L Vilber Lourmat 6 W 365 nm) for 10 min. The cylindrical hydrogel was later pushed out of the mold and placed onto the surface of the agar and the plate was incubated overnight. The next day, the zone of inhibition (ZOI; defined as the diameter of the circular zone where bacterial growth was inhibited) was measured.

2.8. Mathematical modelling

To simulate the vancomycin release profiles, Fick's second law, as shown in Eq. (1), was applied to quantify the amount of drug released as a function of time.

$$\frac{\partial c}{\partial t} = D\frac{\partial^2 c}{\partial x^2} \tag{1}$$

where c is the concentration of the drug; x is the distance travelled by the diffusant; t is time; and D is the diffusion coefficient. Hadgraft [26] derived the mathematical solutions to Eq. (1), to describe the burst release (Eq. (2)) and lag release (Eq. (3)).

$$\frac{M_t}{M_\infty} = 1 - \frac{8}{\pi^2}\left(\sum_{n-1}^{\infty}\frac{1}{(2n-1)^2}exp\left(-\frac{(2n-1)^2\pi^2 Dt}{4l^2}\right)\right) \tag{2}$$

$$\frac{M_t}{M_\infty} = \frac{\alpha Dt}{l^2} - \frac{1}{6} - \frac{2}{\pi^2}\sum_{n-1}^{\infty}\frac{(-1)^n}{n^2}exp\left(-\frac{n^2\pi^2\alpha Dt}{l^2}\right) \tag{3}$$

where M_t is the amount of vancomycin released from the hydrogel at time t; M_∞ is the amount of drug released after an infinite amount of time; D is the diffusion coefficient; l is the thickness of the hydrogel. For lag release, the vancomycin solution is placed on top of hydrogel, hence two phases exist. When vancomycin permeates from the solution to the gel the diffusion rate decreases. Hence, a diffusion loss factor, namely, α, has been added, as shown in Eq. (3), to account for the phase change [26,29–31].

2.9. Programming

C language in Microsoft Visual Studio 2022 was used for coding to simulate drug release profile over time, based on Eq. (2) and Eq. (3). The codes can be found in Supplementary Information (SI)1. The parameters were obtained from the experimental measurement and literature (Table 1). The experimental data were compared with the simulated results to validate the mathematical models.

2.10. Animal experiments

To evaluate the potential of PF-PEGDA hydrogel for bone healing applications in cardiovascular medicine, we performed a proof-of-concept median sternotomy in rabbits. All animal experiments were approved and performed in compliance with the NUS Institutional Animal Care and Use Committee protocol R15–0409 and carried out in accordance with the National Advisory Committee for Laboratory Animal Research (NACLAR) Guidelines. White New Zealand rabbits ($n = 13$, age 4 months, weight 3.2 ± 0.7 kg, Charles River Laboratories, Wilmington, MA, USA) were randomly assigned to treatment groups: a) no treatment (Control, $n = 3$), treatment with surgical bone wax (Bonewax, n = 3) or with PF-PEGDA hydrogel with varying concentrations of additional PEGDA (0 %, n = 1; 2 %, $n = 2$; 6 %, $n = 4$) and underwent a modified median sternotomy adapted from previous studies [32,33]. Briefly, animals were anesthetized with a mixture of 35 mg/kg ketamine (Ceva Ketamine, Ceva Animal Health Australia, Glenorie, NSW, Australia), 5.0 mg/kg xylazine (ilium Xylazil 20, Troy Laboratories Australia, Sydney, NSW, Australia), and 0.1 mg/kg glycopyrrolate (Glycopyrronium bromide, Martindale Pharmaceuticals, Brentwood, Essex, UK) via intramuscular injection and intubated. Anesthesia maintenance and oxygenation was performed with isoflurane (1–3 %, Isoflurane B.P., Pharmachem, Eagle Farm, QLD, Australia) with a ventilator. Each rabbit received an intravenous catheter placed in the marginal ear vein for intravenous supplementation of lactated Ringer's solution (5–15 mL/h, B. Braun, Melsungen, Germany) and was operated in a supine position, hair was removed, with skin disinfected with iodine-ethanol solution. Hypothermia was prevented with a surgical warming pad. The sternum was exposed by a midline incision and

Table 1
The related values of hydrogel and its properties used in modelling.

Property (Units)	Value	Property (Units)	Value
Hydrogel thickness: burst release (m)	0.015	Drug in hydrogel: burst release (μg)	45,000
Hydrogel thickness: lag release (m)	0.01	Drug in solution: lag release (μg)	30,000
Diffusion coefficient in 6 %, 2 % and 0 % PEGDA hydrogel ($10^{-10} m^2/s$)	0.25, 0.36, 0.47	The experience factor α	0.68
Time step (s)	100		

dissection of both pectoralis major muscles. Each sternal vertebra was separated with a surgical chisel and surgical scissors while the sternum was lifted to avoid pleural and pericardial injury. Xiphoid was excluded from the surgical procedure and the presternum was separated only partially to secure cranio-sternal stability. Hemostasis was performed using sterile sponges. Exposed sternal vertebrae were treated with bone wax ($n = 1$, Bone wax, B. Braun, Melsungen, Germany), PF-PEGDA hydrogel (0 %, 2 %, or 6 %), or no treatment was applied. The sternum was closed with simple interrupted sutures using 2.0 polyamid (2–0 Ethilon Polyamide 6, Ethicon, Johnson&Johnson, New Brunswick, NJ, USA). All remaining tissue layers including the skin were closed using 4–0 polyglactin (4–0 Vicryl Polyglactin 910, Ethicon, Johnson&Johnson, New Brunswick, NJ, USA) with simple continuous suture. Animals received buprenorphine 0.05 mg/kg (ilium Temvet, Troy Laboratories Australia, Sydney, NSW, Australia) and 4 mg/kg carprofen (Rimadyl, Inovat Industria Farmaceutica, Sao Paulo, Brazil) subcutaneously for five days. Additionally, the animals received 5 mg/kg enrofloxacin (Baytril, Elanco Animal Health Korea, Seoul, South Korea) subcutaneously for seven days. Daily inspection of the wound was performed for seven days. Any remaining sutures were gently removed on the tenth day. A short anesthesia was performed at Week 3 for the PET-CT evaluation and the animals were euthanized with 150 mg/kg pentobarbital (Valabarb, Jurox, Rutherford, NSW, Australia) intravenously before the PET-CT evaluation at Week 6. The evaluation of sternal osteogenesis was performed with an mCT PET/CT system (128-slice Siemens Biograph, Siemens, Munich Germany). All animals undergoing CT evaluation were under anesthesia depending on the evaluation time point. Reconstruction was performed with a slice thickness of 0.44 mm and a reconstruction increment of 0.6 mm. The field of view was adapted to the sternum size (FOV 50 mm), and a convolution kernel dedicated to bone was adopted. All datasets gathered by the mCT PET/CT system were transferred to CD-R discs. Bone density (BD) was calculated, in Hounsfield units (HU), on transversal images (perpendicular to the long axis of the sternum) utilizing a dedicated medical imagining data examiner (AMIDE, 64-bit version, SourceForge). The circular region of interest (ROI) was determined by the manual outlying of the whole of each of the sternal vertebrae on every transversal slice. Five evenly spaced slices per vertebra were evaluated by measuring HU values in ROI. BD was determined by calculating the average of the collected HU values. To evaluate the different tissue composition during the bone healing hematoxylin-eosin (H&E), Safranin (Safranin-O), and Masson-Goldner trichome staining was performed. Selected samples were fixed in 10 % neutral buffered formalin (NBF, Sigma-Aldrich, St. Louis, MO, USA), embedded in paraffin (Surgipath Paraplast Plus, Leica Biosystems, Nussloch, Germany), and sectioned at 5 μm for H&E, Safranin-O and Masson-Goldman trichome staining following standard procedures and manufacturer's instructions. Histological sections were imaged with an upright brightfield microscope (Evos XL Core, ThermoFisher Scientific, Waltham, MA, USA). Acquired images were processed with ImageJ (version 1.52q, Rasband WS, National Institutes of Health, Bethesda, MA, USA).

2.11. Statistical treatment

Results were presented as mean ± standard deviation. The data normal distribution was checked by using Shapiro-Wilk test. Analysis for nonparametric data was determined by Kruskal-Wallis analysis of variance (ANOVA) test using Origin Pro 2022. Statistical evaluation of multiple animal data groups was performed using one-way or two-way ANOVA with Tukey's post-hoc test as appropriate, which was performed using QuickCalcs and GraphPad Prism (version 10.2.0., GraphPad Software, San Diego, CA, USA, graphpad.com). Statistically significant p-values are indicated as $^{****}P < 0.0001$; $^{***}P < 0.001$; $^{**}P < 0.01$; $^{*}P < 0.05$. NSD represents no significant difference.

3. Results

3.1. Rheological properties of the hydrogel

PF-PEGDA hydrogel networks are formed via UV crosslinking of prepolymer solutions. The rigidity of the hydrogel is affected by this gelation process and the degree of crosslinking. Fig. 2 shows the typical gelation curve of PF hydrogel with varied PEGDA concentrations, with and without vancomycin. Right after being exposed to UV light from 100 s onwards on the gelation curve, a hydrogel network was formed, resulting in the rise of storage modulus (G') and loss modulus (G"). The hydrogel was completely formed when G' and G" reaches constant, i.e., the plateau on the gelation curve. The time during which G' and G" starts increasing and reaches plateau is known as the gelation time.

As shown in Fig. 2(a), the storage modulus was the highest for PF hydrogel with 6 % PEGDA (blue), followed by 2 % (red) and the lowest for 0 % PEGDA (green). This shows that higher PEGDA concentrations result in stiffer hydrogels, as higher gelator concentration can result in denser network in the gel. Besides, the PF hydrogels containing vancomycin show longer gelation time as compared to PF hydrogels without vancomycin. This suggests that the presence of ingredients other than the gelators in the prepolymer solution can interfere with the gelation process.

3.2. Vancomycin release from the hydrogel

Cumulative release of vancomycin from PF hydrogel with varied PEGDA concentration was shown in Fig. 3. The cumulative curve in Fig. 3a shows typical burst release for vancomycin laden gel configuration and Fig. 3b shows lag release for vancomycin solution on top of blank hydrogel configuration. The results show that for hydrogels with higher PEGDA concentrations, drug release is slower. In other words, the harder the hydrogel is, the slower the drug release, for both configurations.

In Fig. 3b, 1 mL of 30 mg/mL vancomycin was put on top of cured hydrogel at the beginning of the experiment, hence the total amount of drug was 30 mg. After 48 h of experiment, the amount of drug accumulated in the receptor solution was determined to be ~3 mg for the 0 % vancomycin gel, as shown in Fig. 3b. So, the amount of drug remaining in the solution and the 1 mL gel together was ~27 mg. Besides, the permeation curves, as shown in Fig. 3b, are typical of the condition of a constant reservoir. Taken together, the Hadgraft's condition of constant reservoir in the donor compartment was met for the lag release experiments as shown in Fig. 3b.

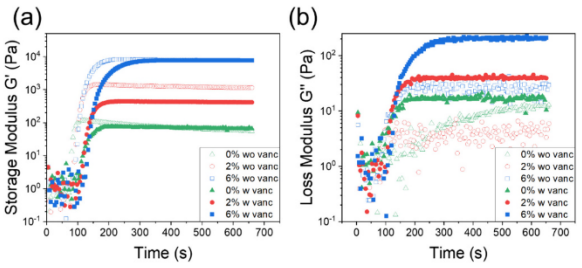


Fig. 2. Hydrogels with 0 %, 2 % and 6 % PEGDA concentrations with and without vancomycin. Rigidity of the hydrogel is measured by (a) storage modulus (Pascals), (b) loss modulus and plotted against time (seconds) to represent the gelation process. The gelation curves show, the higher the PEGDA concentration, the more rigid the hydrogel; and the addition of vancomycin slows down the gelation process. (w: with; wo: without; vanc: vancomycin) ($n = 3$).

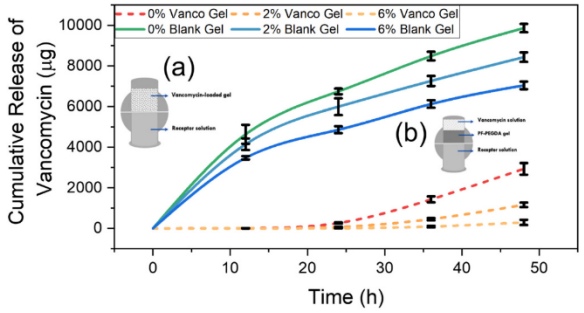


Fig. 3. Cumulative release of vancomycin from PF hydrogels with varied PEGDA concentrations over time: (a) Vancomycin laden PF-PEGDA hydrogel, (b) Vancomycin solution on top of PF-PEGDA hydrogel. Harder hydrogels with higher PEDGA concentrations have slower drug release for both configurations. (a) displays burst release and (b) displays lag release. Vanco: vancomycin.

3.3. Relationship between gel rigidity and drug release

To further explore this relationship between rigidity and drug release, the steady flux, J (μg cm ^{2} h ^{1}) and diffusion coefficient, D (m^2/s), were plotted against the maximum complex modulus, G^*_{max} (Pa). The linear regression and exponential regression from the graph (Fig. 4a and b) with $R^2 = 0.99867$ and $R^2 = 0.99982$ show a strong correlation between $\ln G^*_{max}$ and ln(1/J) as well as D, respectively, highlighting the inverse relationship between gel rigidity and drug release rate. From the previous findings, gel rigidity can be controlled by altering the PEGDA concentration, hence, by altering the PEGDA concentration, drug release rate can be controlled.

3.4. Antibacterial activity of vancomycin laden hydrogel

Molds modified from a **1** mL syringe as shown in Fig. 5a were used to prepare hydrogel cylinders (Fig. 5b). Then the hydrogels were placed at the center of the *S. aureus* culture plates (Fig. 5c). Vancomycin laden hydrogels inhibit *S. aureus* growth as indicated by ZOI (mm) on the culture plates. ZOI appears at the center of the plates with hydrogels containing 0 %, 2 %, and 6 % PEGDA. The diameter of ZOI varied depending on the PEGDA concentration. As the PEGDA concentration increases, ZOI decreases (Fig. 5d). The result agrees well with the vancomycin release study, i.e., higher PEGDA concentration results in slower drug release.

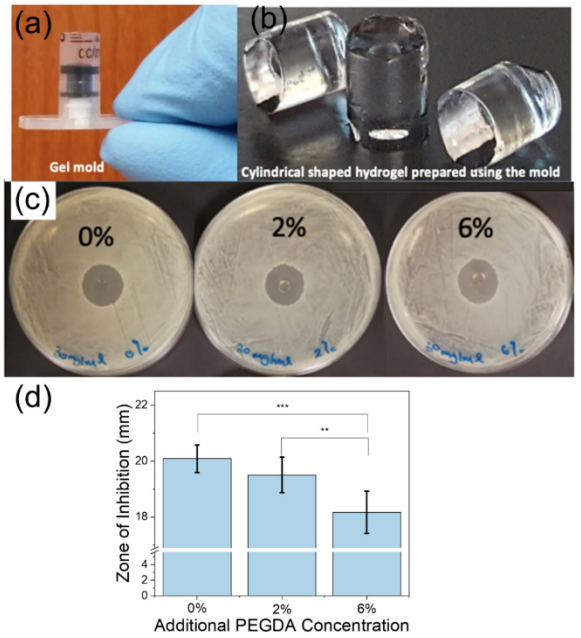


Fig. 5. (a) The mold to make hydrogel blocks. (b) Hydrogel cylinders made using the mold. (c) Zone of inhibition (ZOI) appears at the center of the *S. aureus* culture plate where the vancomycin laden PF-PEGDA hydrogel cylinder is located. (d) ZOI for vancomycin laden hydrogels with varied PEGDA concentrations.

3.5. Fickian diffusion of vancomycin from hydrogel

Diffusion is the major mechanism of drug release from hydrogel. Increased rigidity of the hydrogel caused a decreased drug release rate. As illustrated in Fig. 3, vancomycin laden hydrogel undergoes a burst release, i.e., initially, there is a fast release of drug from the hydrogel then the rate of drug release decreases and becomes steady. In the hydrogel, vancomycin is dispersed throughout the gel matrix. When it meets the receptor solution, the drug at the gel surface is quickly released, hence showing the initial burst release effect.

This is different from the blank hydrogel with vancomycin solution on top as a drug depot. It undergoes a lag release instead of a burst release, i.e., the drug release rate starts slow and then reaches a steady

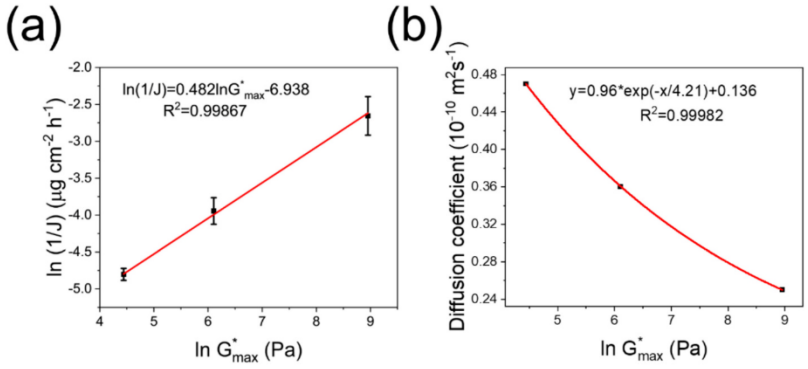


Fig. 4. The relationship between rigidity and drug release, represented by complex modulus, G^*_{max} (Pa) with steady flux, J (μg cm^{-2} h^{-1}) and diffusion coefficient, D (m^2/s). (a) The inverse correlation between G^*_{max} and J implies the more rigid the gel, the lower the drug release. (b) The inverse correlation between G^*_{max} and D implies the more the rigid the gel, the lower the drug diffusion rate in the hydrogel.

state after a period. The lag time is approximately 24 h before the drug is released at a steady rate, as it takes time for the drug to first diffuse into the hydrogel and then into receptor solution.

The diffusion coefficient of vancomycin in aqueous solution was 3.25×10^{-10} m^2/s at 25 °C [34], and 2.83×10^{-10} m^2/s at 37 °C [35]. However, there is no report of diffusion coefficient of vancomycin inside PF-PEGDA hydrogels. To find D value of vancomycin in the hydrogels, the experimental results in burst release were used to fit the equation by using the least-square method. The D values were found to be 0.47×10^{-10}, 0.36×10^{-10}, and 0.25×10^{-10} m^2/s for 0 %, 2 % and 6 % PEGDA hydrogel, respectively, as shown in Table 1.

An alternative method to estimate the values of D is by the slope of the initial linear part of the experimental cumulative release data versus square root of time in the burst release study, as shown in Fig. 6b, through Eq. 20 of Hadgraft's paper [26]. As shown in SI2, the D values were found to be 0.56×10^{-10}, 0.37×10^{-10}, and 0.26×10^{-10} m^2/s for 0 %, 2 % and 6 % PEGDA hydrogels, respectively. The D values are very close to those obtained above, showing both methods are valid to estimate the diffusion coefficient.

The calculated D values in the hydrogel are ~10 times smaller than those in the aqueous solutions, likely because the porous structures of the hydrogels hinder drug diffusion. Afterwards these calculated D values were used in the lag release simulation to predict the parameter of α, the best-of-fit of which was found to be 0.68.

3.5.1. Mathematical modelling of burst release

In this study, vancomycin was encapsulated inside the hydrogel and the receptor solution was maintained in sink condition. This is to simulate the in vivo conditions, in which the drug laden hydrogel will be applied to the surgical site. The drug concentration in the tissue is negligible, as the permeated drug will reach blood circulation and then be cleared from the surgical site. The parameters and their values used in the modelling are listed in Table 1.

The cumulative amount M_t represents the theoretical burst release, as shown in Fig. 6a. The predicted curve matched with the experimental data, where the R-squared values for 0 %, 2 % and 6 % PF-PEGDA hydrogels are 0.967, 0.973 and 0.968. It shows that the simulation is an accurate representation of the actual drug release.

In addition, the cumulative drug release from vancomycin laden hydrogel was also plotted against the square root of time (Fig. 6b). The linear correlation shows that the drug release follows a 'square root of time' release kinetic, dictated by Fick's Law [36].

3.5.2. Mathematical modelling of lag release

In contrast to the vancomycin laden hydrogel, for the configuration of vancomycin solution on blank hydrogel, no drug was loaded inside the hydrogel. The drug release was drawn by dash line in Fig. 6c. The theoretical and the experimental drug release follow a similar profile, i.e., the initial time lag and subsequent steady state. The R-squared values for 0 %, 2 % and 6 % PF-PEGDA hydrogels are 0.963, 0.982 and 0.937, respectively, showing satisfactory data fitting. In addition, the numerical value of factor α was found to be 0.68, showing that the diffusion rate of vancomycin decreased from the solution to the hydrogel.

3.5.3. The effect of parameters on vancomycin releasing from hydrogel

It was found that rigidity of the hydrogel significantly affects the vancomycin diffusion coefficient in hydrogel, i.e., stiffer hydrogels result in slower release (Fig. 6a). Apart from gel rigidity, we also performed simulation to investigate two additional parameters, namely, drug loading in hydrogel for burst release and the thickness of the hydrogel for lag release. Fig. 6d shows that higher drug loading results in faster drug release for burst release, suggesting that high drug loading is needed to achieve fast drug release. Fig. 6e shows that thinner hydrogels result in faster drug release, as determined by the slope of the linear portion for lag release.

3.5.4. Mathematical modelling of combined release

Hypothetically the burst release and lag release can be combined, to achieve fast onset of action, resultant from the loaded drug inside the hydrogel and subsequent sustained drug release, resultant from the drug depot, to maintain continual pharmacotherapy. The actual configuration is to place the drug depot on top of the drug-laden hydrogel, which is then placed on the surgical site.

Fig. 6f shows the simulation results of combinatory release profile. Initially, the release is dictated by the burst release from the drug laden hydrogel, with minimal contribution from the drug depot. Subsequently,

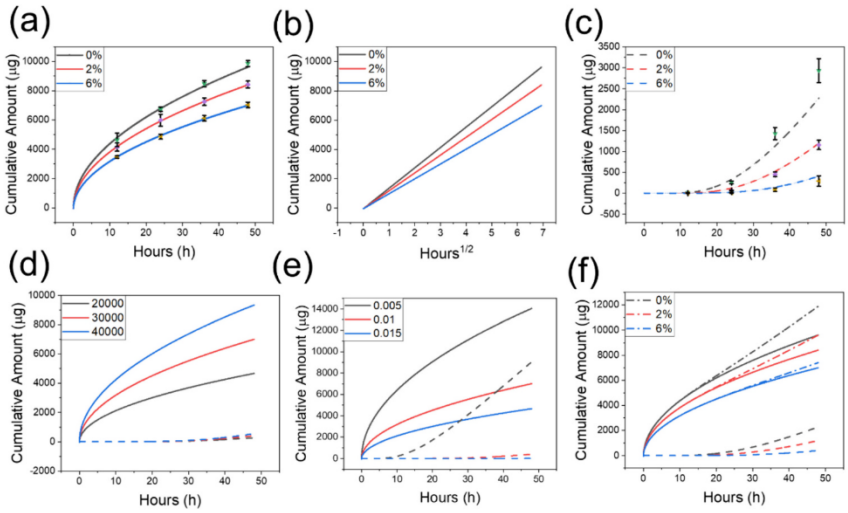


Fig. 6. (a) Experimental and simulated vancomycin release profiles from vancomycin laden hydrogels containing 0 %, 2 % and 6 % PEGDA. (b) Cumulative drug release from drug laden hydrogel against the square root of time. (c) Experimental and simulated drug release of vancomycin solution through blank hydrogel. (d) Effect of drug loading on drug release. (e) Effect of hydrogel thickness on drug release. (f) Theoretical drug release profile, obtained by combing burst and lag release. (Solid lines represent vancomycin laden hydrogels releasing profile, dash line represents vancomycin solution on top of blank hydrogel, and dash dot line indicate the combined release profile of two configurations).

as the time exceeds 12 h, the drug depot on top of the hydrogel begins to contribute to the combined drug release profile, eventually becomes the main contributor in the combinatory drug release, to provide sustained release of vancomycin into the receptor.

3.6. The effect of PF-PEGDA hydrogel on median sternotomy in rabbits

To evaluate the customizability and toxicity of the PF-PEGDA hydrogel, we assessed the hydrogel performance in a median sternotomy in rabbits (Fig. 7a). Hypothermia was prevented with a surgical warming pad. The sternum was exposed by a midline incision and dissection of both pectoralis major muscles. Each sternal vertebra was separated with a surgical chisel and surgical scissors while the sternum was lifted to avoid pleural and pericardial injury. Xiphoid was excluded from the surgical procedure and the pre-sternum was separated only partially to secure cranio-sternal stability (Fig. 7b and Fig. S1a and b in SI3).

PF-PEGDA hydrogels with the additional PEGDA concentrations of 0 %, 2 %, and 6 % were used to evaluate the influence of stiffness material in bone healing. No obvious adverse effects were observed during the sternotomy and the wound healing post-sternotomy. The evaluated PF-PEGDA hydrogel with additional 0 %, 2 % and 6 % PEGDA showed different levels of applicability. Although the 0 % additional PEGDA PF-PEGDA hydrogel was friable during manipulation and application, the material demonstrated a high degree of exudate absorption (Fig. S1c and d in SI3). The 2 % and 6 % PF-PEGDA hydrogels as materials with a

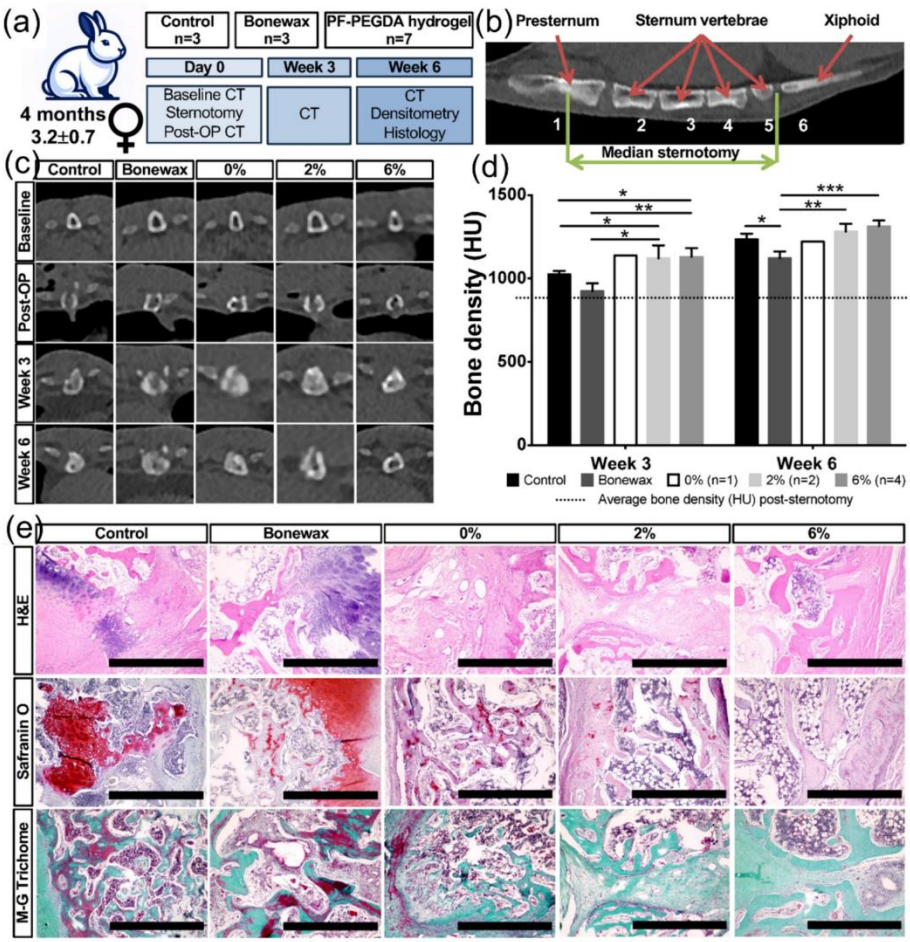


Fig. 7. PF-PEGDA hydrogel increases osteo-induction and osteogenesis in a median sternotomy rabbit model. (a) Schematic diagram of the animal study workflow. Female White New Zealand rabbits (4 months old, 3.2 ± 0.7 kg) were treated with surgical bone wax (Bonewax, $n = 3$), PF-PEGDA hydrogel (PF-PEGDA hydrogel, $n = 7$) or received no additional treatment (Control, n = 3) during a median sternotomy. Computed tomographic (CT) assessment was performed pre- (Baseline) and post-surgery (Post-OP), at Week 3 and Week 6 time points. Bone healing was evaluated by bone densitometric (Densitometry) and histopathological (Histology) assessment. (b) Anatomical visualization of median sternotomy of sternal vertebrae 1–5. (c) Representative transversal CT images illustrate varying degrees of radiographic density across sternal vertebrae (1–5) at selected time points (Baseline, Post-OP, Week 3, Week 6). (d) Bone densitometry. CT images quantification of sternal bone of non-treated animals (Control), animals treated with bone wax (Bonewax), and PF-PEGDA hydrogel (0 %, 2 % and 6 % PEGDA concentration) evaluated at Week 3 and Week 6 post sternotomy. Multiple images per sternal vertebrae (1–5) were assessed. Bone density quantified with Hounsfield Units (HU). Mean bone density post-sternotomy is represented as a dotted line. All results are represented as mean ± SD. (e) Histopathological evaluation of sternal vertebrae showed a higher presence of maturing and mature bone tissue over immature bone, fibrotic, and cartilage tissue. Histological sections were evaluated across all treatment (Control, Bonewax, 0 %, 2 % and 6 % PF-PEGDA hydrogel) groups. Representative images of hematoxylin-eosin (purple – cartilage tissue, dark pink – bone tissue), Safranin-O (Safranin-O, red – cartilage tissue), and Masson-Goldman Trichome (M-G Trichome, green – mature bone matrix, red – immature bone matrix) staining of sternal vertebrae. Scale bar – 1 mm.

higher stiffness, have also shown easier manipulation during application and suturing between the sternal vertebrae albeit with a lower exudate absorption (Fig. S1 e-h in SI3). None of the PF-PEGDA hydrogels demonstrated hemostatic properties when compared to bone wax.

Hyper-density with a hypertrophic callus was observed 3 weeks postoperatively in all animal groups (Fig. 7c). Six weeks postoperatively, a higher density in the cortical zones with respect to the inner cancellous bone was observed in all groups but the group treated with bone wax. PF-PEGDA hydrogel (2 % and 6 %) treated animals showed increased sternal vertebrae bone density (1120 ± 79 HU and 1130 ± 53 HU respectively) when compared to control and bone wax-treated animals (1025 ± 21 HU and 924 ± 47 HU respectively) three weeks post-operatively (Fig. 7d and Fig. S2 in SI3). Although higher bone density was observed across all animal groups six weeks postoperatively, no significant difference was observed between the PF-PEGDA-treated and control groups. Notably, the bone wax-treated animals showed lower bone density than the PF-PEGDA-treated and control groups across both time points. Evaluation of bone density of individual sternal vertebrae across groups and time points showed fluctuations in bone density values without any trends and statistically significant differences (Fig. S3 in SI3).

Histological examination showed typical bone morphology across all animal groups albeit with differences (Fig. 7e). Evidence of cartilaginous and immature bone tissue was observed in animals treated with bone wax and controls observationally larger patches than in animals treated with PF-PEGDA hydrogels. Despite the foreign origin of the biomaterial used, minimal mononuclear infiltration was observed. Furthermore, no traces of the PF-PEGDA materials were found in histological samples.

4. Discussion

4.1. Vancomycin laden hydrogels

Hydrogels are three-dimensional network structures composed of hydrophilic polymers immobilizing a large amount of liquid. It provides a porous structure that permits the transfer of gas and small molecules to the wound [37]. These characteristics render hydrogels suitable for antibacterial applications and promote tissue regeneration [38]. Controlled release of vancomycin can be achieved by varying the concentration of PF-PEGDA in the hydrogel. Moreover, different drug loading methods also provide different drug release kinetics, such as burst release or lag release.

The vancomycin laden hydrogel with burst release allows high concentrations of vancomycin to be delivered at the initial stage, hence may be more desirable for surgical prophylaxis purposes to prevent rapid onset infections (Figs. 3a and 6a). For this configuration, it can either be implanted or injected [39]. The PF-PEGDA precursor solution mixed with vancomycin can be cured by UV irradiation to form the hydrogel first and then implanted in the surgical site. The other option is by injecting the PF-PEGDA-vancomycin precursor solution into the surgical site then using UV light for in situ photopolymerization of the hydrogel.

As discussed in a previous study by Nguyen and colleagues, rheological data is important in the development of controlled release hydrogel systems as it can be used to predict steady flux for drug permeation using an empirical formula, known as the universal power law [29]. According to the fractional Stokes-Einstein relation, $D(G^*_{max})^{\varepsilon}$ = constant. In addition, the Stokes Law for steady state condition is $J = C_0/(R_{gel} + R_{nylon})$, where R_{gel} and R_{nylon} are the resistance of the gel and nylon membrane, respectively.

In the current study, the PF-PEGDA gels were placed over a nylon filter membrane with pore size of 0.45 μm in diameter, in place of the rat skin membrane used in the previous study [29]. As the filter membrane is very permeable compared with the hydrogel, and its diffusional resistance is much smaller compared with the hydrogel's diffusional resistance, i.e., $R_{gel} >> R_{nylon}$. As a result, $J = C_0/R_{gel}$ where $R_{gel} = 1/D_{gel} = a(G^*_{max})^{\varepsilon}$. It can be easily deduced that $1/J = a(G^*_{max})^{\varepsilon}/C_0$, where J is the flux of the diffusants through a membrane, C_0 is the initial concentration of the diffusants in the gel, while a and ε are constants depending on diffusant-gel types. Hence, $\ln(1/J) = \ln(a) + \ln(G^*_{max})^{\varepsilon} - \ln(C_0) = \varepsilon \ln(G^*_{max}) + \text{constant}$.

In the current study it was found that drug permeation and gel rigidity was strongly correlated (Fig. 4a and b). This relationship is represented by the equation $\ln(1/J) = 0.482 \ln G^*_{max} - 6.938$. The result shows, for the first time, that PF-PEGDA gels, as a polymeric gel, also follow the universal power law, with the power $\varepsilon = 0.482$. This finding is important owing to the following two reasons. First, unlike the previous study where organo-gels were used [29], hydrogels were used in the current study. This has demonstrated that universal power law is applicable to both organo-gels and hydrogels. Second, rat skin samples were used in the previous study while nylon filter membranes were used in the current study. Compared with the rat skin membrane, the filter membrane poses little or no diffusion resistance to the diffusants. However, the drastic change of diffusion membranes did not affect the applicability of the universal power law, which depends solely on the diffusant-gel system.

When designing the drug delivery system, it is important to consider both gel rigidity and drug release rate. Excessive rigidity can retard drug release from hydrogel, potentially compromising the therapeutic efficacy of the hydrogel formulation. On the other hand, a gel that is too soft may not be stable to be applied onto the surgical sites.

4.2. Vancomycin depot on top of hydrogel

In this study, the vancomycin solution is envisaged as a drug depot, which facilitates a constantly and slowly release of the carried drugs. The blank hydrogel pad is envisaged as a hydrogel dressing, widely used in wound healing for hydration purposes. Placing a drug depot on top of hydrogel dressing can provide a means of adding antimicrobial agents onto the wound to facilitate wound healing. Compared with the first configuration, namely, drug laden hydrogel, this approach may be easier to implement in clinical settings.

In a recent report which used a similar setting to the lag release in the current study, it was found that the lag time is inversely related to the diffusion coefficient of the diffusant [40]. In the current study, similar results were obtained, i.e., greater diffusion coefficient resulted in shorter lag time, as shown in Fig. 3b. Besides, it was reported that the lag time is proportional to the squared thickness of the hydrogel [16,40]. Hence, the drug releasing profile can be customized by changing the characteristics of the hydrogel. For example, softer and thinner gels can be used if shorter lag time is needed.

4.3. Combinatory configuration

The two configurations can be combined, although experiments were not conducted in the current study. When burst release and lag release are combined, the drug release profile exhibits an initial burst release, which is followed by a near zero-order continual drug release (Fig. 6f). This approach may offer a fast onset of action and sustained drug release, preferable for wound healing.

In addition, two different drugs may be loaded into the hydrogel and drug depot respectively. The drug inside the hydrogel can be used for fast release to inhibit onset of microbial infections. The other drug, e.g., growth factors or other active ingredients, can be added in the depot placed on top of the hydrogel, which is to be released after a time lag, to aid in long term tissue regeneration and/or post-operative infections [41]. It should be noted that vancomycin may be unsuitable to treat multidrug-resistant bacteria caused infections [42,43]. In this case alternative antibiotics should be used. In addition, long-term exposure to a single antibiotic agent may cause antimicrobial resistance. To address this issue, the concurrent use of multiple antimicrobial agents may be considered [44].

Using this approach, clinicians may tailor treatment plans based on individual patient needs, for example, drug loading of 12 mg to release 6 mg within the first 12 h to inhibit the onset of microbial infections, and further 6 mg within 24 h for sustained microbial infection suppression. The mathematical model allows for customized design of hydrogels to fine-tune key parameters such as gel rigidity/dimension and drug loading.

4.4. Median sternotomy in rabbit model

As the use of PF-PEGDA hydrogel formulations may be advantageous in clinical applications, we evaluated the hydrogel in an animal model using rabbits. We selected median sternotomy (MS) as our model of choice, as MS has been shown with a complication rate of up to 5 %, a mortality rate approaching 80 %, and a high secondary infection during repeated sternotomies [45–47].

We included in our comparison bone wax, a known hemostatic agent widely used in MS for clinical applications [48]. PF-PEGDA hydrogels can be easily prepared off-site and kept surgically sterile before application. Several other materials have been evaluated previously for their osteogenic and osteoconductive capabilities in MS but with less customizability than PF-PEGDA hydrogels [32,48,49].

Notably, customizing the PEGDA concentration demonstrated beneficial properties during surgical manipulation albeit with a lower hemostatic function. However, it has been shown that hemostatic material, such as surgical bone wax, inhibits osteogenesis, increases inflammation, and may increase infection risk [48]. Although higher cellularity, fuzzy hyper-density, and enlarged callus formation, at the third week postoperatively, indicated a degree of inflammation and misalignment of sternal halves in some of the animals, an increased bone density with lower cellular infiltration in all PF-PEGDA hydrogel treated animal groups confirmed faster onset of osteo-genetic processes, when compared to control and bone wax-treated animals. The porous structure of hydrogel may have provided a cellular guidance leading to faster bone healing [32,48,49].

4.5. Applicability of the hydrogels in clinical settings

The first formulation, designed for direct application to the cut sternal edges, can provide localized antibiotic delivery while minimizing systemic toxicity. To mitigate concerns regarding tissue regeneration, the formulation strategy included optimizing the hydrogel's mechanical properties to support, rather than hinder, the healing process. Furthermore, the UV-initiation process is designed to be rapid and conducted at a wavelength that minimizes tissue damage, a consideration that is critical for applications involving open wounds.

Crucially, we emphasize the hydrogel's customizability, which is a significant advantage in its clinical applications. The PF-PEGDA hydrogel's composition can be varied to produce materials with different stiffness levels, thereby allowing for tailored application depending on the nature of the surgical site or skin wound.

Additionally, we have conducted thorough examinations of the material's UV-crosslinking characteristics prior to surgical applications. This step is essential to confirm the hydrogel's stability and performance in a surgical environment, ensuring that it meet the stringent requirements for both safety and efficacy in wound management.

Regarding the second configuration, which involves a vancomycin solution applied atop the hydrogel, one concern is about the practicality of maintaining the solution on the gel. However, with the development of carefully designed secondary dressings, the maintenance of the vancomycin solution atop the hydrogel becomes a viable option. These specially designed wound dressings would not only retain the solution but also ensure that it remains in effective contact with the hydrogel. This formulation was developed as an alternative strategy for scenarios where direct hydrogel application may not be feasible or in cases where additional vancomycin delivery is required after the initial application.

4.6. Limitations and future study

In the current study, the mathematical models based on Fick's second law was used, which could only describe drug release from isotropic hydrogels with uniform drugs distribution. With this method, the simulation of drug diffusion within non-uniform hydrogels is challenging, as local variation in gel rigidity and diffusion characteristics impact drug distribution. The issue can be addressed by using finite element methods, which use integration, instead of differential methods [30,50]. Finite element methods, when assisted by high-performance computing, could yield more accurate predictions, accounting for intricate structural variations and boundary conditions.

Second, the combinatory configuration, as simulated based on burst release and lag release, can be tested by performing drug release experiments using the hydrogels. When burst release and lag release are combined, fast onset of action plus near zero-order continual drug release can be achieved, which may be preferable for clinical applications, especially when multiple antibiotics need to be administrated.

In addition, a more detailed characterization of osteogenic, osteoinductive, and/or osteoconductive properties is necessary to parse the mechanisms of PF-PEGDA hydrogels' effects on bone remodeling and regeneration. Furthermore, in vivo studies of PF-PEGDA hydrogel formulations containing antibiotics, such as vancomycin, are needed to demonstrate its translatability into a clinical application to manage SSI.

5. Conclusion

PF-PEGDA hydrogel is a promising drug delivery system to administer vancomycin in situ to manage surgical site infection. As an injectable hydrogel, it offers quick gelation in minutes via photopolymerization for use in the clinical setting. Additionally, the drug release rate can be easily adjusted by using the simulation methods to suit different therapeutic needs. The proof-of-concept animal testing showed the potential of the hydrogel formulations to be used in clinical settings.

Ethics approval and consent to participate

All animal experiments were approved and performed in compliance with the National University of Singapore (NUS) Institutional Animal Care and Use Committee protocol R15–0409 and carried out in accordance with the National Advisory Committee for Laboratory Animal Research (NACLAR) Guidelines. All experiments were performed with the approval of the NUS Institutional Biosafety Committee protocol 2018–00717.

Consent for publication

Not applicable.

Funding

Funded by the Singapore National Medical Research Council under its Cooperative Basic Research Grant (NMRC/BNIG/2029/2015). Yunong Yuan is a recipient of University of Sydney-China Scholarship Council scholarship (No. 202008320366). Lifeng Kang is a recipient of the China Pharmaceutical University Global Partnership Program (HBJH202308).

CRediT authorship contribution statement

Duc-Viet Nguyen: Writing – original draft, Methodology, Investigation, Formal analysis, Data curation. **Yunong Yuan:** Writing – review & editing, Visualization, Validation, Software, Methodology, Investigation, Formal analysis, Data curation. **Marek Kukumberg:** Data curation, Investigation, Validation, Visualization, Writing – original draft.

Lingxin Wang: Writing – review & editing, Visualization, Validation, Formal analysis, Data curation, Conceptualization. **Seng Han Lim:** Writing – original draft, Methodology, Investigation, Formal analysis. **Ammar Mansoor Hassanbhai:** Writing – review & editing, Methodology, Investigation. **Mark Chong:** Writing – review & editing, Investigation, Formal analysis, Conceptualization. **Theodoros Kofidis:** Validation, Supervision, Resources, Funding acquisition. **Edwin C.K. Tan:** Writing – review & editing, Validation. **Dror Seliktar:** Validation, Methodology, Investigation. **Lifeng Kang:** Writing – review & editing, Validation, Supervision, Resources, Methodology, Investigation, Formal analysis, Conceptualization. **Abdul Jalil Rufaihah:** Writing – review & editing, Supervision, Resources, Project administration, Methodology, Investigation, Funding acquisition, Conceptualization.

Declaration of Generative AI and AI-assisted technologies in the writing process

No generative AI and AI-assisted technologies were used in the writing process.

Declaration of competing interest

The authors declare that they have no known competing financial interests or personal relationships that could have appeared to influence the work reported in this paper.

Data availability

All data are available from the corresponding authors upon request.

Appendix A. Supplementary data

Supplementary data to this article can be found online at https://doi.org/10.1016/j.bioadv.2024.213896.

References

[1] C.H. Liao, C.S. Chen, Y.C. Chen, N.E. Jiang, C.J. Farn, Y.S. Shen, M.L. Hsu, C. H. Chang, Vancomycin-loaded oxidized hyaluronic acid and adipic acid dihydrazide hydrogel: bio-compatibility, drug release, antimicrobial activity, and biofilm model, J. Microbiol. Immunol. Infect. 53 (2020) 525–531, https://doi.org/10.1016/j.jmii.2019.08.008.

[2] Y.D. Shi, F.Z. Qi, Y. Zhang, Treatment of sternal wound infections after open-heart surgery, Asian J. Surg. 37 (2014) 24–29, https://doi.org/10.1016/j.asjsur.2013.07.006.

[3] H.L. Lazar, T.V. Salm, R. Engelman, D. Orgill, S. Gordon, Prevention and management of sternal wound infections, J. Thorac. Cardiovasc. Surg. 152 (2016) 962–972, https://doi.org/10.1016/j.jtcvs.2016.01.060.

[4] C.T. Gustafson, F. Boakye-Agyeman, C.L. Brinkman, J.M. Reid, R. Patel, Z. Bajzer, M. Dadsetan, M.J. Yaszemski, Controlled delivery of vancomycin via charged hydrogels, PloS One 11 (2016) e0146401, https://doi.org/10.1371/journal.pone.0146401.

[5] A. Pradeep, J. Rangasamy, P.K. Varma, Recent developments in controlling sternal wound infection after cardiac surgery and measures to enhance sternal healing, Med. Res. Rev. 41 (2021) 709–724, https://doi.org/10.1002/med.21758.

[6] R. Engelman, D. Shahian, R. Shemin, T.S. Guy, D. Bratzler, F. Edwards, M. Jacobs, H. Fernando, C. Bridges, The society of thoracic surgeons practice guideline series: antibiotic prophylaxis in cardiac surgery, part II: antibiotic choice, Ann. Thorac. Surg. 83 (2007) 1569–1576, https://doi.org/10.1016/j.athoracsur.2006.09.046.

[7] H.L. Lazar, A. Ketchedjian, M. Haime, K. Karlson, H. Cabral, Topical vancomycin in combination with perioperative antibiotics and tight glycemic control helps to eliminate sternal wound infections, J. Thorac. Cardiovasc. Surg. 148 (2014) 1035–1040, https://doi.org/10.1016/j.jtcvs.2014.06.045.

[8] H.L. Lander, J.I. Ejiofor, S. McGurk, K. Tsuyoshi, P. Shekar, S.C. Body, Vancomycin paste does not reduce the incidence of deep sternal wound infection after cardiac operations, Ann. Thorac. Surg. 103 (2017) 497–503, https://doi.org/10.1016/j.athoracsur.2016.10.020.

[9] T.J. Vander Salm, O.N. Okike, M.K. Pasque, A.T. Pezzella, R. Lew, V. Traina, R. Mathieu, Reduction of sternal infection by application of topical vancomycin, J. Thorac. Cardiovasc. Surg. 98 (1989) 618–622, https://doi.org/10.1016/S0022-5223(19)34366-1.

[10] H.L. Lazar, H.L. Lander, Vancomycin paste and sternal wound infections, Ann. Thorac. Surg. 105 (2018) 335–336, https://doi.org/10.1016/j.athoracsur.2017.02.062.

[11] M. Servito, A. Khani-Hanjani, K.M. Smith, R.T. Tsuyuki, J.C. Mullen, Topical vancomycin and risk of sternal wound infections: a double-blind randomized controlled trial, Ann. Thorac. Surg. 114 (2022) 1555–1561, https://doi.org/10.1016/j.athoracsur.2021.11.012.

[12] A. Mandal, J.R. Clegg, A.C. Anselmo, S. Mitragotri, Hydrogels in the clinic, Bioeng Transl Med 5 (2020) e10158, https://doi.org/10.1002/btm2.10158.

[13] R. Narayanaswamy, V.P. Torchilin, Hydrogels and their applications in targeted drug delivery, Molecules 24 (2019) 603, https://doi.org/10.3390/molecules24030603.

[14] A.L. Lakes, R. Peyyala, J.L. Ebersole, D.A. Puleo, J.Z. Hilt, T.D. Dziubla, Synthesis and characterization of an antibacterial hydrogel containing covalently bound vancomycin, Biomacromolecules 15 (2014) 3009–3018, https://doi.org/10.1021/bm5006323.

[15] J. Hoque, B. Bhattacharjee, R.G. Prakash, K. Paramanandham, J. Haldar, Dual function injectable hydrogel for controlled release of antibiotic and local antibacterial therapy, Biomacromolecules 19 (2018) 267–278, https://doi.org/10.1021/acs.biomac.7b00979.

[16] L. Almany, D. Seliktar, Biosynthetic hydrogel scaffolds made from fibrinogen and polyethylene glycol for 3D cell cultures, Biomaterials 26 (2005) 2467–2477, https://doi.org/10.1016/j.biomaterials.2004.06.047.

[17] D. Dikovsky, H. Bianco-Peled, D. Seliktar, The effect of structural alterations of PEG-fibrinogen hydrogel scaffolds on 3-D cellular morphology and cellular migration, Biomaterials 27 (2006) 1496–1506, https://doi.org/10.1016/j.biomaterials.2005.09.038.

[18] I. Frisman, D. Seliktar, H. Bianco-Peled, Nanostructuring PEG-fibrinogen hydrogels to control cellular morphogenesis, Biomaterials 32 (2011) 7839–7846, https://doi.org/10.1016/j.biomaterials.2011.06.078.

[19] B.A.G. de Melo, Y.A. Jodat, E.M. Cruz, J.C. Benincasa, S.R. Shin, M.A. Porcionatto, Strategies to use fibrinogen as bioink for 3D bioprinting fibrin-based soft and hard tissues, Acta Biomater. 117 (2020) 60–76, https://doi.org/10.1016/j.actbio.2020.09.024.

[20] M. Samberg, R. Stone 2nd, S. Natesan, A. Kowalczewski, S. Becerra, N. Wrice, A. Cap, R. Christy, Platelet rich plasma hydrogels promote in vitro and in vivo angiogenic potential of adipose-derived stem cells, Acta Biomater. 87 (2019) 76–87, https://doi.org/10.1016/j.actbio.2019.01.039.

[21] C. Fuoco, M.L. Salvatori, A. Biondo, K. Shapira-Schweitzer, S. Santoleri, S. Antonini, S. Bernardini, F.S. Tedesco, S. Cannata, D. Seliktar, G. Cossu, C. Gargioli, Injectable polyethylene glycol-fibrinogen hydrogel adjuvant improves survival and differentiation of transplanted mesoangioblasts in acute and chronic skeletal-muscle degeneration, Skelet. Muscle 2 (2012) 24, https://doi.org/10.1186/2044-5040-2-24.

[22] C.T. Drinnan, G. Zhang, M.A. Alexander, A.S. Pulido, L.J. Suggs, Multimodal release of transforming growth factor-β1 and the BB isoform of platelet derived growth factor from PEGylated fibrin gels, J. Control. Release 147 (2010) 180–186, https://doi.org/10.1016/j.jconrel.2010.03.026.

[23] C.A. Joseph, C.W. McCarthy, A.G. Tyo, K.R. Hubbard, H.C. Fisher, J.A. Altscheffel, W. He, R. Pinnaratip, Y. Liu, B.P. Lee, R.M. Rajachar, Development of an injectable nitric oxide releasing poly(ethylene) glycol-fibrin adhesive hydrogel, ACS Biomater Sci. Eng. 5 (2019) 959–969, https://doi.org/10.1021/acsbiomaterials.8b01331.

[24] D. Ben-David, S. Srouji, K. Shapira-Schweitzer, O. Kossover, E. Ivanir, G. Kuhn, R. Müller, D. Seliktar, E. Livne, Low dose BMP-2 treatment for bone repair using a PEGylated fibrinogen hydrogel matrix, Biomaterials 34 (2013) 2902–2910, https://doi.org/10.1016/j.biomaterials.2013.01.035.

[25] Q. Lu, M. Pandya, A.J. Rufaihah, V. Rosa, H.J. Tong, D. Seliktar, W.S. Toh, Modulation of dental pulp stem cell odontogenesis in a tunable PEG-fibrinogen hydrogel system, Stem Cells Int. 2015 (2015) 525367, https://doi.org/10.1155/2015/525367.

[26] J. Hadgraft, Calculations of drug release rates from controlled release devices, Int. J. Pharm. 2 (1979) 177–194, https://doi.org/10.1016/0378-5173(79)90019-X.

[27] E. Tsakalozou, A. Babiskin, L. Zhao, Physiologically-based pharmacokinetic modeling to support bioequivalence and approval of generic products: a case for diclofenac sodium topical gel, 1%, CPT: Pharmacomet Syst Pharmacol 10 (2021) 399–411, https://doi.org/10.1002/psp4.12600.

[28] K. O'Donnell, A. Boyd, B.J. Meenan, Controlling fluid diffusion and release through mixed-molecular-weight poly(ethylene) glycol diacrylate (PEGDA) hydrogels, Materials 12 (2019), https://doi.org/10.3390/ma12203381.

[29] D.V. Nguyen, F. Li, H. Li, B.S. Wong, C.Y. Low, X.Y. Liu, L. Kang, Drug permeation through skin is inversely correlated with carrier gel rigidity, Mol. Pharm. 12 (2015) 444–452, https://doi.org/10.1021/mp500542a.

[30] Y. Yuan, C. Abeykoon, W. Mirihanage, A. Fernando, Y.-C. Kao, J.A.W. Harings, Prediction of temperature and crystal growth evolution during 3D printing of polymeric materials via extrusion, Mater. Des. 196 (2020) 109121, https://doi.org/10.1016/j.matdes.2020.109121.

[31] C. Emoto, T.N. Johnson, B.T. McPhail, A.A. Vinks, T. Fukuda, Using a vancomycin PBPK model in special populations to elucidate case-based clinical PK observations, CPT Pharmacometrics Syst. Pharmacol. 7 (2018) 237–250, https://doi.org/10.1002/psp4.12279.

[32] A. Rainer, C. Spadaccio, P. Sedati, F. De Marco, S. Carotti, M. Lusini, G. Vadalà, A. Di Martino, S. Morini, M. Chello, E. Covino, V. Denaro, M. Trombetta, Electrospun hydroxyapatite-functionalized PLLA scaffold: potential applications in sternal bone healing, Ann. Biomed. Eng. 39 (2011) 1882–1890, https://doi.org/10.1007/s10439-011-0289-2.

[33] T. Kamitani, H. Masumoto, H. Kotani, T. Ikeda, S.H. Hyon, R. Sakata, Prevention of retrosternal adhesion by novel biocompatible glue derived from food additives, J. Thorac. Cardiovasc. Surg. 146 (2013) 1232–1238, https://doi.org/10.1016/j.jtcvs.2013.02.001.

[34] S. Miyamoto, K. Shimono, Molecular modeling to estimate the diffusion coefficients of drugs and other small molecules, Molecules 25 (2020), https://doi.org/10.3390/molecules25225340.
[35] Q. Zhu, X. Gao, M.D. Brown, F. Eismont, W. Gu, Transport of vancomycin and cefepime into human intervertebral discs: quantitative analyses, Spine 44 (2019) E992–E999, https://doi.org/10.1097/BRS.0000000000003028.
[36] J. Siepmann, N.A. Peppas, Higuchi equation: derivation, applications, use and misuse, Int. J. Pharm. 418 (2011) 6–12, https://doi.org/10.1016/j.ijpharm.2011.03.051.
[37] I. Firlar, M. Altunbek, C. McCarthy, M. Ramalingam, G. Camci-Unal, Functional hydrogels for treatment of chronic wounds, Gels 8 (2022), https://doi.org/10.3390/gels8020127.
[38] H. Chen, Y. Cheng, J. Tian, P. Yang, X. Zhang, Y. Chen, Y. Hu, J. Wu, Dissolved oxygen from microalgae-gel patch promotes chronic wound healing in diabetes, Sci Adv 6 (2020) eaba4311, https://doi.org/10.1126/sciadv.aba4311.
[39] J.D. Caplin, A.J. Garcia, Implantable antimicrobial biomaterials for local drug delivery in bone infection models, Acta Biomater. 93 (2019) 2–11, https://doi.org/10.1016/j.actbio.2019.01.015.
[40] G. Kalosakas, E. Panagopoulou, Lag time in diffusion-controlled release formulations containing a drug-free outer layer, Processes 10 (2022), https://doi.org/10.3390/pr10122592.
[41] Z. Lv, T. Hu, Y. Bian, G. Wang, Z. Wu, H. Li, X. Liu, S. Yang, C. Tan, R. Liang, X. Weng, A MgFe-LDH nanosheet-incorporated smart thermo-responsive hydrogel with controllable growth factor releasing capability for bone regeneration, Adv. Mater. 35 (2023) e2206545, https://doi.org/10.1002/adma.202206545.
[42] Y. Cong, S. Yang, X. Rao, Vancomycin resistant Staphylococcus aureus infections: a review of case updating and clinical features, J. Adv. Res. 21 (2020) 169–176, https://doi.org/10.1016/j.jare.2019.10.005.
[43] R.P.J. Willems, K. van Dijk, M. Vehreschild, L.M. Biehl, J.C.F. Ket, S. Remmelzwaal, C. Vandenbroucke-Grauls, Incidence of infection with multidrug-resistant gram-negative bacteria and vancomycin-resistant enterococci in carriers: a systematic review and meta-regression analysis, Lancet Infect. Dis. 23 (2023) 719–731, https://doi.org/10.1016/S1473-3099(22)00811-8.
[44] L. Yang, A.A. Yergeshov, Y. Al-Thaher, S. Avdokushina, E. Statsenko, T.I. Abdullin, P. Prokopovich, Nanocomposite orthopaedic bone cement combining long-acting dual antimicrobial drugs, Biomater Adv 153 (2023) 213538, https://doi.org/10.1016/j.bioadv.2023.213538.
[45] P. Hota, C. Dass, C. Erkmen, A. Donuru, M. Kumaran, Poststernotomy complications: a multimodal review of normal and abnormal postoperative imaging findings, AJR Am. J. Roentgenol. 211 (2018) 1194–1205, https://doi.org/10.2214/AJR.18.19782.
[46] J.E. Losanoff, B.W. Richman, J.W. Jones, Disruption and infection of median sternotomy: a comprehensive review, Eur. J. Cardiothorac. Surg. 21 (2002) 831–839, https://doi.org/10.1016/s1010-7940(02)00124-0.
[47] C. Heilmann, R. Stahl, C. Schneider, T. Sukhodolya, M. Siepe, M. Olschewski, F. Beyersdorf, Wound complications after median sternotomy: a single-Centre study, Interact. Cardiovasc. Thorac. Surg. 16 (2013) 643–648, https://doi.org/10.1093/icvts/ivs554.
[48] T. Wellisz, J.K. Armstrong, J. Cambridge, Y.H. An, X. Wen, C.M. Hill, T.C. Fisher, The effects of a soluble polymer and bone wax on sternal healing in an animal model, Ann. Thorac. Surg. 85 (2008) 1776–1780, https://doi.org/10.1016/j.athoracsur.2007.11.042.
[49] M. Shibata, G. Takagi, M. Kudo, J. Kurita, Y. Kawamoto, Y. Miyagi, M. Kanazashi, T. Sakatani, Z. Naito, Y. Tabata, M. Miyamoto, T. Nitta, Enhanced sternal healing through platelet-rich plasma and biodegradable gelatin hydrogel, Tissue Eng. Part A 24 (2018) 1406–1412, https://doi.org/10.1089/ten.TEA.2017.0505.
[50] Y. Yuan, Y. Han, C.W. Yap, J.S. Kochhar, H. Li, X. Xiang, L. Kang, Prediction of drug permeation through microneedled skin by machine learning, Bioeng Transl Med (2023) e10512, https://doi.org/10.1002/btm2.10512.